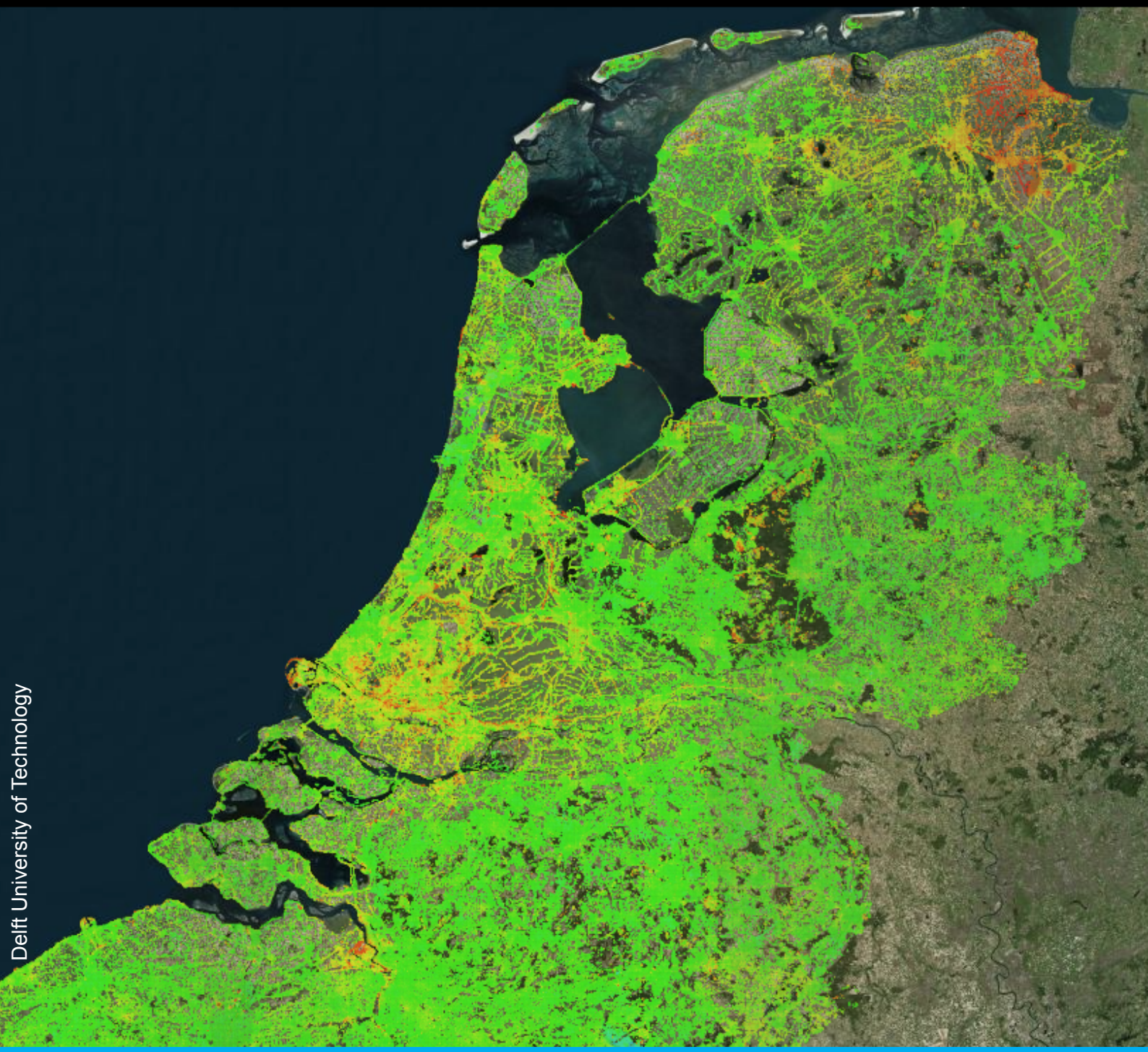

Delft University of Technology

On the robustness of InSAR displacement estimates for monitoring purposes

Yuran Gelejinse

TU Delft

On the robustness of InSAR displacement estimates for monitoring purposes

by

Yuran Geleijnse

to obtain the degree of Master of Science
at the Delft University of Technology,
to be defended publicly on Thursday January 18, 2024 at 15:00 AM.

Student number:	4956109	
Project duration:	March 21, 2023 – January 18, 2024	
Thesis committee:	Prof. dr. ir. R. F. Hanssen,	TU Delft, supervisor, chair of the committee
	Ir. W. S. Brouwer,	TU Delft, daily supervisor
	Prof. dr. ir. B.J.H. Van de Wiel,	TU Delft, supervisor

An electronic version of this thesis is available at http://repository.tudelft.nl/.

TU Delft

Preface

This thesis marks the end of my journey in Delft which has spanned five and a half years in total. The pages that follow contain my master's thesis, the product of ten months of dedicated research, and countless moments of ups and downs. Luckily, this work has not been a solitary one, but a collaborative effort, enriched by the wisdom and encouragement of numerous individuals who have played a role in shaping my academic work and me as a person. Therefore, I would like to thank many of these people.

First, I would like to express my appreciation to Wietske as my daily supervisor. Your unwavering support and clear explanations have been a guiding beacon throughout this thesis journey and the willingness to lend a helping hand and share invaluable insights have been crucial in the realization of this work. Next, I want to thank Ramon, my chair for challenging me beyond the boundaries I had set for myself. Your guidance to explore uncharted territories has been both enlightening and empowering, pushing me to exceed my limits. Also, I would like to thank Bas for his feedback and contribution as my third supervisor. The CAROLINE group deserves special mention for the nice discussions during our daily huddles. The collective knowledge and willingness to aid whenever challenges arise are very much appreciated.

There are many other people, to whom I owe a great thank you for guidance in life next to the thesis. To my roommates, consistently bringing light to the evenings, and to everyone in the 'afstudeerhok' for the daily conversations and challenging games that turned each day into an enjoyable experience. To my mom, dad, sister, and Ilse- your belief in me fuel my perseverance, and your support and encouragement are the pillars of my robust life. Last, but certainly not least, I express my gratitude to my friends who have been an unmissable part of my studies. Your presence and shared experiences have made these years truly unforgettable.

Delft, January 2024

Abstract

Interferometric Synthetic Aperture Radar (InSAR) stands as a widely adopted technique for monitoring displacements on the Earth's surface, providing millimeter-level precision. Several InSAR studies show the efficacy in retrospectively identifying hazardous situations, such as the failure of a structure. The next imperative step is to detect and identify anomalous points proactively. This necessitates robust and repeatable displacement estimates to avoid misinterpretation and instill confidence in the results.

Many InSAR studies use a batch estimation process requiring a robust algorithm to obtain reliable results. Here we propose a test recipe and introduce metrics to assess the robustness of the InSAR displacement estimates quantitatively, comparing the batch-estimated results of varying SAR acquisition inputs. Robustness characterizes the stability of displacement estimates in the face of disturbances and uncertainties, demonstrating resilience against changing conditions and input. Our quantification of robustness involves three core metrics to assess InSAR displacement estimates.

Case studies conducted over the city center of Amsterdam and a coastal region at the North Sea reveal the useful insight provided by robustness testing in identifying ambiguities and fallacies in the applied algorithm. Notably, the main challenges arise from the estimation of atmospheric delay, which emerges as a sensitive step with ample room for enhancement. A robust atmospheric estimation appears very dependent on the use of a sufficiently large area of interest while the estimation is sensitive to first-order network changes.

Through the implementation of appropriate measures, an average metric improvement of a factor of four can be achieved, reducing the likelihood of a misinterpretation of the InSAR time series. This underscores the effectiveness of the proposed test recipe in improving existing InSAR software.

Glossary

batch estimation estimating parameters based on all observations available at the time of the estimation, without taking prior estimation results into account.

brute force The production of outcomes ignoring any prior awareness of results obtained for identical parameters.

measurement update The process of incorporating a newly acquired SAR acquisition into an existing stack.

realization Result of a brute force DePSI run on a given set of SAR acquisitions.

recursive estimation estimation of the values of unknown parameters by combining (i) the results of earlier estimation runs and (ii) new observations from more recent acquisitions.

run Brute force processing of a certain stack.

stack Collection of SAR SLC datasets, coregistered to a single reference (mother) acquisition.

Acronyms

ΔASTM Differential Atmospheric Space-Time Matrix.

ΔSTM Differential Space-Time Matrix.

AO Ambiguity Overview.

APS Atmospheric Phase Screen.

AWLTD Area-Wide Long-Term Deviation.

AWSTD Area-Wide Short-Term Deviation.

CCDS Continously Coherent Distributed Scatterer.

CCPS Continously Coherent Point Scatterer.

DePSI Delft implementation of Persistent Scatterer Interferometry.

FAM Fraction of Ambiguous Measurements.

FLLTA Fraction of Localized Long-Term Ambiguities.

FLSTA Fraction of Localized Short-Term Ambiguities.

IDD Incremental Displacement Difference.

IDS Incoherent Distributed Scatterer.

IGRS Integrated Geodetic Reference Station.

InSAR Interferometric Synthetic Aperture Radar.

IRM Incremental Robustness Metrics.

LLTD Localized Long-Term Deviation.

LSTD Localized Short-Term Deviation.

NAD Normalized Amplitude Dispersion.

NMAD Normalized Median Absolute Deviation.

PS Point Scatterer.

PS1 First-order Point Scatterer.

PS2 Second-order Point Scatterer.

RMSD Root Mean Squared Difference.

TCDS Temporary Coherent Distributed Scatterer.

TCPS Temporary Coherent Point Scatterer.

Contents

1 Introduction

1.1. Background and context

Since the 80s, the concept of utilizing Interferometric Synthetic Aperture Radar (InSAR) to measure displacements of (objects on) the surface of the Earth has been extensively developed (J. Hu et al., 2014). InSAR is based on the phase difference of scatterers in two radar satellite acquisitions taken at distinct epochs in order to estimate their relative displacement in time (Massonnet & Feigl, 1998).

With the displacement over time, one can see the effect of events such as landslides, earthquakes, and changes in groundwater levels (Osmanoğlu et al., 2016). Also, the stability of crucial civil structures can be monitored (F. Hu, van Leijen, et al., 2019). Studies have shown that the displacement of for instance levees could be monitored with mm precision (Özer et al., 2019). In the case of levees, the use of InSAR has many advantages over the current monitoring methods involving mostly visual inspections. The crucial advantage of radar data is that the data is there to use, meaning that the costs are negligible compared to reoccurring visual inspections of these levees. Besides, the revisit times are way shorter, and measurement possibilities do not depend on weather conditions. Locally optimized InSAR even outperforms leveling on the reliability of monitoring buildings in an inner city (Venmans et al., 2020). Compared to for instance the use of GPS, the point density will be much higher as well.

1.2. Caroline

This study is part of the CAROLINE project which is devoted to the monitoring of infrastructure (and possibly beyond). CAROLINE refers to *Contextual and Autonomous processing of satellite Radar Observations for Learning and Interpreting the Natural and built Environment* (Hanssen, 2021). The fundamental idea is to create a self-operating computer system in which InSAR and contextual data will be used to reach two objectives. The first objective is to produce a database of points with attribute values and displacement time series. At the moment, a table with points containing information such as the displacement on each epoch and a linear displacement rate exists, commonly referred to as the Space-Time Matrix (STM). However, much data is still to be added to improve the obtained estimates and the interpretation of the results by adding for instance the instantaneous velocity or non-linear deformation rates. In the context of monitoring a dike region, the inclusion of contextual information, such as temperature or water levels, has the potential to enhance our understanding of the dike behavior allowing for a better monitoring assessment. Besides, the points are to be labeled, since different conclusions can be drawn if a point represents either the crest or the slope of

a dike.

The second objective is to receive push notifications for points behaving beyond normality, meaning an anomaly to the expected behavior of a point. At the moment, a lot of data is available such as the Bodemdalingskaart (SkyGeo, 2023) or the European Ground Motion Service (Copernicus, 2023) on which there are millions of data points. These points can impossibly all be manually to detect a potential anomaly. Besides, every point is different requiring a specific function or stochastic model to describe the behavior. Therefore, an algorithm is required to enable the identification of potentially hazardous points that need further attention from an InSAR expert. With every new satellite overpass, a new measurement is obtained. This measurement informs us about any changes in the observed behavior, indicating whether preventative measures to avert a collapse should be implemented.

1.3. Problem statement

For the automatic monitoring objective, it is crucial that results are robust and reproducible. In this context, ”robust” implies that the estimated displacements for a single point at a specific moment in time exhibit minimal variation when using a different set of radar acquisitions. Given that InSAR is capable of detecting displacements on the order of millimeters (Özer et al., 2019), it would be unexpected that displacement estimates vary significantly, e.g. by a few millimeters when only the number of radar acquisitions varies. On the other hand, ”reproducible” signifies that employing the same input consistently yields the same result. The term robustness will be more extensively defined in section 3.1. Robustness is required to ensure that the algorithm is reliable enough to flag only points that have an anomalous behavior, instead of false alarms due to shortcomings in our algorithm. If points are often falsely flagged, one would lose faith in the use of InSAR for monitoring. Currently, robustness is rarely used in an InSAR context. Wang & Zhu (2016) use it to cover the improvement of a specific framework or estimators, ignoring a simple quantification of what robustness in InSAR really means.

We are aiming for an efficient way to perform the monitoring. Specifically, in the process of incorporating a newly acquired SAR acquisition into an existing stack, referred to as a *measurement update*, it is undesirable to recalculate every single displacement estimate. Such an approach, where a new acquisition triggers the entire estimation procedure anew, with complete disregard for estimation results from earlier estimation runs, is referred to as *batch estimation* (Teunissen, 2017). Batch estimation is therefore a *brute force* approach.

A more efficient way to deal with a new acquisition would be to update existing estimates recursively by using the newly acquired observation (Verburg, 2017). F. Hu et al. (2022) propose a *recursive estimation* monitoring procedure using the SAR amplitude to detect temporally consistent points and a Kalman filter to update parameters. However, this method of updating underscores the importance of having a degree of certainty about the accuracy of previous estimates. There is a risk of presuming that displacement time series have been unwrapped correctly when, in reality, the integer number of cycles may be fundamentally incorrect. Building upon an incorrect result will yield falsely detected points, for instance, points falsely implying downward acceleration or, even worse, undetected hazardous situations. In essence, the robustness of displacement estimates from previous epochs is crucial, and moreover, they should not depend on the stack length when constructing a time series.

Literature comprises numerous studies that suggest the *possibilities* of automatic monitoring of infrastructure using InSAR, providing specific examples where it could have proven beneficial in hindsight (Macchiarulo et al., 2022; Bianchini Ciampoli et al., 2019). An example is depicted in Fig. 1.1, where a collapsed quay wall in the old city center of Amsterdam is detected with InSAR in hindsight. More quay walls and bridges are on the verge of collapse and it would therefore be extremely convenient to detect hazardous locations before collapse

to possibly avoid loss of lives.

Figure 1.1: Monitoring batch result of a collapsed quay wall in the city center of Amsterdam (SkyGeo, 2023). The colored points represent scatterers in Amsterdam with the color indicating the average displacement velocity. The framework plot shows the behavior of a selected point at the collapsed quay wall indicated with a marker. The blue framework dots represent the displacement estimates and the grey dots the solutions of plus and minus one ambiguity level. This point accelerates in time, exemplified by the black line fit, until the collapse on the 1st of Sep 2020.

Automatic monitoring systems using a similar approach as in CAROLINE are already operational in some regions. For instance, Tuscany has implemented a semi-automatic monitoring system that provides information on the type of anomaly (i.e., slope instability, subsidence, uplift and geothermal activity) and corresponding risk to regional authorities (Raspini et al., 2018). Subsequent field investigations are then conducted to assess the severity of the anomalous points. Nevertheless, no definitive conclusions are drawn on the accuracy or validity of all detected anomalies through the field investigations in real-time monitoring. The problem is that hindsight is always 20/20. Analyzing and evaluating situations in retrospect is always easier than doing so in the present moment. The crucial future direction involves conducting actual real-time monitoring case studies detecting anomalies that can be validated. This approach will provide genuine insights into the capability of using InSAR for monitoring purposes. At the moment, the challenge lies not in the detection of potentially hazardous situations, but rather in achieving a robust and accurate estimation, enabling a reliable interpretation of anomalies.

Adding (obtaining) an extra SAR acquisition to the existing stack is anticipated to add more information to the point's behavior rather than redefining it. Especially in the case of a large number of acquisitions, the previously estimated displacement results are expected to converge to a certain estimate rather than suddenly significantly change. When monitoring, suddenly changing results can cause a wrong or inconsistent conclusion with the previous result. This way, we can not detect which epoch specifically changed. For a certain location, one could get a false warning or leave a dangerous situation undetected.

As an example, Fig. 1.2 shows the result of a neighboring quay wall perpendicular to the collapsed one in Fig. 1.1 in the center of Amsterdam. This dataset uses a different number of

acquisitions explaining different point locations and colors (velocities). The selected quay wall is estimated to experience a strong uplift. However, one could very much question this solution as other solutions seem at least as likely as the chosen path. The grey dots represent the plus and minus one ambiguity level of the (blue) displacement estimates. The displacement solution at the end of 2021 would for instance follow the lower grey path if one would judge by eye, resulting in a different velocity. As all estimated parameters from heights to velocities and displacements together form a total phase observation, the misinterpretation of one of the parts can have dramatic effects on the other estimated phases. The question is whether this solution is an incident or if a different batch estimated solution would yield the same result.

It could lead to a loss of confidence in the algorithm by users who expect consistent results if it appears that a lot of points are falsely flagged due to a lack of robustness. Especially if the time series estimates significantly change when new observations arrive, monitoring results will be worthless. As will be seen later in Figs. 2.10 and 2.11, some locations and epochs show very dramatic differences in line of sight displacements making it hard, if not impossible, to trust a single result for this location. The interpretation of these two graphs would lead to entirely different conclusions regarding the potential danger of the situation. Consequently, we can not monitor recursively as the newly added epoch depends on estimates that would be fundamentally different if processed at a different moment.

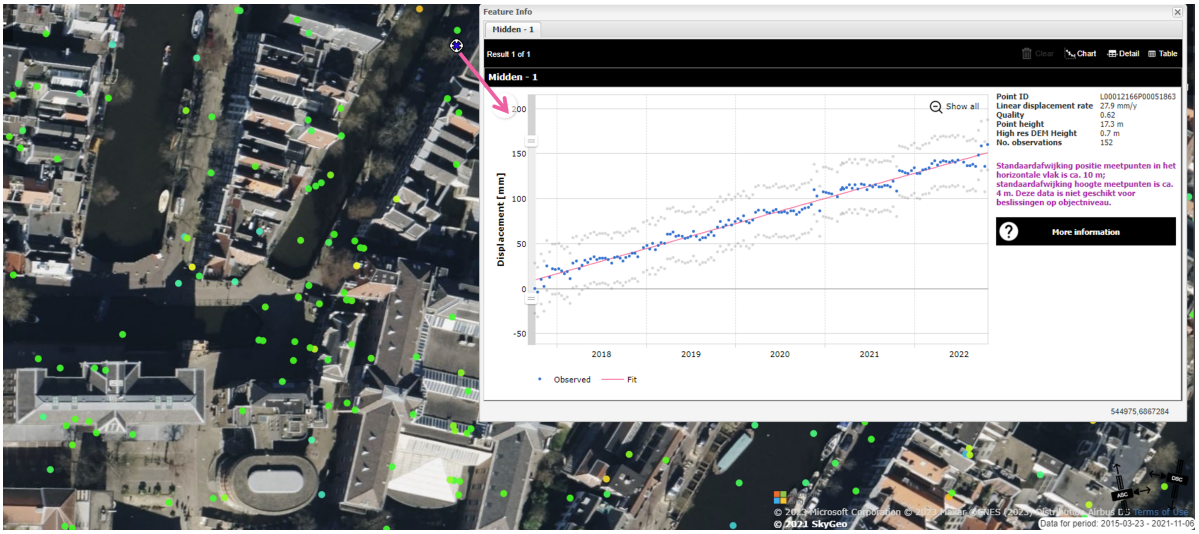

Figure 1.2: Monitoring batch result of a quay wall perpendicular to the collapsed quay wall in Fig. 1.1 the city center of Amsterdam (SkyGeo, 2023). The colored points represent scatterers in Amsterdam with the color indicating the average displacement velocity. The framework contains a plot showing the behavior of a selected point at a wall indicated with a marker. The blue dots in the framework represent the displacement estimates and the grey dots the solutions of plus and minus one ambiguity level. This point shows a strong uplift, though the behavior is questionable to say the least as following a different solution (grey dots) seems plausible as well.

Currently, several uncertainties surround the issue of robustness in the InSAR time series: (i) it remains unclear whether this robustness is a genuine problem. We do not know if the estimate changes are problematic, and how often they occur. (ii) The different kinds of problems we run into are not well-defined. Probably, the problems are correlated and not just randomly occurring. (iii) Equations and methods for detecting and quantifying these problems are undetermined as little to no research has been performed to quantify the robustness. (iv) The causes of the problems are unknown, and (v) corresponding solutions to solve these problems are not researched. These last two issues are inherent to each other as solutions can only be proposed if the causes of the problems are known. Tackling these uncertainties will be an essential step toward a robust, reliable, and reproducible result for monitoring purposes.

1.4. Research goal

While monitoring with the current batch estimation setup is undesirable as it is inefficient, it is currently unknown whether the displacements are reproducible and robust enough. Thus, this research aims to gain more insight and make recommendations to avoid these problems. The main research question within this thesis will be:

How can we assess the robustness of InSAR time series processing?

This main question will be answered with the help of the following sub-questions:

- When measurement updates arrive, do the InSAR time series parameter estimates change? If yes, what types of displacement estimate differences occur, and what is their impact?
- How can we quantify the robustness of InSAR displacement estimates?
- What is the cause for these displacement estimate differences?
- What are the requisites to obtain robust displacement estimates for monitoring civil infrastructure with InSAR?

In the end, all these questions together should lead to an insight into InSAR time series robustness and produce a recommendation for future monitoring.

1.5. Outline

The outline will roughly follow the addressed sub-questions which will also be the basis of the results chapter:

- In Chapter 2, the state of the art will be reviewed to see the current progress in the CAROLINE project and DePSI. First, some important basics of the DePSI algorithm will be described. Thereafter, current error types will be shown and hypotheses will be formulated.
- In Chapter 3, robustness will be defined and corresponding metrics will be developed to quantify the robustness. Besides, the testing recipe will be explained together with the graphs to interpret the results.
- Chapter 4 will see the application of the introduced metrics and graphs on the current DePSI algorithm (zero-state). After the analysis of the zero-state, several recommendations will be proposed to improve the robustness.
- Chapter 5 covers the result of these proposed improvements in the light of robust monitoring.
- Chapter 6 covers the conclusions and recommendations for future InSAR based monitoring.

2

Advancements in InSAR time series

Before any conclusions can be made about (the origin of) displacement estimate changes, we need to understand the underlying algorithm (DePSI) and current CAROLINE progress. Taking these considerations into account, we can differentiate between various error types and formulate hypotheses accordingly.

2.1. State of the Art: DePSI

Van Leijen (2014) developed an algorithm that forms the basis of the current displacement time series estimation in CAROLINE, called DePSI (Delft implementation of Persistent Scatterer Interferometry). Displacement time-series are estimated for Point Scatterers (PS) with a strong and coherent signal showing sufficient consistency in the reflections over time (Ferretti et al., 2001; Kampes, 2006). The principle of point scattering versus distributed scattering with concrete examples is depicted in Fig. 2.2. The input consists of several radar images provided by the user.

DePSI is a complex process well documented by Van Leijen (2014), which will thus not be discussed entirely in this thesis. Only the crucial steps leading to the phase unwrapping and the atmospheric delay will be touched upon in this chapter to create a context for robust displacement estimates and proposed improvements. Fig. 2.1 contains the flowchart of DePSI with all intermediate steps treated in this section. For extra details and more information, we refer to Van Leijen (2014).

2.1.1. InSAR basics

All data used in this thesis is obtained from Sentinel-1 satellites. The Sentinel-1 mission originally contained two polar-orbiting satellites (1A and 1B) and works with C-band radar imaging, centered around 5.405 GHz (European Space Agency, 2014). This corresponds to a wavelength of 5.55 cm. The spatial ground resolution is $\sim$5 m by $\sim$20 m and the corresponding pixel spacing is 4 m in azimuth and 13.9 m in range direction. Unfortunately, Sentinel 1B lost power in December 2021 and was subsequently deemed inoperable (ESA, 2022). For the Netherlands, this meant the temporal repeat period of Sentinel-1 shifted to 12 days instead of an observation every 6 days, meaning that scatterers with potential anomalous behavior are detected with a larger delay.

As observations with radar are from active remote sensing, a complex observation is made which can be converted to the amplitude A, indicating the amount of reflection reaching back to the satellite, and the phase φ, indicating the fraction of a wave returning to the satellite, without knowing the number of integer wavelengths (Hanssen, 2001). A SAR acquisition consists of

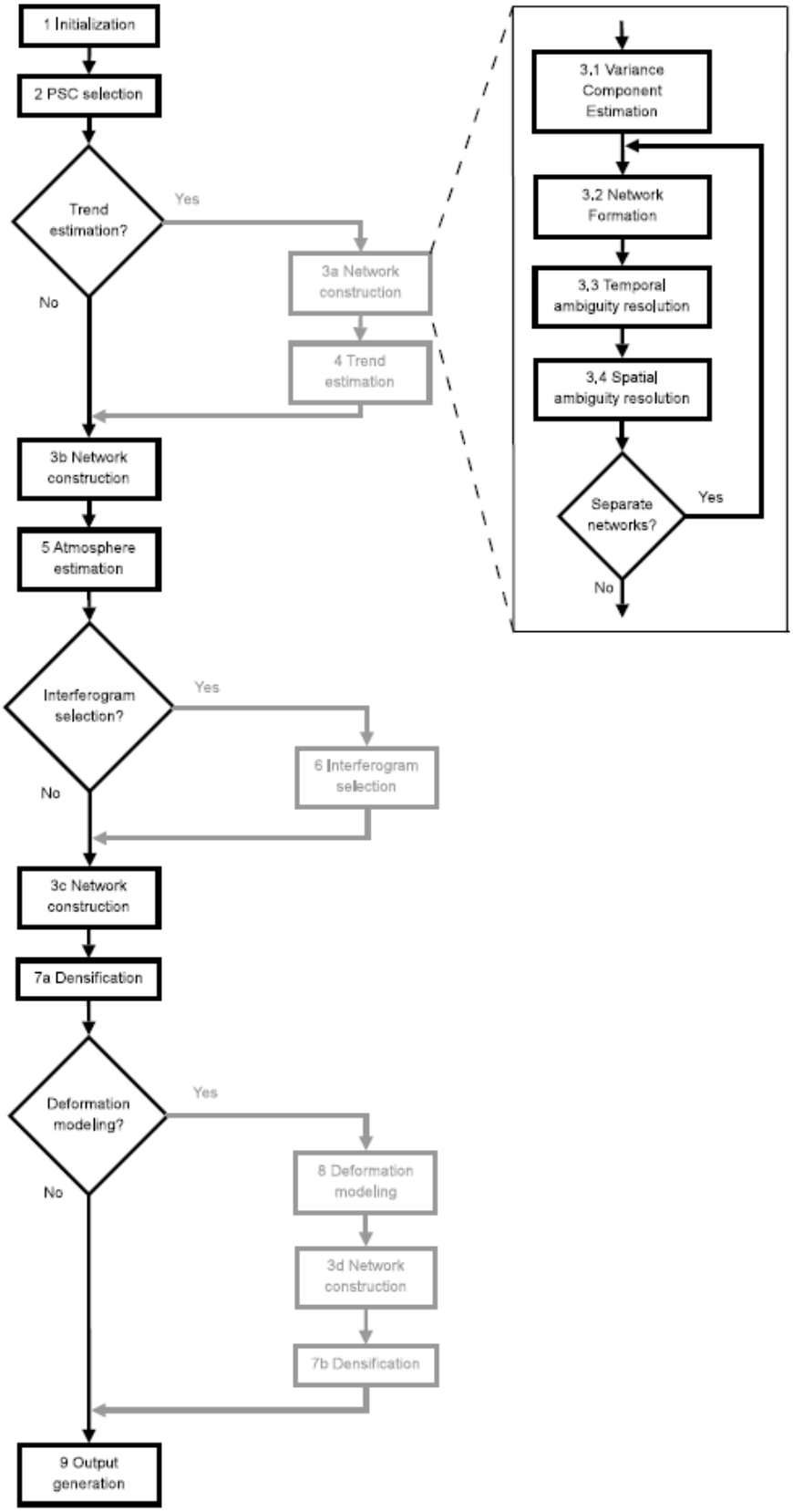

Figure 2.1: DePSI flowchart. Nine modules can be distinguished, indicated by a number. Reoccurring modules have an additional letter. The standard processing flow is shown in black, optional steps are indicated in gray. (Van Leijen, 2014, Figure 3.1)

a regular grid of individual pixels (i), represented in complex form by:

$$y_i = |A_i| e^{j\varphi_i}, \tag{2.1}$$

where A_i represents the amplitude and φ_i the phase in the interval $[-\pi,\pi)$.

2.1.2. Objective DePSI

The observed phase of one single pixel consists of many different signals. The observed Single-Look Complex phase, observed as in Eq. (2.1), is given by Hanssen (2001):

$$\varphi_{\text{obs}} = 2\pi a + \varphi_{2\times\text{range}} + \varphi_{\text{atmo}} + \varphi_{\text{scat}} + \varphi_{\text{noise}} \tag{2.2}$$

where a is the number of full phase cycles or integer ambiguity, φ_{range} the range from the Eucledian distance the radar signal has to travel, φ_{atmo} the phase due to the atmospheric delay, φ_{scat} the phase due to scattered signals and φ_{noise} represents the phase due to noise. A single phase estimate for a pixel is useless in itself as we do not know the exact number of integer cycles, and φ is unknown. Thus, we need to work with a relative or interferometric phase in time and space to achieve sufficient accuracy.

The interferometric phase is the phase difference between the mother image m with the radar image of a subsequent coregistered overpass d (daughter) in time. Taking the phase difference in space between two point scatterers, the reference point i, and another point j leads to the double-differenced phase φ_{ij}^{md} (Brouwer et al., 2023):

$$\varphi_{ij}^{md} = \varphi_j^{md} - \varphi_i^{md} = -2\pi a_{ij}^{md} + \varphi_{ij,D}^{md} + \varphi_{ij,H}^{md} + \varphi_{ij,S}^{md} + \varphi_{ij,n}^{md}, \tag{2.3}$$

where a again represents the real number of full-phase cycles, and φ_H, φ_S, φ_n the phases due to the height, atmospheric delay, and noise respectively. φ_D is the desired displacement phase, and the goal of DePSI is to estimate this displacement as accurately as possible.

The PS are linked in time by coregistration. In principle, all daughter images are resampled such that the pixels in a stack of daughter images cover the same geometry as the mother image. This stack of interferograms, or simply *stack*, will be the input for the DePSI algorithm. Given that the observed phase comprises various distinct components, it is important to capture all phase constituents correctly. This precision is crucial to capture a final displacement phase, as any variation in the estimated atmospheric phase e.g. will yield a corresponding alteration in the estimated displacement phase. The subsequent sections include some procedures to attain other phase constituents.

2.1.3. PS1 selection

One of the mentioned advantages of monitoring with InSAR is the spatial density of the observations. However, in certain instances, the coherence of signals from certain pixels may exhibit temporal inconsistency, or their estimation may lack sufficient certainty, thereby hindering the attainment of a reliable estimate for φ_{atmo} and, consequently, the displacement φ_{ij}^{md}. We only want to calculate and estimate parameters based on phase measurements of superior quality, meaning the result of coherent point scattering. Moreover, the drawback of complex images consisting of billions of pixels is that it poses a challenge to the efficient analysis of processing steps (Van Leijen, 2014). Therefore, strong and coherent Point Scatterer (PS) are selected based on their Normalized Amplitude Dispersion (NAD). The NAD (D_A), also referred to as *dispersion index* is a measure for the phase stability, and is given by Ferretti et al. (2001):

$$\sigma_\psi \approx \frac{\sigma_A}{\mu_A} \triangleq D_A, \tag{2.4}$$

where μ_A and σ_A represent the mean and standard deviation of the pixel's amplitude time series. By employing a threshold, only PS characterized by a notably low NAD will be retained. For the computation of the atmospheric phase delay, only PS with an arbitrary NAD value of less than 0.3 are considered. The different scattering and coherence combinations are shown in Table 2.1. In DePSI, the aim is to use the lowest NADs possible therewith mainly considering Continously Coherent Point Scatterers. The principle of point scattering versus distributed scattering is depicted in Fig. 2.2 containing concrete examples.

Table 2.1: Taxonomy of classes of scatterers based on coherence, including their acronyms, and expected normalized amplitude dispersion (NAD), from F. Hu, Wu, et al. (2019)

	Continuously Coherent	Temporary Coherent	Incoherent
Distr.Scat	**CCDS** NAD low	**TCDS** NAD high	**IDS** NAD medium
Point.Scat	**CCPS** NAD lowest	**TCPS** NAD highest	unlikely
	CCS	**TCS**	

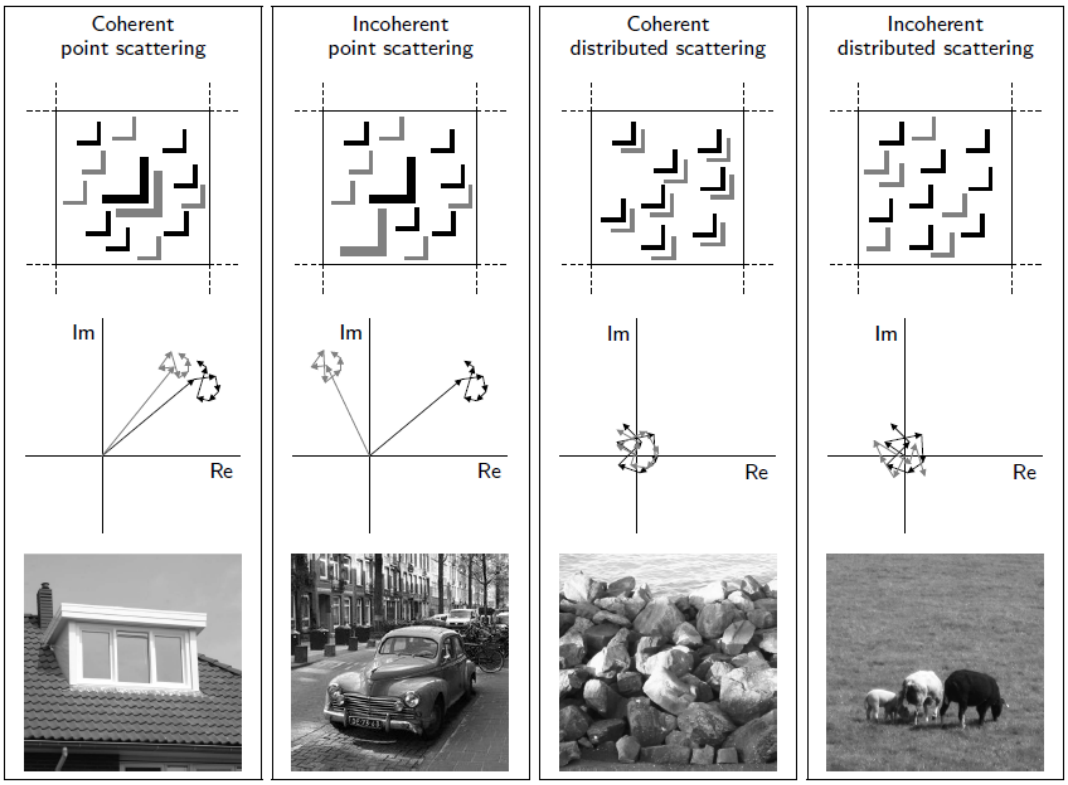

Figure 2.2: Point scattering versus distributed scattering in case of coherence or incoherence. Top) Scattering objects within a resolution cell at two acquisitions (indicated by black and gray reflecting objects). A large object corresponds to a strong reflection, whereas the small objects represent weak reflections. Middle) Phasors for the two acquisitions (again in black and gray). Bottom) Examples of scattering objects. (Van Leijen, 2014, Figure 2.2)

The selected PS together form a first-order network making them a First-order Point Scatterer (PS1). This selection step is represented by "2 PSC selection" in Fig. 2.1. Later this PS1 network will be densified by Second-order Point Scatterer (PS2) to obtain a better spatial resolution.

Thereafter, a relative radiometric calibration is performed to correct for different factors such as power loss and sensor differences (Laur et al., 2002). In DePSI, it is chosen to use a thousand pixels with the lowest amplitude dispersion to perform this calibration. This is needed to get a fair amplitude comparison for the stable scatterers and avoid other influences such as moisture differences between the images (Ketelaar, 2009). In this amplitude calibration algorithm, the calibration factors of 20 subsets, each containing 50 randomly selected points, are averaged to obtain one calibration value per epoch. After the radar image calibration, a subselection of PS1 is made to ensure a homogeneous distribution in space using shifted grids where only the PS with the lowest amplitude dispersion is kept in each grid cell. In the end, a PS1 network remains where points are connected via arcs. Kampes (2006) developed an algorithm where the closest neighboring points are connected until each point achieves a minimal number of connections. These arcs represent the phase difference of one point relative to a reference epoch and a reference point, and based on this network the phases are unwrapped and the atmospheric and orbital phase screens are estimated.

2.1.4. Phase unwrapping

After the creation of a network with arcs, the relative phase ambiguities a_{ij}^{md} need to be resolved, called phase *unwrapping*. Some possibly isolated points with limited stable arcs towards other PS1 are removed from the PS1 set, based on the ensemble coherence or variance factor quality indicator. The phase unwrapping step includes the (topographic) height difference, mother atmosphere, and displacement between PS1s and is therefore also referred to as parameter estimation. In DePSI, we choose to first unwrap the phase for each pixel temporally followed by the spatial unwrapping, see ”3a Network construction” in Fig. 2.1. To reduce the number of unknown parameters in the phase unwrapping step, functional model assumptions are made. The simplest assumption for the displacement $D_{md}^{i,j}$ is given by a steady-state model:

$$D_{md}^{i,j} = v^{i,j}(t_d - t_m), \tag{2.5}$$

where $v^{i,j}$ represents the average displacement rate of pixel j relative to pixel i, and t_m, t_d the time acquisition of the mother and daughter image. A stochastic model with all parameters is estimated by a variance component estimation (VCE), where the model gets an update after the removal of for instance the atmospheric phase screen. Spatially, a testing scheme is used to detect and adapt or remove incoherent PS1 as ambiguity inconsistencies in the network are changed until a closing network exists. This step is iteratively applied after the estimation of a new phase screen as well. The remaining points are subsequently used to spatially detrend the data caused by orbit inaccuracies.

2.1.5. Network selection

All parameters per arc, apart from the atmospheric phase delay, are estimated after the first network construction. Using the network of arcs created in section 2.1.3, one can get the individual estimations per PS relative to a single reference point. This means that the noise and displacement of the reference PS propagate into all other PS. If not explicitly specified in the parameter file, DePSI will choose a reference location selecting the PS1 with the highest temporal coherence. However, using the temporal coherence does not indicate anything of the displacement behavior of this reference PS.

2.1.6. Atmospheric phase screen

After the estimation of the displacements, height difference, and integer ambiguities, the Atmospheric Phase Screen (APS) for the PS1 is assumed to be lumped into the sum of the last two components of Eq. (2.3). These two components need to be disentangled. It is es-

timated in the fifth module, see Fig. 2.1. The atmosphere causes a phase (delay) difference between points (locations) and epochs, which needs to be estimated. Thus, this APS needs to be estimated to obtain the displacement in Eq. (2.3). However, to avoid the leakage of non-parameterized displacement into the atmosphere estimates, a deterministic low-pass (yearly) filter is run over the residual phase separating the non-parameterized displacement and APS. Fig. 2.3 contains an example of an arc where the atmosphere in blue and non-parameterized displacement in green are separated by the filter from the residual phase in red by means of a Gaussian window of one year.

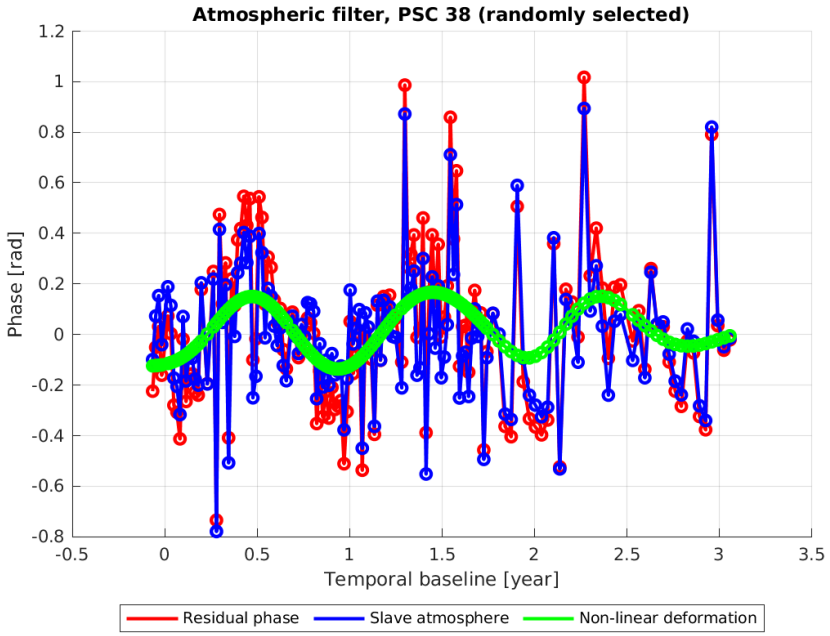

Figure 2.3: Seperation of the unmodelled non-parameterized displacement and the atmospheric signal from the residual phase by means of a low-pass (one-year Gaussian window) filter for a randomly selected PS1 relative to the reference PS1.

The APS is spatially correlated (Hanssen, 2001) and to make a smooth estimation over an area a variogram is constructed for each epoch in the stack. Only the PS1s are used as they appeared to be the most temporally coherent and thus expected to be the most reliable to base the atmospheric delay upon. The experimental semi-variogram is constructed by using (Matheron, 1962):

$$\hat{\gamma}(h) = \frac{1}{2N_h} \sum_{i=1}^{N_h} \left(Z(x_i + h) - Z(x_i)\right)^2, \tag{2.6}$$

where $Z(x_i + h)$ and $Z(x_i)$ are the atmospheric delay estimations of PS1 at locations x_j and x_i at a distance $h = |x_i - x_j|$ apart. N_h represents the number of pairs in bin $N(h)$.

A function is fitted to these experimental semi-variance observations to obtain a theoretical semi-variogram. Multiple functions exist to describe the experimental semi-variogram, from which the spherical, exponential, and Gaussian models are the most widely used functions (Oliver & Webster, 2014). From this theoretical semi-variogram, three parameters are deduced. The *nugget*, *sill*, and *range* describe the variogram's principal behavior. Fig. 2.4 visualizes a theoretical semi-variogram, indicating the meaning of the *nugget*, *sill*, and *range* parameter. The nugget describes the initial uncertainty in the data or measurement errors,

the sill indicates the value at which the semi-variogram levels out, and the range describes the distances to which sample locations are spatially correlated.

In summary, the atmospheric estimation process involves numerous parameters and choices, by which the displacement estimates are directly influenced if these change. The Atmospheric Phase Screen can then be estimated for all second-order PS (PS2) by means of interpolation using a Kriging method to densify the network and get a better spatial resolution for monitoring.

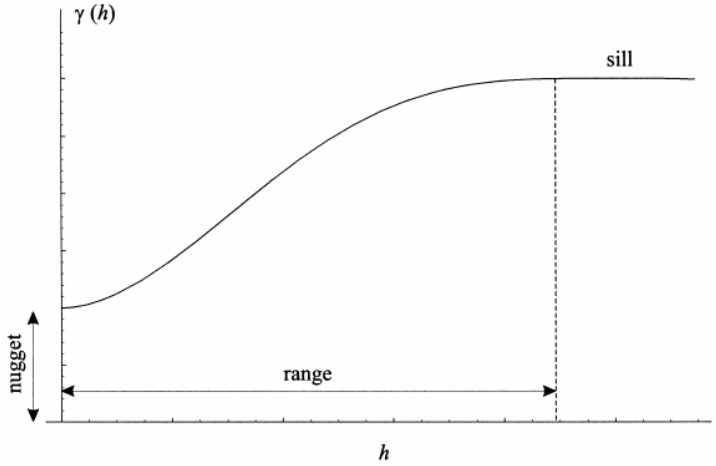

Figure 2.4: Schematic example of a theoretical semi-variogram fit, indicating the meaning of the *nugget*, *sill*, and *range* parameter (De Doncker et al., 2006, Figure 2).

2.2. Current CAROLINE progress

In the current progress for CAROLINE, the idea is to automatically process a 1 by 1 km region over Amsterdam by the DePSI algorithm for every Sentinel 1 track passing by. Every 12 days (current Sentinel-1 repeat period), a new image arrives for the same track. When a new satellite image is acquired, DePSI will be run with all collected radar images. This means that we start again from scratch, disregarding the phase estimates in the previous time series construction. With that, a new time series is estimated where all corresponding parameters such as the height, velocity, and atmospheric delay are re-estimated. Fig. 2.5a shows a screenshot of the principal layout in the CAROLINE portal. On the left-hand side of the map, a drop-down menu with all batch estimated solutions from 4 different tracks. These individually processed stacks can be selected based on the date of addition to the portal. For each processing, dots appear in space representing the estimated linear displacement in mm/year of a single PS. Selecting a point (dot) of interest, given the linear displacement rate, will show the brute forced time series of that particular PS, see Fig. 2.5b.

2.2.1. Schematic measurement updates

As mentioned in the problem statement, the literature contains no well-defined robustness tests to quantify the InSAR displacement results. While the batch estimation method may not represent the ultimate desired approach for monitoring due to its inefficiency and inconvenience, it serves as a valuable means to evaluate the extent of change in displacement estimation. Consequently, we will compare distinct batches of estimated results, as schematically illustrated in Fig. 2.6. The different solutions for the displacement estimates, after a measurement update, can be compared by linking the location in the radar image.

In the flat plane (top layer), we visualize the space-time matrix, with 'space' as rows, where each row represents a point scatterer (ten example PS in this case), and 'time' as columns,

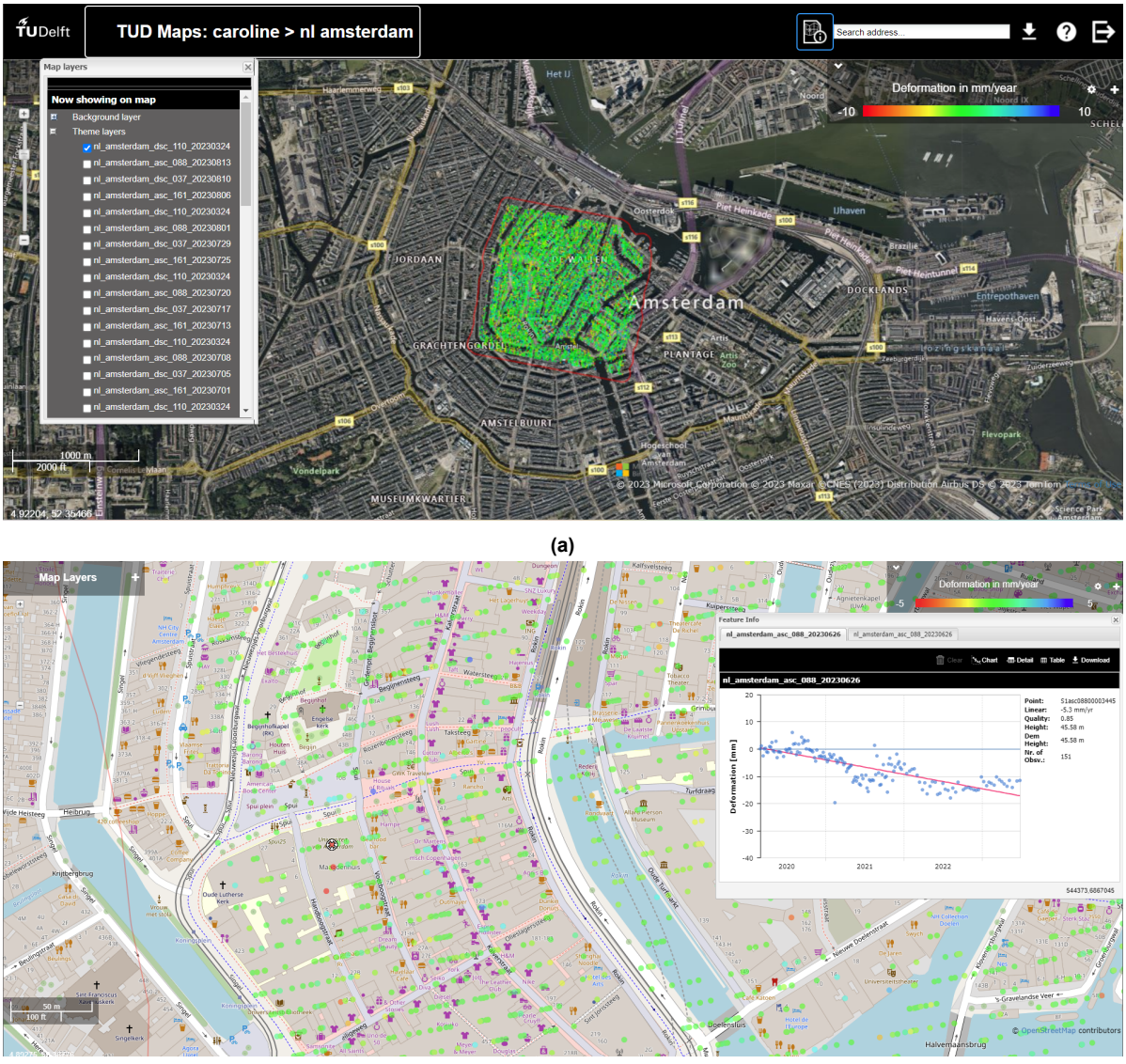

(a)

(b)

Figure 2.5: Screenshot of the starting view in the CAROLINE portal (a) and an example of a time series when selecting a point scatterer (b).

where each column corresponds to an acquisition/epoch. The top layer represents estimates for all epochs calculated after acquisition seven but before acquisition eight. In the second, underlying layer, we see the same space-time matrix: obtained after epoch eight but before epoch nine. This way, we sequentially create new space-time matrices, represented as layers in Fig. 2.6, with the majority of elements sharing the same parameter estimate (the displacement of point x at epoch t). The only difference between the different layers is that the estimates are based on a different number of input acquisitions. This number of input acquisitions is referred to as realizations. For example, realization eight is the space-time matrix obtained based on all acquisitions up to and including acquisition eight.

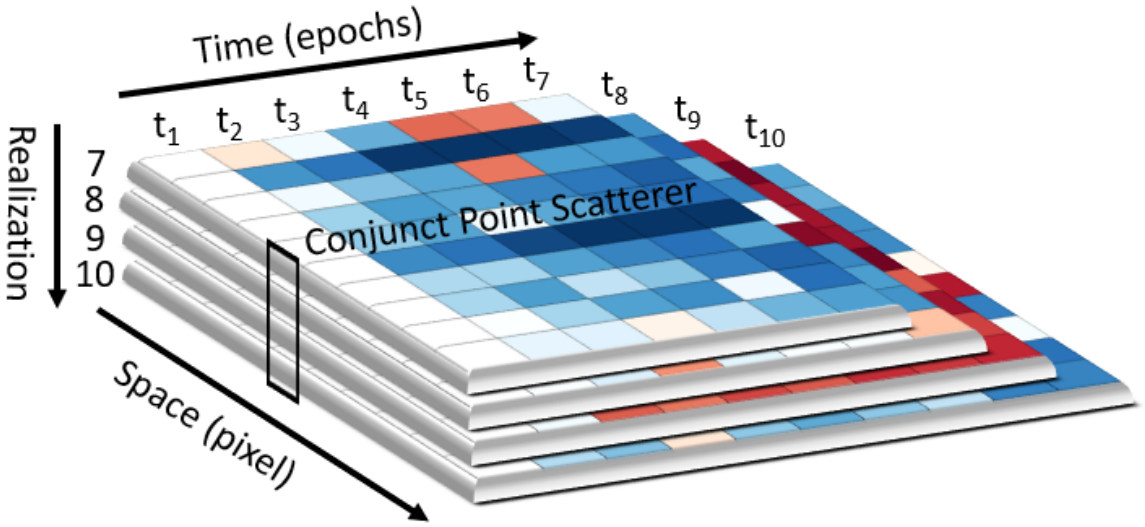

Figure 2.6: Schematic overview of several used terms. A red square indicates a high displacement value and a blue square a low value for all epochs included in ten conjunct example Point Scatterers (PS). With every new realization, a new epoch is included as a new satellite overpassed.

In Fig. 2.6, a red square signifies a positive displacement value (moving away from the satellite), and a blue square a negative value for that particular PS and that particular epoch. Each new realization comes with a new epoch as a new satellite is overpassed. To enable a meaningful comparison between realizations, only those PS that are common between realizations will be considered.

So, realization eight and realization ten contain estimates of the same parameters for epochs one through eight. Ideally, adding new epochs (i.e., SAR acquisitions nine and ten) should make little difference to the estimates of those earlier epochs (1-8). However, because the solutions are performed 'in batch', it may be possible that this is not the case. Therefore, we consider the differences between (the conjunct part of) epochs one to eight as a metric for the robustness of the estimation. If adding a new SAR acquisition, say acquisition 100, will cause significant changes in the estimated parameters compared to the estimated parameters from realization 99, that would be an indication of poor robustness.

Subsequently, we can take the conjunct part of two runs and take the difference between the two displacement matrices to obtain a *Differential Space-Time Matrix* (ΔSTM). An example of the construction of a *Differential Space-Time Matrix* is schematically shown in Fig. 2.7. Realization N is subtracted from realization $N-1$ to obtain $\Delta STM_{N,N-1}$ with $N-1$ overlapping acquistions.

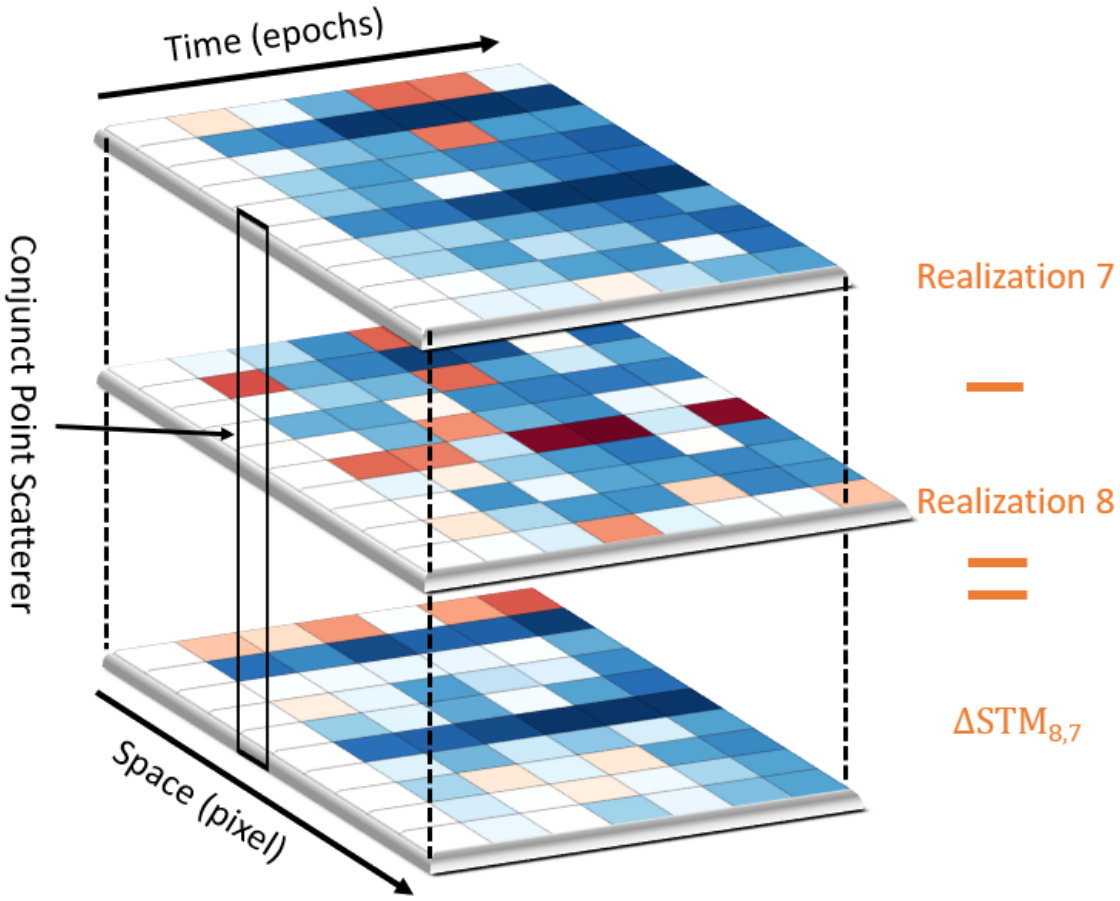

Figure 2.7: Schematic representation of the calculation of a Differential Space-Time Matrix. A red square indicates a high displacement value and a blue square a low value for all epochs included in ten conjunct example Point Scatterers (PS). The two top layers (realization 7 and 8) are the batch estimated results obtained when using 7 and 8 SAR acquisitions respectively.

2.2.2. Real case measurement updates

The current CAROLINE measurement updates also rely on this batch estimating procedure. All phase estimations (such as atmospheric and topographic corrections) are redone once a new image arrives, meaning the displacement estimates may change as well. Thus, we can evaluate the robustness of this real case simulation. At first sight, the time series from Fig. 2.5b looks plausible as there appears to be a clear signal. However, based on this visualization of the time series containing 140 acquisitions it is impossible to judge how robust the estimates are for the displacement. To check the stability of the estimates, these displacement estimates can be compared with the results for the batch estimation processing after the next satellite overpass some 12 days later with 141 acquisitions. Now, two realizations from the current CAROLINE output are used to create a real case ΔSTM using realizations 140 and 141. The entire DePSI process, starting from obtaining a new acquisition to the displacement estimates (realization), will be referred to as a *run*.

Fig. 2.8 shows a schematic representation of the output obtained from a DePSI run. There are three main parts. The yellow part contains the main PS-specific information. Table 2.2 shows an elaborated example of the DePSI output for the yellow part of an example PS. This information comprises the location parameters in WGS84, the pixel location in the image, linear deformation rate, spatial-temporal consistency, and coherence. The spatial-temporal consistency is a quality indicator comparing PS behavior in space and time with surrounding PS (Hanssen et al., 2008).

The green and blue parts of Fig. 2.8 contain the displacement and atmosphere estimation for each epoch. Table 2.3 shows an example of the displacement estimates output from DePSI. The same exists for the atmospheric delay estimates. We can extract the displacement data from the tabular format and organize it into a matrix resulting in a Space-Time Matrix. Here, time is represented along the horizontal axis and space along the vertical axis, see Fig. 2.6. Based on the PS Range and Azimuth value in the image, the Space-Time Matrices of two realizations are linked and a ΔSTM of the conjunct part can be constructed. Note that we take the absolute value of the differences since negative or positive differences are equally important.

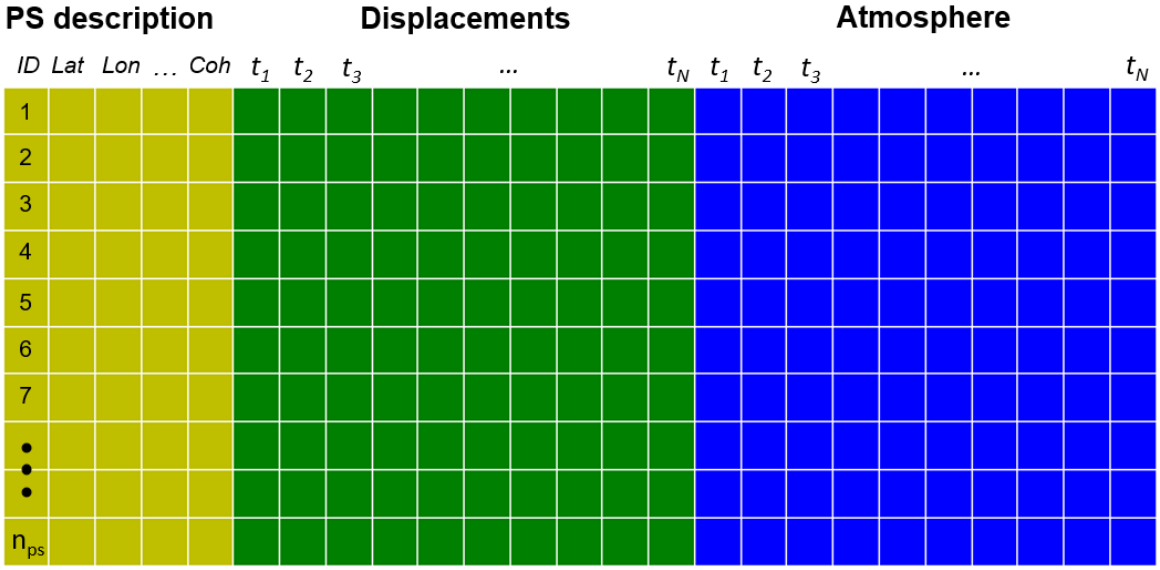

Figure 2.8: Schematic representation of the output from DePSI. The first yellow part contains the PS-specific information such as location and coherence. Thereafter, the green and blue parts contain the displacement and atmosphere estimates for all epochs 1 to N. Every row contains the information of one Point Scatterer.

Table 2.2: PS-specific output for an example PS.

ID	Lat [deg]	Lon [deg]	Height [m]	Azimuth	Range	Defo [mm/y]	STC [mm]	Coh
PS #1	52.266°	4.899°	50.50 m	1	182	1.13 mm/y	2.30 mm	0.906

Table 2.3: Example DePSI displacement output for the first three Point Scatterers.

ID	Displacements [mm]			
	1-Mar-'20	7-Mar-'20	...	2-Feb-'23
PS #1	0	−1.61	⋯	−1.66
PS #2	0	−3.55	⋯	−3.30
PS #3	0	−0.19	⋯	0.59

2.2.3. Deviation types

A visualization of the Δ*STM* can be generated, as depicted in Fig. 2.9. This Δ*STM* contains around 13500 points (rows, example in a horizontally shaped rectangle) conjunct in both realizations and 140 epochs (columns, example in a vertically shaped rectangle). Thus in total, there are almost two million conjunct estimates between realization 141 and realization 140. It is important to note that this matrix represents a simple time series difference on a single row, but now for all locations with a shared azimuth and range coordinate in the two datasets. The heatmap visualization has a logarithmic color scale, ranging from an insignificant difference (0.01 mm) to exactly one ambiguity level (27.7 mm in the case of the Sentinel-1 mission) to clearly discriminate between both small as well as large differences. This matrix will be noted as $\Delta STM_{y,x}$ where y and x represent the number of acquisitions as input in the two realizations. As the matrix in Fig. 2.9 represents the double differenced difference between stacks with 141 and 140 acquisitions, it is denoted by $\Delta STM_{141,140}$.

The displacement differences in Fig. 2.9 are not randomly spread over the Point Scatterer and epochs, but contain a pattern. Therefore, we define four 'deviation' categories to be able to group the differences. Table 2.4 shows the four categories, separating short-term and long-term, and localized and area-wide deviations., Three of these deviations are clearly distinguishable in the $\Delta STM_{141,140}$, indicated by the green rectangles. Fig. 2.9 contains (i) several horizontal white lines, highlighting a *Localized Long-Term Deviation*, (ii) incidental white stripes within a horizontal line, highlighting a *LSTD*, and (iii) clearly correlated vertical bands with higher values on certain epochs, highlighting an *Area-Wide Short-Term Deviation*. The fourth and last deviation category that is not visible in this figure is the *Area-Wide Long-Term Deviation*. This deviation type can occur as will be elaborated in the section 2.2.4. To keep an overview of the deviations and their hypotheses, a schematic chart has been made in Fig. 4.8.

Table 2.4: Classes of displacement estimate deviations possibly present comparing two batch estimated realizations.

	Short-term deviations (single epoch)	Long-term deviations
Localized deviations (single scatterer)	**LSTD**	**LLTD**
Area-wide deviations	**AWSTD**	**AWLTD**

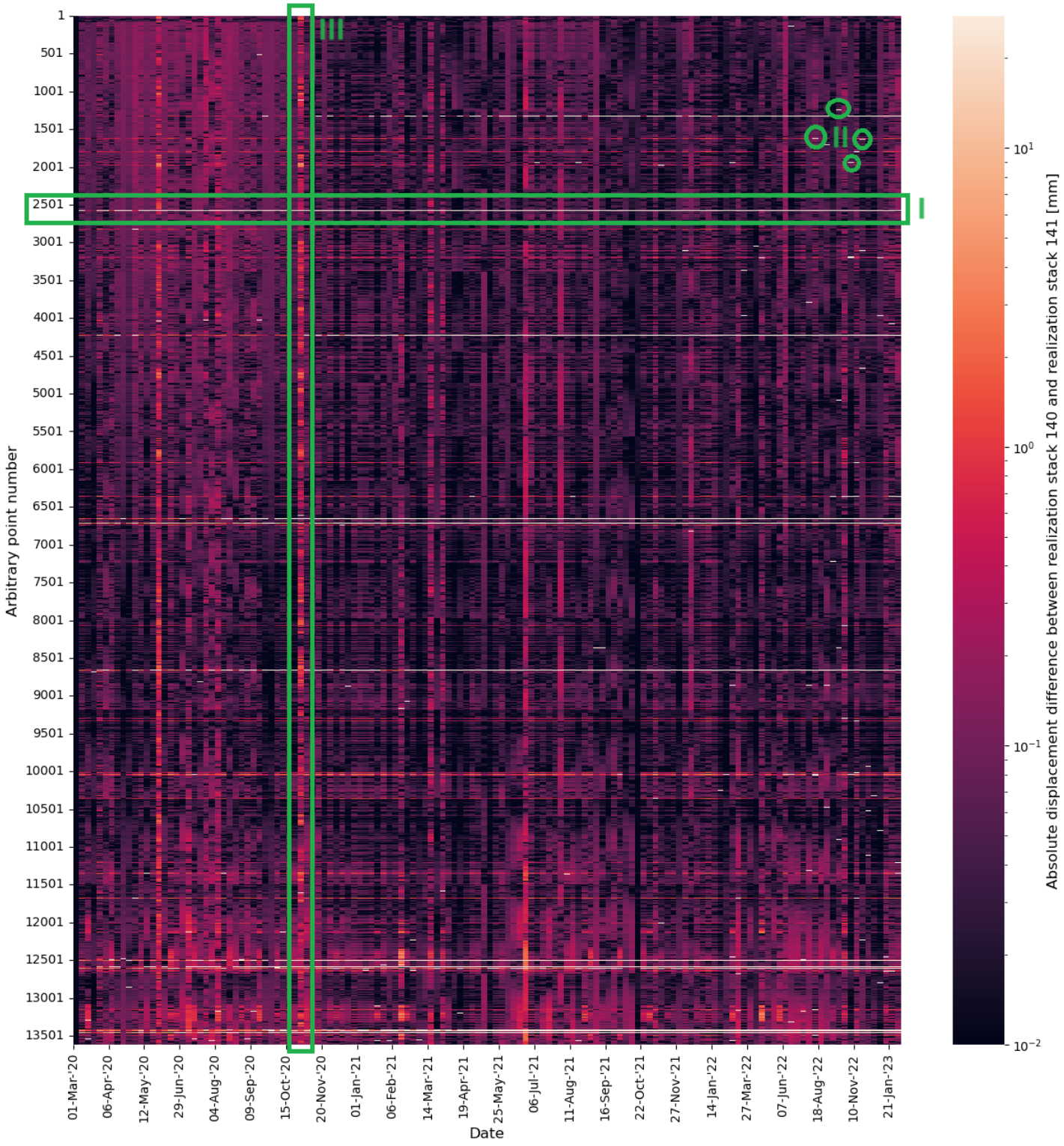

Figure 2.9: Visualization of the absolute $\Delta STM_{141,140}$ obtained from comparing the same PS in two different realizations 140 and 141. The horizontal axis contains the epoch date, starting from the 1st of March 2020 and the vertical axis represents an arbitrary point number. The green rectangles highlight three of the four deviation categories. The heatmap has a logarithmic color scale, ranging from an insignificant difference (0.01 mm) to one ambiguity level (27.8 mm).

Localized Long-Term Deviation

The first category of deviations is the *Localized Long-Term Deviation* illustrated as a horizontal white stripe and highlighted by green rectangle I in Fig. 2.9. Within this main category, we distinguish two subtypes. Firstly, we have the distinct horizontal white lines indicating that two totally different displacement time series were estimated, even though the difference was just one acquisition extra. Since the influence of a single additional acquisition is so significant, this is a clear indication of (a lack of) robustness. Secondly, $\Delta STM_{141,140}$ shows, brighter values that are horizontally correlated. These are deviations with a relatively small value, and because they are only significantly occurring at PS containing a white incidental stripe, they will be focussed upon in the next subsection of the Localized Short-Term Deviation.

The most severe deviation category consists of three further distinct types of deviations. In Fig. 2.10, an example of such a Point Scatterer appearing as a white line in $\Delta STM_{141,140}$ is shown. The result is substantial as the final displacement estimates of current dates differ over 150 mm, meaning that all parameters such as the velocity completely changed, while it ought to cover the same information. However, a closer examination of the displacement difference plot on the right in Fig. 2.10 suggests that the initial received phases were not significantly different, but the unwrapping changed. As the plot transitions between instances of integer ambiguities, variations in the phase unwrapping result in an upward trend rather than a downward one. Therefore, this deviation type is denoted as *ambiguous drift*. Undoubtedly, both solutions lead to a different conclusion when assessing the behavior of the PS. Such discrepancies can lead to a lack of trust among possible users of monitoring software as locations are falsely flagged or not identified as potentially dangerous.

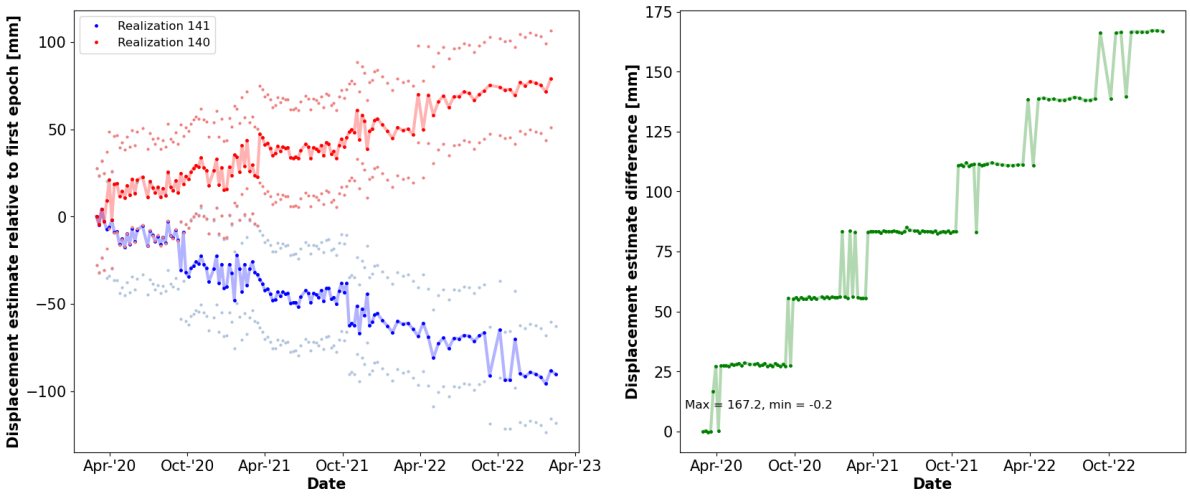

Figure 2.10: Example of a PS containing large displacement estimate differences in $\Delta STM_{141,140}$ of type *ambiguous drift*. The left plot shows both time series together with their ambiguities. The difference in line of sight displacement of these time series is plotted on the right.

The second type of LLTD is the *consequent ambiguity*. Fig. 2.11 contains an example of a PS that very quickly made one different integer ambiguity choice and almost consequently stays one ambiguity apart. For this deviation type, the estimated velocities and other parameters will be different as well.

The third and last severe LLTD type is the *uncorrelated difference*, see Fig. 2.12. In this graph, we see a very dynamic PS in both time series with differences that fluctuate tens of millimeters over time. As both time series seem to have little resemblance, one could have low confidence in the monitoring results for this particular location.

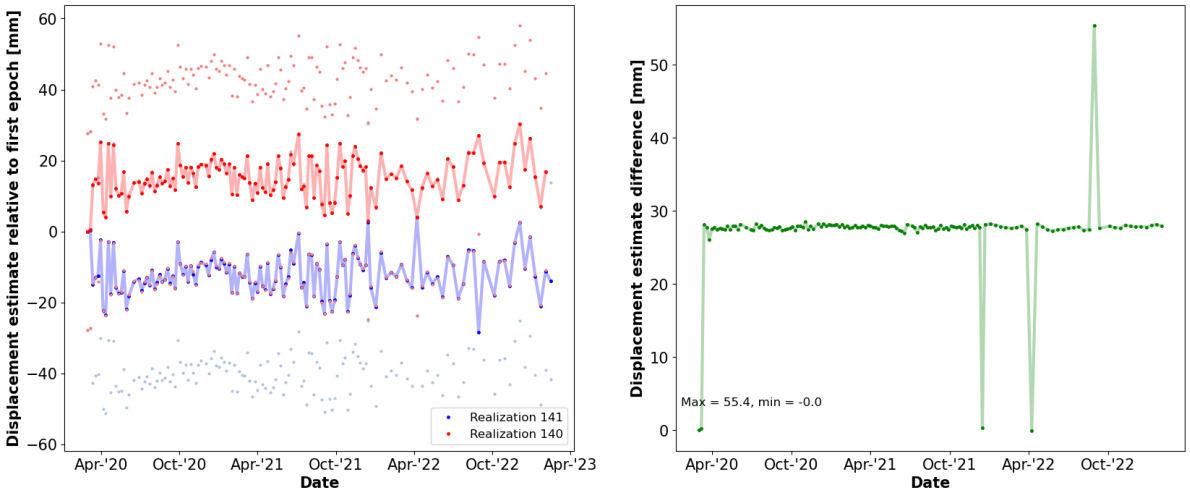

Figure 2.11: Example of a point scatterer containing large displacement estimate differences in $\Delta STM_{141,140}$ of type *consequent ambiguity*. The left plot shows both time series together with their ambiguities. The difference in line of sight displacement of these time series is plotted on the right.

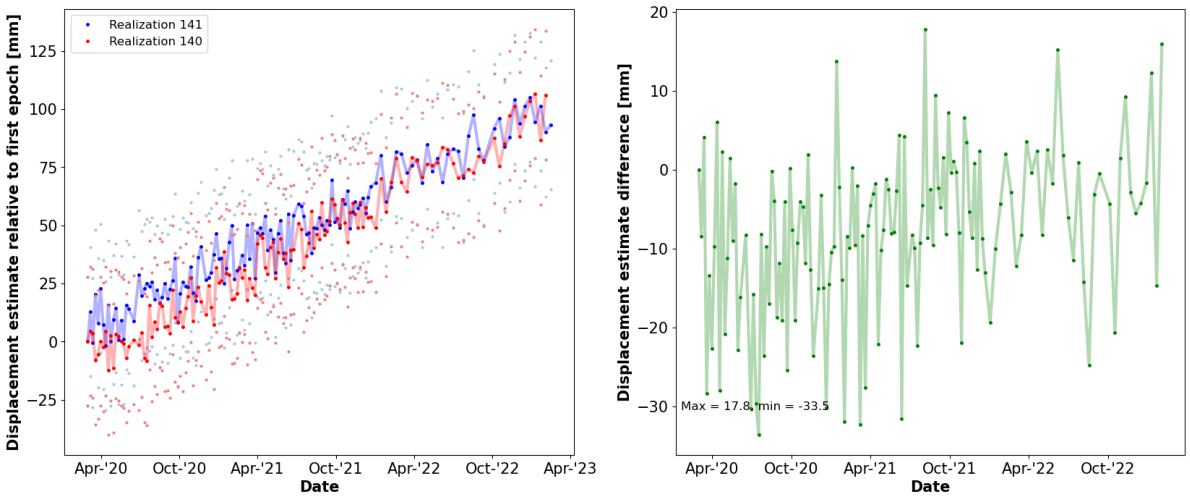

Figure 2.12: Example of a point scatterer containing large displacement estimate differences in $\Delta STM_{141,140}$ of type *uncorrelated difference*. The left plot shows both time series together with their ambiguities. The difference in line of sight displacement of these time series is plotted on the right.

Localized Short-Term Deviation

The second deviation category is the *Localized Short-Term Deviation*. This category is dominated by incidental ambiguity slips that frequently occur, looking at the incidental white stripes in the $\Delta STM_{141,140}$ heatmap, exemplified green circles II in Fig. 2.9. In Fig. 2.13, an example of such a PS with a localized short-term deviation is depicted. Across all epochs, the differences between the two estimated displacement time series are within 1 mm. However, one single displacement phase unwrapped differently even though this epoch was almost 2 years before the measurement update. These localized incidental ambiguities often occur in the last few epochs as well. This implies that monitoring based on instantaneous velocities over the last month (5 measurements), for instance, would yield different conclusions. Moreover, it suggests that the solution for some epochs is precarious, as it almost always coincides with a moderate Localized Long-Term Deviation complicating the determination of the correct solution.

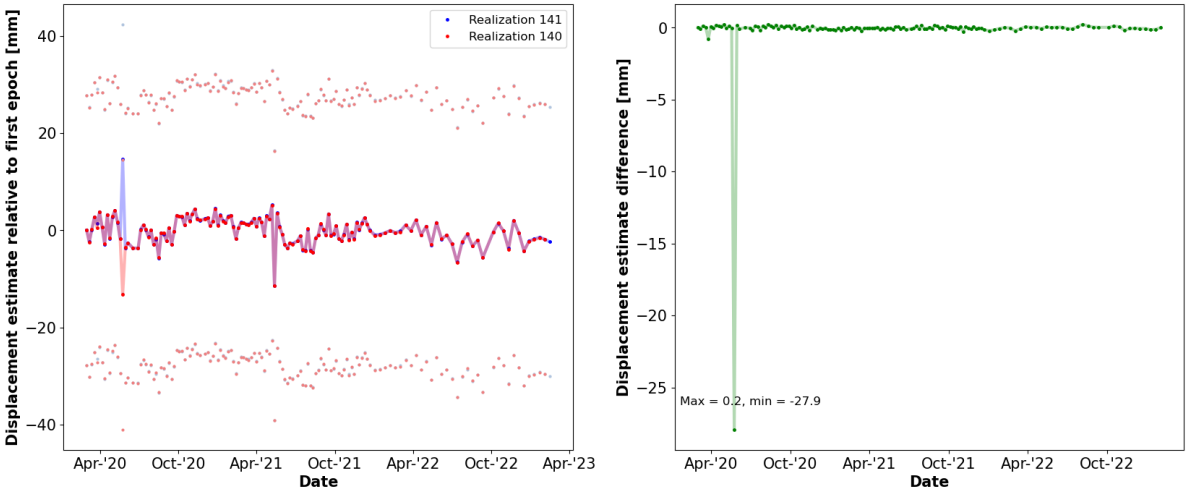

Figure 2.13: Example of a point scatterer containing a *localized short-term deviation*. The left plot shows both estimated displacement time series together with their ambiguities. The difference in line of sight displacement of these time series is plotted on the right.

Area-Wide Short-Term Deviation

The third deviation category is the effect of *Area-Wide Short-Term Deviation*. Some epochs significantly underperform compared to the other dates, see the brighter column in Fig. 2.9 indicated by green rectangle III. In this case, the overall or instant velocities are not affected severely, meaning that a monitoring interpretation will likely not change. Still, it remains odd that adding the radar acquisition on 14 February 2023 (number 141 in the stack) mostly affects the displacement estimates of 18 May 2020, see an example in Fig. 2.14. Moreover, this could again lead to for instance different instant velocities if these anomalies occur more to the end of the stack. Besides, it could lead to people questioning the reliability of the results as it keeps changing the results on dates over one year ago.

Area-Wide Long-Term Deviation

The last deviation category is the effect of Area-Wide Long-Term Deviation. This phenomenon was not visible in Fig. 2.9, but could occur if the mother (reference) acquisition or reference location changes. section Section 2.2.4 will elaborate on this last specific case.

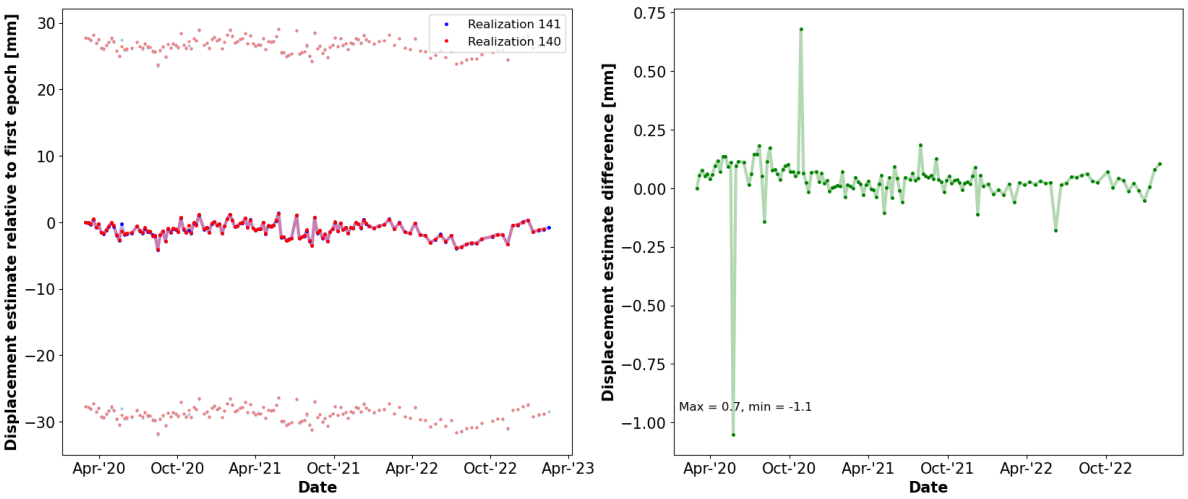

Figure 2.14: Example of a point scatterer containing *Area-Wide Short-Term Deviation*. The left plot shows both estimated displacement time series together in one plot. The difference in line of sight displacement of these time series is plotted on the right.

2.2.4. Hypothesis deviation types

As the algorithm to produce these results was identical for both runs, each of these deviation types is a direct consequence of (choices within) the algorithm. There are many estimated parameters and variables during the process, thereby leading to multiple hypotheses causing the deviations.

Localized Long-Term Deviation

First of all, the ambiguity differences will most likely be caused by the phase unwrapping step of section 2.1.4. The first two subtypes of LLTD are caused by temporal unwrapping. In the case of the *ambiguous drift*, the estimated deformation rate is entirely different, working through to the temporal unwrapping. This could be caused by the limited initialized displacement model assumption that was identical in both runs. A different initial displacement model with for instance a seasonal signal will cause a different interpretation of the integer ambiguities and could thus provide more robustness.

A *consequent ambiguity* could originate from the same displacement velocity uncertainty or could be caused by a slightly different estimation of the other parameters such as the APS.

The *uncorrelated difference* on the other hand is believed not to be caused by specific choices in the algorithm. As there seems to be very little correlation between the two time series in terms of phase cycles, this phenomenon will not be triggered by the phase unwrapping step. The question is whether these are the points that have a high NAD value (low quality) anyway. Looking at the PS around this devious location it can not be due to the estimation of the APS as well. A possible solution could be that the pixel just underwent some change. As we are performing an analysis right over an urban environment it is not unthinkable that the real situation changed by means of construction or other urban developments.

Localized Short-Term Deviation

Looking at the *Localized Short-Term Deviation* in $\Delta STM_{141,140}$ (Fig. 2.9), we see that the occurrence of this deviation is correlated in time. A large portion of the slips seem to occur in the last 20 epochs indicating that it is often caused by a phenomenon mostly adjusting later epochs. This hints at a difference in the separation of the non-linear displacement from the atmospheric signal, see section 2.1.6. The addition of acquisition 141 to the stack may cause the non-linear displacement to be estimated differently, potentially leading the algorithm to

make a different unwrapping decision in those PS that are close to being unwrapped differently. Furthermore, moderate Localized Long-Term Deviations are (almost) only occurring in combination with an incidental ambiguity. This can be explained as an ambiguous measurement has a large effect on the estimation of other parameters as the velocity, atmosphere, and estimated height are all influenced causing a significant change in all other epochs other than the incidental ambiguity. If this happens at some location it could impact some other PS as well during the spatial unwrapping procedure. This needs to be further investigated in Chapter 3.

Area-Wide Short-Term Deviation

In the *Area-Wide Short-Term Deviation* such as previously highlighted by green rectangle III, we see significantly higher area-wide differences over all PS compared to other epochs. This leads to the belief that there might be some spatial correlation in displacement deviations. The differential displacement of this epoch is depicted in Fig. 2.15 (column in the $\Delta STM_{141,140}$). The colored points represent all conjunct PS2 locations in the two realizations, with the color scale indicating the $\Delta STM_{141,140}$ value on that location for 24 May 2020. The larger green and black dots are the locations of the PS1 in both realizations. There are only two locations differing, indicated by the arrows. Fig. 2.15 shows that the displacement differences are without doubt spatially correlated. There seems to be a smooth signal that is forced through the PS1. Looking at this signal, it is almost certainly related to the interpolation parameters obtained from the semi-variogram during the APS estimation, as touched upon in section 2.1.6.

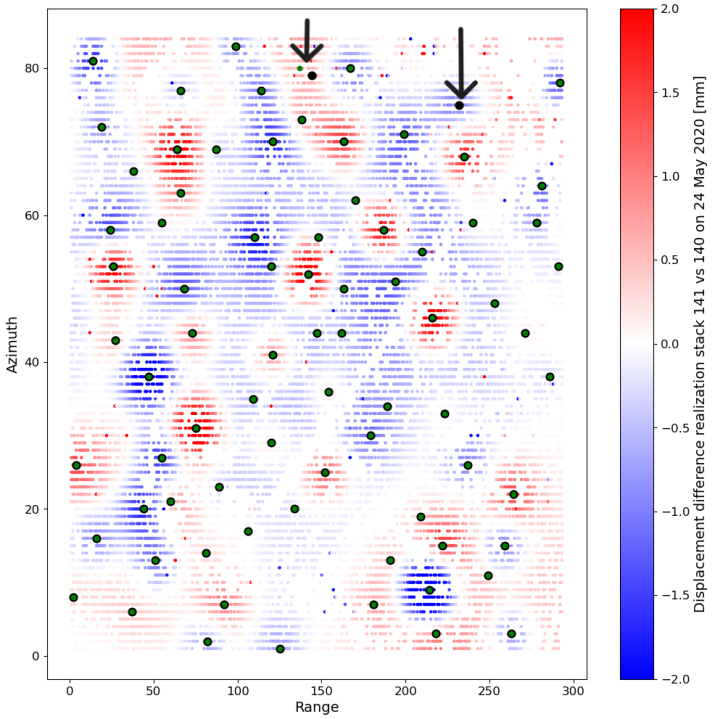

Figure 2.15: Difference in displacement estimates on 24 May 2020 comparing results from realization 140 and 141. The horizontal axis contains the azimuth number and the range number. The circles are the locations of the PS1 and the arrows a different psc location. The spatial trend is clearly centered around these PS1 locations.

The total measured phase consists of various factors that need to be estimated to arrive at a displacement phase, see Eq. (2.3). A change in atmospheric phase estimates directly propagates to the displacement estimates. To investigate the underlying cause of the spatial pattern, the intermediate atmospheric output is examined. The difference in atmospheric

phase estimation of the two independent realizations is shown with the help of an Differential Atmospheric Space-Time Matrix ($\Delta ASTM_{141,140}$), which contains the same information as the $\Delta STM_{141,140}$ but then only for the atmospheric delay estimates. In Fig. 2.17 the $\Delta ASTM_{141,140}$ is visualized in the same way as the $\Delta STM_{141,140}$ and comparing this figure to Fig. 2.9, we can state that the area-wide differences one epoch indicated by a green rectangle in the ΔSTM visible in the $\Delta ASTM$ as well indicated by the green rectangles.

A significantly changing atmospheric estimation of a date two years prior to the processing date is, to say the least, unusual. Given that the APS estimation involves multiple steps, we can formulate various hypotheses. Fig. 2.16 shows an overview of the main steps possibly influencing the estimates of the APS, starting from a new SAR acquisition going through the steps towards an atmosphere estimation. First, the addition of a new acquisition changes all amplitude dispersions as an extra amplitude value is added to the time series. These changes in NAD per PS lead to a possibly different set of PS1, and the estimated atmospheric phase delay might change for the already existing locations as other parameters such as the velocity and non-parameterized displacement have changed in the new batch estimated solution. A new set of PS1 or new delay values cause a change in the experimental semi-variogram of each atmosphere. Subsequently, different interpolation parameters are obtained from a theoretical fit to the semi-variogram leading to a different interpolation when estimating the delay for PS2. In the end, one new amplitude for a newly acquired acquisition can lead to larger consequences during the estimation process.

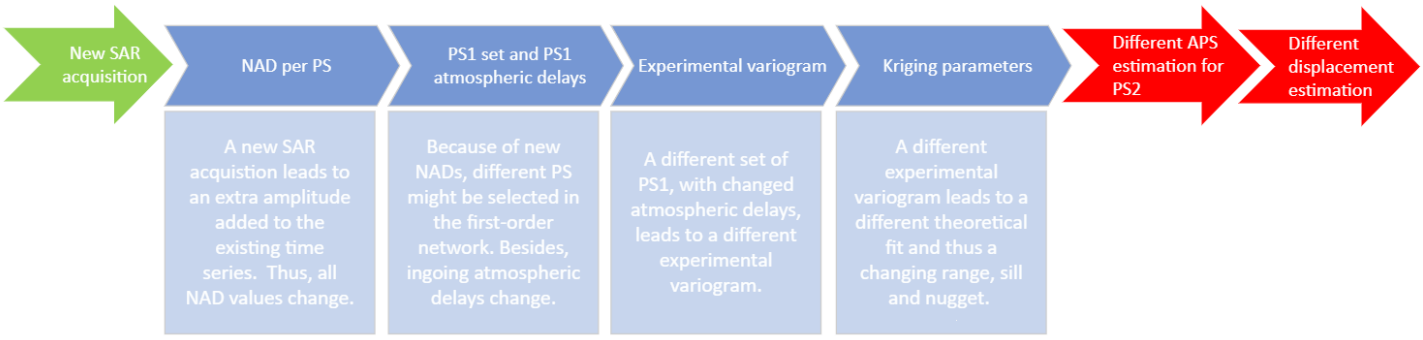

Figure 2.16: Overview of the main flow of from the addition of an acquisition leading to changes in the APS estimates. The top arrows describe the main concept flow supported by an explanation in the bracket below the arrow.

One of the intermediate steps can not robustly withstand new input changes and the experimental semi-variogram is a possible explanation. Oliver & Webster (2015) conducted an experiment comparing an experimental semi-variogram computed from data at 434 sampling locations with 87 locations. Their findings demonstrated that the parameters derived from a theoretical fit are unreliable for sparse datasets. In our case, with only 78 locations used for constructing the experimental semi-variogram, a similar situation arises. This implies that the obtained atmospheric interpolation estimates are not robust enough for monitoring purposes.

The *range* represents the distance from which two points are spatially uncorrelated. Looking at the intermediate DePSI outcomes, we see that the range is sometimes taken as just tens of meters. However, previous studies showed a correlation of several hundreds of kilometers for the atmospheric delay (Li et al., 2019), which means that a range of less than 100 m is implausible. The same applies to the *nugget* and *sill* parameters. An implausible *nugget* value could erroneously compel the smooth signal to assume the exact value at a PS1 location as is probably the cause for the spatial pattern in Fig. 2.15.

Fig. 2.18 supports this hypothesis, while we can see the relation between the AWSTDs

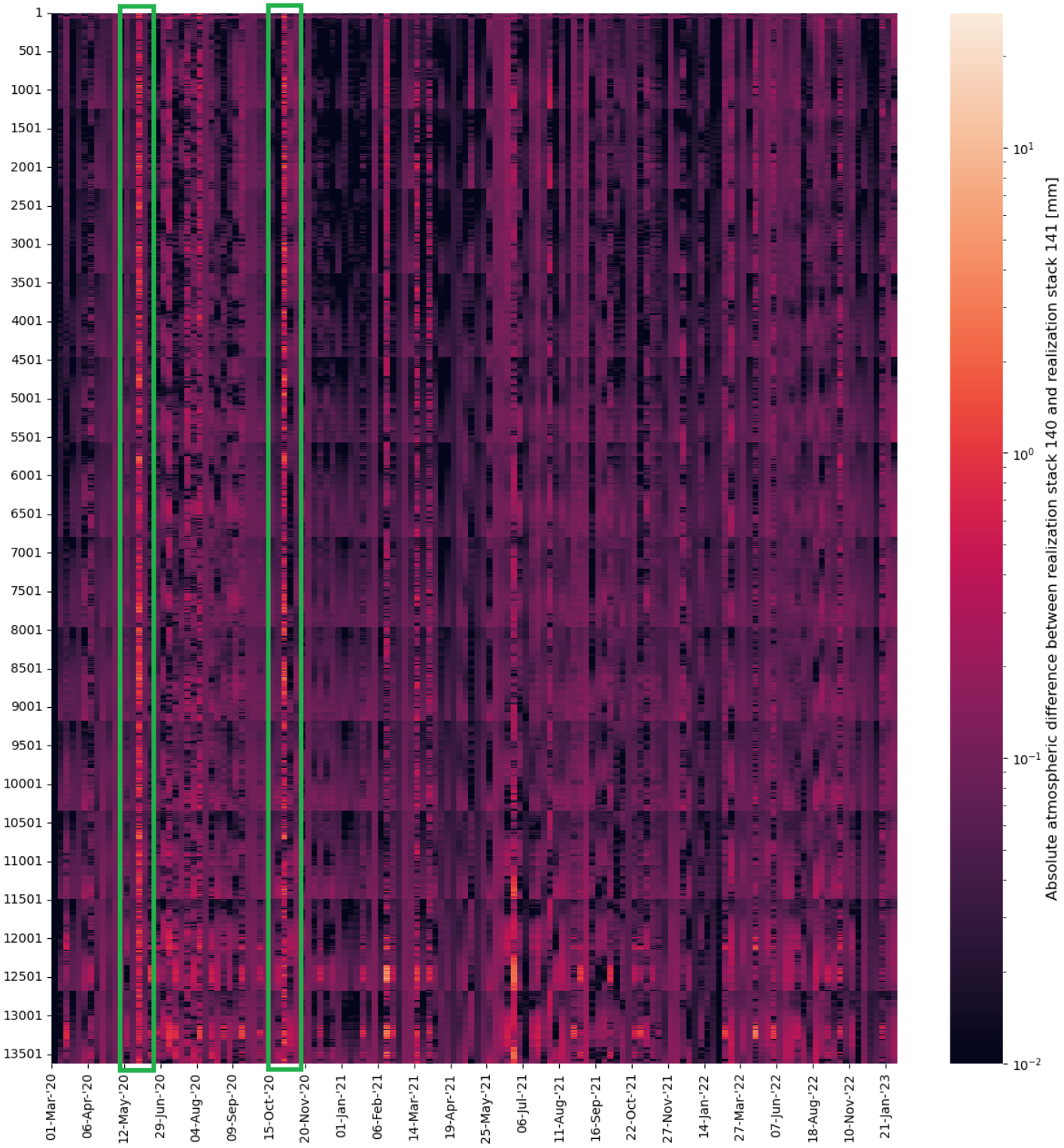

Figure 2.17: Absolute difference in estimated atmospheric delay of conjunct measurements from two realizations 140 and 141. The horizontal axis contains the date, starting from the 1st of March 2020 and the vertical axis represents an arbitrary point number (location). The green rectangles indicate the two most colorful epochs marking two occurrences of Area-Wide Short-Term Deviations.

from $\Delta STM_{141,140}$ (higher red dots) and the difference in nugget estimation between the two realizations (blue vs. yellow line). As the location and the input value of PS1 are slightly different, the atmospheric signal is modeled differently. The following changes in estimated range and nugget are such large, the APS of PS2 will be sensitive to the kriging parameter differences. In this case, the nugget estimated for a date in May 2020 changes from $\mathcal{O}\left(10^{-3}\right)$ to $\mathcal{O}\left(10^{-1}\right)$. Not only slightly altered input values can pose a problem for the atmospheric estimates. A change in PS1 locations could alter the atmospheric results even more as the whole network and thus the experimental semi-variogram will be different. To get a better feeling for the Kriging process, the atmospheric parameters will be extensively researched in section 4.2.

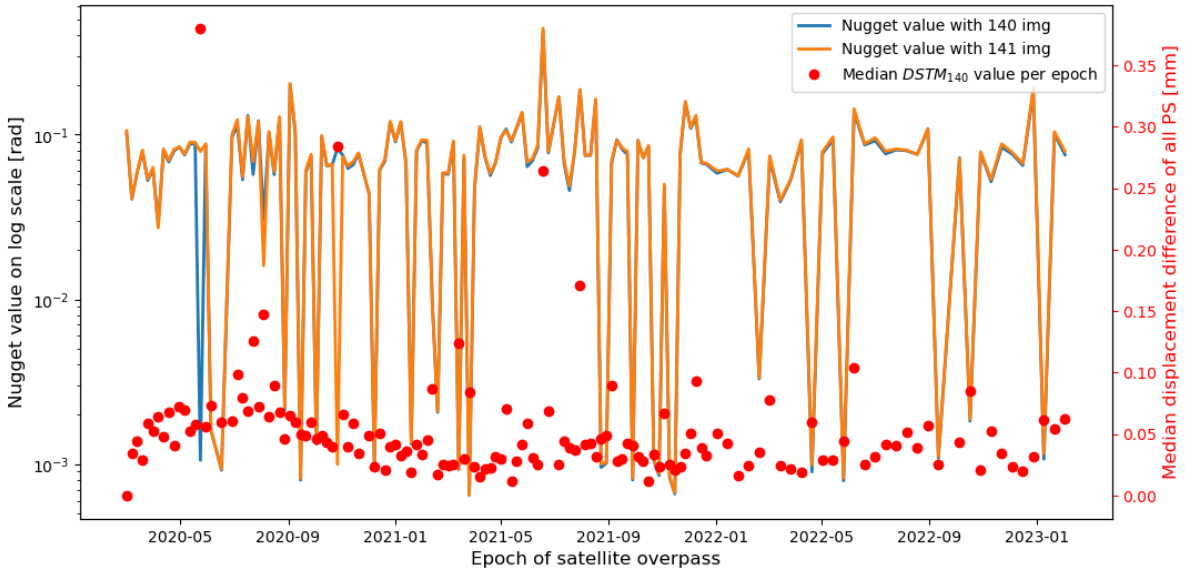

Figure 2.18: Nugget values of the realizations 140 in blue and 141 in yellow together with the median estimated displacement difference per epoch. The blue and yellow lines are almost identical apart from two epochs in May 2020 and Oct 2020. These epochs are in correspondence with the occurrence of the largest median estimated displacement difference in red.

It could be thought that the AWSTDs are just a result of a more dynamic atmosphere on that date which could be harder to capture correctly. However, repeating the analysis for the same track using two different stacks, such as utilizing the time series from analysis $\Delta STM_{131,130}$, results in dissimilar epochs showing large differences. This indicates that the epochs found in $\Delta STM_{141,140}$ are not structurally more prone to atmosphere delays, but are incidents.

As previously mentioned, one of the possible causes for a change in APS estimation is a change in PS1 locations. Fig. 2.19 shows the PS1 locations for three realizations (one extra epoch per run). On some occasions, the coordinate of a PS1 just shifted slightly in azimuth or range compared to the previous realization as can be seen at coordinate (32,58/59). It could be the case that this location is a result of strong scattering from the same point as the area from which information is received is larger than the actual pixel size. However, 2.20 shows an example of the neighboring (1 azimuth difference) PS1 across two realizations, where the amplitude signal is not coming from an identical scatterer. Looking at multiple amplitude time series of neighboring locations it rejects this hypothesis of leaking. The choice for a different location is also not driven by a different calibration time series as they do not differ significantly as depicted in the right plot of Fig. 2.20. For this number of radar acquisitions in the processing, a new overpass changes the amplitude dispersion in such a way that there is just a different location with the lowest amplitude dispersion within a grid cell.

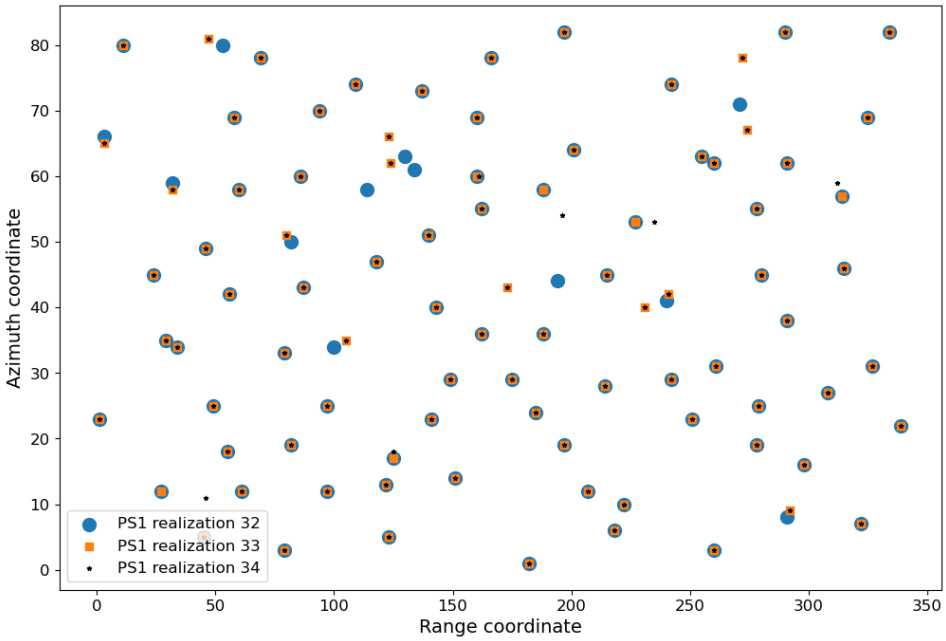

Figure 2.19: Location of the first-order PS obtained processing three consecutive realizations 32, 33, and 34. Most of the locations coincide, though a few slightly differ or do not appear at all in the different realizations.

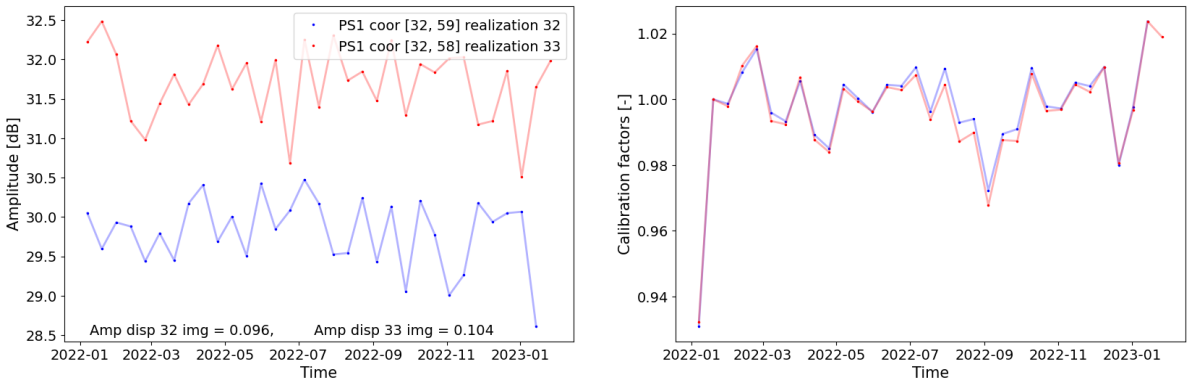

Figure 2.20: Amplitude time series (left) and the corresponding calibration factors (right) for two psc coordinates from a run of two neighboring PS1 in two different realizations. As the amplitude series do not contain the same signal, it is very unlikely that they are coming from the same scatterer.

Area-Wide Long-Term Deviation
The deviation category not visually apparent in the analyzed ΔSTM is the Area-Wide Long-Term Deviation. However, the selection of a reference point will appear to cause overall displacement differences mainly shorter stacks. All final displacement estimates are linked to one single reference point as described in section 2.1.5. This means that all remaining displacement artifacts in this reference point are propagated to all other displacement results. Changing to another reference will thus influence all displacement estimates. The locations of the reference point are shown to change a lot over the realizations 5 to 100, indicated by Fig. A.1 with the locations and number of times that certain locations have been used as reference. The more acquisitions in a realization, the less often the reference location changes. The changing reference can explain displacement deviations when visualizing a Differential Space-Time Matrix as a different reference behavior translates to all PS.

Impact of unrepeatability
In the amplitude calibration process explained in section 2.1.3, the random function causes an unrepeatable result primarily affecting shorter (fewer acquisitions) stacks. Since the calibration values differ slightly due to this randomness when rerunning DePSI with the same input, other PS are present in the first-order network. To investigate the direct impact, DePSI has been performed three times with the same number of acquisitions, e.g. three times realization 32, while changing nothing to the algorithm. Fig. 2.21 shows the locations of the three PS1 sets in realization 32. It can be observed that the same acquisition stack as input does not lead to the same result as the selection of PS1 differs, though only in 3 locations. While only one to three locations differ from roughly 90 locations, one would not expect a significantly different result in the atmospheric estimates. In Fig. 2.22 the atmospheric estimate differences are shown in a $\Delta ASTM_{32,32}$ for run versions 2 and 3 (only one different location). Clearly, the interpretation of the atmospheric estimates on some epochs is affected severely, and with it the displacement results as well.

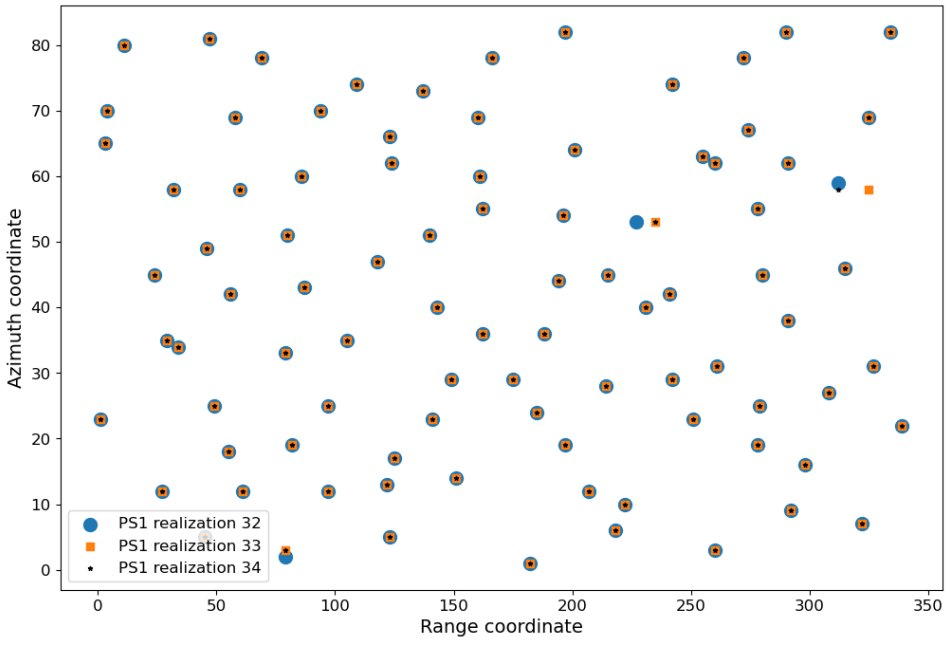

Figure 2.21: Location of the first-order PS obtained from three runs on the same stack of acquisitions. Due to a random function, different PS1 are selected while nothing changes in the input.

Unrepeatability is undesirable for monitoring purposes, thus a different method is needed

for the amplitude calibration. Therefore, we choose to take fifty PS evenly with equal integer step sizes apart from each other. This ensures a spread over the region and gives the same result once one decides to rerun the process. Because repeatability is such a vital condition for monitoring and our analysis, this measure is the only measure set up front for further analysis in Chapter 4.

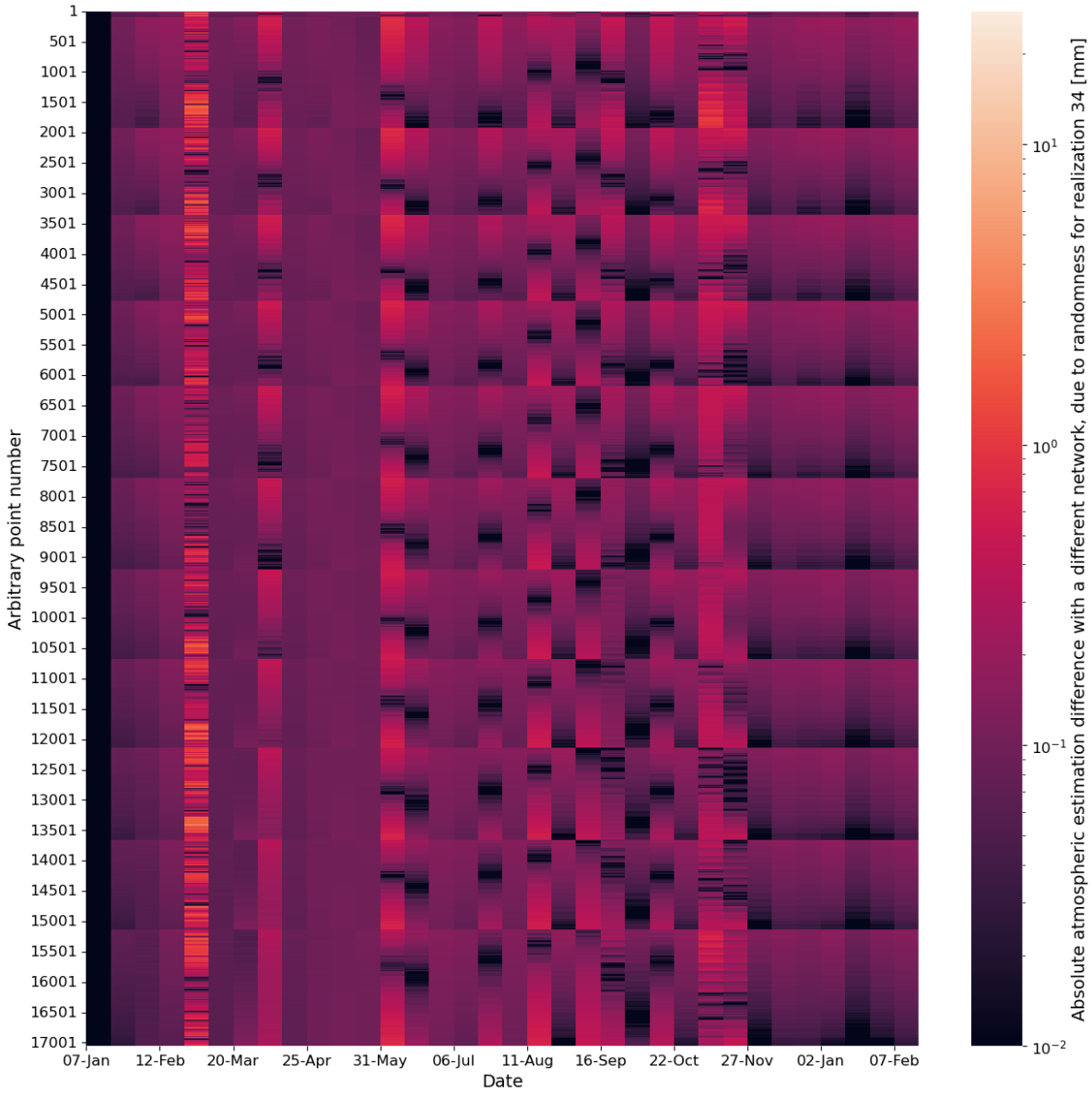

Figure 2.22: Difference in atmospheric estimates between two realizations having exactly the same input. However, randomness in the calibration step caused one PS1 to be different, already impacting the APS estimation.

3

Metrics Definition and Robustness Test Recipe

To evaluate the robustness of the current algorithm, it is essential to employ metrics that can effectively quantify and express the results. The visualizations created for ΔSTM and $\Delta ASTM$ serve as examples to visualize and weigh the displacement estimates. In the upcoming section, the concept of robustness will be elaborated upon, followed by an introduction to the metrics employed for quantifying this characteristic. Subsequently, a test recipe and output graphs will be presented to facilitate the quantification, visualization, and interpretation of the robustness. Lastly, the areas of interest will be introduced to provide context for the processed outcomes.

3.1. Robustness

Robustness can be a bit of a vague concept and as robustness analyses are very context-specific, we will define the term in more detail. In a scientific context, robustness can be defined as the degree to which an estimator is resistant to perturbation and variations in the input variables or conditions (Hampel, 1971). Besides, it gives a good indication that the obtained parameter estimates are not overly dependent on specific assumptions, or constant conditions. There are many assumptions or conditions that influence the outcome of DePSI. We primarily center the attention on six conditions that have arisen as significant factors from Chapter 2. The location of the reference point, the PS1 locations, atmosphere (Kriging) parameters, initial displacement model, PS threshold, and the input radar acquisitions.

In the context of the monitoring with InSAR, we define robustness as the sensitivity to the addition of one (or more) extra acquisition(s) for the displacement results of previously estimated epochs. Robust results, in this context, imply an algorithm or process that minimizes significant alterations to previously estimated displacements or other parameters when integrating a new acquisition into the existing stack. The objective is to maintain stability in previously derived results while still ensuring accuracy in the updated outcomes.

3.1.1. Robustness: Quantification

To comprehensively assess the displacement estimates, their robustness will be quantified using. Given that the three distinct error types cannot be adequately captured by a single metric, this quantification approach involves the use of three core statistics. These statistics will be further elaborated upon in the following subsection, resulting in a robustness vector with three values for a single robustness test. Additionally, these core statistics will be complemented by

additional metrics to provide a more comprehensive depiction of the three primary robustness quantifiers. The algorithm will be tested by comparing all estimated displacement parameters acquired. Comparing realization N versus the independent preceding realization $N-1$. Realization N means there were N SAR acquisitions in the DePSI stack input. The number of conjunct point scatterers between two realizations is denoted by $n_{PS,x}$ with x conjunct corresponding epochs.

3.1.2. Robustness: Metrics

Statistics or metrics are needed to quantify the dissimilarities in the displacement estimates from different realizations. With those statistics, one could see the development of the robustness over the number of acquisitions in a realization. Adding a new acquisition to an existing realization is expected to have less impact on the parameter estimates once the stack is already more numerous, while relatively less new information is added to better estimate the APS for instance. In Fig. 3.2, an example of a conjunct PS in two realizations is given. Following the introduction of a statistic or metric, reference will be made to this figure to elucidate its contribution to a metric. This will give a feeling for the introduced metric.

The following statistics are going to be used throughout this thesis, where the first three statistics form the robustness vector:

1. **Fraction of points and measurements containing an ambiguous cycle difference**
   By quantifying the magnitude of the displacement difference between realization N and $N-1$ at successive (incremental) epochs, one can detect the occurrence of an ambiguity difference, or cycle slip, between two time series. This step size or Incremental Displacement Difference (IDD) is calculated by:

$$IDD_i^s = \left|\Delta STM_i^s - \Delta STM_i^t\right|, \tag{3.1}$$

   where $s \in [0, N-2]$ and $t \in [1, N-1]$ indicate the epochs and ΔSTM_i the displacement difference time series of a certain PS i. Fig. 3.1 shows an example for the construction of the IDD using the schematic $\Delta STM_{8,7}$ from Fig. 2.7.

   One could argue that a displacement difference larger than an ambiguous cycle (~28 mm) is sufficient to detect cycle slips. However, this would not lead to the desired cycle slip detection. To grasp the rationale behind this we revisit Fig. 2.11. Here, the displacement on the third epoch was unwrapped differently. Thereafter, the displacement estimates almost behaved identically. Simply using a boundary for the displacement difference would flag almost all epochs, but this limits our information about the actual occurrence of the cycle slip. Thus, it is chosen to look at this IDD to identify localized short-term cycle slips.

   With the incremental displacement differences, the cycle slips ($IDD_i^s > 20\ mm$) are counted and divided by the total number of points (n_{PS}) and incremental epochs ($x-1$) in realization comparison x to get a quantitative idea of the localized short-term cycle slips. Thus the Fraction of Ambiguous Measurements is given by:

$$FAM_x = \frac{\sum_{i=1}^{n_{PS,x}} \sum_{s=1}^{x-1} \left(IDD_i^s > 20\right)}{(x-1) \times n_{PS,x}}, \tag{3.2}$$

   where x represents the used realizations in the comparison ($N, N-1$), and IDD_i^s the absolute incremental displacement difference from epoch s and for PS i. In Fig. 3.2, the $FAM_{100,99}$ would be 6/98 as there is a jump 6 times of the incremental displacement estimates. The threshold value for identifying a cycle slip is set at 20 mm, rather than

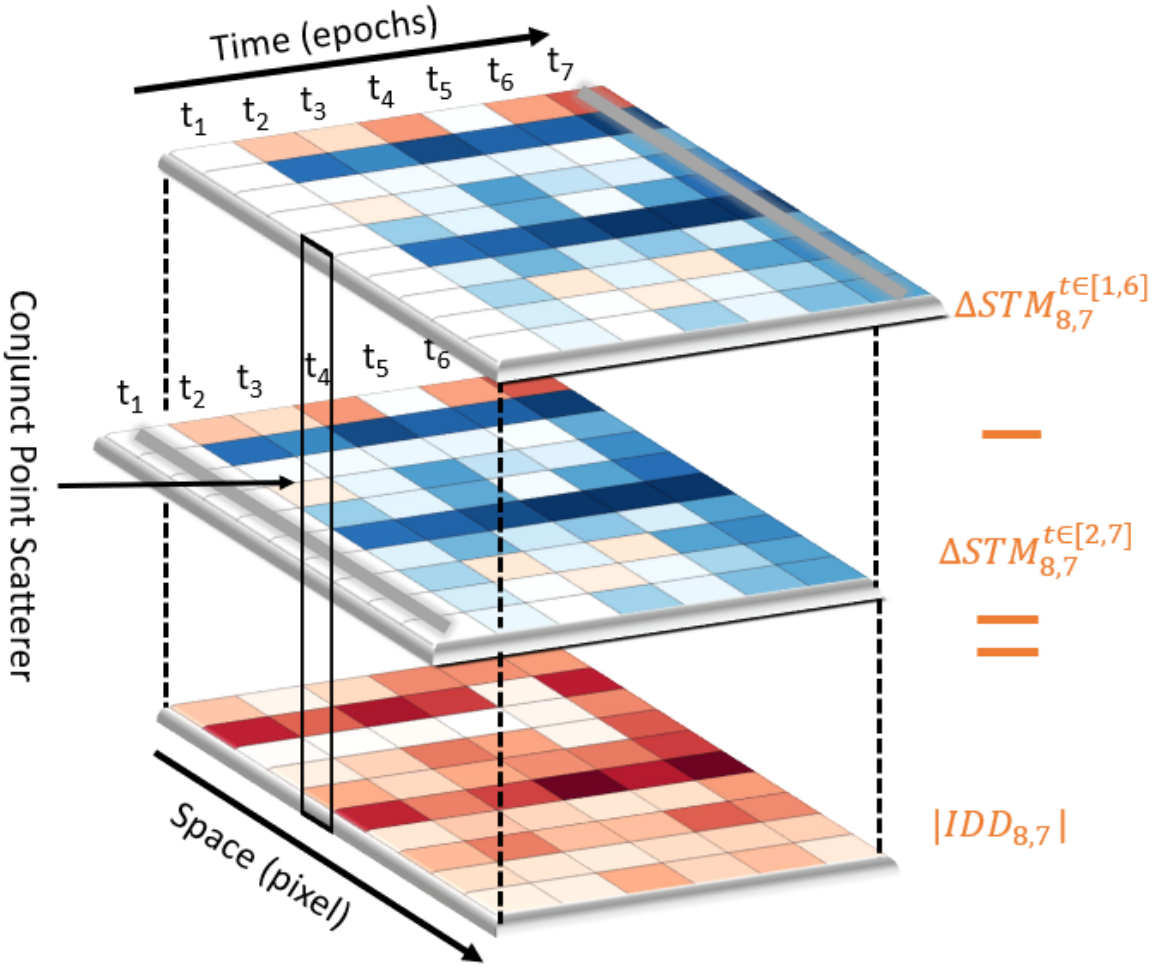

Figure 3.1: Schematic representation of the calculation of a Incremental Displacement Difference (bottom layer). A red square indicates a high value and a blue square a low value for all epochs included in ten conjunct example Point Scatterers (PS). The two top layers are the same $\Delta STM_{8,7}$ but shifted one epoch apart.

exactly at 27.7 mm directly as there are still other parameter estimations that cause a difference. This could cause a different unwrapping to end up slightly below half a phase length.

Instead of looking at cycle slips per measurement, we are interested in how many PS contain at least one cycle slip. This leads to the definition of the Fraction of Localized Short-Term Ambiguities:

$$FLSTA_x = \frac{\sum_{i=1}^{n_{PS,x}} \left(IDD_i^{any} > 20\right)}{n_{PS,x}}, \tag{3.3}$$

where x represents the number of overlapping acquisitions in the comparison $(N, N-1)$, and IDD_i^{any} the absolute incremental displacement difference from any epoch for PS i. The example PS would thus count 1/1 in Fig. 3.2.

2. **Fraction of points containing a long-term ambiguity difference**
This statistic focuses more on the points where cycle slips are not incidents, the previously called localized long-term cycle slips. A PS is marked as a long-term cycle slip if the median estimated displacement difference lies above one ambiguity level (27.7 mm). The equation for this Fraction of Localized Long-Term Ambiguities (FLLTA) is thus:

$$FLLTA_x = \frac{\sum_{i=1}^{n_{PS,x}} \left(\text{median}|\Delta STM_x^{i,t}| > 27.7\right)}{n_{PS,x}}, \tag{3.4}$$

where x represents the number of overlapping acquisitions in the comparison $(N, N-1)$, and $\Delta STM_x^{i,t}$ the displacement difference of PS i on epoch t. The PS in Fig. 3.2 has a median that clearly lies below the 27.7 mm and therefore this example PS will have contributed 0 out of 1 to the $FLLTA$.

3. **Root Mean Squared Difference**
The last statistic calculates the overall PS performance comparing realization N with $N-1$, excluding the cycle slips. This is to avoid a low robustness bias to more numerous stacks as the cycle slips dominate the statistic. Besides, they have already been adequately addressed by the previous two metrics. The root-mean-squared error (RMSE) is a well-established statistic to assess the performance of an algorithm, comparing estimates with a truth. Moreover, the statistic is also used to test an algorithm in terms of robustness and sensitivity (Saha et al., 2014). There has been a debate on the use of the mean absolute error (MAE) over the RMSE, but Hodson (2022) shows that RMSE is optimal for normally distributed errors. The displacement differences mostly follow a Gaussian distribution and therefore justify the use of the RMSE. In this case, we look at differences instead of errors and therefore we define the statistic as *Root Mean Squared Difference* (RMSD). The RMSD is defined as:

$$RMSD_{N,N-1} = \frac{1}{x}\sum_{t=1}^{x}\sqrt{\frac{\sum_{i=1}^{n_{ps}}\left(\varphi_i^N - \varphi_i^{N-1}\right)_t^2}{n_{PS}}} = \frac{\text{tr}\left(\sqrt{\frac{A^TA}{n_{ps}}}\right)}{x}, \tag{3.5}$$

where φ_i^N represents the displacement phase of a single PS from realization N at location i on epoch t, x represents the number of conjuct epochs and n_{PS} the total number of conjunct non-ambigous PS. This formula can be simplified by taking the trace of A^TA, where matrix A represents our $(n_{PS} \times x)$ ΔSTM_x matrix without ambiguous PS. The PS in Fig. 3.2 contains cycle slips and will therefore be ignored in this statistic. Fig. 2.14 on the other hand would contribute to the statistic while only containing some minor deviations.

4. **Fraction of PS containing a short-term ambiguity per epoch**
   To get more details about the ambiguities, the cycle slip occurrences per epoch are registered to get an overview of which epochs often contain different unwrapping choices and what the influence is on the other displacement results. The example PS in Fig. 3.2, will contribute $1/n_{PS,x}$ to the two epochs around the three peaks in Jul, Oct, and Nov 2021 as the jumps ($IDD > 20$) concern those epochs.

5. **RMSD per epoch**
   Similar to the case with the cycle slips, we gather more information about the RMSD than a singular value per realization comparison. Consequently, the RMSD values per epoch are stored for each realization comparison, yielding an RMSD vector denoted as $RMSD_{vector,N-1}$, representing the sum of all differences on a single epoch in the comparison. The corresponding mathematical equation is:

$$RMSD_{vector,N-1} = \sqrt{\frac{\sum_{i=1}^{n_{ps}} \left(\varphi_i^N - \varphi_i^{N-1}\right)_t^2}{n_{PS}}} = \sqrt{\frac{\mathrm{diag}^{-1}\left(A^T A\right)}{n_{PS}}}, \tag{3.6}$$

   where φ_i^N represents the displacement phase of a single PS from realization N at location i on epoch t, and n_{PS} the total number of conjunct non-ambigous PS. This formula can be simplified by taking the diagonal from the square matrix $A^T A$, where matrix A represents our $(n_{PS} \times x)$ ΔSTM_x matrix without ambiguous PS. The PS in Fig. 3.2 contains cycle slips and will therefore be ignored in this statistic. If a dataset would consist of similar PS as Fig. 2.14, one would see relatively high values in May 2020 and Dec 2020 indicating that these epochs contained dynamic displacement estimates.

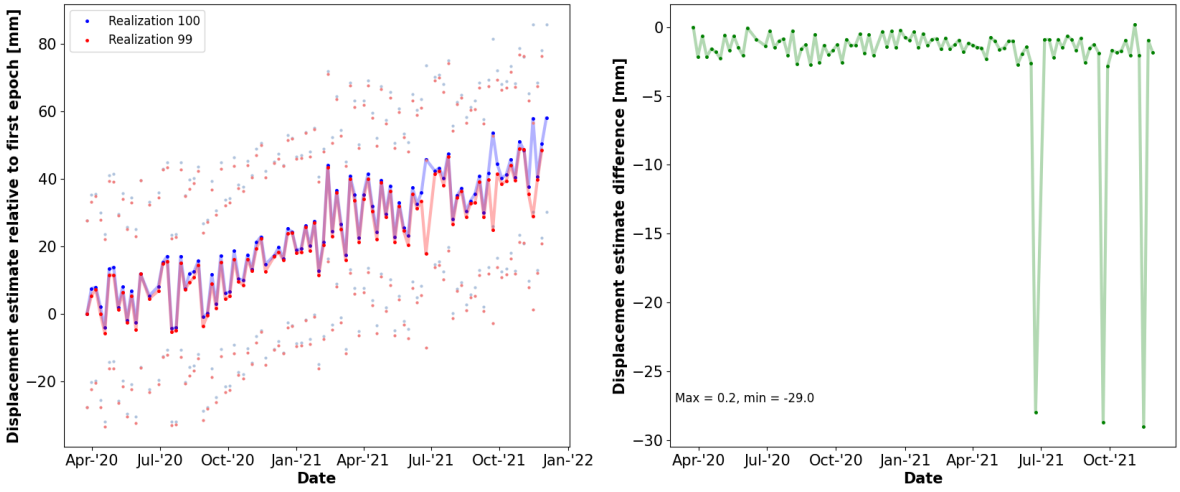

Figure 3.2: Example of a PS contributing to multiple metrics. The left plot contains the two individual estimated displacement time series obtained from realizations 99 (red) and 100 (blue). The right plot contains the difference in the estimated line of sight displacement. In this example, the PS is contributing to $1/n_{PS}$ for the *Fraction of Localized Short-Term Ambiguities* metric, $6/(n_{PS} \times n_{epochs})$ for the *Fraction of Ambiguous Measurements*, but not for the *Fraction of Localized Long-Term Ambiguities* metric.

With these statistics' help, we can create multiple figures to assess the robustness of a particular run and interpret the results in the blink of an eye.

3.2. Test Recipe

To diagnose the impact of uncertainties and DePSI choices, multiple real-case simulations are performed. In principle, we pretend to start with no acquisitions over the area of interest and add one acquisition for every satellite overpass. Batch estimating a full new parameter set, estimating new atmospheric delays, heights, displacements, etc. for each realization. As it is impossible to construct a relative time series with limited acquisitions due to singularity constraints in the spatial unwrapping process, we start with five acquisitions. This is the minimum amount to generate plausible results. The whole DePSI algorithm will be rerun when a new acquisition (artificially) arrives and all the output is stored in a separate folder. This is repeated until the one-hundredth acquisition has been added to the total stack. Hereafter, the previously mentioned metrics can be calculated to make the graphs and interpret the results.

3.2.1. Proposed output

For the evaluation of the algorithm's robustness, several figures will be generated. These figures serve to test the robustness across multiple scenarios and DePSI settings. Additionally, the fixed set of figures will be supplemented with figures specifically interesting for certain cases or improvements. For instance, the spreading of PS1 can be interesting when comparing the use of two different amplitude dispersion equations to construct a first-order network. The main set of figures will consist of the following five visuals:

1. Figure containing the three discussed core robustness metrics over the number of acquisitions N in a realization (using statistics 1, 2 and 3). This will be called the *Incremental Robustness Metrics* or $IRM_{y,z}$ graph, where y marks the realization length when starting the analysis and z the final processed realization length.

2. Matrix of the displacement estimate difference of realization 100 and 99. As introduced before this matrix will be called $\Delta STM_{100,99}$.

3. Matrix of the atmospheric estimate difference of realization 100 and 99. As introduced before this matrix will be called $\Delta ASTM_{100,99}$.

4. Diagonal matrix of the short-term cycle slips per epoch over the number of acquisitions $N-1$ in a realization comparison (using statistic 4). This will be called the *Ambiguity Overview* (AO).

5. Diagonal matrix of the $RMSD_{vectors}$ over the number of acquisitions $N-1$ in a realization comparison (using statistic 5). This will be called the *RMSD Overview* (RMSDO) graph.

All produced figures will be added to the appendices for each scenario and area, but only the most significant ones will be added to the main text.

3.2.2. Output interpretation

Before delving into the interpretation of case study findings, it is crucial to establish a comprehensive understanding of how to interpret the generated results. The first figure, the *IRM* graph, contains the three core metrics of robustness. Ideally, all values should equal zero, regardless of the realization comparison, indicating the absence of any displacement estimate differences and hence a perfectly robust algorithm. However, this will not be the case in practice. It is important to note that the values themselves should not be interpreted in isolation but rather in a broader context. While they offer valuable insights into variability and the presence of ambiguities, they should not be used blindly for a direct comparison between two different regions. By increasing the number of acquisitions as DePSI input we can uncover anomalies

in the use of particular acquisitions and APS estimation as the three core robustness statistics exhibit unexpected behavior such as clear distinct peaks in the number of ambiguities compared to the other realization comparisons.

The $\Delta STM_{100,99}$ and $\Delta ASTM_{100,99}$ have extensively been explained in section 2.2.2. As they only represent one realization comparison, one should not draw a hard conclusion based only on these two acquisitions. Nonetheless, they do provide insight into the robustness of the displacement estimates and the influence of the atmospheric estimates. If significant dissimilarities in displacement are consequently observed in the same epochs in $\Delta STM_{100,99}$ as in $\Delta STM_{100,99}$, it necessitates a closer examination of the APS estimation. Again, in a perfectly robust situation, both matrices should comprise solely zeros.

The things standing out from the *IRM* and ΔSTM graphs can be further examined in the Ambiguity Overview and RMSD Overview. Every realization comparison results in two vectors with $N - 1$ elements for the number of cycle slips or RMSD value per epoch respectively. As we initiate the comparison with only five acquisitions, the initial vectors (resulting from the comparison between realizations 5 and 6) will consist of five elements, corresponding to the number of conjunct epochs (five). Incrementing the stack with one acquisition at a time results in the growth of this vector by one epoch for each subsequent comparison. Visualizing this progression in a graph produces a diagonally shaped matrix, as exemplified in the layout of Fig. 3.3. The red pixels indicate the presence of a value in that pixel. A vertical column, as highlighted by the green rectangle, represents the vector that is obtained for one realization comparison. Of course, there are only statistics for the epochs present in that realization comparison. A horizontal line, indicated by the blue rectangle, represents RMSD or ambiguity fractions for the same epoch but originating from a different comparison. Similar to the vertical columns, a statistic is only present if the comparison encompasses that epoch. Therefore, in the blue example, a value for epoch number ten is present when comparing realization 10 and 11.

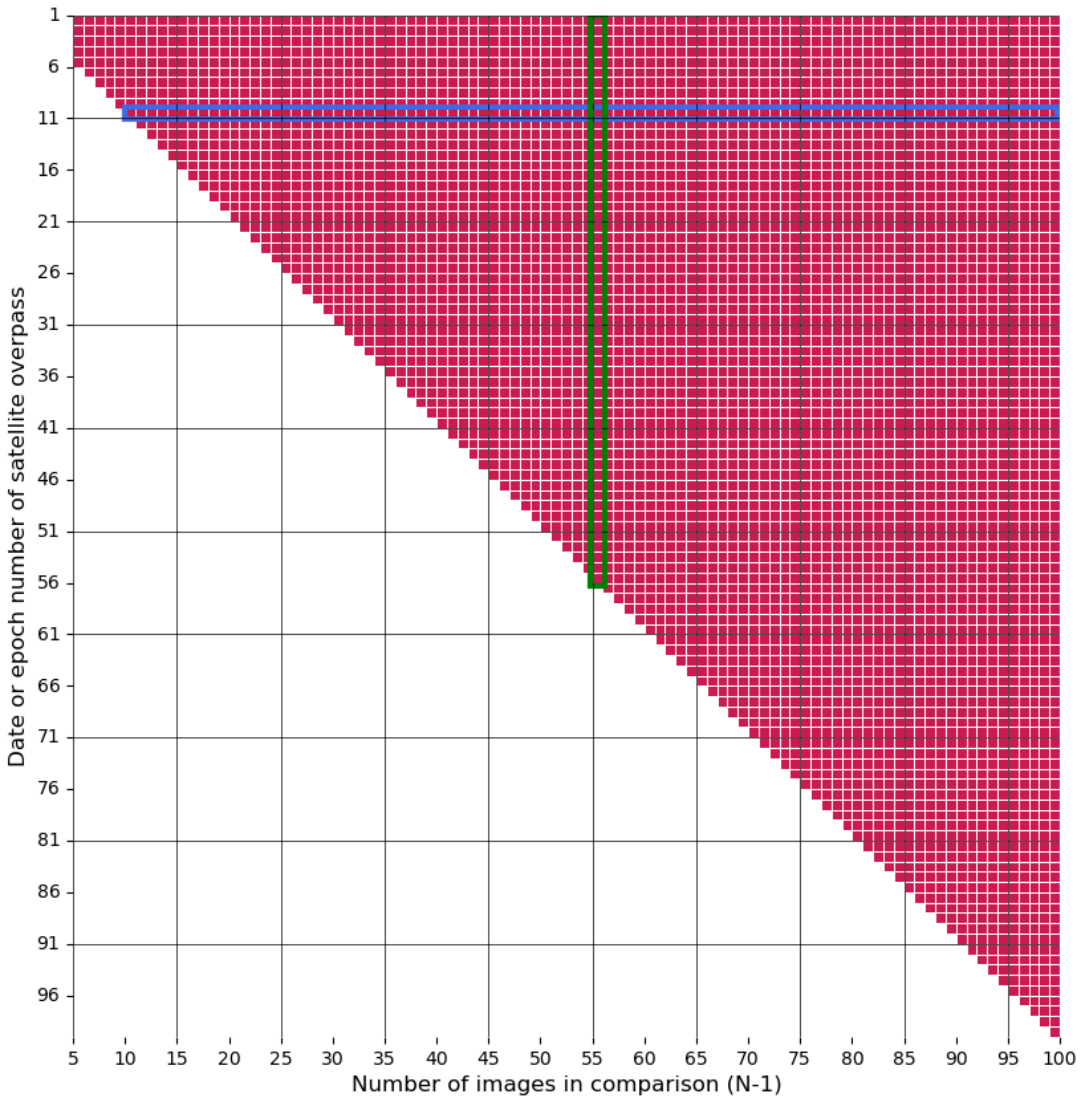

Figure 3.3: Example of the layout of the Ambiguity Overview and RMSD Overview. The red squares indicate the presence of a value in that pixel. A vertical column, as highlighted by the green rectangle, represents the vector that is obtained for one realization comparison. A horizontal row, indicated by the blue rectangle, represents RMSD or ambiguity fractions for the same epoch but originating from a different comparison.

3.3. Areas of interest

Multiple different areas or area sizes in The Netherlands will be used to avoid a Taylor-made solution only working for one specific region/landscape type. The first area of interest will be a 1x1 km area over the city center of Amsterdam, which the current CAROLINE portal covers. Subsequently, a 5x5 km Amsterdam area with the exact same center point as the CAROLINE area will be used. For this, the ascending track 88 will be used. Finally, another area over a rural region close to the 'Hondsbossche Zeewering' near the coast, will be used in this simulation as a counterbalance to the urban areas. The location at the coast can be seen as a simulation that for instance would be used to monitor sea dikes. It is chosen to use an area of 1x1 km as well as a 5x5 km to ensure a reasonable ratio between the computational time of the process, the number of point scatterers, and the capturability of spatially differing atmospheric delays. The location of the Hondsbossche Zeewering is depicted in Fig. 3.4 together with the boundaries of the 1x1 km and 5x5 km area. For this region, a descending track is chosen, to get a better coverage of the sea defense itself. The 5x5 km area includes (parts of) villages, whereas the 1x1 km area almost purely contains rural surroundings.

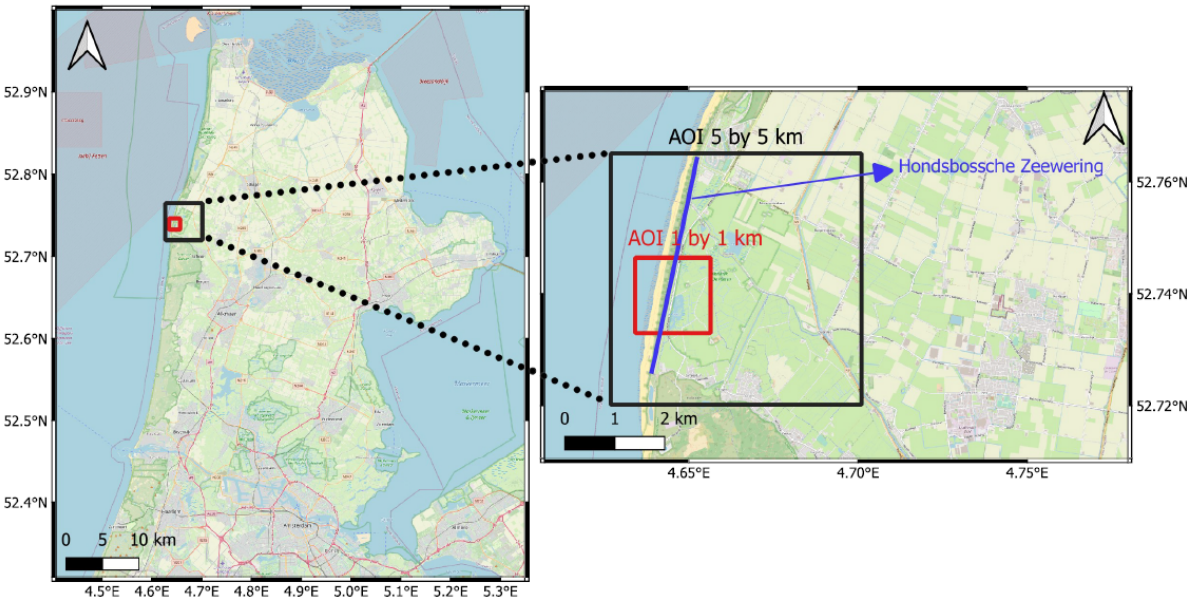

Figure 3.4: The 1 by 1 km and 5 by 5 km area of interest shapefiles around the Hondsbossche Zeewering.

4

Zero-state

In section 2.2.4 the possible causes for the ever-changing displacement results have been touched upon. This chapter treats the results of robustness analysis for the current CAROLINE region, a 1 by 1 km region over the center of Amsterdam. Starting with a realization of five acquisitions from 25 March 2020, an acquisition is added one by one till the one-hundredth acquisition is attained. The primary objective of this simulation is to explore the various underlying factors that may cause the observed variations in displacement estimates. Besides, zero-state results are created to substantiate proposed improvements thereafter. Section 2.1.5 addressed the repeatability issue, which is the only measure taken upfront in all cases to avoid randomness. Any interested party can replicate the analysis for their respective algorithm by systematically varying the number of acquisitions used as input and subsequently applying the same metrics for assessment. This approach allows for a comprehensive exploration of the algorithm's performance under different data conditions, enabling a nuanced understanding of its robustness and efficacy across varying input scenarios.

Firstly, the robustness of the zero-state will be evaluated. To assess the robustness, we will make use of the metrics and graphical representations introduced in the preceding chapter. Secondly, the atmospheric estimation will be thoroughly examined, followed by a discussion on the obtained zero-state robustness. By comprehending the factors contributing to the present lack of robustness in displacement estimates, we propose potential improvements in the last section.

4.1. Robustness zero-state

All corresponding figures for the basic DePSI algorithm not included in this section can be found in Appendix A.1. Displacement estimate differences are still present when adding the 100th acquisition to the stack, see $\Delta STM_{100,99}$ in Fig. A.2. The atmospheric estimates affect the displacement estimates in some epochs structurally, see 3 October 2020, mainly originating from the atmospheric estimates as observed from $\Delta ASTM_{100,99}$ in Fig. A.3. The $IRM_{5,100}$ in Fig. 4.1 shows the robustness metrics.

The RMSD of the non-ambiguous PS seems to contain a somewhat downward trend with the increasing number of acquisitions in the realization comparison which is as expected. The higher the number of acquisitions present in a stack, the less impact we expected the addition of an acquisition to have. The fraction of PS containing at least one short-term cycle slip (FLSTA,) as well as the fraction of localized long-term ambiguities (FLLTA) do not show a downward trend and somewhat stabilize after 50 acquisitions. The overall trend and the occurrence of some distinct peaks indicate no real global robustness improvement based on

the ambiguities. In fact, the FLSTA seems to contain a structural jump from around 50 acquisitions, where the values are significantly higher afterward. This will be further researched with the help of the Ambiguity Overview. Running DePSI with five and six acquisitions only, proved to produce unusable results while merely containing differences larger than a cycle slip when adding new acquisitions, see the red upper left dots and crosses in Fig. 4.1. Thus, the runs of potential improvements will only contain realizations with seven acquisitions or more.

The RMSD starts at around 3 mm at 7 acquisitions, whereafter the metric strongly decays to around 0.5 mm at 30 acquisitions. From this point, there seems to be no real improvement while the RMSD fluctuates around this 0.5 mm. One can interpret a single RMSD value as the average degree of variability in a single displacement measurement when comparing two realizations. The best robustness in terms of RMSD was obtained with comparisons of around 80 acquisitions with RMSD drops to 0.2 mm. However, some realizations further the RMSD at least peaks to 0.8 mm multiple times which is four times more than just before. Further, the red lines show some peaks as well. Overall the fraction of PS that contains at least one cycle slip is around 1:10 with exceptional fractions up to 2:10. Meaning that almost 20% of the time series contains a serious difference from the previous realization. The fraction of PS with a long-term cycle slip is gradually increasing till some 50 acquisitions where it flattens off around 4:1000 PS. The summary of these statistics is displayed in Table 4.1.

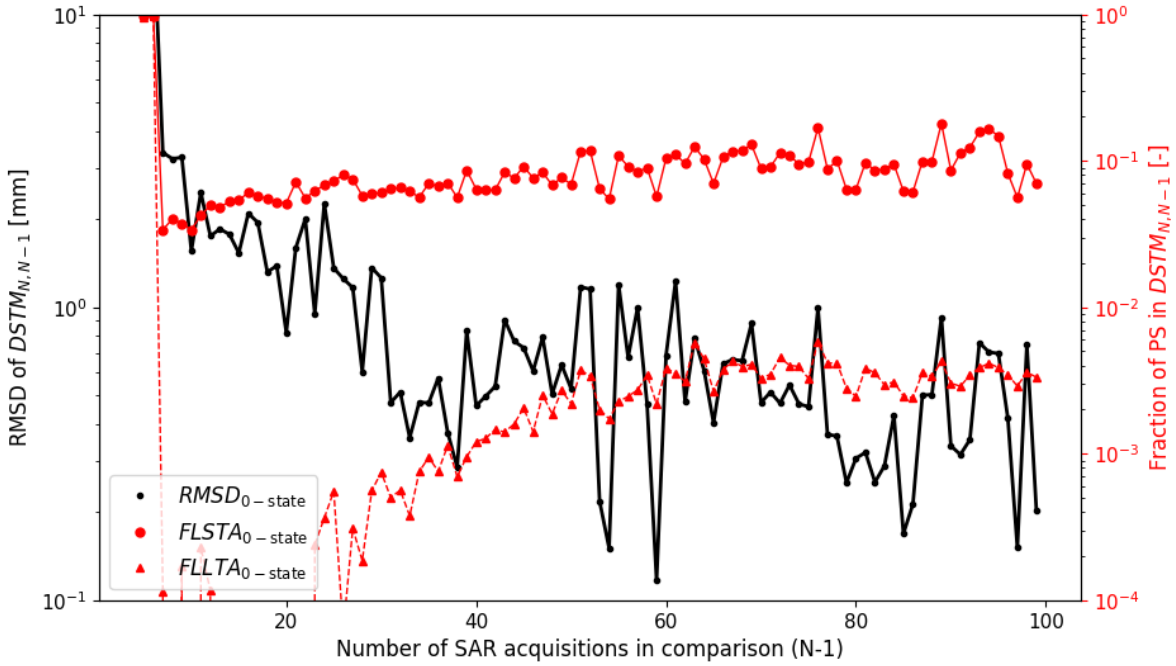

Figure 4.1: Incremental Robustness Metrics graph of the zero-state, comparing the displacement estimates from realizations N and $N-1$. The black line shows the Root Mean Squared Difference, indicating the average degree of variability in a single displacement estimate, the solid red line represents the Fraction of Localized Short-Term Ambiguities, and the solid dashed line the Fraction of Localized Long-Term Ambiguities. These lines show that the robustness is not structurally improving as the number of acquisitions in the stack increases.

In Fig. 4.2 the Ambiguity Overview per epoch over the number of acquisitions in the comparison, $N-1$, is shown. The figure indicates on which dates and in which realizations cycle slips occur. Clearly, two epochs catch the eye. From the 6th to the 12th of February 2021 and the 12th to the 18th of February 2021, up to 10% of the PS contained an ambiguity difference mainly adding acquisitions to realizations stacks 76 and 90-95. This indicates that 12 February 2021 proved to be inconsequent in the unwrapping choices over the number of acquisitions

Table 4.1: Summary of the robustness statistics for the zero-state in Fig. 4.1

Statistic	Trend over $N-1$	Average	Peaks
MRF	Decreasing till 30 acquisitions, thereafter wiggling	$0.5\ mm$	$1\ mm$
FAP	Slightly increasing	$6 \cdot 10^{-2}$–$1 \cdot 10^{-1}$	$2 \cdot 10^{-1}$
FSAP	Increasing till 50 acquisitions, thereafter wiggling	$4 \cdot 10^{-3}$	$6 \cdot 10^{-3}$

N in the realization stack. This is without exception the worst-performing date and causes an unacceptable change in displacement estimates for monitoring.

The question that arises is what caused such a poor performance on one specific date. Early February 2021, a snowstorm called Darcy passed over the Netherlands resulting in a snow cover of multiple centimeters lasting several days (KNMI, 2021). In Fig. 4.3, the repercussions of this snowstorm on the coherence between radar acquisitions are evident. The radar acquisition during the snow period causes a low coherence with the other acquisitions, thus impacting the unwrapping choices and thereby the displacement estimates and the overall robustness.

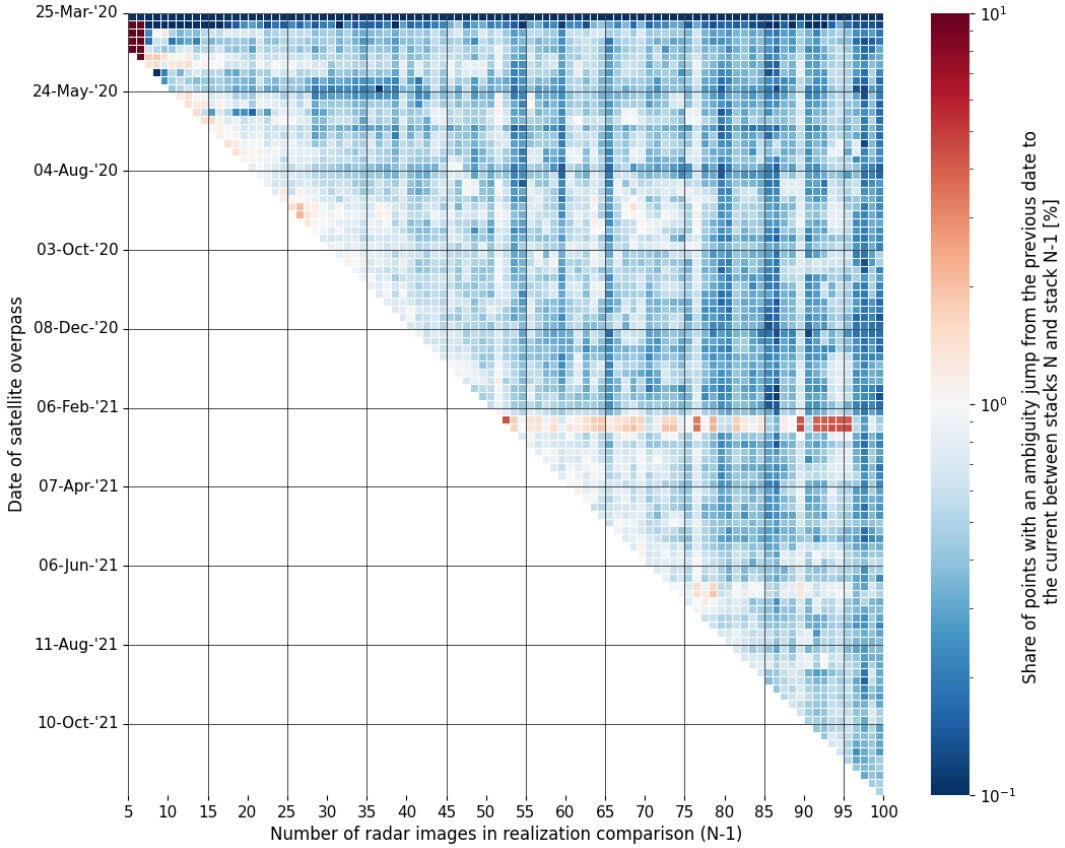

Figure 4.2: Ambiguity Overview for the occurrence of cycle slips in the displacement estimates per epoch, comparing acquisition realization N with realization $N-1$. Moving horizontally, the same epoch is compared but with a different DePSI input. A vertical column contains the cycle slips of one realization comparison. Dark red indicates many cycle slips on that epoch and dark blue indicates almost no cycle slips.

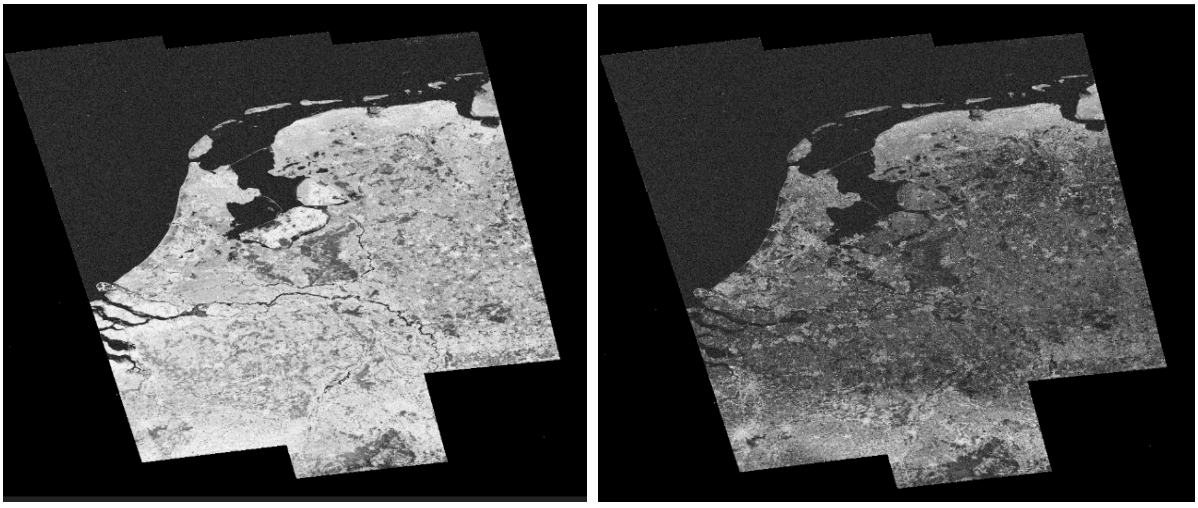

(a) (b)

Figure 4.3: Radar coherence over the Netherlands of an interferogram from 31 Jan to 6 Feb (a) and 6 Feb to 12 Feb (b) showing a relatively low coherence with the acquisition on 12 February.

4.2. Atmosphere zero-state

In Chapter 2, the atmosphere appeared to play a major role in the deviation type III, the Area-Wide Short-Term Deviation in Fig. 2.17. The changing Kriging parameters in Fig. 2.18, seemed to have a large effect on the robustness of the DePSI parameters. The zero-state robustness analyses in the previous subsection reinforced this thought by the comparison of $\Delta STM_{100,99}$ and $\Delta ASTM_{100,99}$. Thus we expect to see a correlation between different atmosphere estimations and the RMSD metrics. To get a better understanding of the atmospheric estimates and interpolation consequences, the Kriging parameters are examined in more detail.

The atmospheric parameters have been estimated for each epoch per realization, meaning we have around 90 estimates for the earlier dates (present in each DePSI output). In Fig. 4.4, the boxplot for all three atmospheric Kriging parameters on 30 April 2020 is displayed. Both the estimates from the zero-state 1x1km as well as the 5x5km are included. The 1x1km parameter estimates show a wide range of parameter values, being extremely vulnerable to input changes. The *range* changes from 50 m to several km and the *sill* and *nugget* show significant differences as well just by adding extra acquisitions, but still considering the same epoch and thus the same atmosphere. In section 2.2.4, we discussed that these values of tens of meters are not in accordance with any theoretical physics and can be owed to the low number of PS1 used for generating the semivariogram or the small extent of the processed area which just equals 1 by 1 km. These parameters are estimated from a detailed variogram supported by a low number of pairs. This makes it very vulnerable to outliers in the PS1 network and creates a non-interpretable experimental variogram as visualized in Fig. 4.5. On the other hand, the 5x5 km estimates look way more robust. The *range* still shows some spread but most values are based around the kilometer emphasizing that the values of around 100 m from the 1x1 km were very unlikely. The *sill* and *nugget* parameters are based around a tight boxplot in the 5x5 km indicating better robustness.

As the Atmospheric Phase Screen estimation directly relates to the displacement estimates, we expect atmospheric parameter alterations to manifest in the metric of the RMSD. The query is to what extent these changing parameters exert an influence on the RMSD robustness metric. In Fig. 4.6, the figures for both the nugget parameter and the RMSD Overview are put alongside. Each pixel in Fig. 4.6a corresponds to the estimated nugget value of the atmosphere on a particular epoch (y-axis) present in realization N (x-axis). Important to note

is that the x-axis thus slightly differs compared to the RMSD Overview. The nugget values are the result of each separate realization N. The RMSD is derived from the comparison between realization N and its immediate predecessor, $N-1$. Therefore, for a specific example, one should examine the nugget values of realization 76 and 77 and contrast them with the RMSD vector 76 illustrated in Fig. 4.6b. Both are indicated by a vertically elongated green rectangle. Comparing these rectangles, it becomes evident that the nugget values for almost all epochs exhibit a sudden and substantial increase. This, in turn, leads to higher RMSD values within the realization comparison, especially when contrasted with the ten consecutive comparisons where the atmosphere parameters remain remarkably stable. Furthermore, the most pronounced RMSD values can be directly related to the estimation of the APS estimation. The horizontally elongated green rectangles indicated the pixels with the lowest RMSD robustness. This pattern is consistent with the nugget values, which underwent changes on the order of 100-fold across the indicated realizations. Hence, it is evident that the robustness of atmospheric parameters is essential to improve the overall displacement robustness using InSAR.

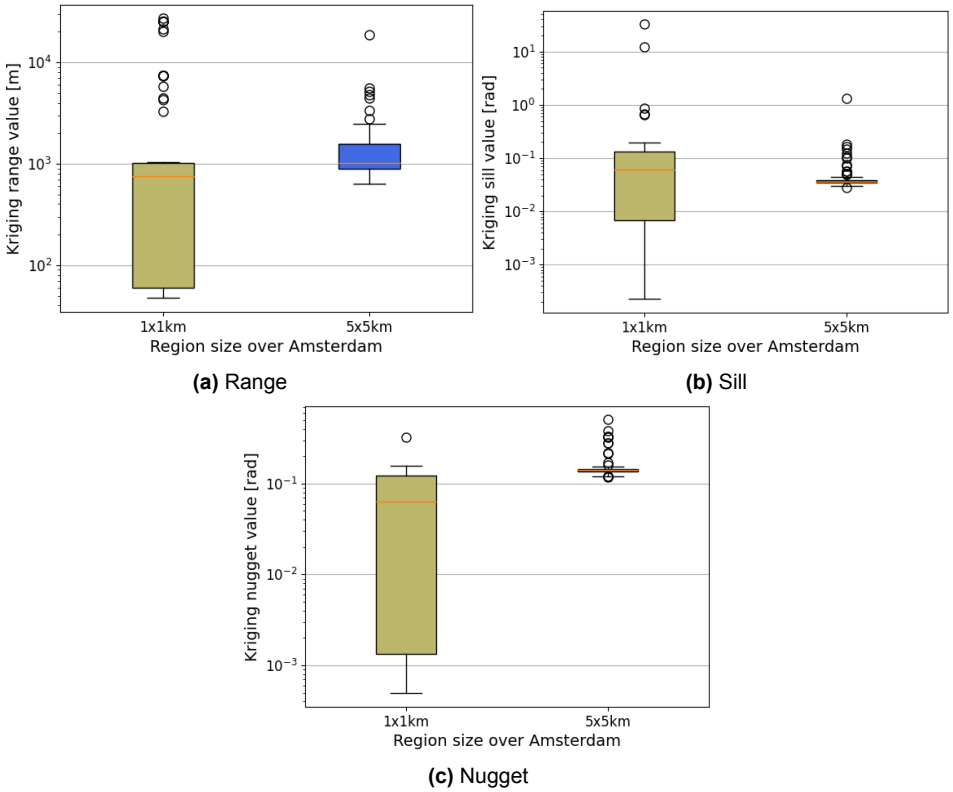

Figure 4.4: Boxplot of the Kriging parameters obtained from an experimental variogram estimating the APS of 30 April 2020 in 90 different realizations. Each subfigure contains one of the three parameters estimated for both the 1x1km as well as the 5x5km over Amsterdam showing a much wider range of estimates for the 1x1km area.

We have multiple options to improve the monitoring robustness by altering the atmosphere estimation. Firstly, one could propose to stay with processing 1x1 km, but take measures to improve APS robustness. These measures could include parameter constraints to avoid implausible Kriging values, the use of a fixed set of PS1 to avoid a different input, and the densification of the PS1 network to improve semivariogram certainty. Unfortunately, these measures all have their own flaws. Parameters could or should be different for different regions since the atmosphere in countries closer to the equator is different than in the Netherlands, meaning that the constraining of parameters is a Taylor-made solution. Prescribing the PS1

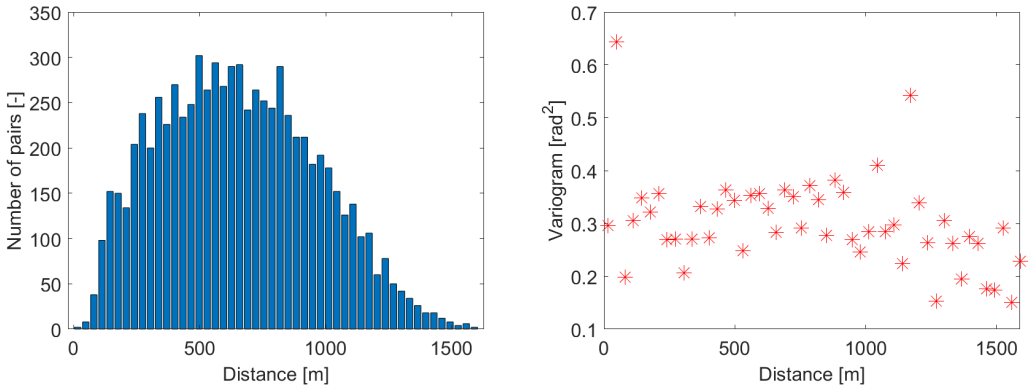

(a) Histogram **(b)** Experimental Variogram

Figure 4.5: Histogram of the distribution of PS1 pairs over the bins (a) side by side with the subsequently obtained experimental variogram (b) by averaging the semivariogram values in each bin.

locations will make you very vulnerable for occasions where PS drop out as they have a too high NAD. The densification of the PS1 network means that lower quality PS (higher NAD) are used to estimate the APS. Secondly, it could also be decided to use parameters resulting from APS estimations with a larger region such as the 5 by 5 km used in this example. This already clearly improves the parameter robustness though it increases computational time/complexity.

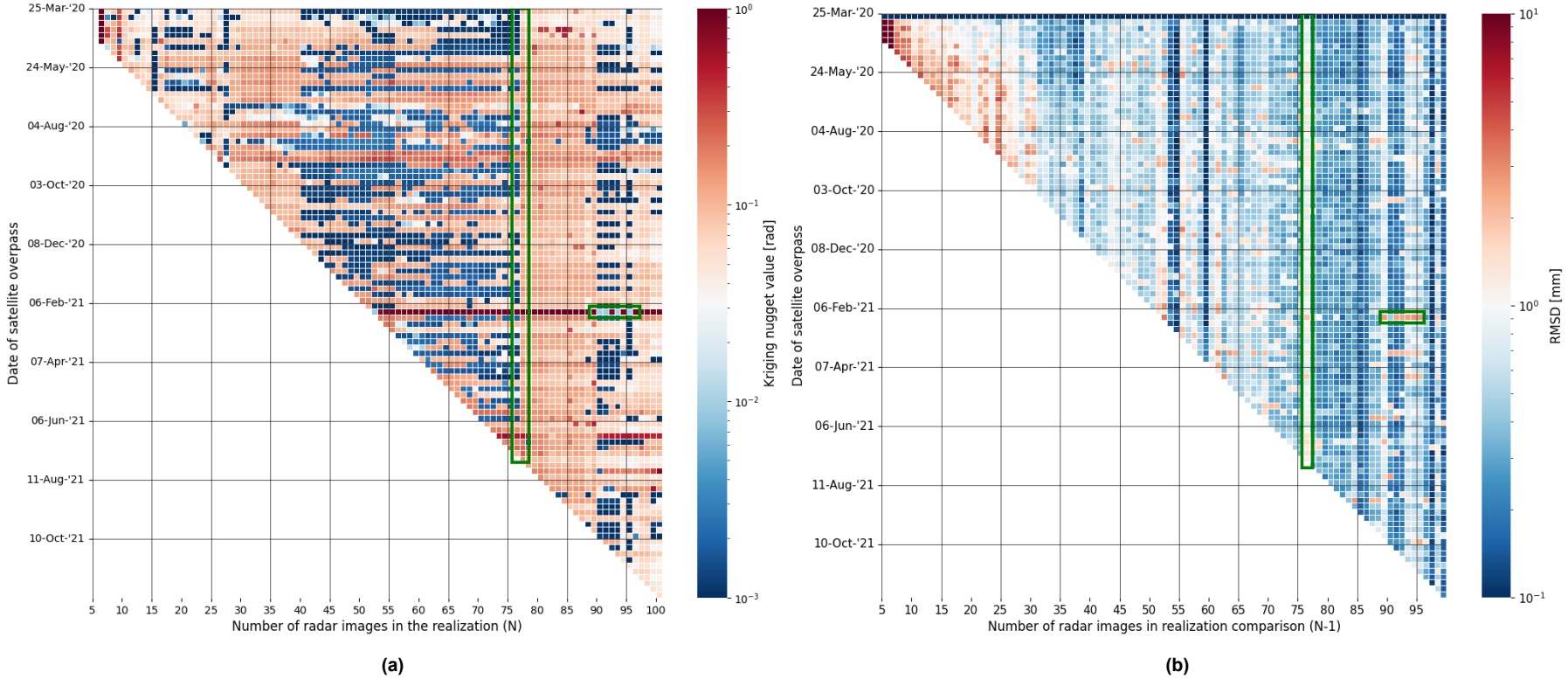

Figure 4.6: Diagonal matrix for the Kriging nugget parameter per epoch in each realization N (a) vs the diagonal matrix for the RMSD per epoch comparing acquisition realization N with realization $N-1$ (b). Moving horizontally, the same atmosphere (a) or displacement (b) is estimated but with a different DePSI input. A red pixel indicates a relatively high value at that epoch for that realization (comparison) and blue a relatively low value. The green rectangles are aimed at linking excessive changes in both plots either by comparing realizations (vertically elongated rectangle) or epochs (horizontally elongated rectangle).

4.3. Discussion zero-state results

In the interpretation of the core robustness metrics in Fig. 4.1, the Incremental Robustness Metrics graph, one could ask itself if it isn't very trivial that the number of PS containing an incidental cycle slip is slowly increasing as the number of epochs is increasing. Thus, there is a higher chance for a cycle slip as it is partly coincidence-based if the value is close to a different unwrapping value. However, this is not the aim of the study per se as the aim lies more in making it insightful how robust the obtained results are and what could be the cause for a large amount of false warnings. For this, the fraction of PS gives a better feeling than the fraction of measurements as one is often considering a single PS displacement time series. That there are some PS with a lot of cycle slips biasing the statistic is not interesting in that case. Thus it is chosen to stick with the fraction of PS instead of the fraction of measurements in the core robustness plot. Still, the fraction of measurement is at the base of the ambiguity overview and is thus not lost.

4.4. Proposed improvements

Taking into account the deviation hypotheses and zero-state results, we have identified several robustness weaknesses in DePSI. Therefore, the following nine measures are anticipated to bolster the performance in terms of robustness:

1. **Taking out randomness in the acquisition amplitude calibration**
   As described in Section 2.1.3, a degree of randomness is present in the acquisition amplitude calibration process. It is imperative to mitigate this randomness and it will be bypassed without question as a single irreproducible outcome is undesirable.

2. **Prescribing a reference location**
   The displacement at the reference location has a cascading effect on the displacement estimates of other PS. Maintaining consistency in the choice of the reference location across different realizations is believed to improve robustness on those occasions where a shift in reference location was present in the zero-state.

3. **Atmospheric measures**
   In section Section 2.2.4, multiple hypotheses for the cause of a changing APS estimation arose. Fig. 2.16 displayed an overview of the steps leading towards the APS estimation. Similarly, an overview with the same steps is depicted in Fig. 4.7, this time together with possible robustness improvements for each step.

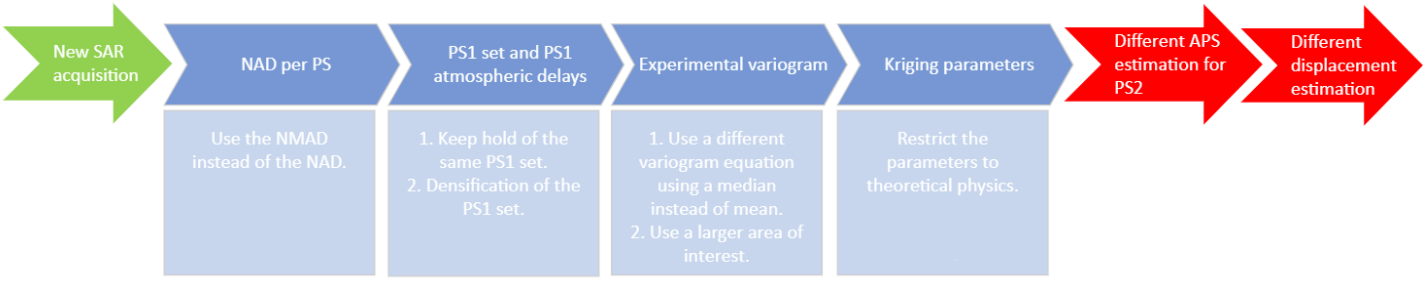

Figure 4.7: Overview of the main flow of from the addition of an acquisition leading to changes in the APS estimates. The top arrows describe the main concept flow supported by possible solutions to improve the robustness of that step in the bracket below the arrow.

The following sub-measures are defined:

3 a) Making use of the NMAD instead of the NAD
Both the mean and standard deviation are sensitive to outliers, which is the dispersion metric currently used in DePSI, see section 2.1.3. An alternative for the normalized amplitude is the Normalized Median Absolute Deviation or NMAD which is considered to be a more robust measure of dispersion (Leys et al., 2013). The NMAD of an amplitude time series *A* is given by:

$$\mathrm{NMAD} = \frac{\mathrm{MAD}}{\mathrm{median}(A)} = \frac{\mathrm{median}\left(|A_i - \mathrm{median}(A)|\right)}{\mathrm{median}(A)}, \tag{4.1}$$

where A_i represents a single observation in the amplitude time series. This NMAD has the potential to yield more robust results as new information is anticipated to alter the location of PS1 less frequently. Consequently, increasing robustness of both the atmosphere and displacement estimates.

3 b) Use a prescribed PS1 set
The first-order network appears to play a crucial role in parameter estimation. Forcing a set of pixels to be used in the first-order network for each run could mitigate fluctuations in APS estimates.

3 c) Constraining Kriging parameters atmospheric estimates
Besides the forcing of a constant PS1 set, another method to enhance the robustness of APS estimation is the constraining of the Kriging interpolation parameters. Our analysis of the 1x1 km region has revealed that these kriging parameters exhibit excessive freedom and variability. By imposing constraints that restrict the kriging parameters to a predefined realistic range, informed by results from the 5x5 km estimates or contextual data, we anticipate an improvement in APS robustness.

3 d) Enlargement of the processed area or PS1 densification
Section 2.2.4 suggested that the current area of interest contains an insufficient number of PS1 to construct a reliable variogram for the estimation of the APS. As an alternative to the previous measure, either the densification of PS1 or the enlargement of the processed area could remedy this problem.

3 e) Using a more robust Kriging technique
The current Kriging parameter estimation proved to be a problem for the robustness of the atmospheric estimation for the current use. As some bins representing the experimental variogram contain few pairs, the estimator behaves poorly if outliers are included (Genton, 1998). Thus, a different, more robust, equation opposed to 2.6 will be tested to get the parameters from a variogram. The equation for the variogram is given by Hawkins & Cressie (1984):

$$2\tilde{\gamma}_{Cressie-Hawkins}(h) = \frac{\mathrm{med}\left(\left|Z(x_j) - Z(x_i)\right|^{1/2}\right)^4}{0.457}, \tag{4.2}$$

where where $Z(x_j)$ and $Z(x_i)$ are the atmospheric delay estimations of PS1 at locations x_j and x_i that are a distance $h = |x_j - x_i|$ apart.
Besides the new equation to calculate the experimental variogram per bin, the number of bins is considerably lowered. The semivariances are obtained from too few comparisons leading to a 'noisy' variogram (Oliver & Webster, 2015). Together, these two adaptations should improve the APS robustness through more consequent parameter estimations.

4. **Exclusion of low(er) coherent acquisitions**
   The zero-state appeared to be heavily influenced by a specific acquisition with low coherence to the other acquisitions. This impact extended beyond the robustness of just that epoch while influencing multiple other epochs as well. Natural circumstances (weather/snow complications) make it harder to construct a robust time series, thus raising the question of whether to use these acquisitions after all in the analysis.

5. **Expansion of the steady-state displacement assumption**
   Finally, it appeared in section 2.2.4 that the steady-state assumption might be the cause for localized long-term cycle slips such as ambiguous drift. Therefore, the displacement model assumption could be expanded by for instance including a seasonal cycle or a second-order polynomial into the model to mitigate the occurrences of localized long-term cycle slips.

An overview of all error types, together with their hypotheses and possible improvements is depicted in Fig. 4.8. All proposed improvements will be tested to see their influence on the atmospheric estimates, cycle slip appearances, and resulting displacement estimates in the following chapter.

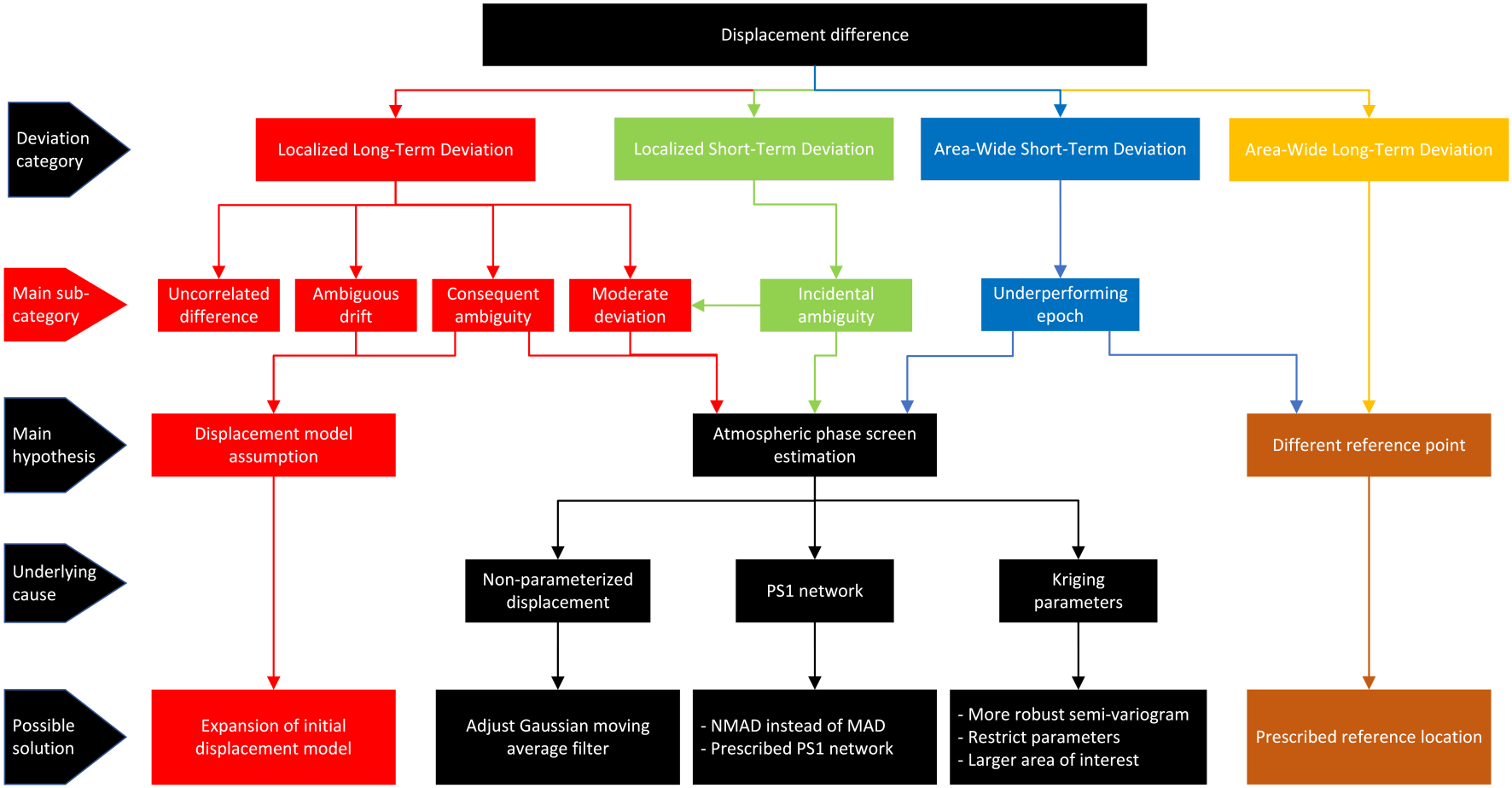

Figure 4.8: Overview flow chart of all types of deviations in the displacement estimates together with the hypotheses and possible solutions to the problem.

5

Improvements

In this chapter, the suggested improvements from section 4.4 will be tested to see the influence on the robustness of the displacement estimates. This excludes the removal of randomness in the calibration step as it was applied to the zero-state already. For the other improvements, we will test them *ceteris paribus*. This means that improvement *I* will cause *R* effect, *all other things being equal* (Schiffer, 1991).

5.1. Use of the NMAD

The PS1 network changes a lot in the zero-state due to the selection based on the Normalized Amplitude Dispersion. The changing network caused APS estimates to change and with it the displacement estimates. The NAD is sensitive to outliers, making new incoming amplitude values change the selection of PS for the first-order network. The Normalized Median Absolute Deviation is expected to be less sensitive to the addition of SAR acquisitions as stated in section 4.4. Therefore, the use of the NMAD is anticipated to improve the displacement estimates robustness.

All corresponding figures for the simulation with the use of the NMAD can be found in Appendix A.2 in full size. It is important to note that the number of Point Scatterers present in the analysis is slightly higher than in the zero-state simulation. This difference arises from the use of a different amplitude dispersion metric, which necessitates distinct values for the PS1 and PS2 selection criteria. To link the NMAD to the NAD thresholds, formulas of Brouwer et al. (2023) are used. For both NAD and NMAD, empirical formulas are deducted that facilitate the translation of threshold values to the phase standard deviation σ_ϕ, representing the quality of a PS. However, linking both dispersion methods is not perfect, given the empirical nature of these formulas, leading to a disparity of roughly a thousand PS between the two analyses.

Looking at the differential matrices for the displacement and atmospheric estimates in Figs. A.5 and A.6 one can see that the results have worsened dramatically as instead of a few brighter epochs in the zero-state, the whole figure brightened. This is confirmed in the $IRM_{7,100}$ graph in Fig. 5.1 where the robustness metrics with the NMAD are visualized together with the metrics from the zero-state. The reference location changed more in this NMAD case and the first-order network as well, worsening the robustness results. As a result, the NMAD is not the preferred choice over the NAD.

5.1.1. Discussion NMAD

That the use of the Normalized Median Absolute Deviation did not work beneficially in hindsight was to be expected. The aim was to get a more stable choice of reference PS or a stable set

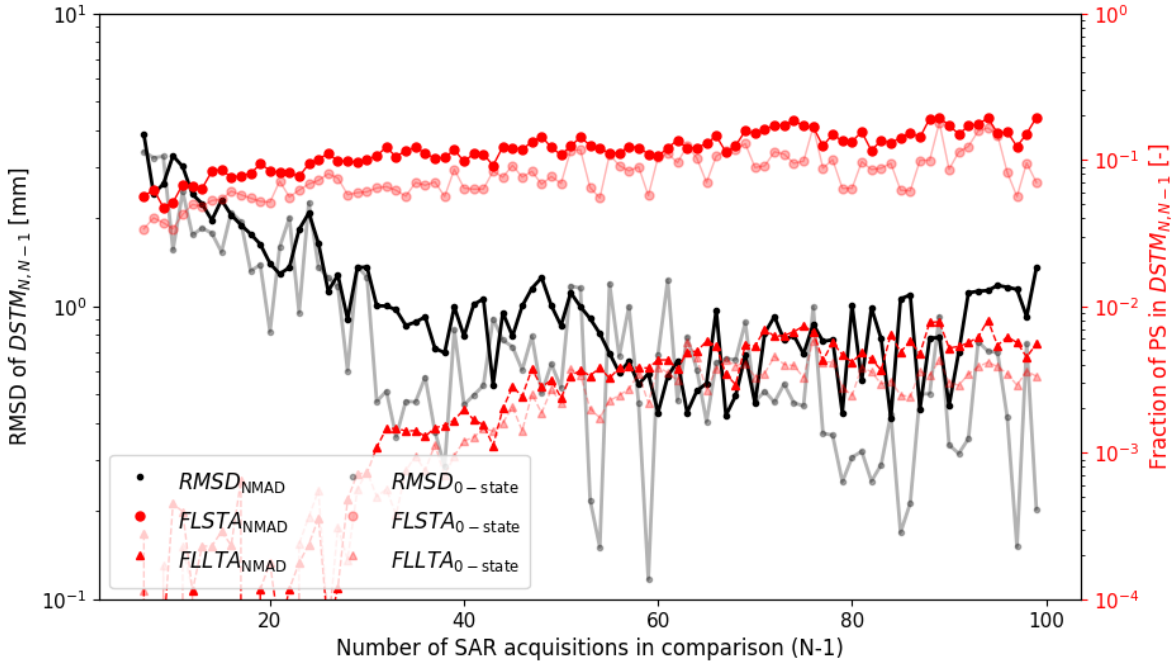

Figure 5.1: Incremental Robustness Metrics graph, comparing the displacement estimates from realizations N and $N-1$ for the base algorithm (transparent lines) versus a case where the NMAD is used instead of the NAD (opaque lines). The black line shows the Root Mean Squared Difference, indicating the average degree of variability in a single displacement estimate, the solid red line represents the Fraction of Localized Short-Term Ambiguities, and the red dashed line the Fraction of Localized Long-Term Ambiguities. These lines show that the robustness deteriorated for all three core metrics.

of PS chosen for the first-order network. However, this came at a cost. Instead of being robust to amplitude changes, we should be sensitive to these changes concerning which points we select in our atmosphere analysis. As F. Hu et al. (2022) showed, the amplitude can used to test hypotheses on the behavior of the PS and if the same ps is still considered in the analysis. In Fig. 5.2 a theoretical example of two PS is given that would be considered a very stable point using the NMAD in contrast to the NAD. Estimating displacements for this PS will not be desired as it appears that something has changed, while for PSI this stability is crucial (Amani et al., 2021).

5.2. Use of a fixed reference point

The constantly changing reference point (see Fig. A.1) in the zero-state was a likely explanation for part of the erroneous epochs as the displacement of a reference PS is propagated to all other PS. Therefore, a single stable reference location coming from a run with ~50 acquisitions is forced into all runs. All corresponding figures for the simulation with one single fixed reference location/pixel can be found in Appendix A.3 in full size.

In comparison to the basic algorithm, where the choice of reference is unconstrained, the ΔSTM heatmaps for the atmospheric and displacement estimates (Figs. A.12 and A.11) appear nearly identical. This is expected since the reference point remained unchanged between the analyses with 99 and 100 acquisitions in the zero-state as well. In the Incremental Robustness Metrics plot in Fig. 5.3, there is an observable improvement in terms of RMSD for all realization comparisons where the reference location differed from its predecessor, indicated by the yellow dots atop the zero-state RMSD values.

The RMSD improvement underscores the importance of the use of a single reference loca-

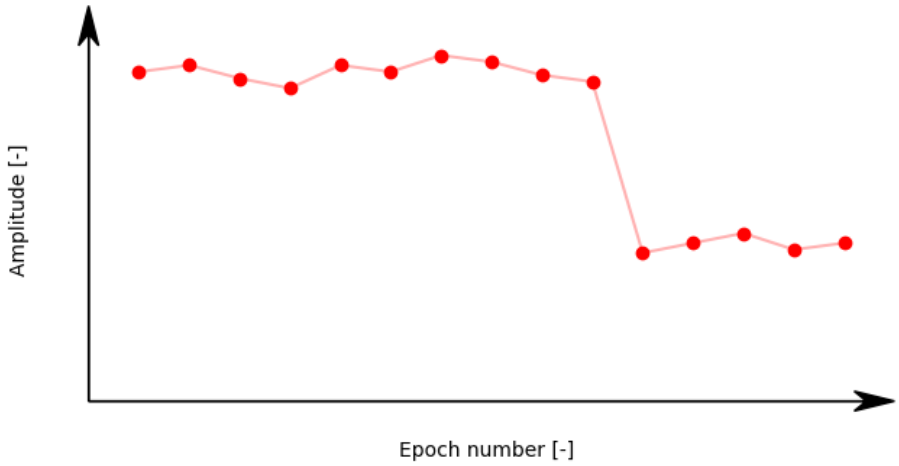

Figure 5.2: Amplitude time series of a theoretical PS having a very low amplitude dispersion in the sense of the Normalized Median Absolute Deviation, but a high dispersion in terms of the Normalized Amplitude Dispersion. This shows that although the NMAD is a more robust measure, it is not the optimal choice for selecting coherent PS.

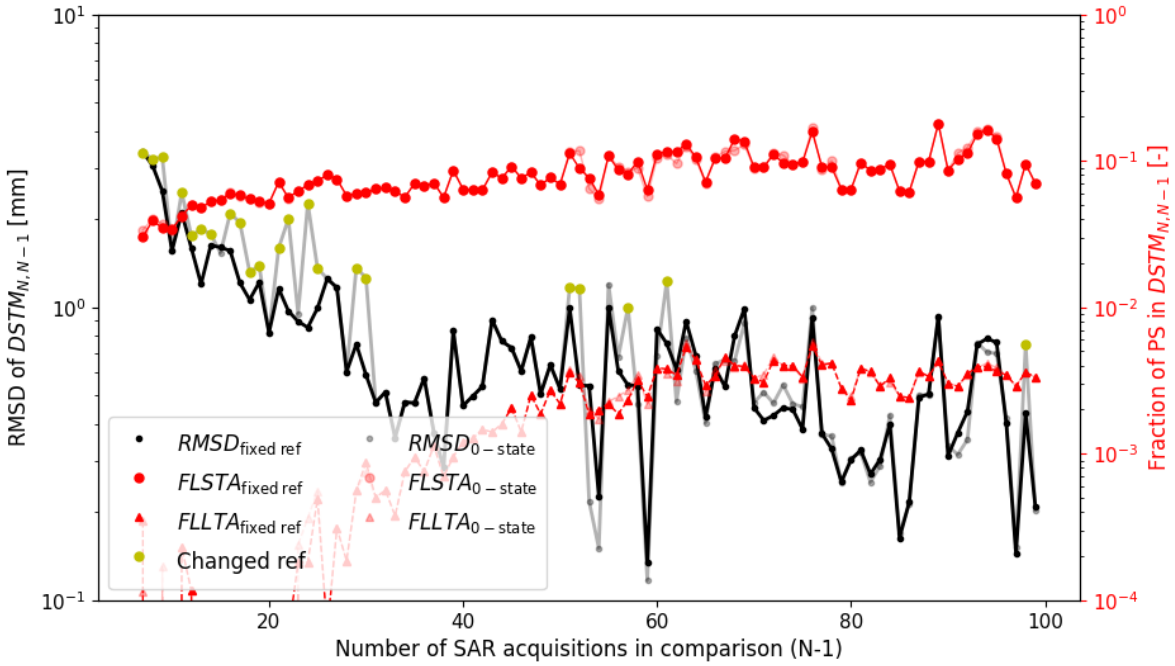

Figure 5.3: Incremental Robustness Metrics graph, comparing the displacement estimates from realizations N and $N-1$ for the base algorithm (transparent lines) versus a case where a certain location is forced to function as reference PS (opaque lines). The black line shows the Root Mean Squared Difference, indicating the average degree of variability in a single displacement estimate, the solid red line represents the Fraction of Localized Short-Term Ambiguities, and the red dashed line the Fraction of Localized Long-Term Ambiguities. The yellow dots indicate the occasions that the basic algorithm switched reference locations in the zero-state. The number of cycle slips remains unchained whereas the RMSD shows a significant improvement in those realization comparisons.

tion for robust monitoring. The reference location switch especially impacted those realizations of lengths 20–30 where the RMSD is up to halved, meaning an enormous increase in robustness and therewith a decrease in false warnings. Thus, one should consider which location to select as a reference when setting up a monitoring system. However, this reference should not just be kept blindly as the reference is of such importance that the displacement propagates into the other PS. Ideally, one should for instance use an Integrated Geodetic Reference Station (IGRS) while we can keep track of the stability of the reference. Moreover, the reference motion can be filtered out as we know the actual displacement of the IGRS through GNSS (Kamphuis, 2019).

On the other hand, the issues related to cycle slips appear to be largely unchanged. Upon reviewing both the Ambiguity Overview and the RMSD Overview in Figs. A.14 and A.15, it is evident that the least robust epochs continue to be primarily influenced by the snow acquisition on 12 Feb 2021.

5.3. Exclusion low coherence acquisition(s)

The zero-state results in chapter 4 showed that a large portion of the cycle slips could be traced back to an acquisition with low coherence to other acquisitions due to snowfall. Although still leading to plausible displacement estimates, the result was not in accordance with the other displacements. Therefore, a possible solution to improve overall robustness is to exclude this date from the processed stack.

By definition of repeatability, the robustness metrics remained unchanged till the 50th acquisition. As illustrated in Fig. 5.4, the opaque zero-state and solid exclude date metrics mirror each other since the excluded date was absent in those realizations. Post the excluded acquisition, a slight improvement is observed in terms of the robustness metrics for both short-term and long-term cycle slips. The improvement is mainly visible around 70 and 90 acquisitions in the comparison where the solid red line of the zero-state previously exhibited distinct peaks. From the Ambiguity Overview in Fig. A.20, it is discerned that there is no longer an outstanding epoch, indicating an overall improvement in robustness based on a decrease in ambiguous measurements. Nevertheless, sporadically high values are still visible in both RMSD and ambiguities. The RMSD occasionally improved, but instances of worsening are observed, with two prominent peaks that can be attributed to a changing reference. To improve the RMSD, we have to dive deeper into the robustness of the APS.

5.4. Atmosphere robustness improvements

As lined out in section 4.2, the atmosphere appeared to be a major cause of frail results. Thus, multiple measures were proposed to improve this robustness in section 4.4. The following subsections will cover the use of a prescribed PS1 network, the constraining of Kriging parameters, the use of a larger area of interest, the densification of the PS1 network, and the usage of a different equation to estimate the variogram.

5.4.1. Use of a prescribed set of first-order network PS

Given that the use of the NMAD did not improve robustness in the first-order network selection and, consequently, the RMSD robustness, the algorithm will be provided with a prescribed network of points randomly taken from a run with around 45 acquisitions. This approach aims to stabilize the displacement estimates. All corresponding figures for the simulation with the use of a prescribed subset of PS1 can be found in Appendix A.5.1 in full size.

When using a fixed set for the PS1 locations, the first results were auspicious when looking at the displacement and atmospheric matrices, see the $\Delta STM_{100,99}$ and $\Delta ASTM_{100,99}$ in Figs. A.22 and A.23. The $\Delta STM_{100,99}$ shows that realizations 99 and 100 almost produced the

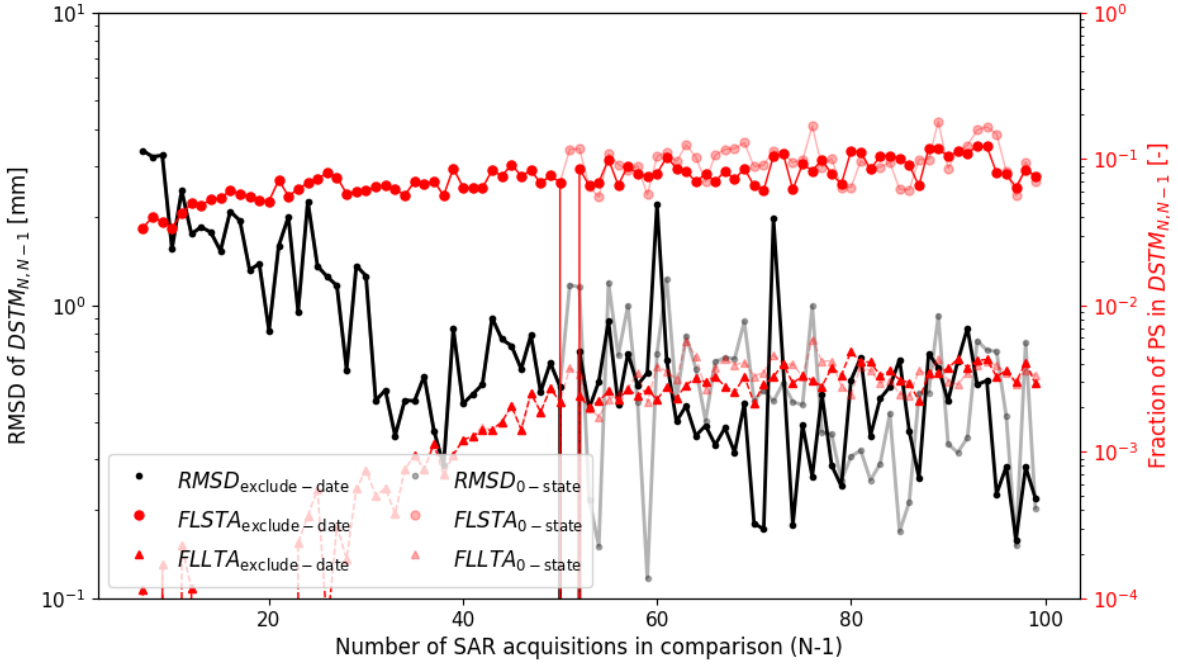

Figure 5.4: Incremental Robustness Metrics graph, comparing the displacement estimates from realizations N and $N-1$ for the base algorithm (transparent lines) versus a case where a SAR acquisition with relatively low coherence has been excluded in the analysis (opaque lines). The black line shows the Root Mean Squared Difference, indicating the average degree of variability in a single displacement estimate, the solid red line represents the Fraction of Localized Short-Term Ambiguities, and the red dashed line the Fraction of Localized Long-Term Ambiguities. The number of cycle slips slightly decreased in the realization comparisons previously containing distinct peaks.

same displacement estimates apart from one epoch. The $\Delta ASTM_{100,99}$ subsequently confirms that this is still caused by a different atmospheric estimate as the most erroneous epoch is the same as for the displacements and of similar magnitude.

In Fig. 5.5, the robustness improvement with a prescribed set of PS1 locations is clearly evident compared to the base algorithm (opaque vs transparent lines). Particularly noteworthy is the significant improvement in the result for RMSD and the localized short-term cycle slips (FLSTA). The occurrence of at least one cycle slip in 1 PS in 10, it decreased to 1 PS in 20, meaning that monitoring results will be less sensitive to false warnings. This improvement suggests that maintaining a fixed PS1 network is highly beneficial for PS situated around the unwrapping boundary and the counteracting of erroneous epochs.

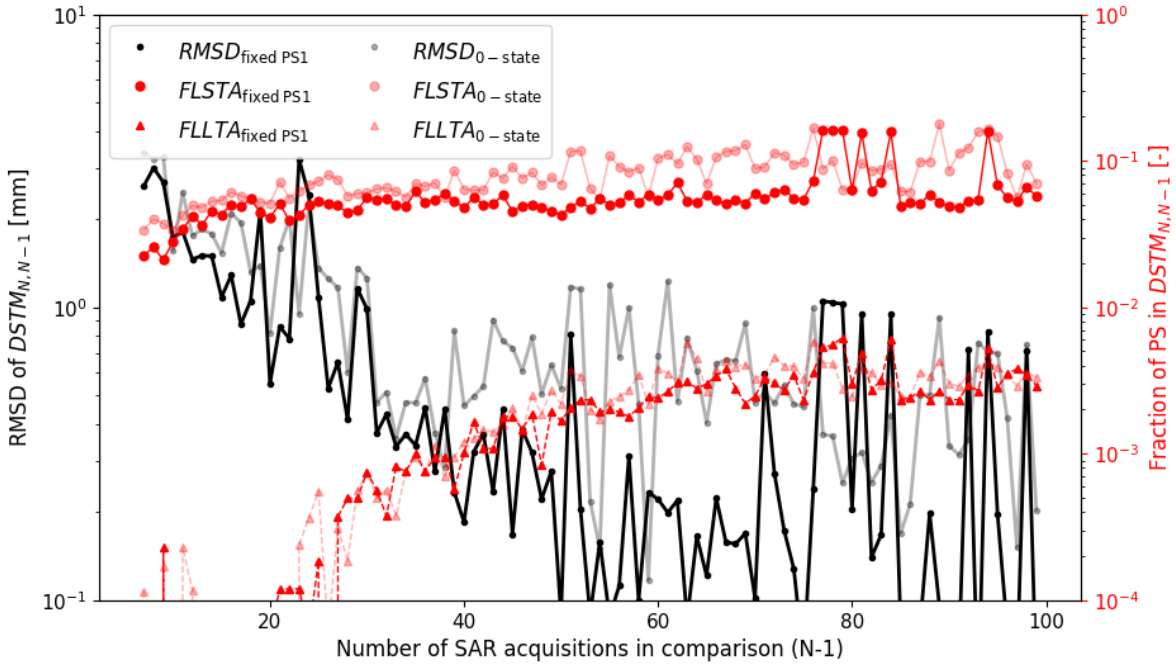

Figure 5.5: Incremental Robustness Metrics graph, comparing the displacement estimates from realizations N and $N-1$ for the base algorithm (transparent lines) versus a case where a prescribed set of locations is used for the PS1 network (opaque lines). The black line shows the Root Mean Squared Difference, indicating the average degree of variability in a single displacement estimate, the solid red line represents the Fraction of Localized Short-Term Ambiguities, and the red dashed line the Fraction of Localized Long-Term Ambiguities. The metrics significantly decrease (improve) apart from some distinct peaks around 80 acquisitions.

Despite the overall improvement with a prescribed PS1 set, a few realization comparisons exhibit worse results than the zero-state, particularly noticeable around the 80th acquisition. Here, an RMSD of 1 mm is observed, contrasting with the 0.2 mm recorded a few realization comparisons earlier, indicating a fivefold difference. The peaks after 90 acquisitions are explained by a changing reference location. However, the peaks around 80 acquisitions present a different scenario. In this instance, fluctuations occurred in the presence of PS1, as depicted in Fig. A.24 illustrating the consistency of the PS1 network. While the value is mostly equal to 100%, as we force a certain set to be used, some PS disappear from the first-order network. Most likely, a point from the network did not meet the NAD threshold value set in the parameter file. This is precisely what happens around realization comparison 80. The disappearance of one or two points from the PS1 network leads to completely different Kriging parameters, akin to the sudden jumps in nugget values seen in Fig. 4.6b. These changing parameters contribute to a different APS and consequently a less robust displacement estimation.

Ultimately, the adoption of a predetermined set of PS1 locations demonstrated significant

benefits for the robustness of the APS and, thus, the InSAR displacement estimates. Nevertheless, the inconsistency in the PS1 network heavily impacts the robustness, highlighting the need for an alternative solution to mitigate vulnerability to disappearances in the first-order network.

5.4.2. Kriging parameter restriction

A more subtle measure to increase the robustness of the atmospheric estimates is to constrain the Kriging parameters. Section Section 4.2 showed that the 1x1 km region over Amsterdam resulted in improbable Kriging parameters based on the results from the 5x5 km region. Therefore, it is thought that robustness could be increased by restricting the *range*, *sill*, and *nugget* based on the more probable results of the 5x5 km area. Based on the consideration of all possible parameter values in the 5x5 km case, the parameters are constrained as in Table 5.1. The *range* and *nugget* do not contain an upper constraint as they are deemed unnecessary.

Table 5.1: Imposed Kriging parameter constraints to improve the APS robustness

Parameter	Lower constraint	Upper constraint
Range	300 m	–
Sill	10^{-2} rad	10 rad
Nugget	$5 \cdot 10^{-2}$ rad	–

The robustness metrics from imposing the parameter constraints are shown in Fig. 5.6. The robustness improved again though less drastically than for the fixed PS1 network. All metrics, both the ambiguity as well as the RMSD, somewhat decreased from the zero-state indicating an improvement in robustness. However, the improvement is not to such an extent that it completely solves the problems causing low atmospheric robustness. For that cause, further constraints on the parameters should be considered. Previous studies have demonstrated that the use of weather research and forecasting (WRF) can enhance InSAR displacement estimates (Jung et al., 2014). Even so, without contextual data, it is challenging to implement accurate constraints that do not falsely limit atmospheric estimation. Therefore, there is a need to enhance information about the atmosphere in a different manner.

5.4.3. First-order network densification

A possible way to strengthen the robustness of the atmospheric phase estimates is the densification of the PS1 network. More PS in the first-order network are believed to lead to a more robust empirical variogram as elaborated on in section 2.2.4. However, there should be enough reliable PS available to base the APS estimates upon. To ensure this, the NAD threshold for a PS1 point is kept similar as in the zero-state. The applied change lies in the PS1 selection grid size which is set to 50 m, while it had been previously set at 100 m.

All corresponding figures for the simulation with the use of a PS1 selection grid size of 50 m can be found in Appendix A.5.3 in full. The robustness metrics are illustrated in Fig. 5.7. It is evident that the RMSD and ambiguities worsened more than they improved in the first 40 acquisitions. Conversely, the RMSD tends to improve after 40 acquisitions. Although the improvement is not to the extent observed in the fixed PS1 case, the adaptation is more subtle. There is a modest improvement in the fraction of short-term cycle slips which exhibits a decrease on average, yet peaks of similar magnitude are occurring elsewhere. This approach does not appear to be a comprehensive solution, as the primary issue of volatile kriging parameters persists similarly to the zero-state, as previously depicted in Fig. 4.6. However, it could be an improvement together with another measure to stabilize the parameter estimates.

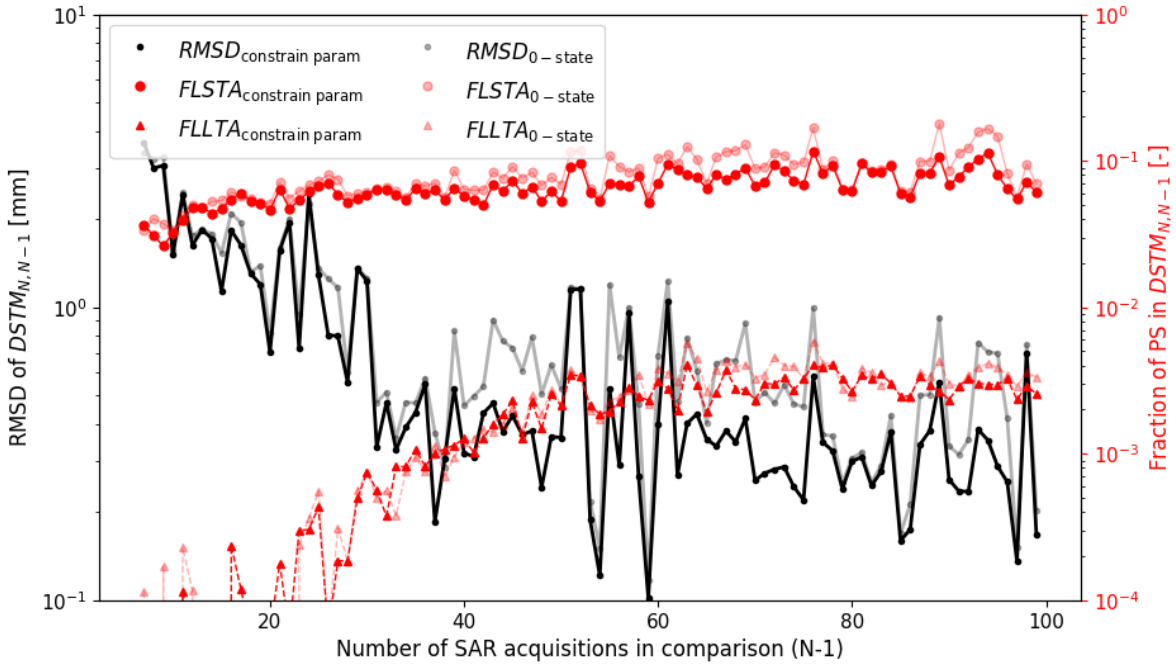

Figure 5.6: Incremental Robustness Metrics graph, comparing the displacement estimates from realizations N and $N-1$ for the base algorithm (transparent lines) versus a case where the Kring parameters are constrained to values that have been deemed probable (opaque lines). The black line shows the Root Mean Squared Difference, indicating the average degree of variability in a single displacement estimate, the solid red line represents the Fraction of Localized Short-Term Ambiguities, and the red dashed line the Fraction of Localized Long-Term Ambiguities. Overall, the metrics show a slight decrease (improvement).

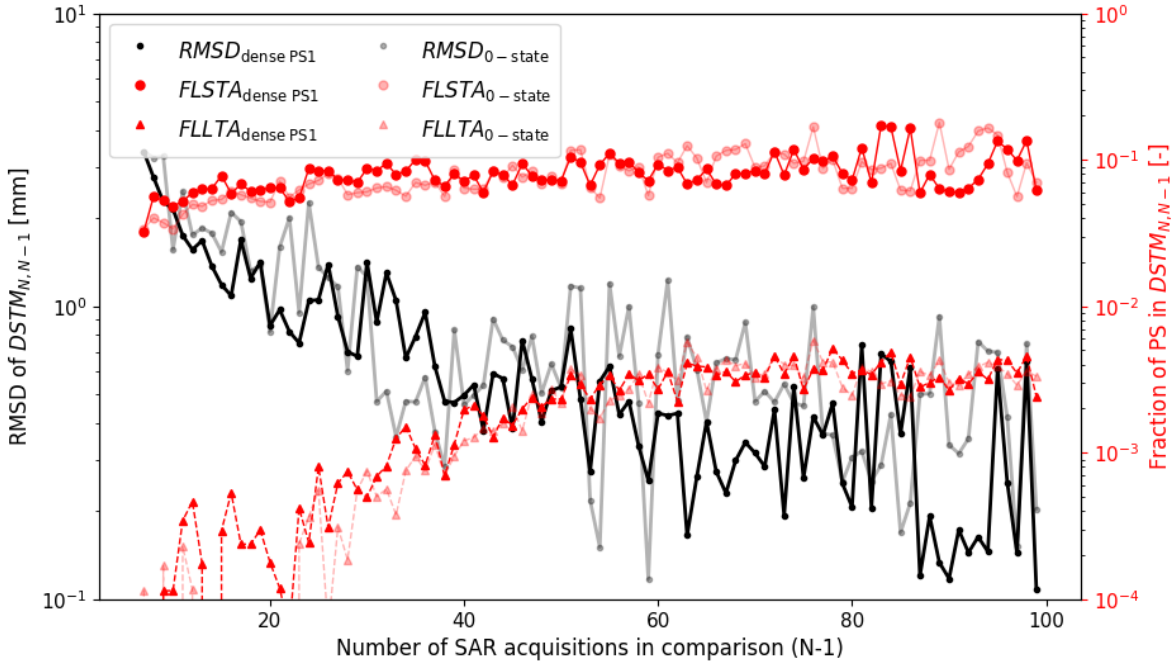

Figure 5.7: Incremental Robustness Metrics graph, comparing the displacement estimates from realizations N and $N-1$ for the base algorithm (transparent lines) versus a case where the PS1 network has been densified by lowering the PS1 selection grid size (opaque lines). The black line shows the Root Mean Squared Difference, indicating the average degree of variability in a single displacement estimate, the solid red line represents the Fraction of Localized Short-Term Ambiguities, and the red dashed line the Fraction of Localized Long-Term Ambiguities. Overall, the metrics show a slight decrease (improvement).

5.4.4. Robust Kriging mechanism

The newly proposed robust variogram estimation mechanism in section 4.4 is believed to stabilize the atmospheric estimation and thereby improve the displacement robustness. All corresponding figures are shown in Appendix A.5.4 in full.

Analyzing the robustness metrics in Fig. 5.8 reveals the notable improvement achieved with the introduction of the new variogram equation. The primary enhancement is evident in those comparisons where Kriging parameters previously underwent sudden jumps in value, such as realization comparison 76 (highlighted by the green patch in Fig. 4.6) or the comparisons around 95. In both cases, the peak fraction of PS with a cycle slip as well as the RMSD were close to halved. Instead of approximately 1:5 PS with a cycle slip, the value became 1:10 points at the peak, signifying an increase of 1500 PS that unwrapped consequently, a major difference. Fig. A.40 displays the new nugget value heatmap, demonstrating a more consistent estimate in nugget value for the same dates (horizontal lines). Incidental outliers are present, suggesting that further improvement in APS robustness would still be beneficial for enhancing the robustness of displacement results.

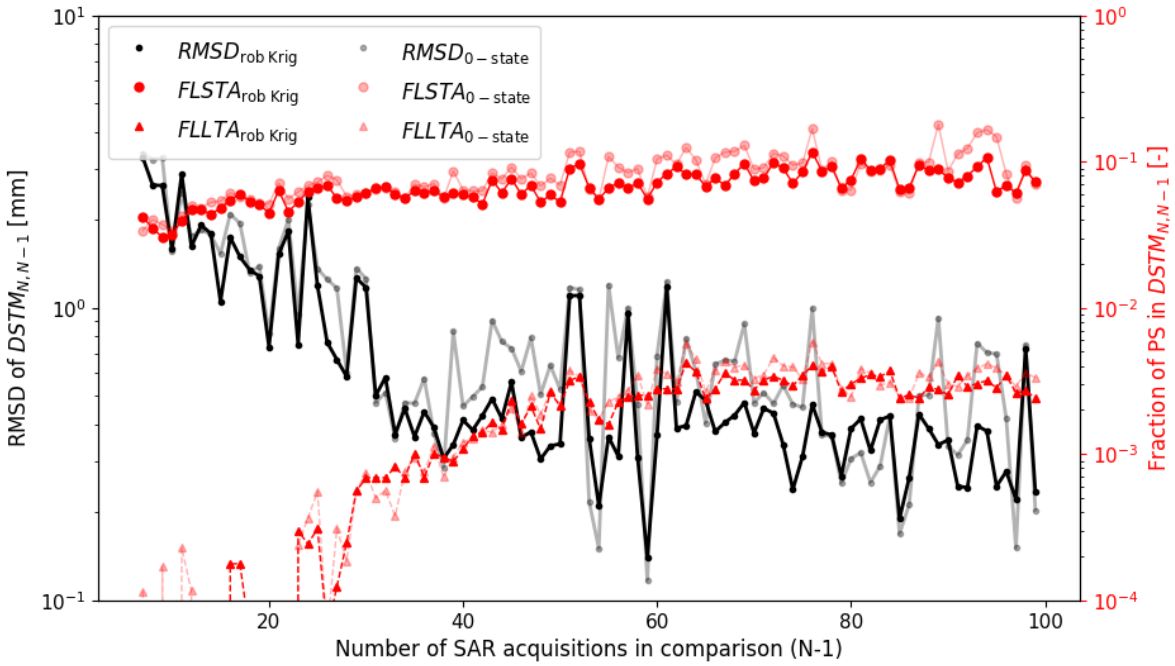

Figure 5.8: Incremental Robustness Metrics graph, comparing the displacement estimates from realizations N and $N-1$ for the base algorithm (transparent lines) versus a case where a more robust experimental variogram equation has been used (opaque lines). The black line shows the Root Mean Squared Difference, indicating the average degree of variability in a single displacement estimate, the solid red line represents the Fraction of Localized Short-Term Ambiguities, and the red dashed line the Fraction of Localized Long-Term Ambiguities. Overall, the metrics show an improvement.

5.4.5. 5x5 km region

The zero-state APS estimation showed that the area is too small to properly digest an atmospheric signal over the 1 by 1 km region. Besides, the other proposed improvements regarding a more robust atmosphere fell short. Therefore, a 5 by 5 km region is processed over the same center point to see the difference a larger area of interest would make. The dataset contained almost 270,000 PS2 in realization 100, considerably increasing the computational time. The DePSI process took almost six hours for this realization whereas it previously had cost just 10

minutes for the 1 by 1 km area. The increasing number of PS with a factor of around 18 came at a computational cost of factor 36.

The full result for the zero-state of the 5 by 5 km region over Amsterdam can be seen in Appendix A.5.5. The robustness metrics are shown in Fig. 5.9, where a few things stand out. The largest difference is in the fraction of PS with a long-term cycle slip (FLLTA, red dashed line). Instead of some 3 in 1000 points, it is more to 1 in 100 points for the 5 by 5 km region. A likely explanation is the inclusion of far more dynamic objects in the area of interest. The area covers large water bodies such as the rivers IJ and Amstel. Besides, some larger parks such as the Vondelpark and Westerpark are included as well in the region while the 1 by 1 km region only contained some smaller canals, but mostly constructions. The different land use types will be further discussed in section 5.8.1, where the land use types are linked to robustness. As mentioned previously, the robustness metrics should therefore not be compared 1 to 1 over different regions or with different acquisition inputs (tracks, dates, asc/dsc). However, the trends and behavior can be compared.

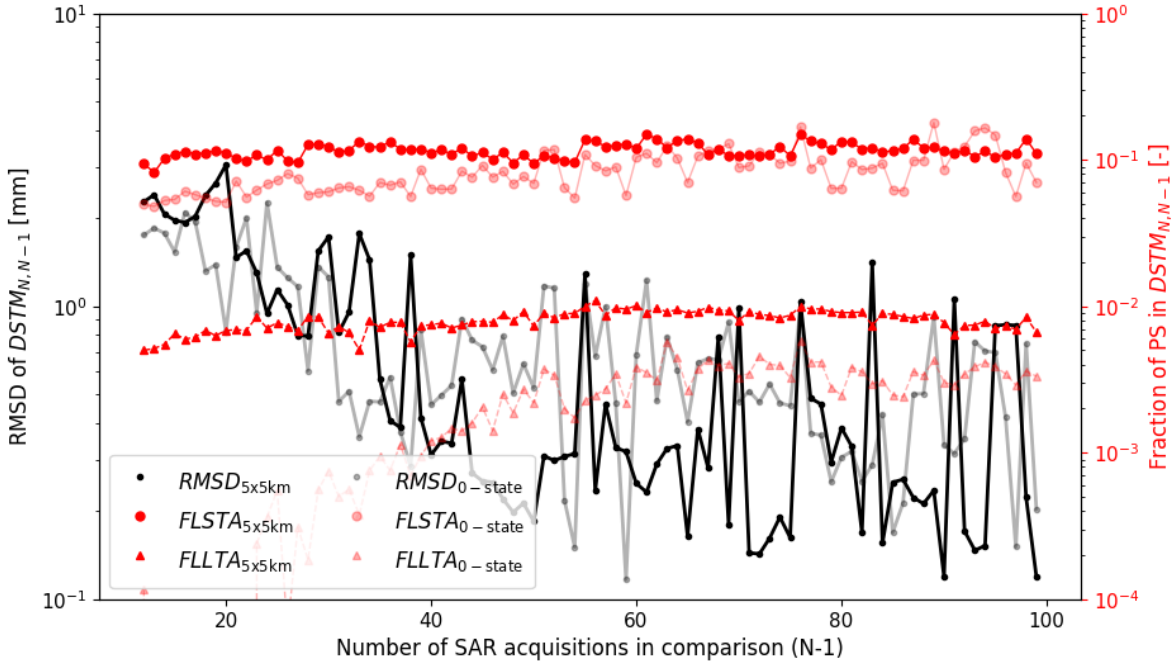

Figure 5.9: Incremental Robustness Metrics graph, comparing the displacement estimates from realizations N and $N-1$ for the base algorithm (transparent lines) versus the 5 by 5 km region over Amsterdam (opaque lines). The black line shows the Root Mean Squared Difference, indicating the average degree of variability in a single displacement estimate, the solid red line represents the Fraction of Localized Short-Term Ambiguities, and the red dashed line the Fraction of Localized Long-Term Ambiguities. The RMSD decreased whereas the fraction of ambiguities increased.

In contrast to the long-term cycle slips, the fraction of PS containing a short-term cycle slip as well as the RMSD (solid black line) exhibit comparable orders of magnitude in both areas. The FLSTA (solid red line) contains less distinct peaks due to a more robust APS estimation. While peaks in the RMSD share similar magnitudes in the 5 by 5 km region, the average value often resides significantly lower due to less volatile atmosphere estimation, as indicated by the Kriging nugget values in Fig. A.47. The nugget values are consistently estimated due to a better interpretable variogram.

Fig. 5.10 portrays the same estimated atmosphere, containing the same number of acquisitions as the variogram shown in Fig. 4.5. The extended area of interest results in a substantial increase in the number of pairs, contributing to a more robust variogram. Consequently, a var-

iogram model with meaningful parameters can be fitted through the experimental variogram. Only the tail of the variogram appears a bit noisy due to a scarcity of data points. This challenge could be counteracted by implementing a cutoff value for those bins containing a low number of pairs.

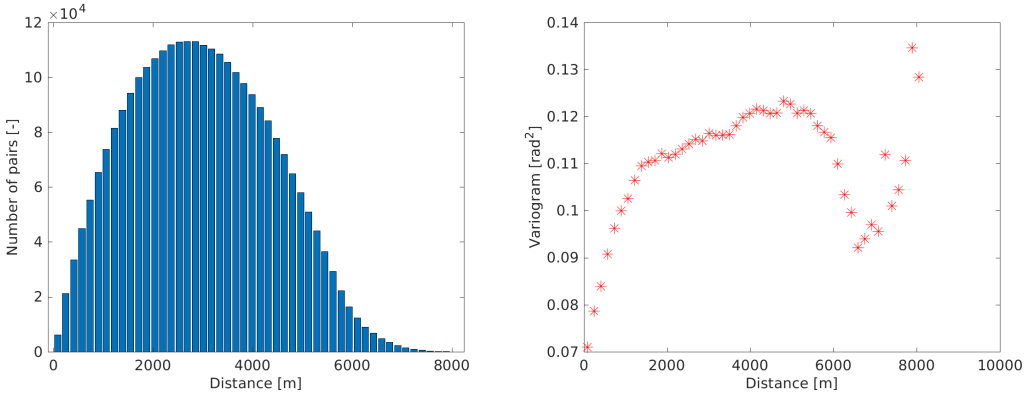

(a) Histogram **(b)** Experimental Variogram

Figure 5.10: Histogram of the distribution of PS1 pairs over the bins (a) side by side with the subsequently obtained experimental variogram (b) by averaging the semivariogram values in each bin. The experimental variogram contains a clear signal in contrast to the variogram in Fig. 4.5

The peaks in the RMSD in the Incremental Robustness Metrics of Fig. 5.9 graph are again explainable by a changing reference PS emphasizing the need for a consequently chosen reference or known reference displacement. The Ambiguity Overview in Fig. A.45 shows that two dates trigger the majority of short-term cycle slips instead of one date. Apart from the snow acquisition (12 Feb '21), the 16th of August 2020 is volatile as well. That evening, a heavy thunderstorm passed over the area (KNMI, 2020) causing a convective atmosphere. A strong convective event causes single-epoch delays to have higher uncertainty (Mulder et al., 2022). We can see this as the date is the most abruptly changing date in the Kriging nugget heatmap, shown in Fig. A.47. Interestingly enough, this date changes the most after the snow acquisition is added to the stack for the first time in the realization comparison.

To make a less biased comparison between both areas, the boundaries of the 1x1 km region are used to extract PS from the 5x5 km region situated within the 1x1 area of interest. Subsequently, a second robustness plot is made in Fig. 5.11 exclusively containing the metrics for the 1x1 km area of interest but derived from processing the 5x5 km region. This figure substantiates our hypothesis that processing a larger region has a positive effect on the robustness. Both, the number of cycle slips and the RMSD improve, ignoring the realization comparisons affected by a change in reference location. These metrics demonstrate a notable reduction, up to a factor of three in the extreme cases. From a monitoring perspective, this implies a strong reduction of false warnings in the automated detection of anomalies.

All in all, processing a larger area of interest improved the RMSD results due to a more robust atmospheric estimation. However, it also comes at a high computational cost and it could therefore be argued whether this is the most efficient measure to take if only interested in the monitoring of a small(er) area.

5.4.6. Discussion and conclusion atmospheric robustness

Upon comprehensive evaluation of measures on the APS robustness, we can conclude that a 1 by 1 km in principal is inadequate for properly capturing an atmospheric signal consistent with the theoretical physics. Nevertheless, specific interventions successfully mitigated some

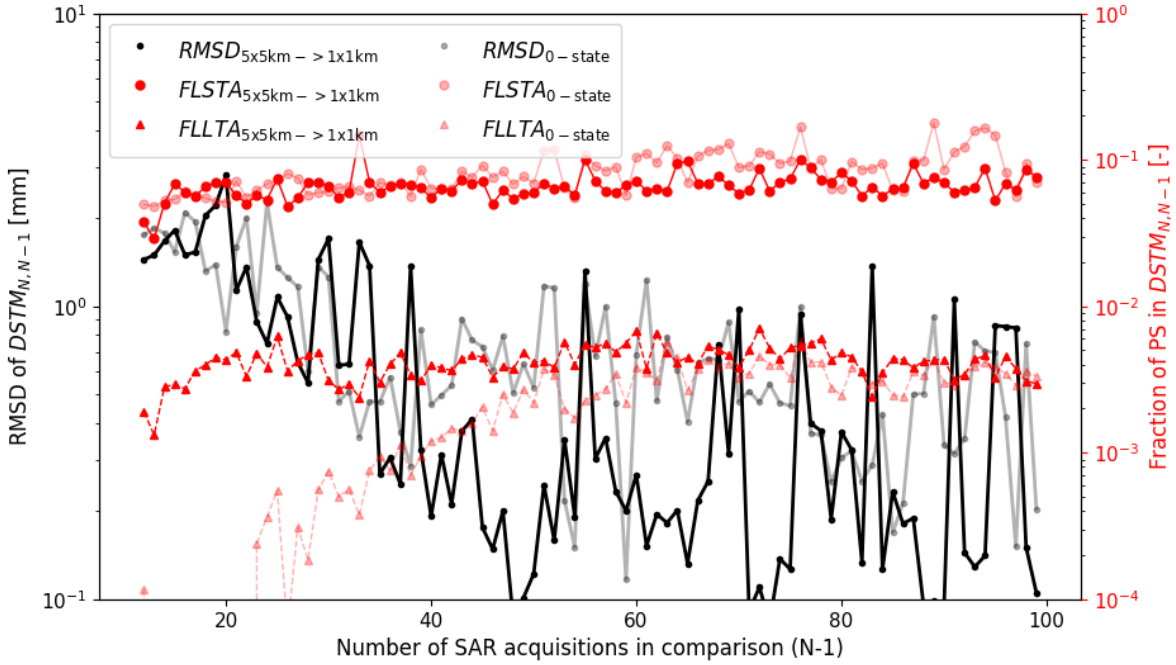

Figure 5.11: Incremental Robustness Metrics graph, comparing the displacement estimates from realizations N and $N-1$ for the base algorithm (transparent lines) versus 1 by 1 km obtained from processing the 5 by 5 km region over Amsterdam (opaque lines). The black line shows the Root Mean Squared Difference, indicating the average degree of variability in a single displacement estimate, the solid red line represents the Fraction of Localized Short-Term Ambiguities, and the red dashed line the Fraction of Localized Long-Term Ambiguities. The short-term cycle slips and RMSD metrics improved significantly.

major associated problems. The use of a fixed set of PS1 network, on average, demonstrated the most favorable impact on the robustness considering the three main metrics. However, this solution came at the cost of diminished resilience to alterations affecting a point in the PS1 network. Furthermore, this strategy entails the repetition of solutions from a designated PS1 set without discerning their efficacy. Consequently, prescribing a fixed set of PS1 is discouraged, as it imposes limitations on adaptability, prioritizing the stability of results over the generation of superior and more plausible results.

The imposition of constraints on the Kriging parameters, the densification of PS1, and the usage of a more robust variogram estimation all lead to a modest enhancement in the robustness. However, none of these approaches appears to be the definite breakthrough to mitigate the problems without accompanying drawbacks. The restriction of parameters is a Taylor-made solution that needs to be re-evaluated when estimating each individual APS to be effective. Densification of the PS1 network improves the variogram robustness by incorporating more data points, yet does not weigh up to the use of a larger region that more comprehensively captures the atmospheric behavior. The application of a robust Kriging method incorporating a median function to construct the variogram is advised, although it does not solve the problem sufficiently. This underscores the importance of critically reviewing the interpretability of the utilized variograms.

Employing a larger region for atmospheric processing yielded the most promising results. In the absence of hard constraints or a Taylor-made solution, the robustness significantly improved. The primary drawback is the computational cost, albeit this could be minimized by selectively using the larger area for atmospheric purposes without necessitating comprehensive processing of the entire expanded region. Consequently, it is recommended to adopt an area of interest larger than roughly 10 km^2, as smaller regions are anticipated to yield sub-

optimal results. Further research could be undertaken to explore and optimize the ideal area of interest for capturing the atmospheric signal with maximum robustness.

5.5. Expansion steady state

One of the hypotheses for the long-term cycle slips was the influence of the initial displacement model, which is currently a simple linear model as pointed out in section 2.2.4. As a seasonal cycle is quite common in the InSAR results for an urban area following temperature changes (Lyu et al., 2020), we expand the initial model by adding a sinusoidal with a period of one year. As the 1 by 1 km region over Amsterdam contains a very low number of PS in the long-term cycle slips category, the 5 by 5 km area over Amsterdam is used to see the influence as one is less sensitive to the coincidence of single PS.

The robustness results for the inclusion of a seasonal cycle in the initial displacement model are depicted in the Incremental Robustness Metrics in Fig. 5.12. This plot indicates that the number of long-term cycle slips did not decrease incorporating an initial deformation assumption containing a seasonal cycle. In fact, there seems to be no significant change at all. The attempt to enhance the robustness of the temporal unwrapping process by expanding the initial displacement assumption did not yield improvement. Evidently, improving unwrapping robustness is not a straightforward task, and reducing unwrapping uncertainty appears to be a challenging task. While alternative initial displacement models such as second-order polynomials could be explored, such improvements would need to be grounded in the existing literature which is not the case. On the contrary, multiple studies exist that propose improvements for both the temporal (Caro Cuenca et al., 2011) and spatial (Yu & Lan, 2016) unwrapping robustness. Exploring and implementing these methods may offer more promising insights to reduce the fraction of localized long-term cycle slips and thus enhance monitoring certainty.

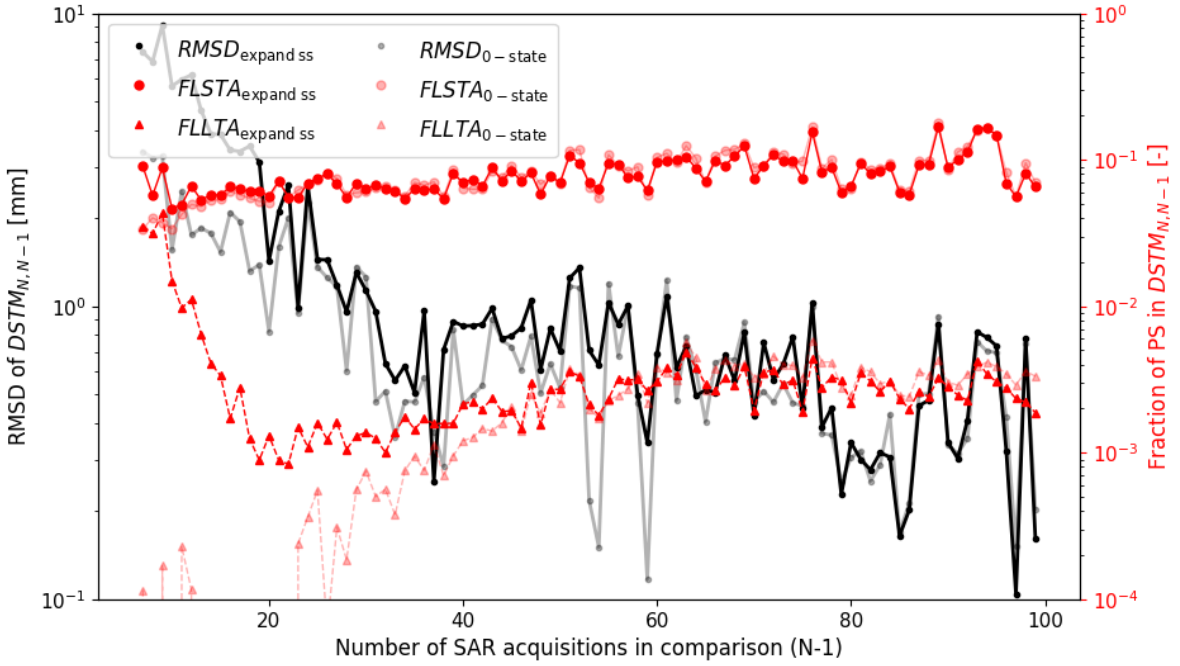

Figure 5.12: Incremental Robustness Metrics graph, comparing the displacement estimates from realizations N and $N-1$ for the base algorithm (transparent lines) versus a case where the initial displacement model has been extended (opaque lines). The black line shows the Root Mean Squared Difference, indicating the average degree of variability in a single displacement estimate, the solid red line represents the Fraction of Localized Short-Term Ambiguities, and the red dashed line the Fraction of Localized Long-Term Ambiguities. All metrics remain virtually equal.

5.6. More strict PS2 NAD threshold

A very theoretically simplistic way to improve the average robustness is to use a stricter NAD threshold, thus using relatively better points based on the amplitude dispersion. A drawback of this measure would be the spatial resolution. Instead of $\sim 15000\ ps/km^2$ in the zero-state one would keep close to half the PS ($\sim 7000\ ps/km^2$) for realization 100.

Fig. 5.13 shows the spectacular robustness improvement for the displacement results. The fraction of PS with a long-term or short-term cycle slip is reduced with a factor of 3. The fraction of PS containing a short-term cycle slip is 1:20 at its peak where it had been 1:5 in the zero-state. On the other hand, the improvement in RMSD is insignificant, indicating that the erroneous epochs are not affected at all. This again proves that the causes for this error type lie in the APS estimation which is not affected by a changing PS2 network threshold.

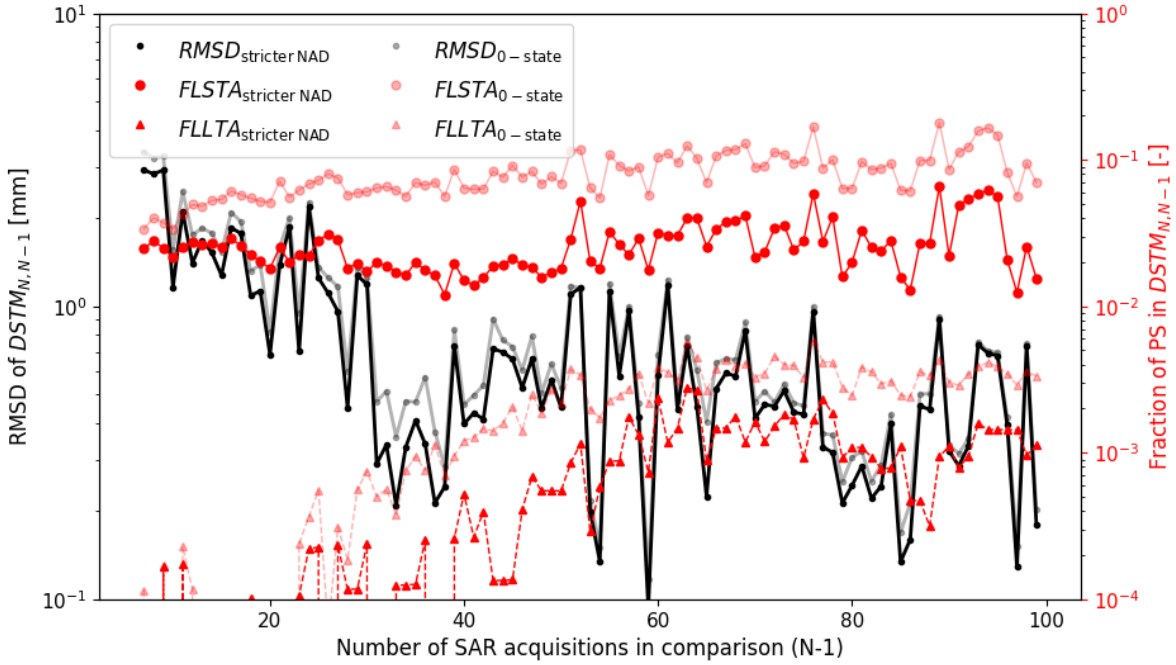

Figure 5.13: Incremental Robustness Metrics graph, comparing the displacement estimates from realizations N and $N-1$ for the base algorithm (transparent lines) versus a case where the NAD (amplitude dispersion) threshold for PS2 has been lowered (opaque lines). The black line shows the Root Mean Squared Difference, indicating the average degree of variability in a single displacement estimate, the solid red line represents the Fraction of Localized Short-Term Ambiguities, and the red dashed line the Fraction of Localized Long-Term Ambiguities. The two metrics considering cycle slips show a spectacular improvement while the RMSD remains (almost) unchanged.

In the end, this measure shows that the amplitude dispersion threshold should be critically reviewed based on the allowable number of misinterpretations and the area of interest for monitoring. In this 1 by 1 km area over Amsterdam, there is still a reasonable amount of PS left. However, implementing such a strict threshold over a rural region such as at the Hondsbossche Zeewering would lead to very few PS and thus no monitoring at all.

5.7. Combination of improvements

In the previous sections, measures were evaluated individually. Some proved to enhance the robustness of the displacement estimates. Now, a combination of the working improvements is performed to check the overall robustness improvement that can be made. For computational purposes, it is decided to only use a 5 by 5 km area for the estimation of the Kriging parameters. Before and after, only the 1 by 1 km will be used for the other parameter estimations.

The following five measures are now implemented simultaneously:

- A prescribed reference location.
- Kriging parameters obtained from the 5 by 5 km region.
- 12 February 2021 is excluded.
- The amplitude dispersion threshold for PS2 is lowered to 0.4.
- The PS1 network is densified.

The robustness results for the combination of these five measurements are depicted in Fig. 5.14. The core robustness metrics show a very significant improvement compared to the base DePSI algorithm. The Root Mean Squared Difference deprecated by a factor of 5 on average, the Fraction of Localized Short-Term Ambiguities by a factor of 4.5, and the Fraction of Localized Long-Term Ambiguities by a factor of 3.5 on average. After around 30 acquisitions, the RMSD is at a lower value than the lowest point in the base algorithm. After realization comparison 30 the improvements are only minor. Thus, it seems like 30 SAR acquisitions could be used as a rule of thumb as initialization for monitoring. The Ambiguity Overview and RMSD Overview show no real extremes.

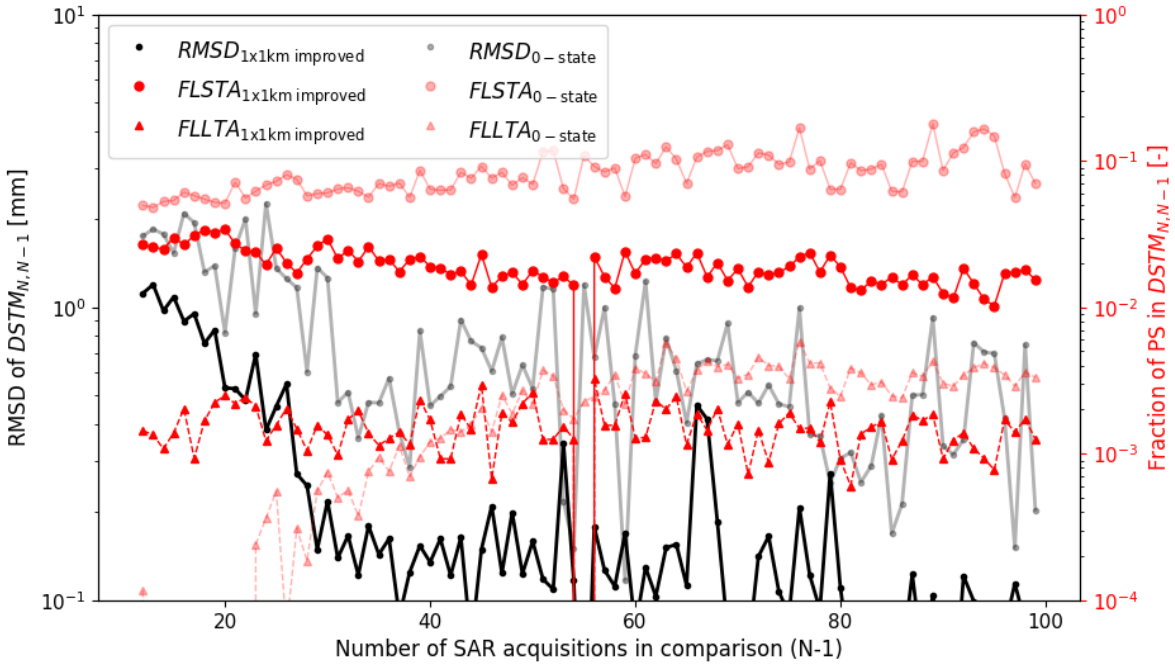

Figure 5.14: Incremental Robustness Metrics graph, comparing the displacement estimates from realizations N and $N-1$ for the base algorithm (transparent lines) versus a case where several improvements have been implemented (opaque lines). The black line shows the Root Mean Squared Difference, indicating the average degree of variability in a single displacement estimate, the solid red line represents the Fraction of Localized Short-Term Ambiguities, and the red dashed line the Fraction of Localized Long-Term Ambiguities. All metrics significantly improve by several factors.

5.8. Hondsbossche Zeewering

As introduced before, an area of 1 by 1 km and 5 by 5 km will be used over a rural dike area, the Hondsbossche Zeewering to avoid a Taylor-made solution over an urban area. The different areas of interest boundaries are depicted in Fig. 3.4. Here we see that the 1x1 km (red) area almost solely consists of countryside. Besides the dike itself, a few roads and houses are included but no more construction than that. On the other hand, the 5x5 km area (black outline) covers two villages. Thus, we expect to see this in the robustness metrics as constructions are believed to produce more consistence results (Perissin & Wang, 2011).

Using the same DePSI settings as for the zero-state over Amsterdam does not lead to a proper result for the 1x1km after realization 25. The reason is a too sparse PS1 network. Only some 8 PS present in the 1x1 km had a low enough amplitude dispersion value to be accepted in the first-order network leading to the breakdown of the process, reinforcing the idea of processing a larger area of interest. Using a higher threshold value for the first-order network leads to the results shown as the transparent lines in Fig. 5.15. These results show very little robustness, looking at the number of short-term and long-term cycle slips, meaning that the displacement estimates are very rapidly changing with a different stack as DePSI input. Without question, these results would be useless for monitoring purposes as the number of false warnings would be unworkable.

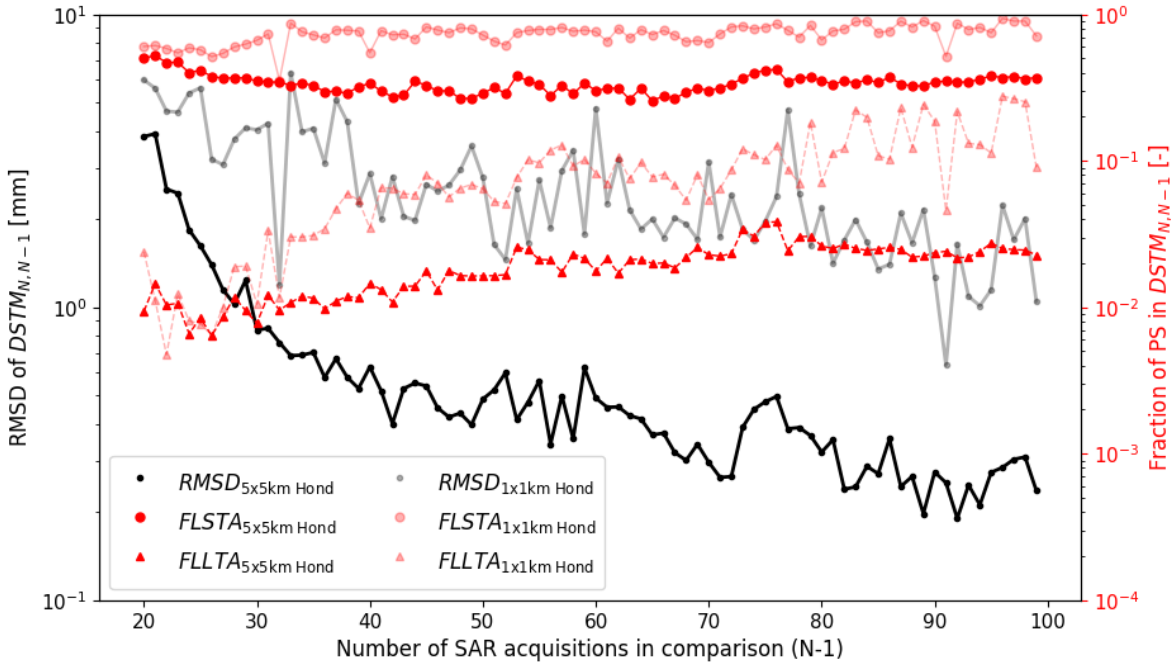

Figure 5.15: Incremental Robustness Metrics graph, comparing the displacement estimates from realizations N and $N-1$ for the base algorithm (transparent lines) versus the 5 by 5 km region over the Hondsbossche Zeewering (opaque lines). The black line shows the Root Mean Squared Difference, indicating the average degree of variability in a single displacement estimate, the solid red line represents the Fraction of Localized Short-Term Ambiguities, and the red dashed line the Fraction of Localized Long-Term Ambiguities. The 1 by 1 km results lead to unsatisfactory robustness whereas the 5x5 km looks promising.

The 1x1 km area appeared too small for such a rural area with little construction. Thus, it would be interesting to see if a 5 by 5 km region around the Hondsbossche Zeewering does lead to satisfactory results. The number of PS, present in the PS2 network lies around 100,000 instead of 8000. The robustness metrics of the 5x5 km region are represented by the opaque lines in Fig. 5.15. The solid red dots show that the number of PS with a short-term cycle slip

deprecated from 80-90 % towards 30-40 %, comparing the 1x1 km results with the 5x5 km results. The number of long-term cycle slips even further reduced from around 1 in 10 to 1 in 40 PS and the same holds for the RMSD, which asymptotically declines to a value of 0.2 mm.

As mentioned before, these robustness metric values are not one-to-one comparable with the results previously obtained over Amsterdam as other acquisitions and area layouts make this impossible. In the 5 by 5 km, it was apparent that using an area containing more water and natural surroundings negatively influences the overall robustness performance. Therefore, the coming subsection will research the robustness of various land use types.

The Ambiguity Overview in Fig. B.5 shows that the cycle slips are more spread out over different epochs than was the case for Amsterdam. There are more groups/clusters of epochs (horizontal rows) that stand out. Only one cluster around February 2021 has a plausible cause as that was the snow period over the Netherlands. However, the more acquisitions included in the realizations, the lower the number of ambiguous measurements. There are a few realization comparisons (around 75) that contain higher values in both the RMSD overview and the Ambiguity Overview. Fig. 5.16 depicts the range values of the experimental variogram. Here, a consistent parameter estimation till realization 75 is visible. Suddenly, the range contains jumps in estimation value and mostly much shorter ranges are estimated. This negatively affects the RMSD and the number of cycle slips. Thus, the proposed improvements over the Amsterdam region are implemented to see the impact on the robustness of the Hondsbossche Zeewering region.

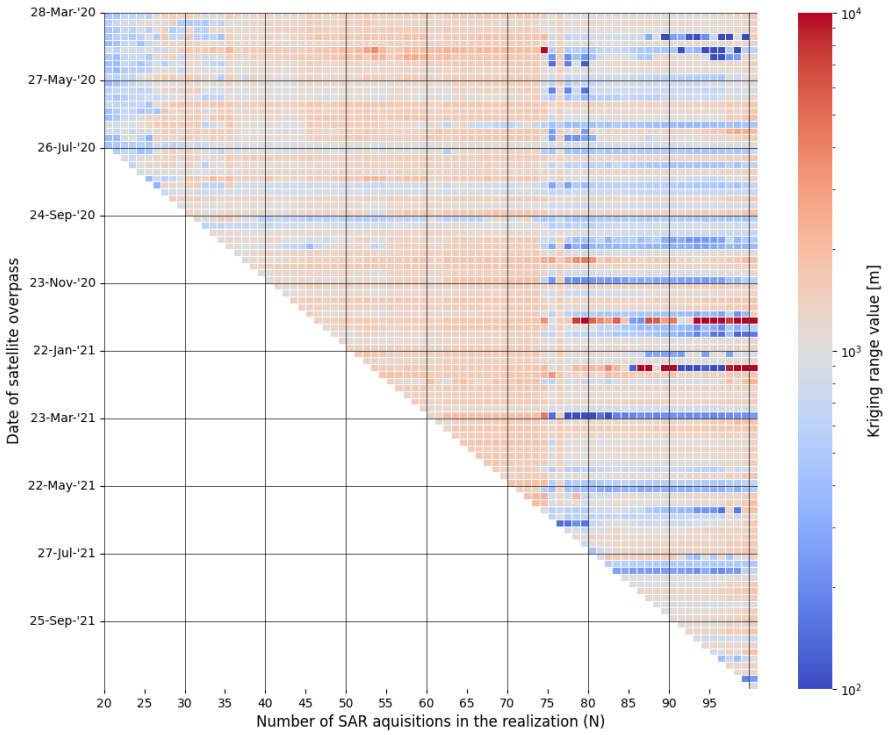

Figure 5.16: Diagonal matrix for the Kriging range parameter per epoch (individual atmosphere) in each realization N. Moving horizontally, the same atmosphere is estimated but with a different DePSI input. A red pixel indicates a relatively high value at that epoch for that realization (comparison) and blue a relatively low range. From realization 75, there is more variability in the estimated atmospheric range leading to higher RMSD values.

5.8.1. Area types breakdown

A large advantage of the 5x5 Hondsbossche area is the variety in the type of area. On the one hand, we have the sea, coast/beach, and sea defense itself. On the other hand, we have a large area with meadows, agriculture, and even villages and other developments. If one only cares about monitoring the sea defense, one would not care that the meadows show very little robustness. Therefore, parts of the 5 by 5 km area are assigned to specific land cover types, sea, sea defense, meadows, or urban, based on their coordinates. Because the land cover types are present in the same process, we can make a fair comparison in the PS robustness of different area types. Calculating the robustness metrics for each land use class separately leads to the results in Fig. 5.17.

The top left plot shows the number of conjunct PS in each class. The backscattering amplitudes from open water rarely form a coherent series as the sea slopes fluctuate randomly averaged over a pixel with each acquisition (Karvonen et al., 2005). This causes the chance for a sea pixel to pass the NAD threshold to decrease as the time series gets longer, e.g. more acquisitions are acquired. Comparing realizations 20 and 21, almost ten thousand conjunct PS are present in contrast to the twenty PS comparing realizations 99 and 100. The other classes contain less and less PS as well while more acquisitions make amplitude time series changes more likely. However, the urban area shows the least decrease in PS as the amplitudes are most consistent in an area with constructions.

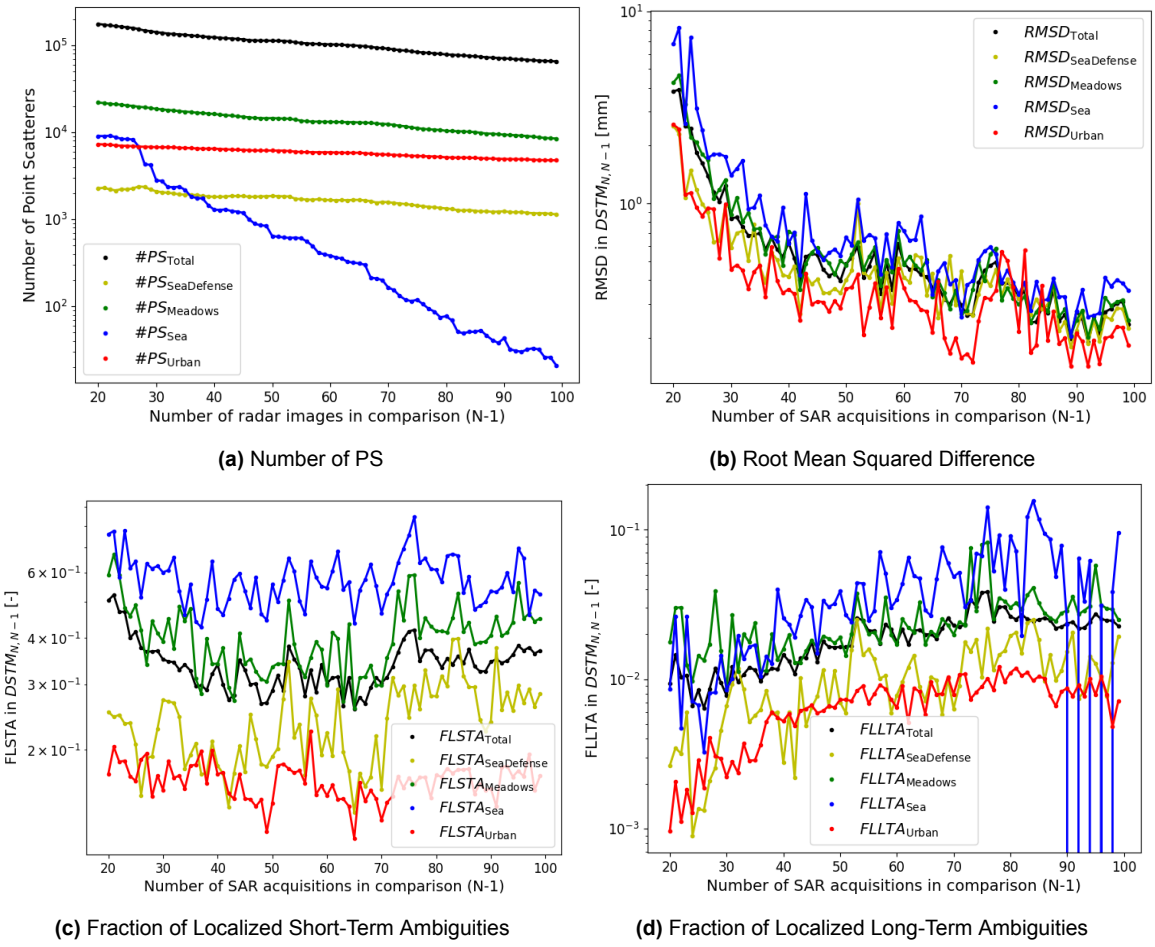

(a) Number of PS

(b) Root Mean Squared Difference

(c) Fraction of Localized Short-Term Ambiguities

(d) Fraction of Localized Long-Term Ambiguities

Figure 5.17: Comparison of the robustness metrics for different land coverage types around the Hondsbossche Zeewering.

The top right plot shows the development of the RMSD, the bottom left the FLSTA, and the bottom right the FLLTA over the realization comparisons. For all metrics, the robustness of the urban land cover type was the best, and the water class the worst albeit the order of magnitude differs significantly. The RMSD for these two classes differ by a factor of two, the FLSTA differs by a factor of three, and the FLLTA by a factor of ten. This shows that a low robustness result over a processed area does not per se mean that the displacement estimates are unusable for monitoring purposes. The robustness metrics of the sea defense follow closest to the robustness of the urban region indicating promising robustness. In the end, this again proves that one should not fixate on the robustness values but rather look at their implementation and the limitations of the InSAR displacement results in their case.

5.8.2. Improvements Hondsbossche Zeewering

Given the successful outcomes of the improvements implemented in the 1 by 1 km region over Amsterdam, the same enhancements are applied to the Hondsbossche Zeewering area. Using the 5 by 5 km region already demonstrated its beneficial impact compared to the 1 by 1 km approach, which led to suboptimal results. Now, the same additional measures as implemented in section 5.7 are included. The only difference lies in the excluded dates since the descending track contains different overpass dates. Consequently, the snow acquisitions excluded are the ones on 9 February 2021 and 15 February 2021.

The Incremental Robustness Metrics are depicted in Fig. 5.18. The robustness again significantly improves, while the RMSD, FLSTA, and FLLTA decrease by a factor of 1.5, 6, and 7, respectively. The improvement in RMSD is less pronounced since the primary improvement in the Amsterdam region proved to be the use of a larger area, a measure that was already implemented for the Hondsbossche Zeewering. Monitoring results obtained from the improved algorithm now substantially reduce the likelihood of misinterpreted situations arising from suboptimal utilization of InSAR capabilities.

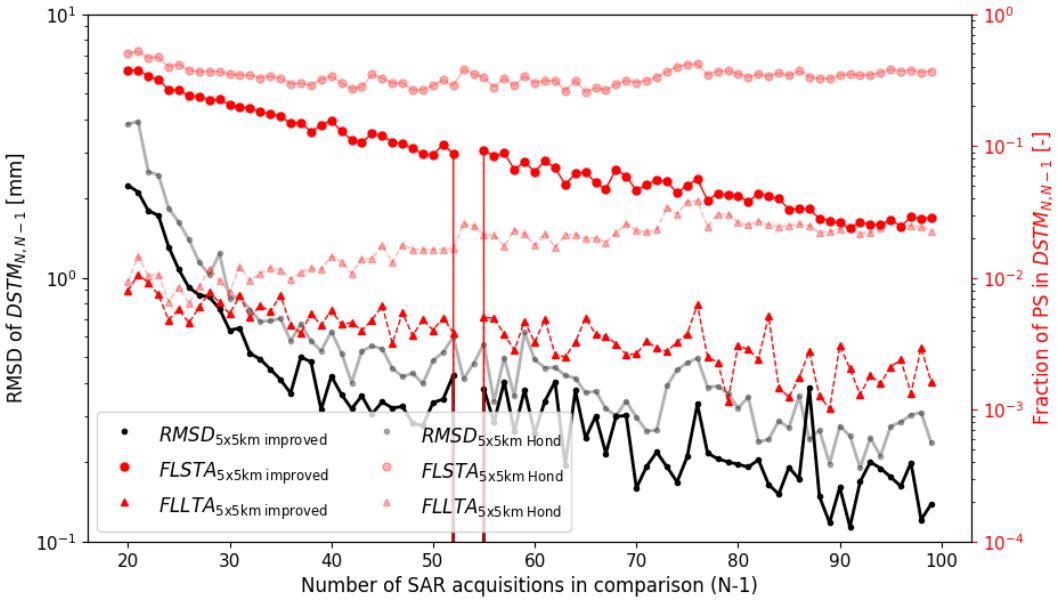

Figure 5.18: Incremental Robustness Metrics graph, comparing the displacement estimates from realizations N and $N-1$ for the base algorithm (transparent lines) versus the 5 by 5 km region over the Hondsbossche Zeewering (opaque lines). The black line shows the Root Mean Squared Difference, indicating the average degree of variability in a single displacement estimate, the solid red line represents the Fraction of Localized Short-Term Ambiguities, and the red dashed line the Fraction of Localized Long-Term Ambiguities. All metrics significantly improved.

Upon reflection on the different land use types, it is observed that the proportions between the various polygons remain essentially unchanged, with the urban polygon being the most robust and the sea polygon the least. However, the values have decreased as the overall robustness improved. The most notable change lies in the number of PS present in the polygon due to a more stringent NAD threshold, illustrated in Fig. 5.19. This threshold severely affected the Sea polygon which did not contain more than 1 PS after 50 acquisitions in the comparison. Besides, the Meadows polygon was heavily affected while the urban polygon now has a considerably higher number of PS compared to the Meadows polygon. The sea defense only retains a few points, indicating a significant reduction in spatial coverage. Ultimately, this graph emphasizes the importance of balancing (un)certainty versus the spatial density of the displacement measurements, depending on the specific objectives of a monitoring campaign.

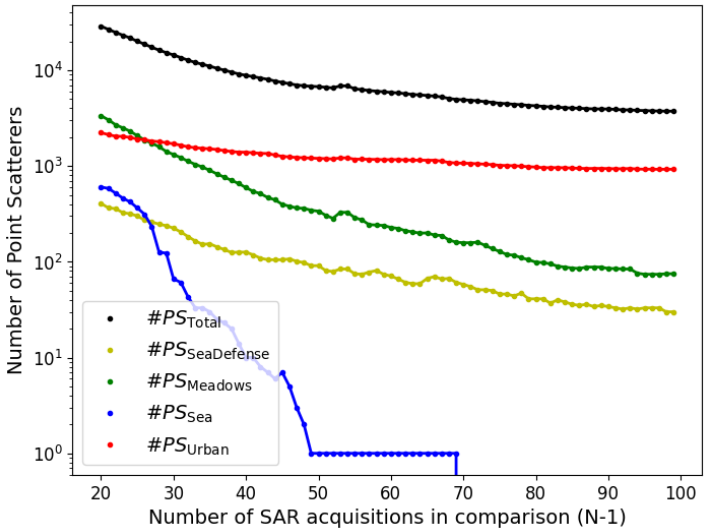

Figure 5.19: Number of Point Scatterers in each polygon, represented by a color, over the number of SAR acquisitions in the comparison after implementing the proposed improvements over the Hondsbossche Zeewering area.

6

Conclusions & Recommendations

In this study, the primary aim was to give insight into issues regarding the automatic monitoring of civil infrastructure with InSAR. Moreover, we aimed to create certain metrics to assess the robustness of the obtained displacement estimates quantitatively. The corresponding main research question is:

How can we assess the robustness of InSAR time series processing?

By means of three core metrics, we can express robustness quantitatively. Assessing the robustness of the current operating DePSI algorithm reveals that this algorithm is not suitable to be used as the basis for automatic monitoring. Displacement estimates changed to such an extent that these estimates can not be used to detect point anomalies reliably.

As the metrics identify possible fallacies in the algorithm, assessments on the robustness of InSAR algorithms are highly recommended. Furthermore, there are several measures and considerations to be taken into account when further developing an automatic monitoring system/algorithm. These considerations will be further elaborated upon by answering the introduced subquestions. The fundamental first question is whether there were significant discrepancies at all:

When measurement updates arrive, do the InSAR time series parameter estimates change? If yes, what types of displacement estimate differences occur, and what is their impact?

In the first place, we show that the current displacement estimates may indeed significantly change by varying the input. Using batch estimated results with a subsequent set of SAR acquisitions, named a realization, the conjunct epochs and conjunct Point Scatterer were compared. The estimates also changed when batch estimating the same stack input of SAR acquisitions due to randomness in the amplitude calibration of the algorithm. This causes changes in the first-order network to which the displacement estimates are very sensitive. Thus, it is needed to use a robust amplitude calibration procedure. By studying the Differential Space-Time Matrix, we distinguished four main 'deviation' categories.

The first, least occurring category, is the *localized long-term* deviation. To this category belongs the most severely changing displacement time series of PS that contain such little resemblance in a realization comparison that the median difference exceeds the value of a single ambiguity cycle, named drifting PS. This category mostly originates from a different integer unwrapping.

The second category comprises PS with a *localized short-term* deviation. The most severe form is the occurrence of an incidental ambiguity. Estimates that already lie close to a

different integer cycle interpretation are unwrapped differently at that epoch due to a difference in the atmospheric estimate, non-parameterized displacement estimate, or a different choice of reference PS. All these things change as a result of one extra measurement influencing the amplitude dispersion and thereby working through the first-order network set, atmosphere parameters, initial displacement model, and unwrapping choices.

The third category is the category of *area-wide short-term* deviations. This is mostly visible at specific epochs that contain a significant displacement estimate difference across the board relative to the other displacement differences. This is mostly due to a different Atmospheric Phase Screen estimate.

A changing reference PS(1) lies at the base of the last category. The *area-wide long-term* deviation can occur as the reference phase propagates through all other (relative) phase estimates.

These 'problems' are shown not only by examples but also by quantification and visualization, leading to an answer to the second subquestion:

How can we quantify the robustness of InSAR displacement estimates?

The four deviation categories are captured in three core metrics to express the robustness. The metrics are designed to separately capture ambiguities from the moderate displacement differences. To achieve this, we compute the fraction of PS exhibiting a structural drift/ambiguous offset in the *Fraction of Localized Long-Term Ambiguities*, the fraction of PS featuring at least one incidental ambiguity cycle difference in the *Fraction of Localized Short-Term Ambiguities*, and the *Root Mean Squared Difference* off all Point Scatterers not in either of two other categories. The use of more than one metric is imperative as reliance on a singular metric would be susceptible to bias introduced by the length of a time series. Longer time series inherently accumulate larger deviations as the phases build upon each other in time.

In our experiment, we start with five acquisitions incrementally incorporating one acquisition for each subsequent batch estimation, progressing until the 100th acquisition is included. The robustness assessment using the three primary metrics is facilitated by comparing realization 5 with realization 6, 6 with 7, and so forth, up to realization 99 with 100. This comparison is presented in an *Incremental Robustness Metrics* graph (page 42), offering insights into the robustness development concerning the number of acquisitions in a realization.

The metrics are not to be interpreted as individual values but rather in a global context. They are meaningful, though biased with the length of time series as the chance of a *localized short-term ambiguity* is larger with more epochs. Therefore, it is more useful to detect notable peaks relative to metric values from other realization comparisons suggesting low robustness and indicating substantial variability in displacement estimates across different inputs. The more detailed Ambiguity Overview (see page 43) can subsequently help to identify possible causes.

For the zero-state, the currently used DePSI version, often at least 10% of all selected PS had an ambiguously interpreted estimate, meaning that at least one single displacement differed around 28 mm just by varying the input acquisitions. However, some peaks reached the 20%. For the non-ambiguous PS, the introduced RMSD appeared to be around 0.5 mm. A detailed examination of the zero-state reveals the answer to the third subquestion:

What is the cause for these displacement estimate differences?

There is not just one cause for the different displacement estimates, given that the estimation process involves multiple distinct steps influenced by numerous variables. A notable observation was the impact of a low-coherence acquisition caused by snowfall, leading to an excessive

number of cycle slips as illustrated in Fig. 4.2 on page 43. Consequently, careful consideration is essential in deciding whether to incorporate a newly acquired SAR acquisition in the analysis. This decision-making process can be achieved by using contextual weather data.

The primary contributor to the *area-wide short-term* zero-state displacement deviations is the Atmospheric Phase Screen estimation. Abruptly changing Kriging parameters, employed for spatial interpolation around the PS1 network, exhibit a strong correlation with the largest RMSD values shown in Fig. 4.6. This means that the atmospheric signal of previously estimated epochs is modeled very differently severely changing obtained displacement estimates. This is strange and undesired as a new acquisition should not be able to largely influence the atmospheric interpretation of an acquisition one year ago. Further investigations indicate that there are two primary causes at the core of the atmospheric estimation challenge.

Firstly, a 1 by 1 km area proves inadequate for capturing an atmospheric signal accurately, as the obtained interpolation parameters do not follow our physical understanding of the atmosphere. This advocates for a preference towards a larger area of interest to model the APS.

Secondly, the variogram should be more critically evaluated and more robustly constructed. At the moment, due to sparse bins, a sparse PS1 network, and a variogram calculation that is not robust, an uninterpretable experimental semi-variogram arises, resulting in three parameters that are not in line with our physical understanding of the atmosphere. Coupled with the suboptimal Gaussian filter process to separate the non-parameterized displacement from the residual phase at the PS1 locations described in section 2.1.6 on page 11, there exists a need of re-evaluating the Atmospheric Phase Screen estimation to improve robustness of DePSI.

6.1. Recommendations

The first recommendation is a trivial though most important outcome of this research. It could be that InSAR users blindly trust their results as if they are quite certain about the outcome. However, we show that blind trust in the result is impossible. Therefore, it would be beneficial to perform a similar robustness analysis for other InSAR algorithms as proposed in the test recipe in section 3.2, batch estimating with varying input. This will not only give insight into the robustness of achieved results but can also explain the causes of anomalies in the monitoring results. Moreover, it can also help decide what threshold or other settings to use for a desired output certainty.

The zero-state results lead to measures that possibly enhance the robustness, see Chapter 5. From the critical evaluation of the different measures, we have several recommendations to answer the last subquestion:

What are the requisites to obtain robust and repeatable displacement estimates for monitoring civil infrastructure with InSAR?

The repeatability requirement can be effectively addressed by mitigating a function using randomness in the algorithm, achieved through adjusting the calibration step where this was explicitly used. This measure guarantees consistent results in case of the repetition of the same experiment by any individual.

On the other hand, ensuring a more robust outcome using InSAR requires more advanced adjustments. A perfectly robust system is unachievable, but also unwanted due to the inherent imperfections in our initial predictions. The main problems or uncertainties lie in the unwrapping and atmosphere. A more robust unwrapping approach is a challenging task requiring more thorough research. On the other hand, much of the lack of robustness in the atmosphere is now caused by the well-described shortcomings in our algorithm, outlined in section 2.2.4 on page 24.

Most of the proposed measures regarding robustness, made based on the deviation hypotheses, indeed enhance the robustness of InSAR results. However, some improvements do not contribute to an increase in the robustness. These improvements are the use of the Normalized Median Absolute Deviation instead of the NAD and the enrichment of the initial displacement model. An alternative measure to the enrichment of the initial displacement is interesting for future research as the solution to mitigate Localized Long-Term Deviation is still unknown.

The following recommendations are made to avoid an outcome depending on the moment of processing as much as possible:

- One single fixed pixel/location should be chosen to serve as a reference throughout the whole monitoring timespan. Ideally, this reference is combined with a second measurement technique such as GNSS to filter and subtract the reference displacement signal from all other displacement estimates. An example of such a combination is achieved with an IGRS.

- To adequately capture the atmospheric signal, it is recommended to use a sufficiently large area of interest, which can be verified through the following steps:

    1. Conduct a robustness test, as outlined in the test recipe on page 36, to compare the $\Delta ASTM_x$ with ΔSTM_x. A strong resemblance of the atmospheric differences in the displacement estimates indicates low atmospheric robustness.
    2. Examine the changes in spatial interpolation parameters to see the variability in the estimation.
    3. Critically evaluate the semi-variogram of multiple atmospheres to see whether these make sense and align with our physical understanding of the atmosphere.

- A more robust Kriging (semi-)variogram equation using a median instead of a mean operation is preferred as this makes the theoretical fit more robust for changes in input.

- To achieve a balance between precision, spatial coverage, and the desired level of uncertainty, careful consideration should be given to selecting an appropriate amplitude dispersion (NAD) threshold. This threshold is mainly depending on the goal of a certain monitoring mission. If we are interested in monitoring a specific dike, we need to be more certain of our result compared to the monitoring of a large gas field. If the expected chances of an ambiguity mistake are known, we can relate that to the margin of error in flagging anomalous locations.

- As shown throughout the whole study, batch estimating is far from ideal. It does provide useful recommendations to improve robustness stacks, but recursive updating of the parameters has the future. To achieve this, research is needed to decide on the most robust implementation of recursively updating. For instance, are we going to update with every acquisition or after three acquisitions? And what do we choose as a first-order network for the atmosphere, do we stick with a fixed set of points, and how do we deal with points that seem to change based on their amplitude behavior?

Performing the proposed test recipe also gives insight into whether a stack contains enough acquisitions to be used as a basis for recursive monitoring. Given the experiments performed in this study, this number lies around 30 acquisitions.

6.2. Future perspective for monitoring with InSAR

Based on this study, should one be skeptical about the use of InSAR displacement time series for monitoring purposes? Our findings suggest that InSAR retains significant potential for monitoring, particularly for global assessments of cities or larger areas using a PSI approach. In scenarios like the gas fields in Groningen, where a few anomalous point scatterers may exist, their impact is negligible as the main signal of the entire area remains distinguishable. However, challenges persist in using InSAR for point-level detection of anomalous behavior, such as monitoring specific structures like quay walls or dike segments. Further developments are needed to overcome these challenges for more localized monitoring applications.

References

Amani, M., Poncos, V., Brisco, B., Foroughnia, F., Delancey, E. R., & Ranjbar, S. (2021). Insar coherence analysis for wetlands in alberta, canada using time-series sentinel-1 data. *Remote Sensing*, *13*(16). doi: 10.3390/rs13163315

Bianchini Ciampoli, L., Gagliardi, V., Calvi, A., D'Amico, F., & Tosti, F. (2019). Automatic network level bridge monitoring by integration of InSAR and GIS catalogues.. doi: 10.1117/12.2527299

Brouwer, W. S., Wang, Y., van Leijen, F. J., & Hanssen, R. F. (2023). *ON THE STOCHASTIC MODEL FOR INSAR SINGLE ARC POINT SCATTERER TIME SERIES.*

Caro Cuenca, M., Hooper, A. J., & Hanssen, R. F. (2011). A new method for temporal phase unwrapping of persistent scatterers InSAR time series. *IEEE Transactions on Geoscience and Remote Sensing*, *49*(11 PART 2). doi: 10.1109/TGRS.2011.2143722

Copernicus. (2023). *European ground motion service.* Retrieved from https://egms.land.copernicus.eu/

De Doncker, P., Dricot, J. M., Meys, R., Hélier, M., & Tabbara, W. (2006). Electromagnetic fields estimation using spatial statistics. *Electromagnetics*, *26*(2). doi: 10.1080/02726340500486450

ESA. (2022). *Mission ends for copernicus sentinel-1b satellite.* Retrieved 2023-11-28, from https://www.esa.int/Applications/Observing_the_Earth/Copernicus/Sentinel-1/Mission_ends_for_Copernicus_Sentinel-1B_satellite

European Space Agency. (2014). *Sentinel-1.* Retrieved 2023-06-28, from https://sentinels.copernicus.eu/web/sentinel/missions/sentinel-1

Ferretti, A., Prati, C., & Rocca, F. (2001). Permanent scatterers in SAR interferometry. *IEEE Transactions on Geoscience and Remote Sensing*, *39*(1). doi: 10.1109/36.898661

Genton, M. G. (1998). Highly Robust Variogram Estimation. *Mathematical Geology*, *30*(2). doi: 10.1023/A:1021728614555

Hampel, F. R. (1971). A General Qualitative Definition of Robustness. *The Annals of Mathematical Statistics*, *42*(6). doi: 10.1214/aoms/1177693054

Hanssen, R. F. (2001). *Radar Interferometry: Data Interpretation and Error Analysis (Remote Sensing and Digital Image Processing)*.

Hanssen, R. F. (2021). *Caroline, vision document.*

Hanssen, R. F., Van Leijen, F. J., Van Zwieten, G. J., Dortland, S., Bremmer, C. N., & Kleuskens, M. (2008). Validation of psi results of alkmaar and amsterdam within the terrafirma validation project. In *European space agency, (special publication) esa sp.*

Hawkins, D. M., & Cressie, N. (1984). Robust kriging-A proposal. *Journal of the International Association for Mathematical Geology*, *16*(1). doi: 10.1007/BF01036237

Hodson, T. O. (2022). *Root-mean-square error (RMSE) or mean absolute error (MAE): when to use them or not* (Vol. 15) (No. 14). doi: 10.5194/gmd-15-5481-2022

Hu, F., van Leijen, F. J., Chang, L., Wu, J., & Hanssen, R. F. (2019). Monitoring deformation along railway systems combining Multi-temporal InSAR and LiDAR data. *Remote Sensing*, *11*(19). doi: 10.3390/rs11192298

Hu, F., Van Leijen, F. J., Chang, L., Wu, J., & Hanssen, R. F. (2022). Combined Detection of Surface Changes and Deformation Anomalies Using Amplitude-Augmented Recursive InSAR Time Series. *IEEE Transactions on Geoscience and Remote Sensing*, *60*. doi: 10.1109/TGRS.2021.3093108

Hu, F., Wu, J., Chang, L., & Hanssen, R. F. (2019). Incorporating temporary coherent scatterers in multi-temporal insar using adaptive temporal subsets. *IEEE transactions on geoscience and remote sensing*, *57*(10), 7658–7670.

Hu, J., Li, Z. W., Ding, X. L., Zhu, J. J., Zhang, L., & Sun, Q. (2014). *Resolving three-dimensional surface displacements from InSAR measurements: A review* (Vol. 133). doi: 10.1016/j.earscirev.2014.02.005

Jung, J., Kim, D. J., & Park, S. E. (2014). Correction of atmospheric phase screen in time series InSAR using WRF model for monitoring volcanic activities. *IEEE Transactions on Geoscience and Remote Sensing*, *52*(5). doi: 10.1109/TGRS.2013.2264532

Kampes, B. M. (2006). *Radar interferometry* (Vol. 12). Springer.

Kamphuis, J. (2019). *Co-location of geodetic reference points: On the design and performance of an Integrated Geodetic Reference Station.* Retrieved from http://resolver.tudelft.nl/uuid:035541d2-b028-41b6-a488-c19c3829b0ef

Karvonen, J., Similä, M., & Mäkynen, M. (2005). Open water detection from baltic sea ice Radarsat-1 SAR imagery. *IEEE Geoscience and Remote Sensing Letters*, *2*(3). doi: 10.1109/LGRS.2005.847930

Ketelaar, G. (2009). *Satellite radar interferometry: Subsidence Monitoring Techniques*.

KNMI. (2020). *Augustus 2020.* Retrieved 2023-12-06, from https://www.knmi.nl/nederland-nu/klimatologie/maand-en-seizoensoverzichten/2020/augustus

KNMI. (2021). *Februari 2021.* Retrieved 2023-07-26, from https://www.knmi.nl/nederland-nu/klimatologie/maand-en-seizoensoverzichten/2021/februari

Laur, H., Bally, P., Meadows, P., Sanchez, J., Schaettler, B., Lopinto, E., & Esteban, D. (2002). *DERIVATION of the BACKSCATTERING COEFFICIENT σ^0 in ESA ERS SAR PRI PRODUCTS* (Tech. Rep.). European Space Agency.

Leys, C., Ley, C., Klein, O., Bernard, P., & Licata, L. (2013). Detecting outliers: Do not use standard deviation around the mean, use absolute deviation around the median. *Journal of Experimental Social Psychology*, *49*(4). doi: 10.1016/j.jesp.2013.03.013

Li, Z., Cao, Y., Wei, J., Duan, M., Wu, L., Hou, J., & Zhu, J. (2019). *Time-series InSAR ground deformation monitoring: Atmospheric delay modeling and estimating* (Vol. 192). doi: 10.1016/j.earscirev.2019.03.008

Lyu, M., Ke, Y., Li, X., Zhu, L., Guo, L., & Gong, H. (2020). Detection of seasonal deformation of highway overpasses using the Ps-InSAR technique: A case study in Beijing urban area. *Remote Sensing*, *12*(18). doi: 10.3390/RS12183071

Macchiarulo, V., Milillo, P., Blenkinsopp, C., & Giardina, G. (2022). Monitoring deformations of infrastructure networks: A fully automated GIS integration and analysis of InSAR time-series. *Structural Health Monitoring*, *21*(4). doi: 10.1177/14759217211045912

Massonnet, D., & Feigl, K. L. (1998). Radar interferometry and its application to changes in the earth's surface. *Reviews of Geophysics*, *36*(4). doi: 10.1029/97RG03139

Matheron, G. (1962). *Traité de géostatistique appliquée* (No. 14). Editions Technip.

Mulder, G., Van Leijen, F. J., Barkmeijer, J., De Haan, S., & Hanssen, R. F. (2022). Estimating Single-Epoch Integrated Atmospheric Refractivity from InSAR for Assimilation in Numerical Weather Models. *IEEE Transactions on Geoscience and Remote Sensing*, *60*. doi: 10.1109/TGRS.2022.3177041

Oliver, M. A., & Webster, R. (2014). *A tutorial guide to geostatistics: Computing and modelling variograms and kriging* (Vol. 113). doi: 10.1016/j.catena.2013.09.006

Oliver, M. A., & Webster, R. (2015). The variogram and modelling. In *Basic steps in geostatistics: The variogram and kriging* (pp. 15–42). Cham: Springer International Publishing. Retrieved from https://doi.org/10.1007/978-3-319-15865-5_3 doi: 10.1007/978-3-319-15865-5_3

Osmanoğlu, B., Sunar, F., Wdowinski, S., & Cabral-Cano, E. (2016). *Time series analysis of InSAR data: Methods and trends* (Vol. 115). doi: 10.1016/j.isprsjprs.2015.10.003

Özer, I. E., van Leijen, F. J., Jonkman, S. N., & Hanssen, R. F. (2019). Applicability of satellite radar imaging to monitor the conditions of levees. *Journal of Flood Risk Management*, *12*. doi: 10.1111/jfr3.12509

Perissin, D., & Wang, T. (2011). Time-Series InSAR Applications Over Urban Areas in China. *IEEE Journal of Selected Topics in Applied Earth Observations and Remote Sensing*, *4*(1). doi: 10.1109/JSTARS.2010.2046883

Raspini, F., Bianchini, S., Ciampalini, A., Del Soldato, M., Solari, L., Novali, F., … Casagli, N. (2018). Continuous, semi-automatic monitoring of ground deformation using Sentinel-1 satellites. *Scientific Reports*, *8*(1). doi: 10.1038/s41598-018-25369-w

Saha, M., Ghosh, R., & Goswami, B. (2014). Robustness and sensitivity metrics for tuning the extended kalman filter. *IEEE Transactions on Instrumentation and Measurement*, *63*(4). doi: 10.1109/TIM.2013.2283151

Schiffer, S. (1991). Ceteris paribus laws. *Mind*, *100*(397). doi: 10.1093/mind/C.397.1

SkyGeo. (2023). *Bodemdalingskaart 2.0.* Retrieved from https://bodemdalingskaart.portal.skygeo.com/portal/bodemdalingskaart/u2/viewers/basic/

Teunissen, P. J. (2017). Batch and recursive model validation. *Springer handbook of global navigation satellite systems*, 687–720.

Van Leijen, F. (2014). *Persistent Scatterer Interferometry based on geodetic estimation theory* (Doctoral dissertation). doi: https://doi.org/10.4233/uuid:5dba48d7-ee26-4449-b674-caa8df93e71e

Venmans, A. A., Op De Kelder, M., De Jong, J., Korff, M., & Houtepen, M. (2020). Reliability of InSAR satellite monitoring of buildings near inner city quay walls. In *Proceedings of the international association of hydrological sciences* (Vol. 382). doi: 10.5194/piahs-382-195-2020

Verburg, Q. (2017). *QUInSAR: Temporal Parameter and Ambiguity Estimation Using Recursive Least-Squares.* Retrieved from http://resolver.tudelft.nl/uuid:5f071176-8737-4123-9b4e-292ae74fc028

Wang, Y., & Zhu, X. X. (2016). Robust Estimators for Multipass SAR Interferometry. *IEEE Transactions on Geoscience and Remote Sensing*, *54*(2). doi: 10.1109/TGRS.2015.2471303

Yu, H., & Lan, Y. (2016). Robust Two-Dimensional Phase Unwrapping for Multibaseline SAR Interferograms: A Two-Stage Programming Approach. *IEEE Transactions on Geoscience and Remote Sensing*, *54*(9). doi: 10.1109/TGRS.2016.2558541

A

Case study figures Amsterdam

A.1. 0-state

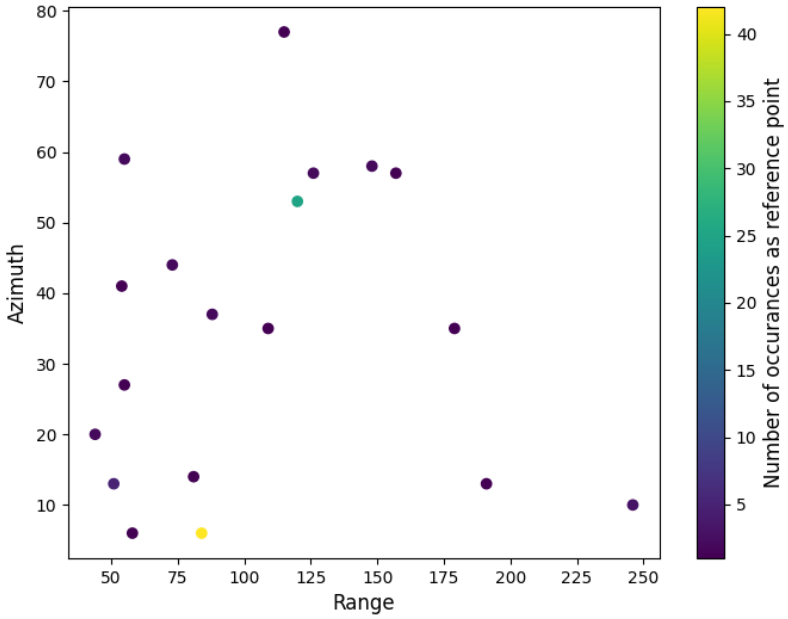

Figure A.1: Locations and number of occurrences of the reference point when the choice of reference is unrestricted.

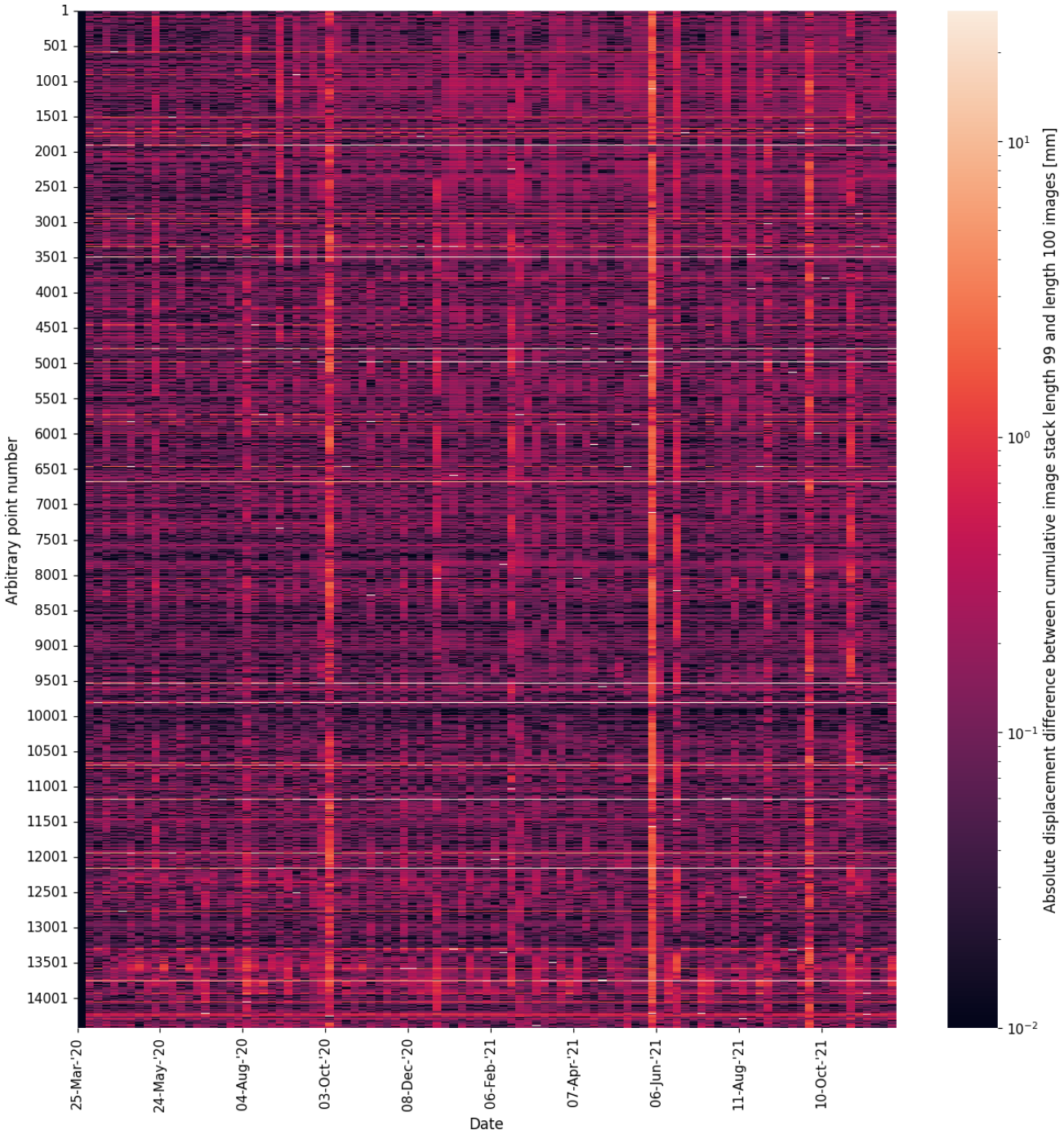

Figure A.2: Absolute Differential Space-Time Matrix containing displacement estimate differences of two Space-Time Matrices obtained from processing the conjunct pixels and epochs in two realizations. The horizontal axis contains the epoch number, starting from the 25th of March 2020 and the vertical axis represents an arbitrary point number (location).

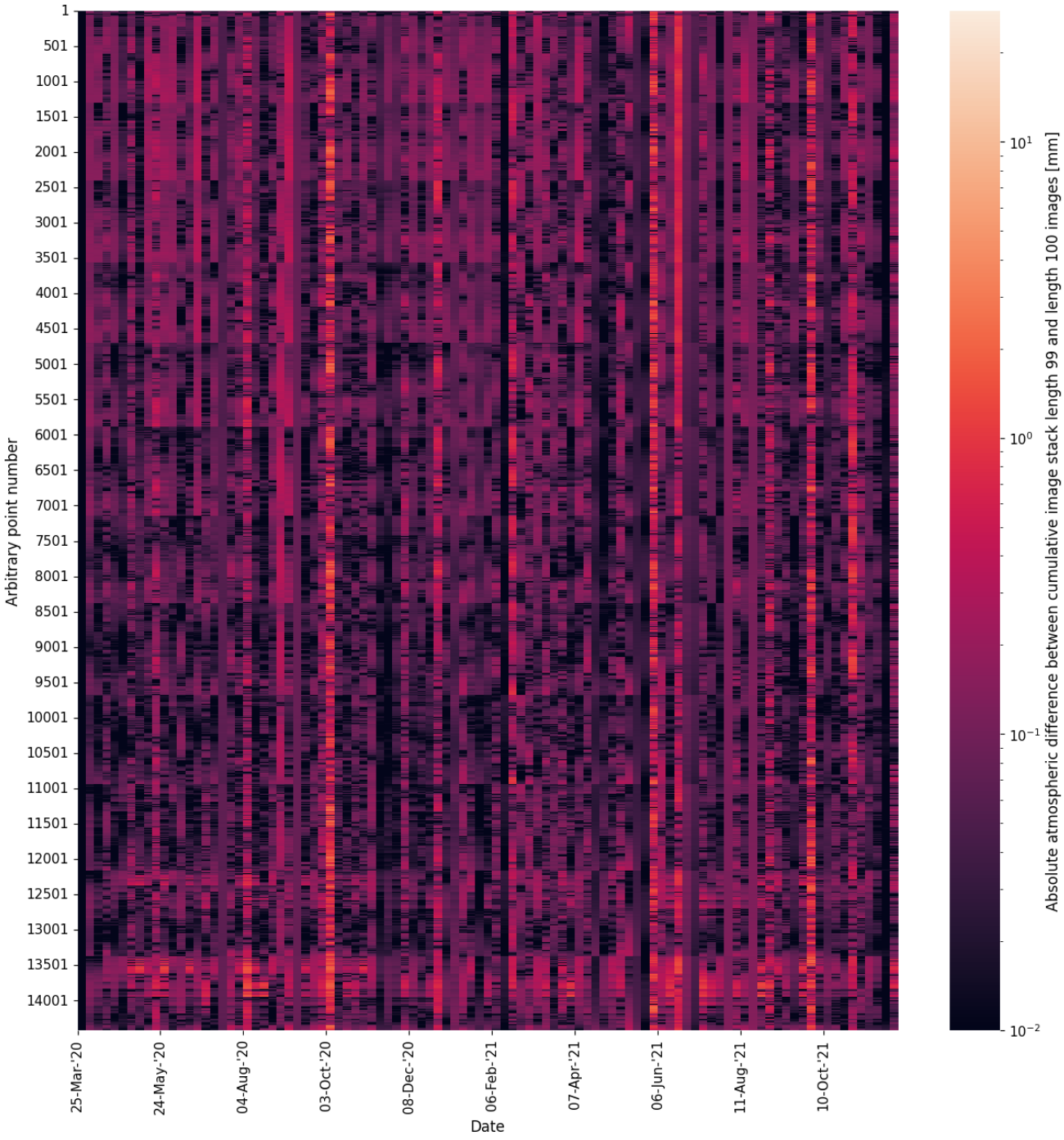

Figure A.3: Absolute Differential Atmospheric Space-Time Matrix containing atmospheric delay estimate differences of two Space-Time Matrices obtained from processing the conjunct pixels and epochs in two realizations. The horizontal axis contains the epoch number, starting from the 25th of March 2020 and the vertical axis represents an arbitrary point number (location).

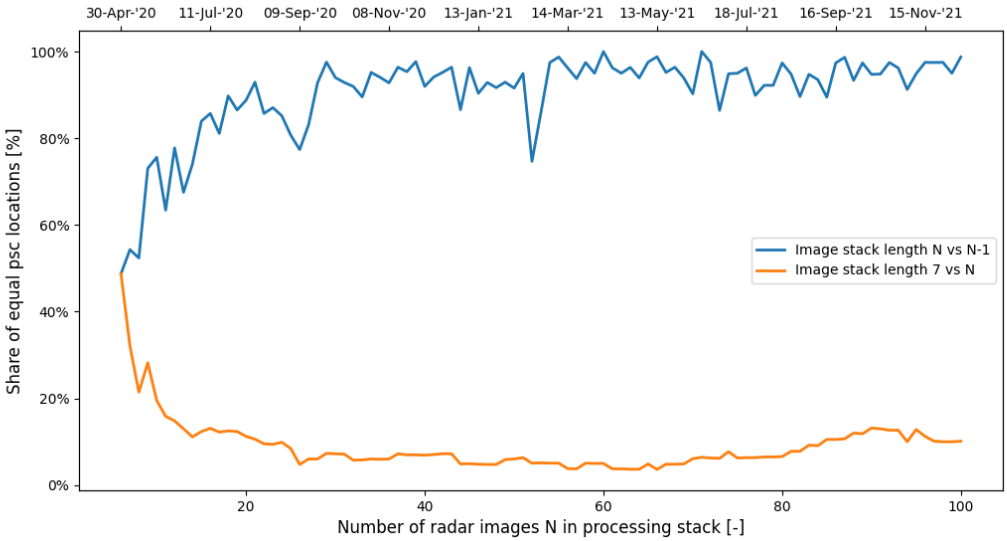

Figure A.4: Figure containing the share of identical PS1 locations over the number of realizations comparing N to $N-1$ (blue line) and N to the starting set (yellow line).

A.2. NMAD

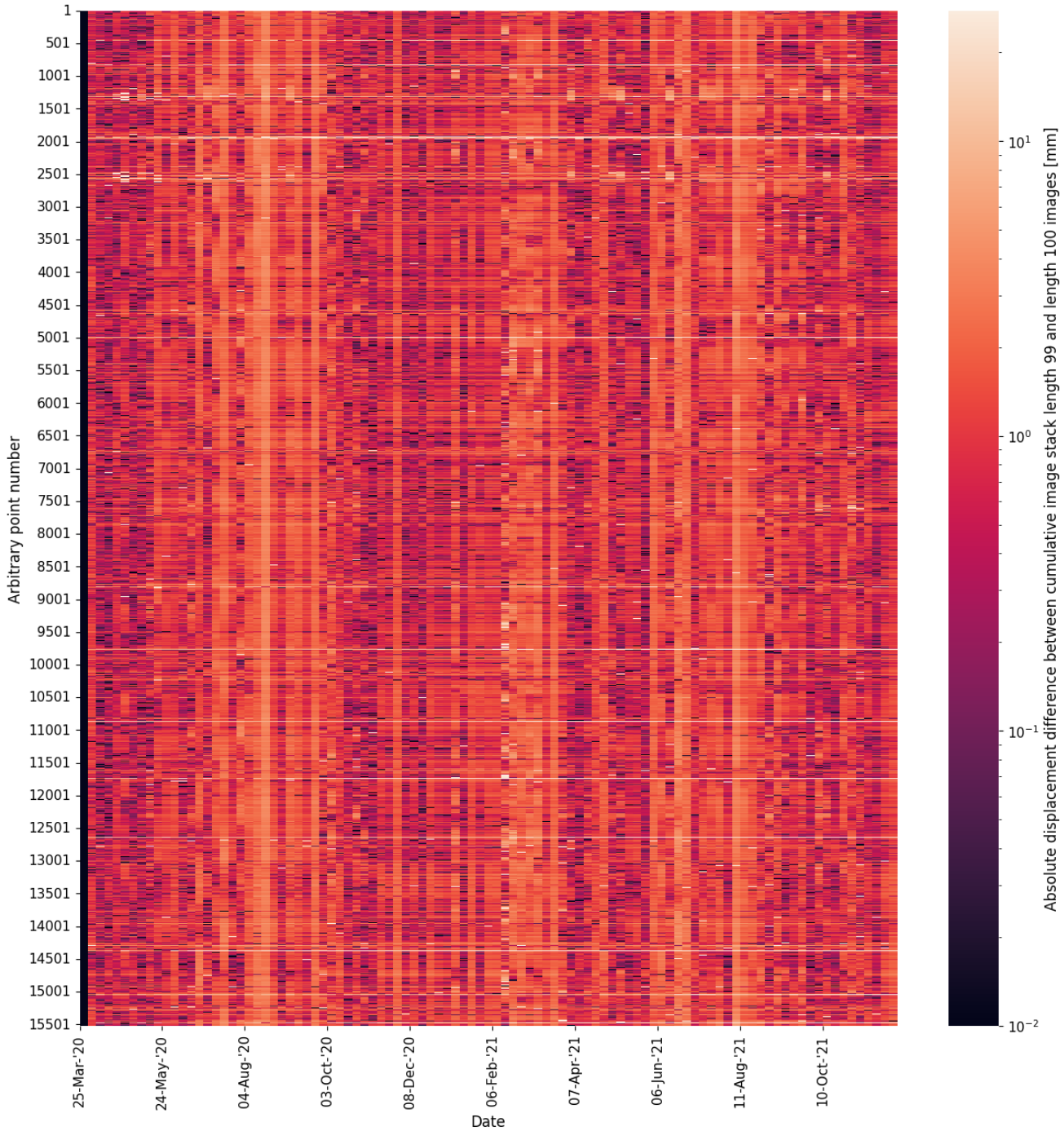

Figure A.5: Absolute Differential Space-Time Matrix containing displacement estimate differences of two Space-Time Matrices obtained from processing the conjunct pixels and epochs in two realizations. The horizontal axis contains the epoch number, starting from the 25th of March 2020 and the vertical axis represents an arbitrary point number (location).

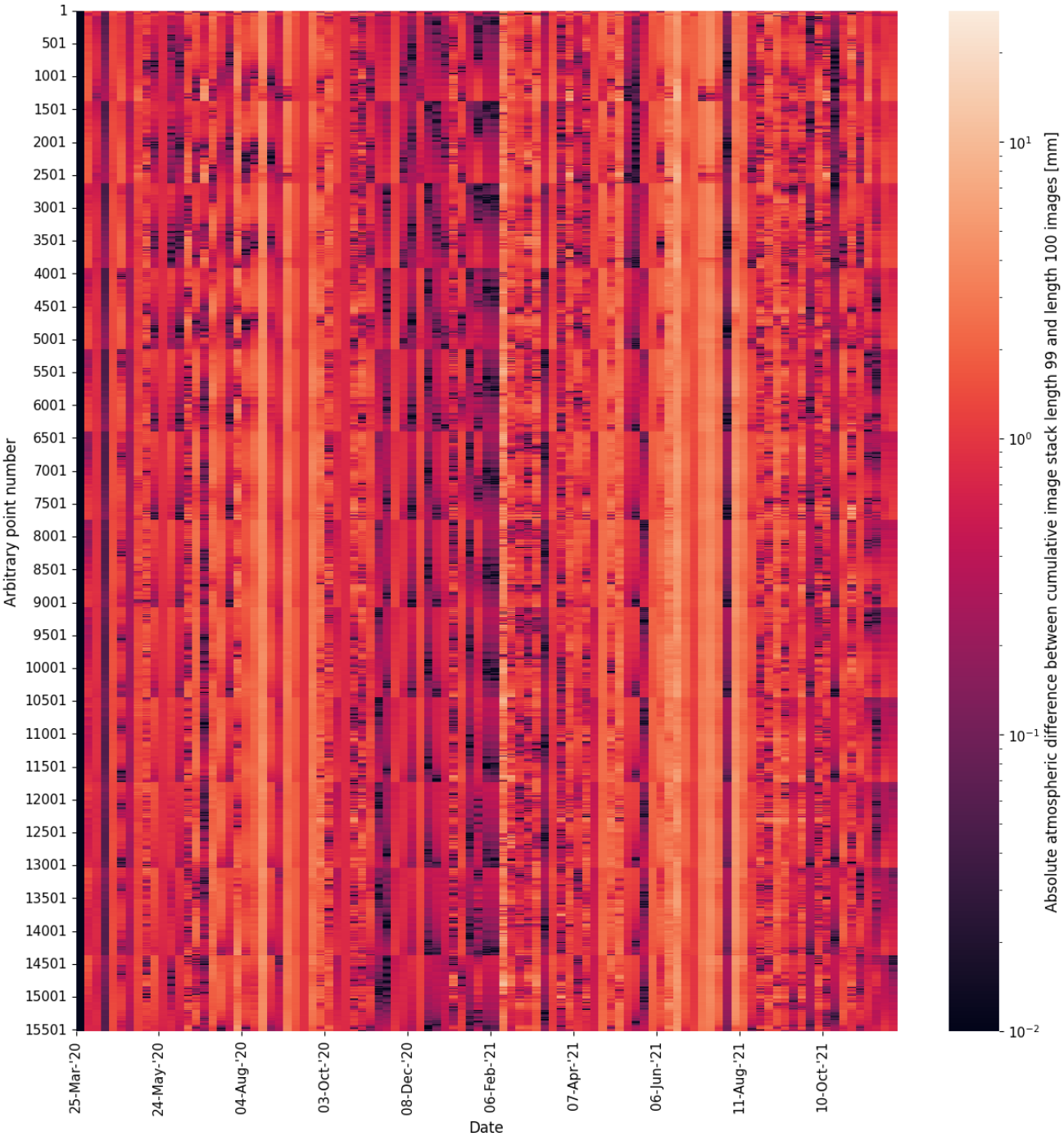

Figure A.6: Absolute Differential Atmospheric Space-Time Matrix containing atmospheric delay estimate differences of two Space-Time Matrices obtained from processing the conjunct pixels and epochs in two realizations. The horizontal axis contains the epoch number, starting from the 25th of March 2020 and the vertical axis represents an arbitrary point number (location).

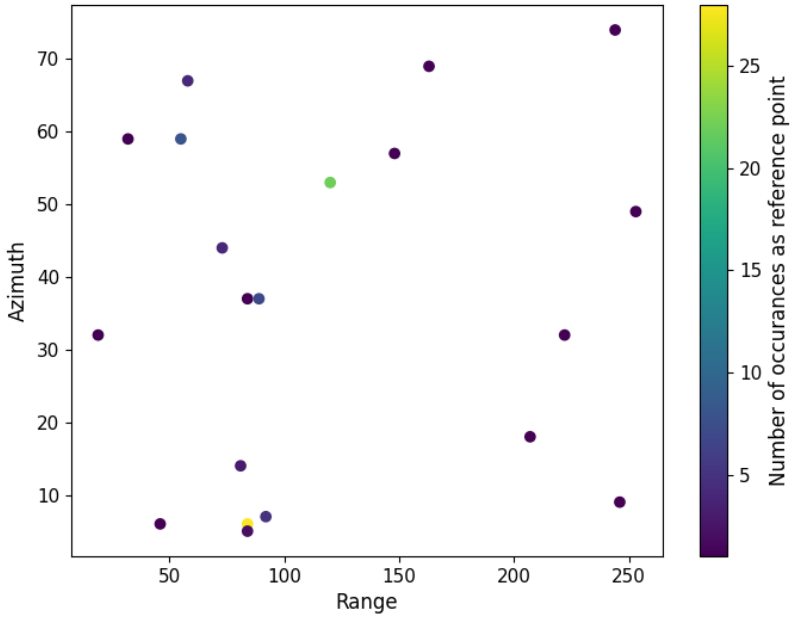

Figure A.7: Locations and number of occurrences of the reference point when the choice of reference is unrestricted.

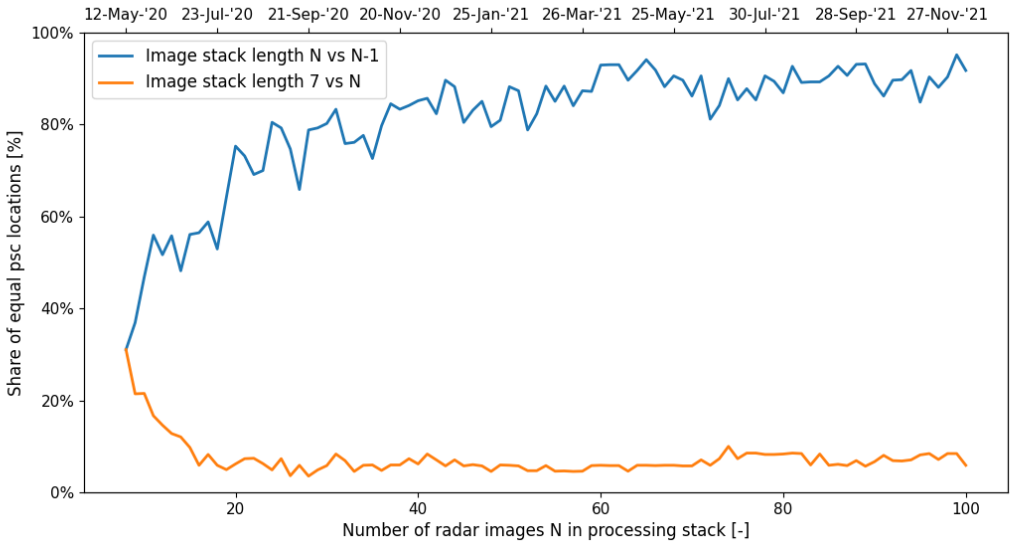

Figure A.8: Figure containing the share of identical PS1 locations over the number of realizations comparing N to $N-1$ (blue line) and N to the starting set (yellow line).

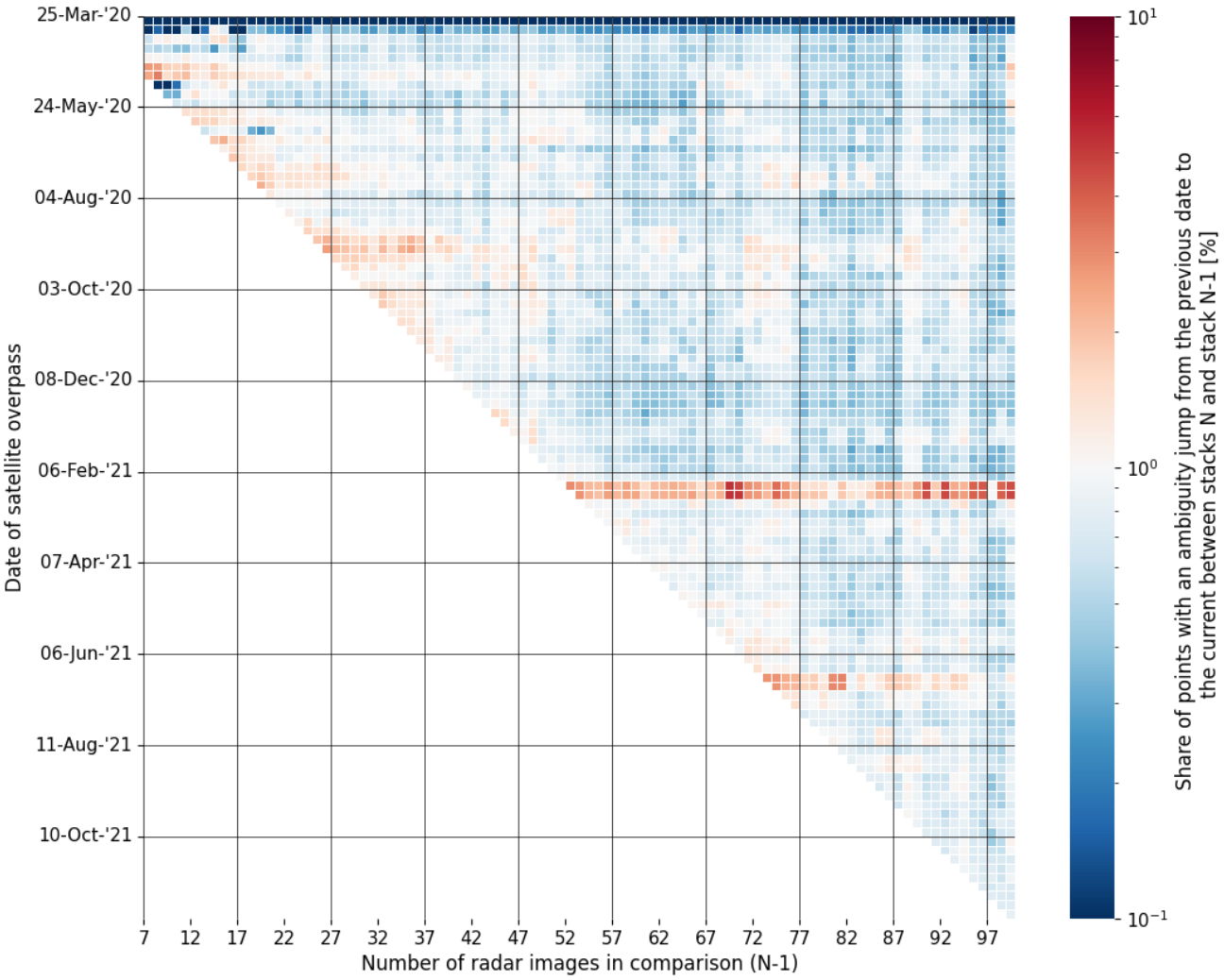

Figure A.9: Ambiguity Overview for the occurrence of cycle slips in the displacement estimates per epoch, comparing acquisition realization N with realization $N-1$. Moving horizontally, the same epoch is compared but with a different DePSI input. A vertical column contains the cycle slips of one realization comparison. Dark red indicates many cycle slips on that epoch and dark blue indicates almost no cycle slips.

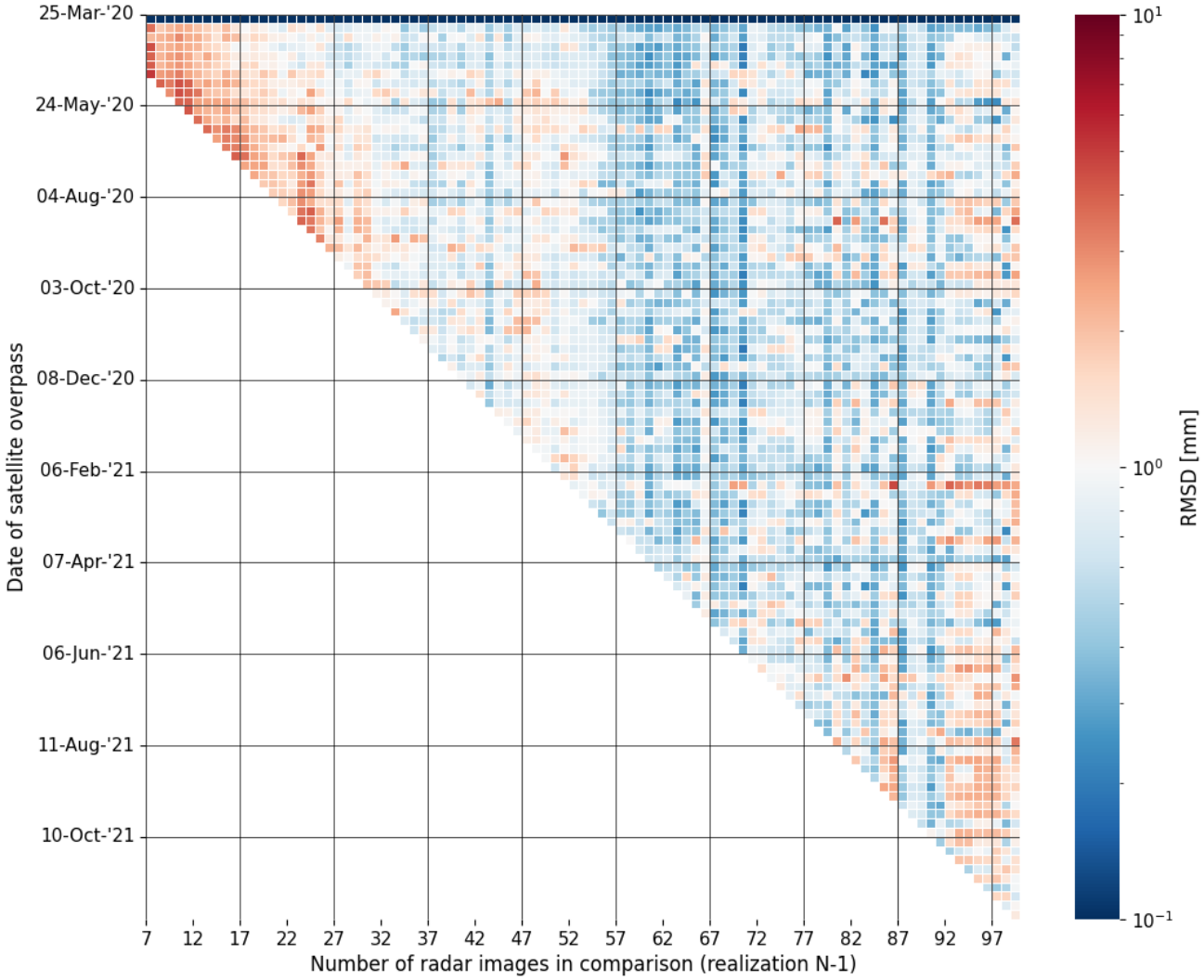

Figure A.10: RMSD Overview for the detailed version of the displacement estimates per epoch, comparing acquisition realization N with realization $N-1$. Moving horizontally, the same epoch is compared but with a different DePSI input. A vertical column contains the RMSD of one realization comparison. Dark red indicates large displacement estimate differences on that epoch and dark blue indicates almost no difference.

A.3. Fixed reference point

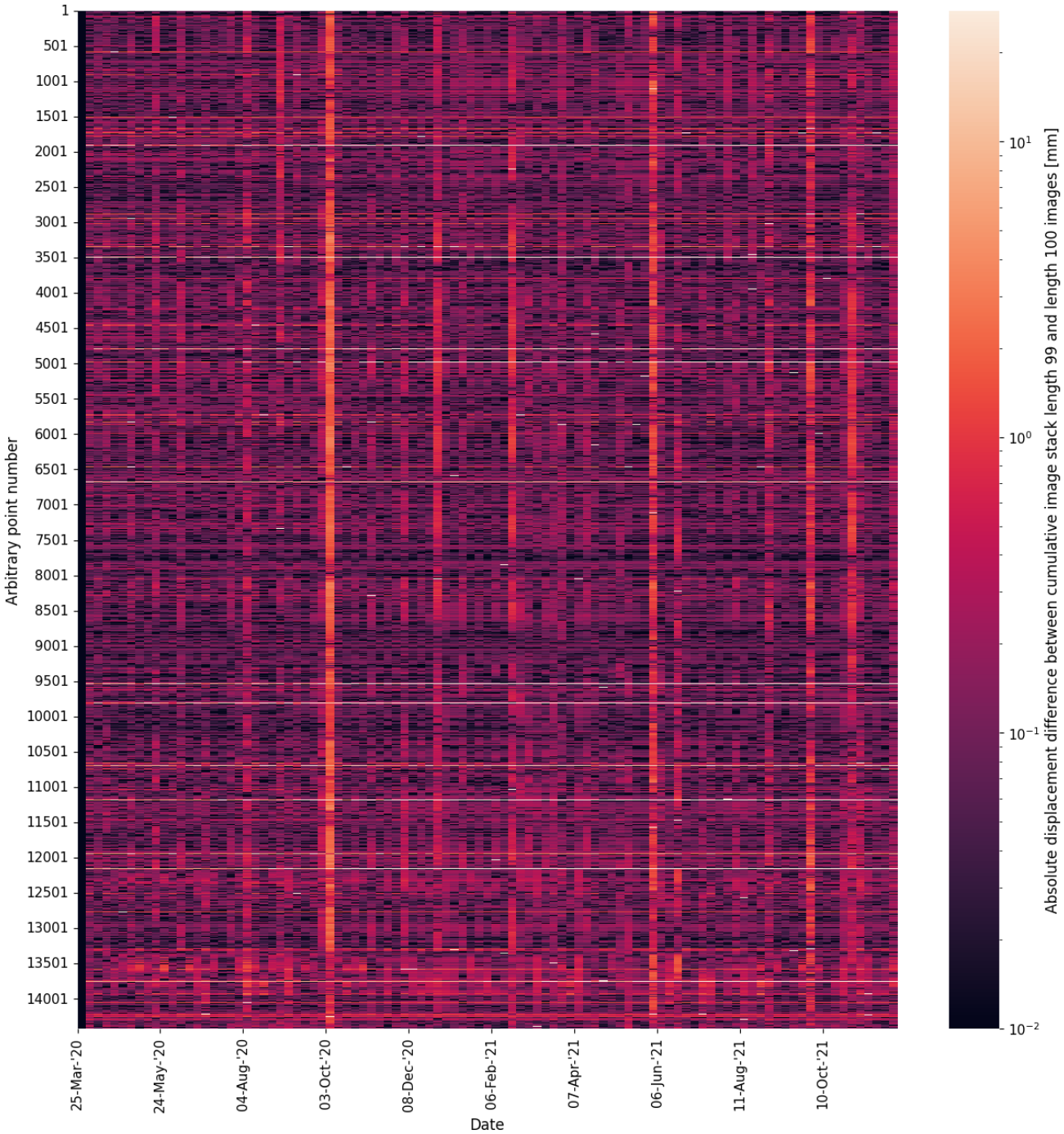

Figure A.11: Absolute Differential Space-Time Matrix containing displacement estimate differences of two Space-Time Matrices obtained from processing the conjunct pixels and epochs in two realizations. The horizontal axis contains the epoch number, starting from the 25th of March 2020 and the vertical axis represents an arbitrary point number (location).

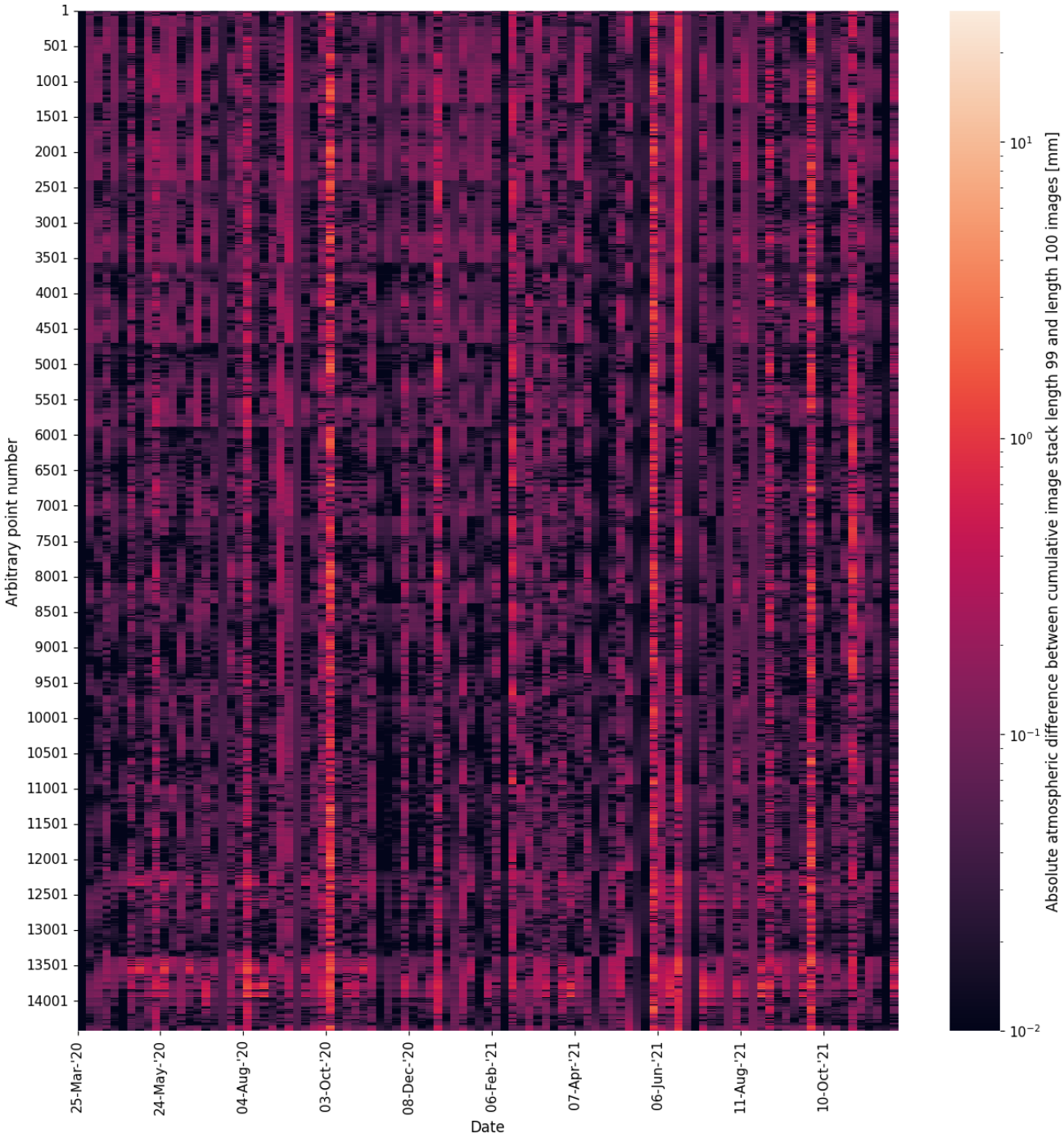

Figure A.12: Absolute Differential Atmospheric Space-Time Matrix containing atmospheric delay estimate differences of two Space-Time Matrices obtained from processing the conjunct pixels and epochs in two realizations. The horizontal axis contains the epoch number, starting from the 25th of March 2020 and the vertical axis represents an arbitrary point number (location).

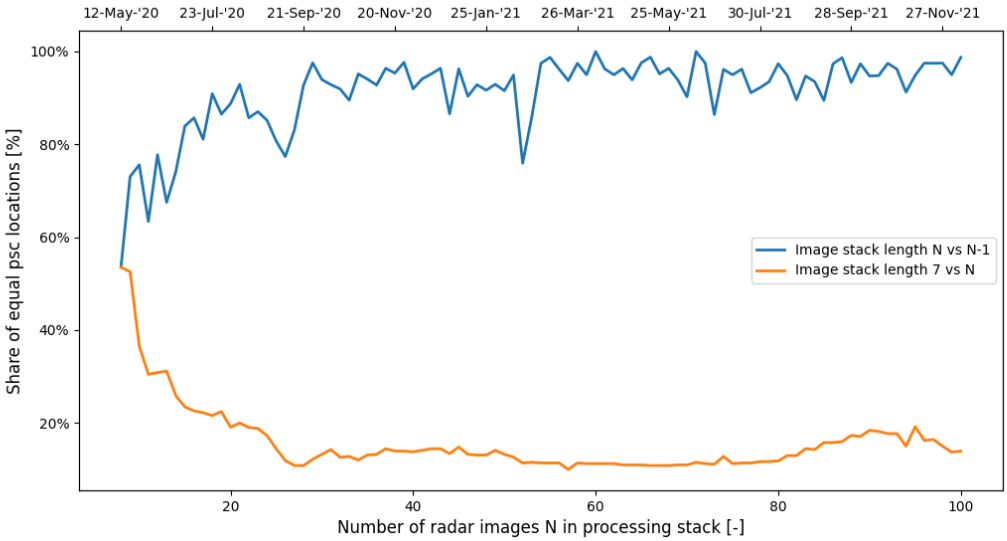

Figure A.13: Figure containing the share of identical PS1 locations over the number of realizations comparing N to $N-1$ (blue line) and N to the starting set (yellow line).

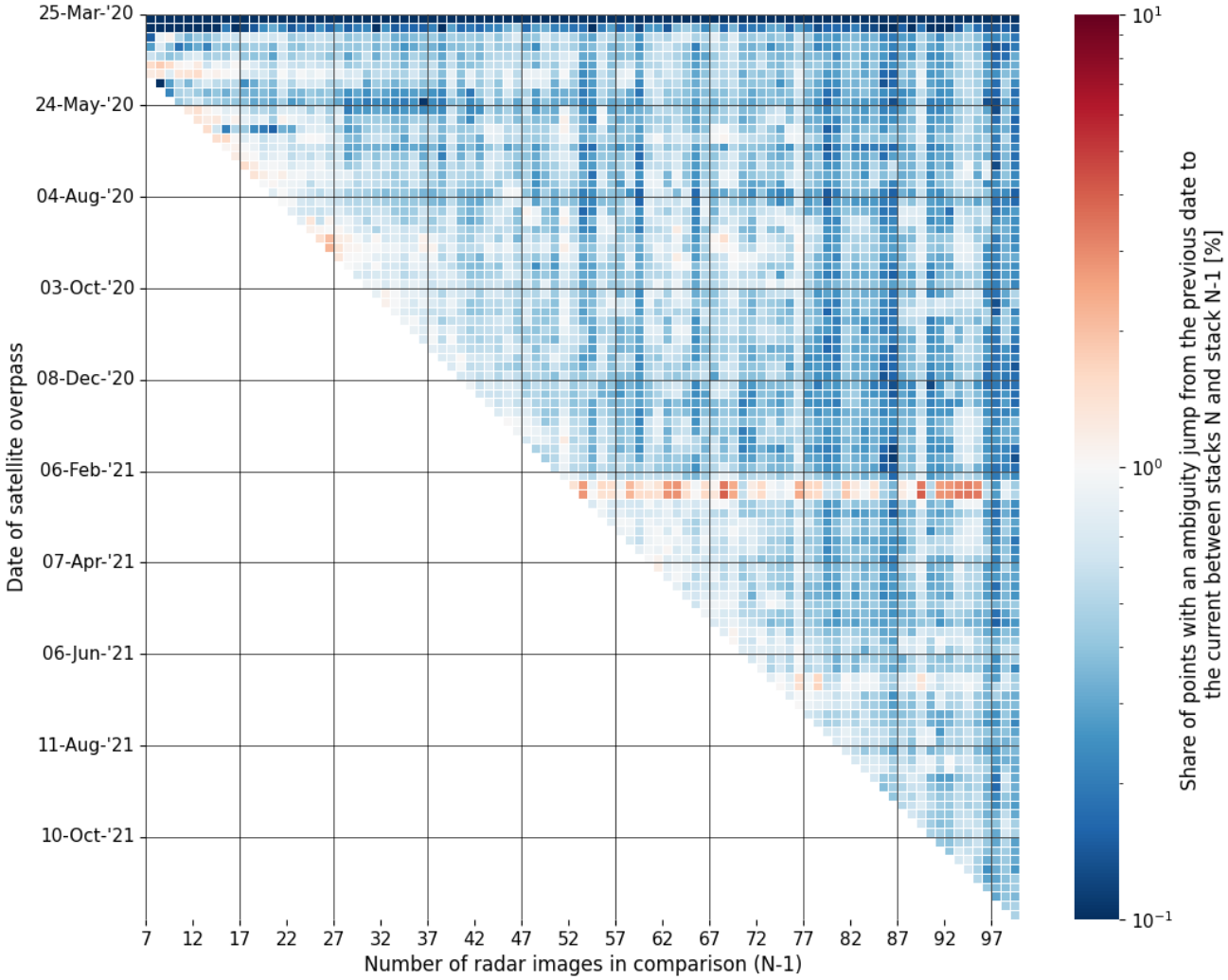

Figure A.14: Ambiguity Overview for the occurrence of cycle slips in the displacement estimates per epoch, comparing acquisition realization N with realization $N-1$. Moving horizontally, the same epoch is compared but with a different DePSI input. A vertical column contains the cycle slips of one realization comparison. Dark red indicates many cycle slips on that epoch and dark blue indicates almost no cycle slips.

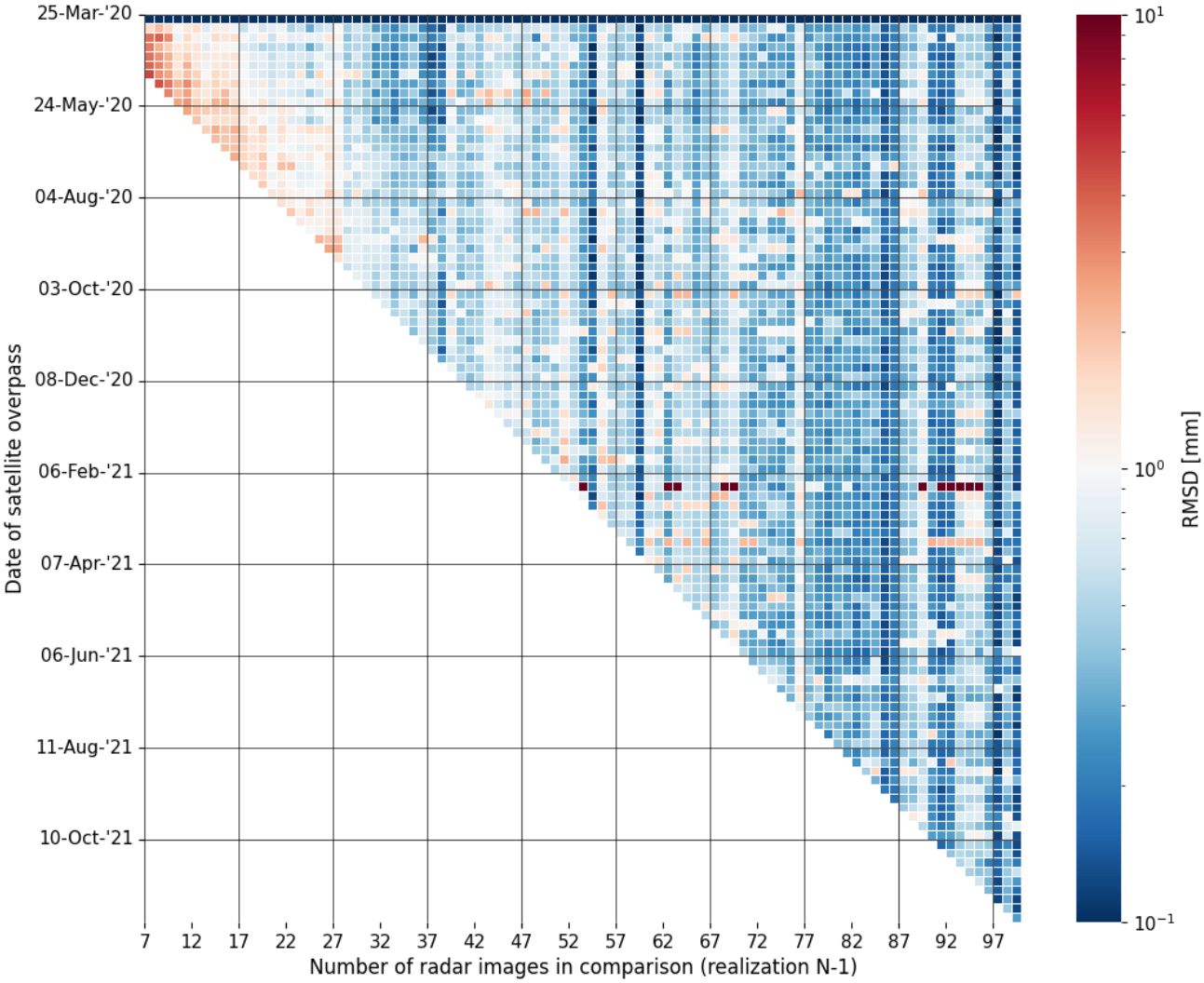

Figure A.15: RMSD Overview for the detailed version of the displacement estimates per epoch, comparing acquisition realization N with realization $N-1$. Moving horizontally, the same epoch is compared but with a different DePSI input. A vertical column contains the RMSD of one realization comparison. Dark red indicates large displacement estimate differences on that epoch and dark blue indicates almost no difference.

A.4. Exclusion frail image(s)

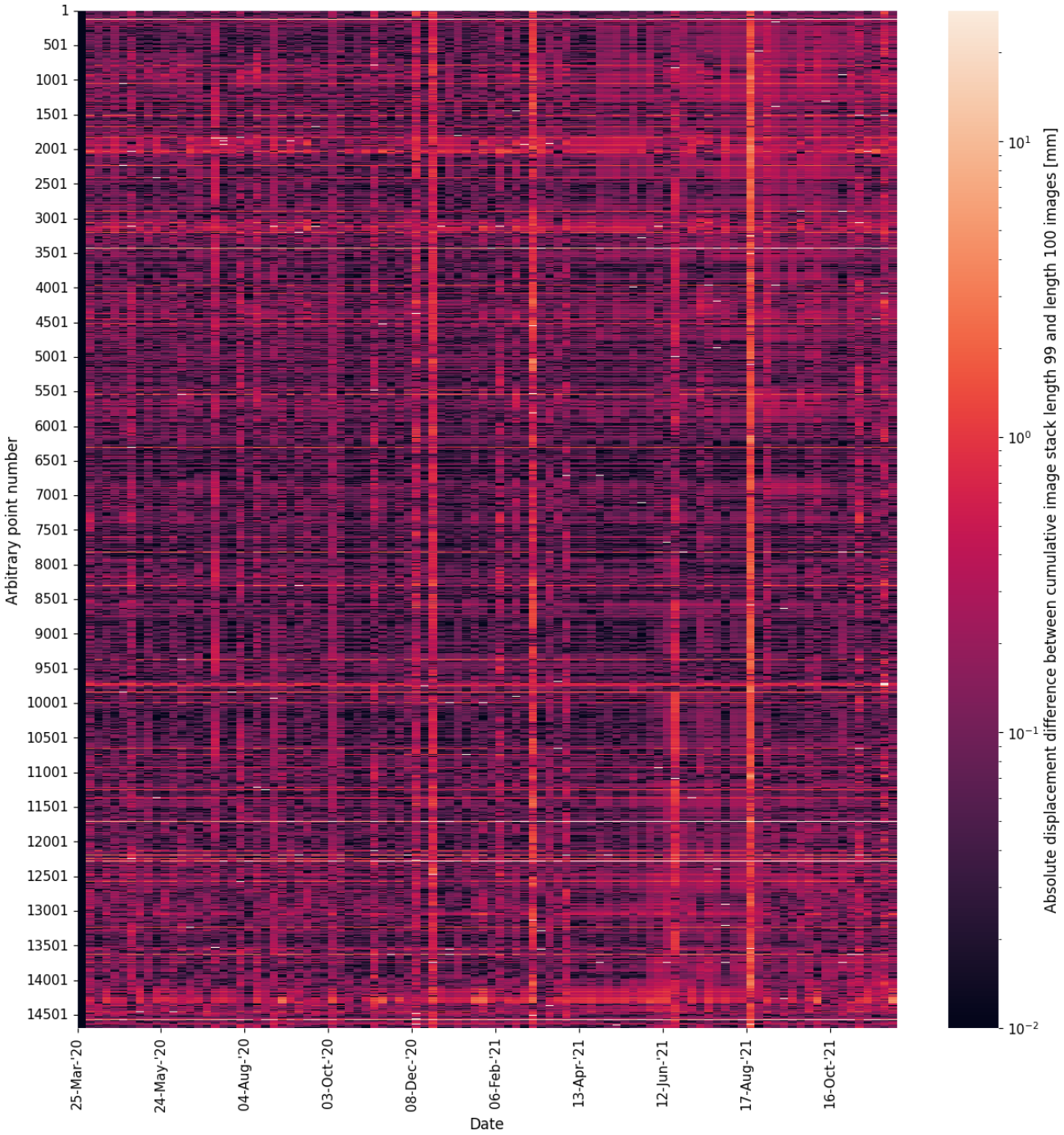

Figure A.16: Absolute Differential Space-Time Matrix containing displacement estimate differences of two Space-Time Matrices obtained from processing the conjunct pixels and epochs in two realizations. The horizontal axis contains the epoch number, starting from the 25th of March 2020 and the vertical axis represents an arbitrary point number (location).

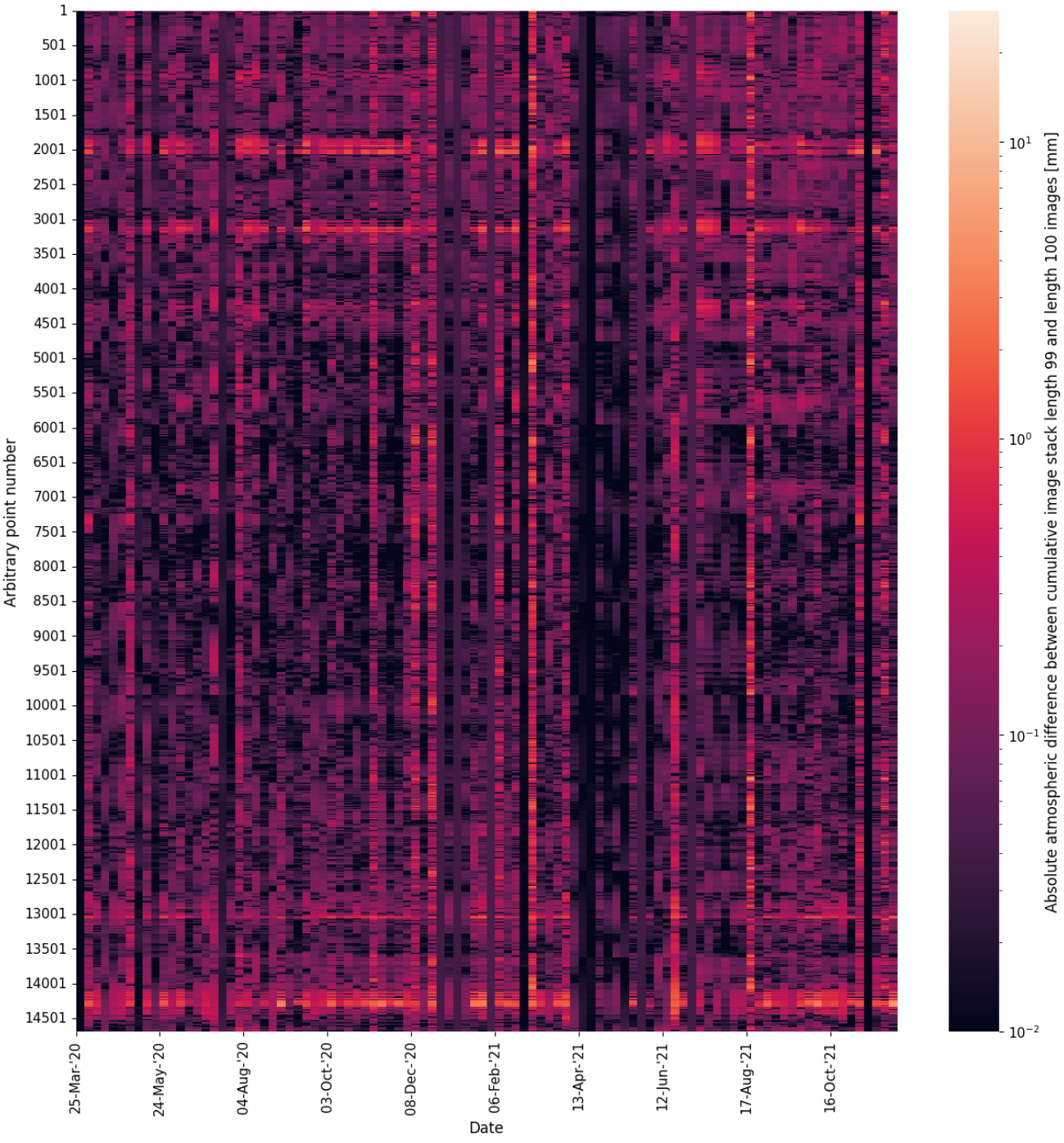

Figure A.17: Absolute Differential Atmospheric Space-Time Matrix containing atmospheric delay estimate differences of two Space-Time Matrices obtained from processing the conjunct pixels and epochs in two realizations. The horizontal axis contains the epoch number, starting from the 25th of March 2020 and the vertical axis represents an arbitrary point number (location).

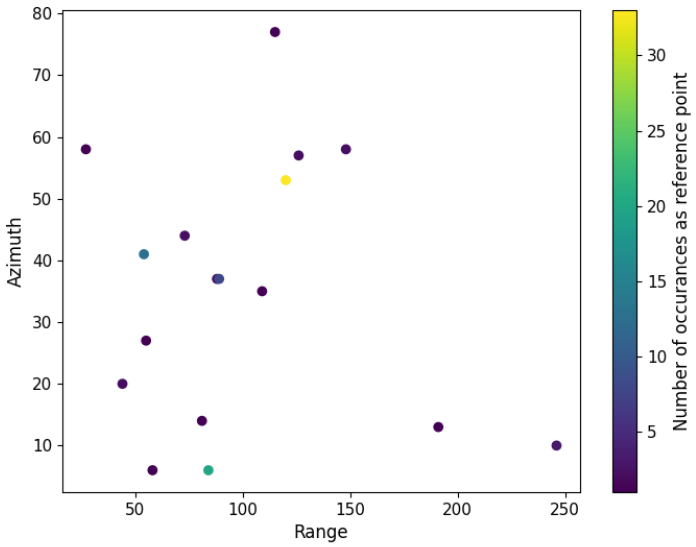

Figure A.18: Locations and number of occurrences of the reference point when the choice of reference is unrestricted.

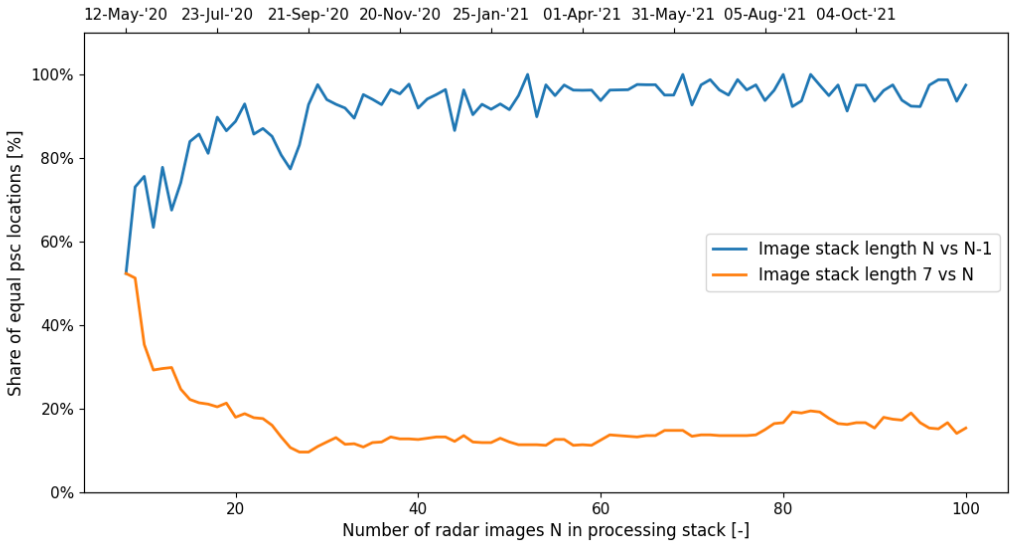

Figure A.19: Figure containing the share of identical PS1 locations over the number of realizations comparing N to $N-1$ (blue line) and N to the starting set (yellow line).

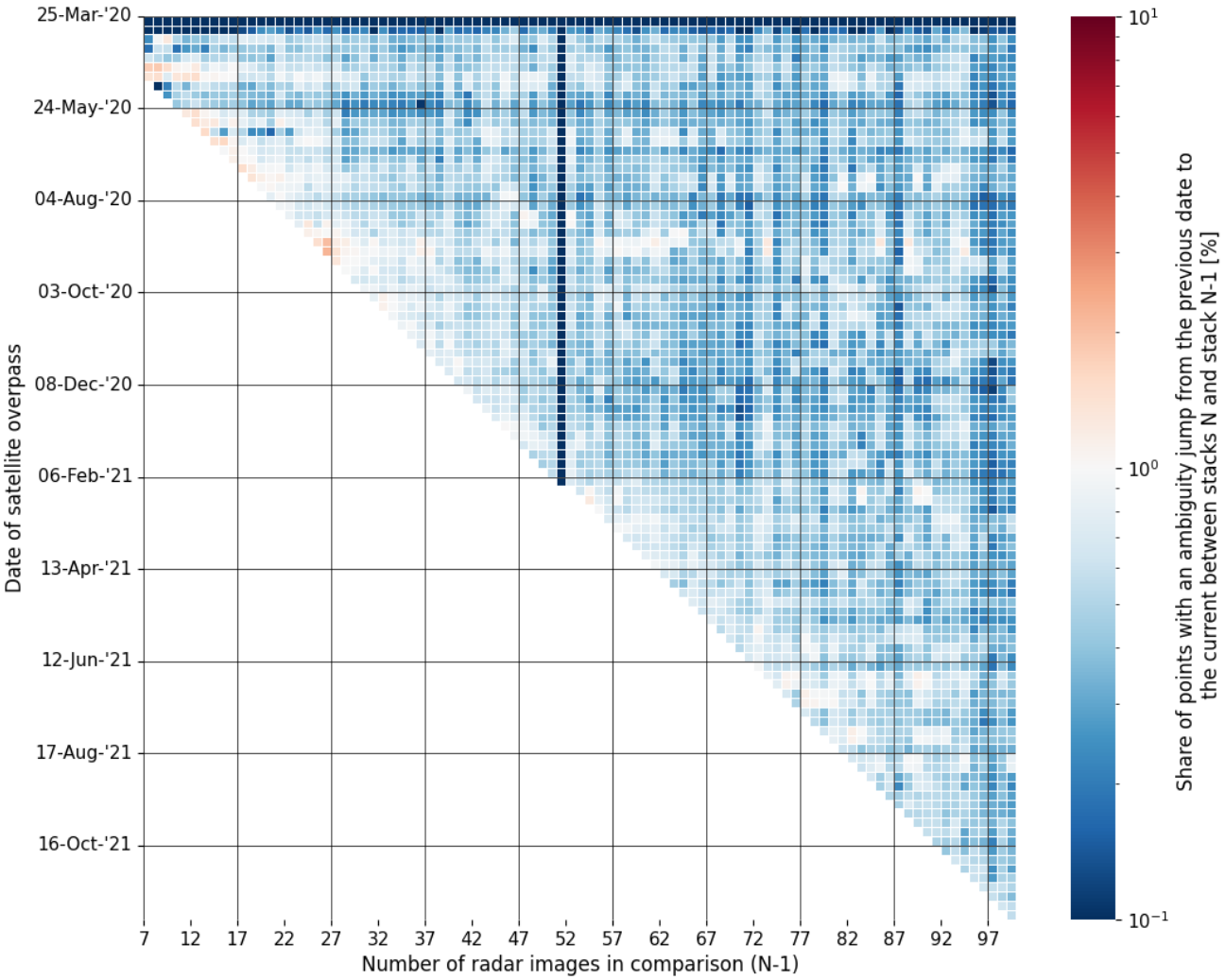

Figure A.20: Ambiguity Overview for the occurrence of cycle slips in the displacement estimates per epoch, comparing acquisition realization N with realization $N-1$. Moving horizontally, the same epoch is compared but with a different DePSI input. A vertical column contains the cycle slips of one realization comparison. Dark red indicates many cycle slips on that epoch and dark blue indicates almost no cycle slips.

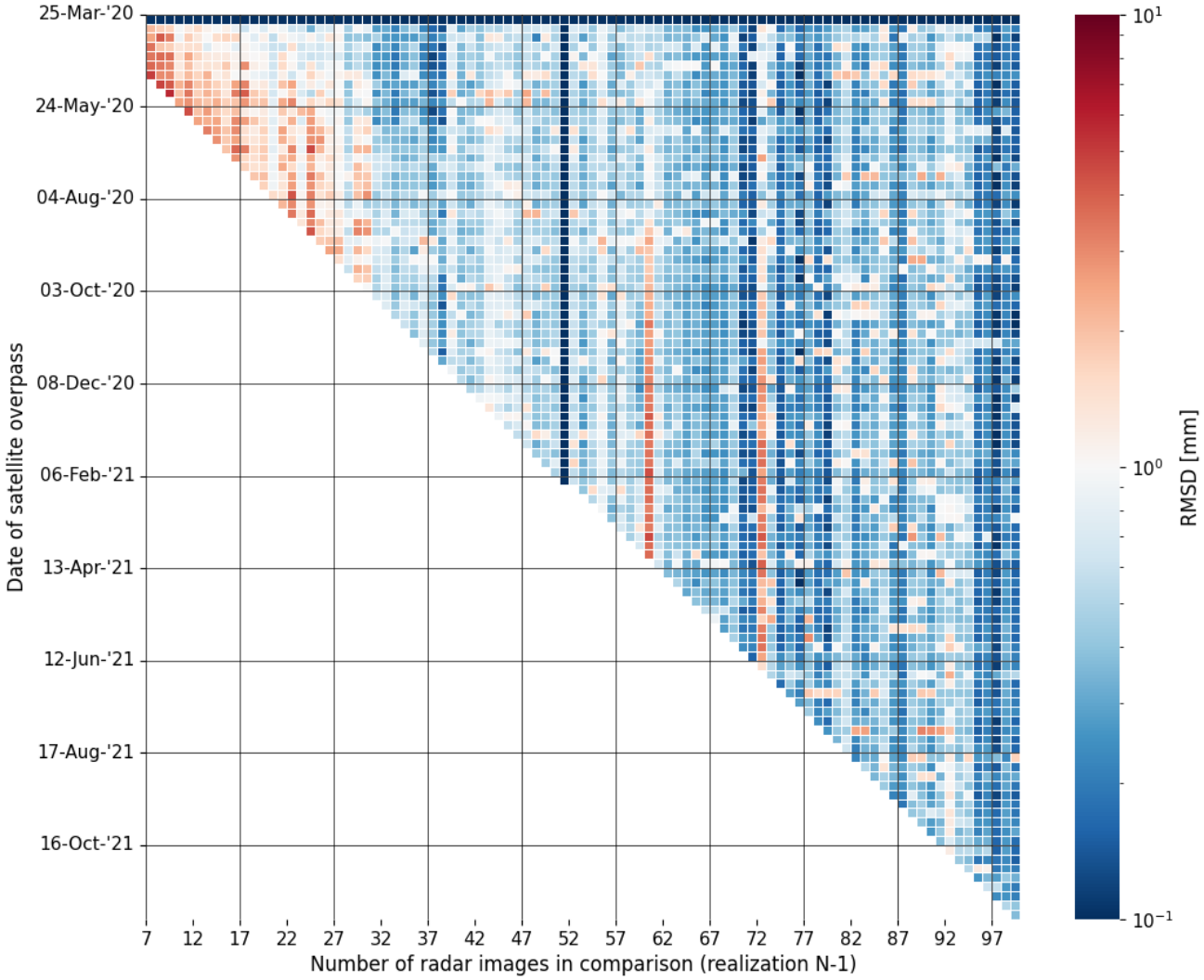

Figure A.21: RMSD Overview for the detailed version of the displacement estimates per epoch, comparing acquisition realization N with realization $N-1$. Moving horizontally, the same epoch is compared but with a different DePSI input. A vertical column contains the RMSD of one realization comparison. Dark red indicates large displacement estimate differences on that epoch and dark blue indicates almost no difference.

A.5. Atmospheric robustness

A.5.1. Prescribe set of first-order network PS

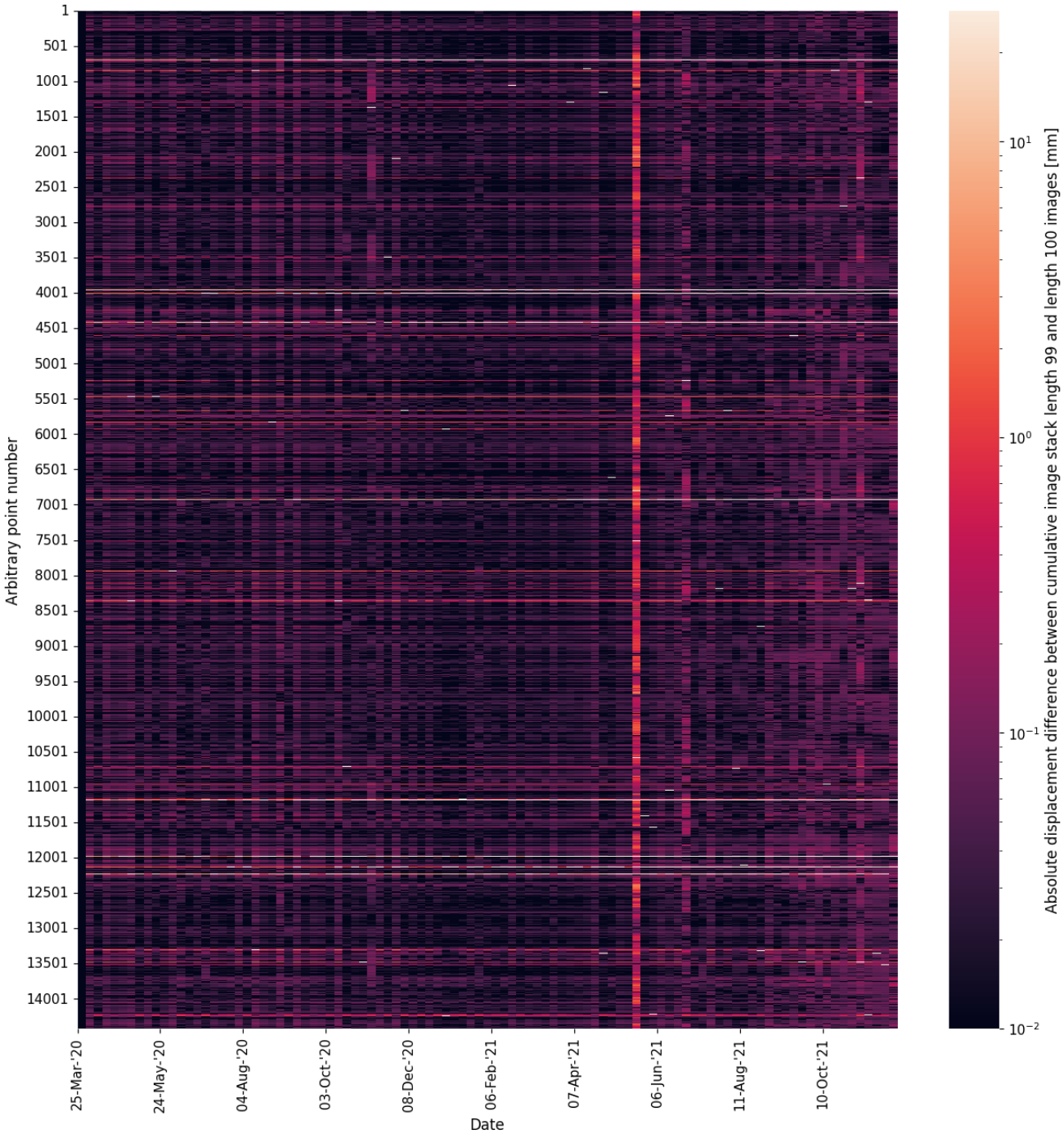

Figure A.22: Absolute Differential Space-Time Matrix containing displacement estimate differences of two Space-Time Matrices obtained from processing the conjunct pixels and epochs in two realizations. The horizontal axis contains the epoch number, starting from the 25th of March 2020 and the vertical axis represents an arbitrary point number (location).

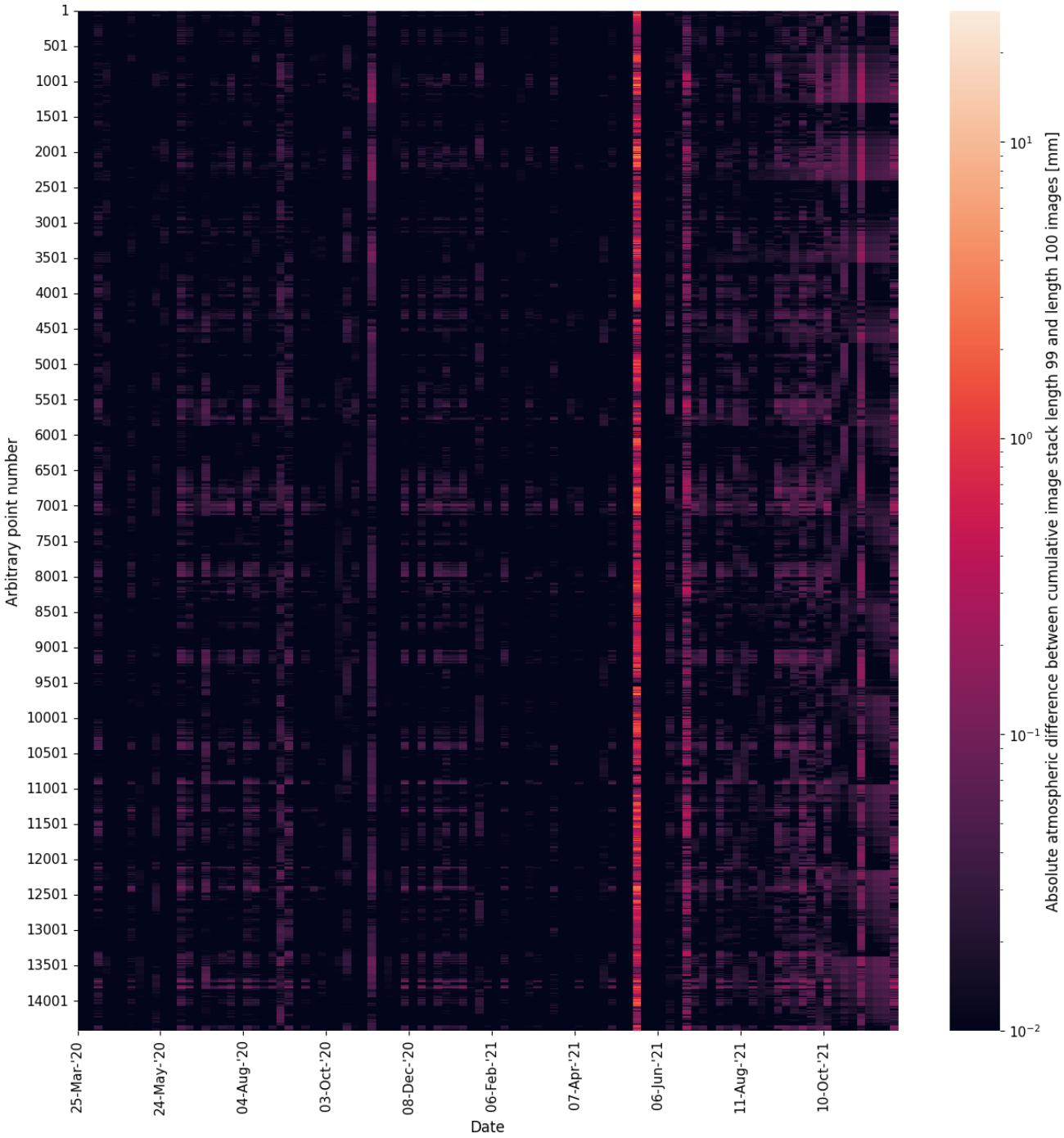

Figure A.23: Absolute Differential Atmospheric Space-Time Matrix containing atmospheric delay estimate differences of two Space-Time Matrices obtained from processing the conjunct pixels and epochs in two realizations. The horizontal axis contains the epoch number, starting from the 25th of March 2020 and the vertical axis represents an arbitrary point number (location).

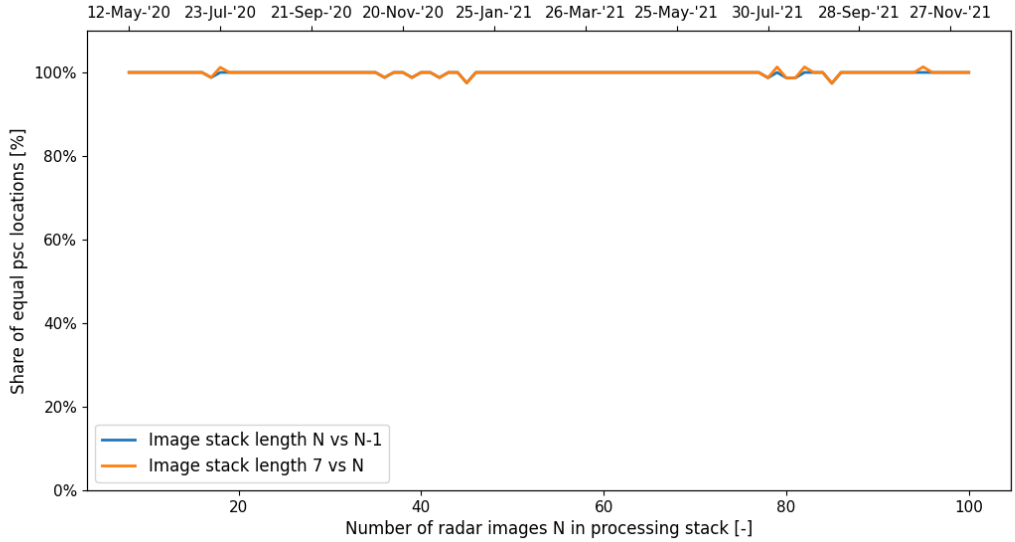

Figure A.24: Figure containing the share of identical PS1 locations over the number of realizations comparing N to $N-1$ (blue line) and N to the starting set (yellow line).

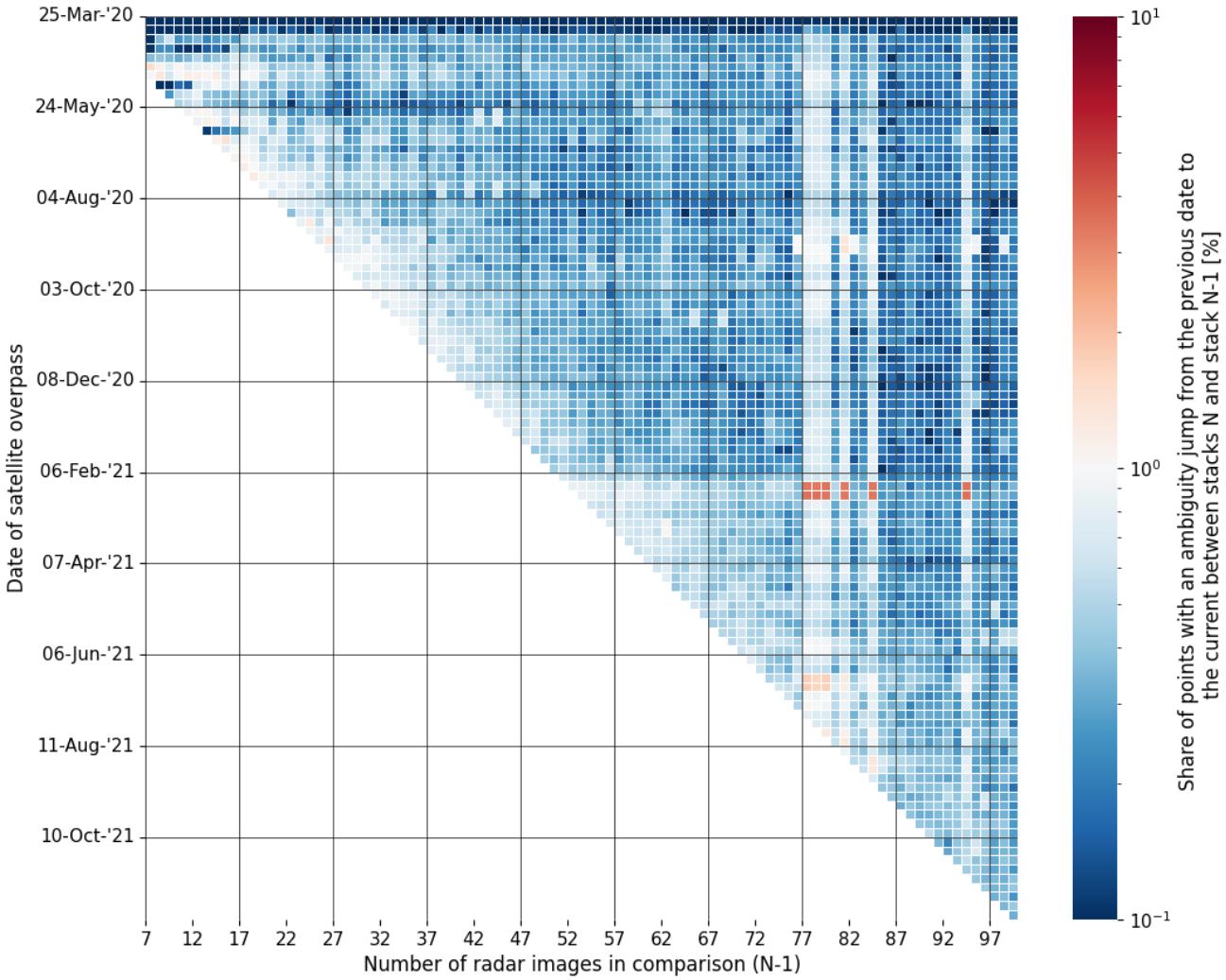

Figure A.25: Ambiguity Overview for the occurrence of cycle slips in the displacement estimates per epoch, comparing acquisition realization N with realization $N-1$. Moving horizontally, the same epoch is compared but with a different DePSI input. A vertical column contains the cycle slips of one realization comparison. Dark red indicates many cycle slips on that epoch and dark blue indicates almost no cycle slips.

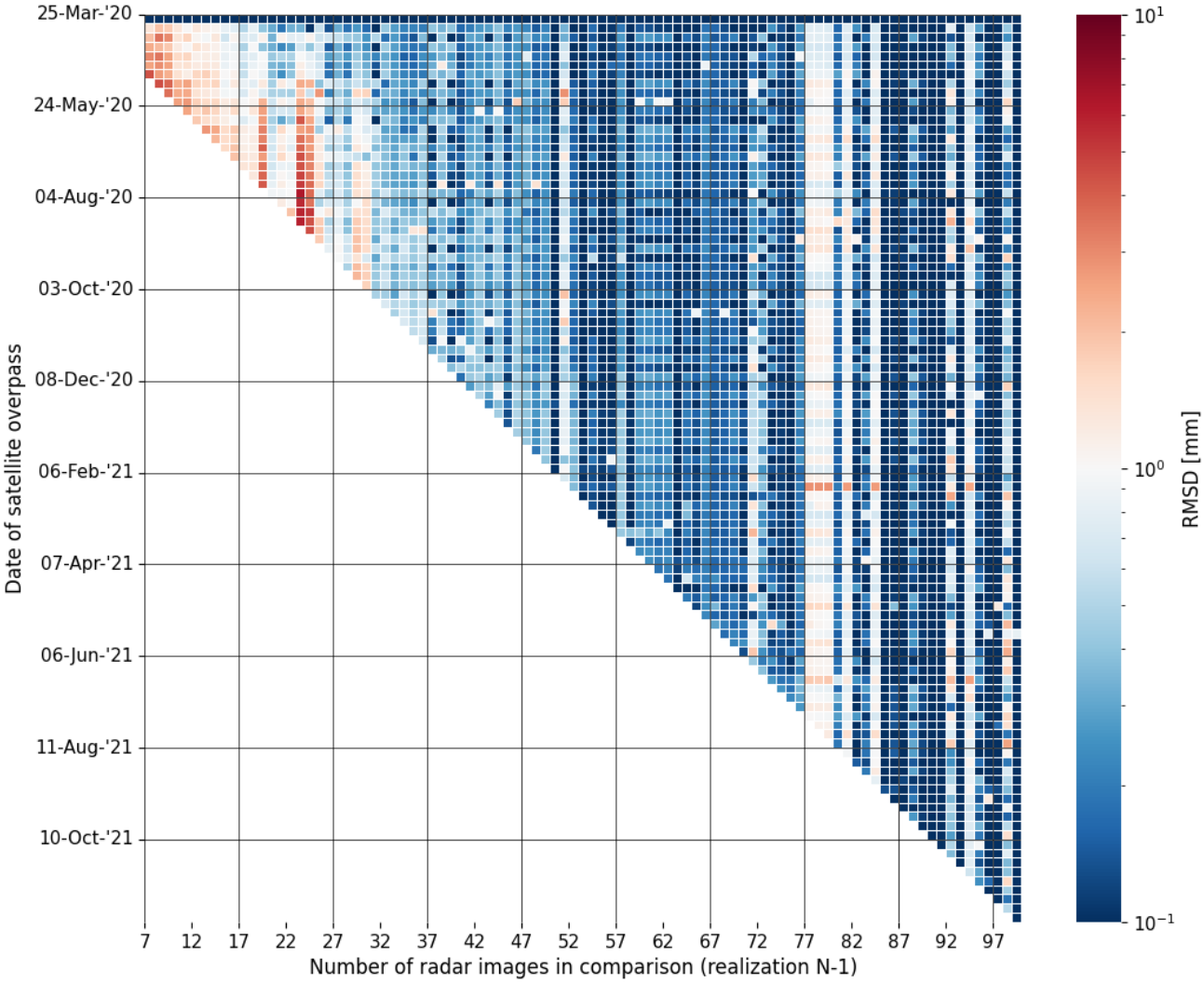

Figure A.26: RMSD Overview for the detailed version of the displacement estimates per epoch, comparing acquisition realization N with realization $N-1$. Moving horizontally, the same epoch is compared but with a different DePSI input. A vertical column contains the RMSD of one realization comparison. Dark red indicates large displacement estimate differences on that epoch and dark blue indicates almost no difference.

A.5.2. Kriging parameter restriction

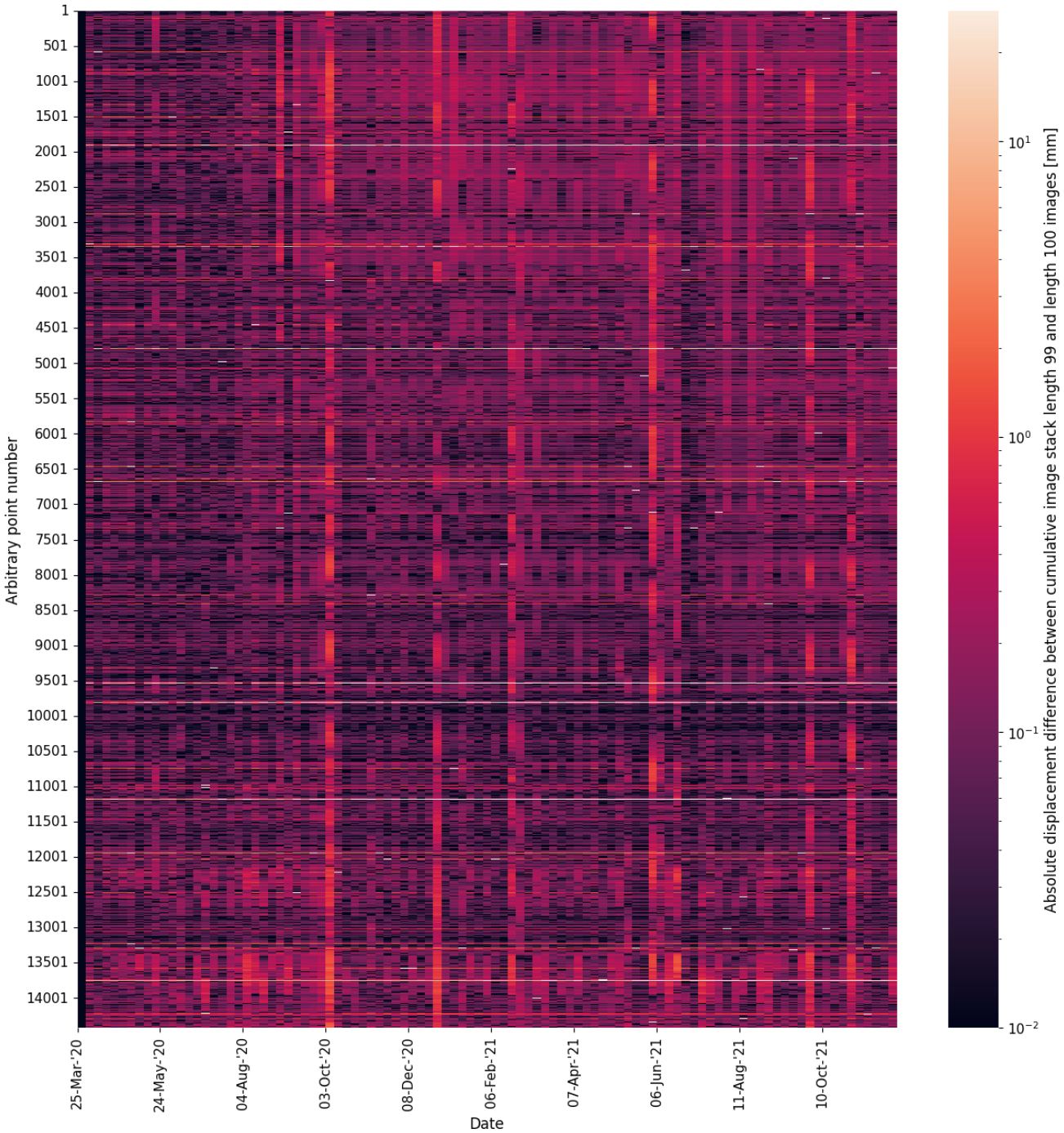

Figure A.27: Absolute Differential Space-Time Matrix containing displacement estimate differences of two Space-Time Matrices obtained from processing the conjunct pixels and epochs in two realizations. The horizontal axis contains the epoch number, starting from the 25th of March 2020 and the vertical axis represents an arbitrary point number (location).

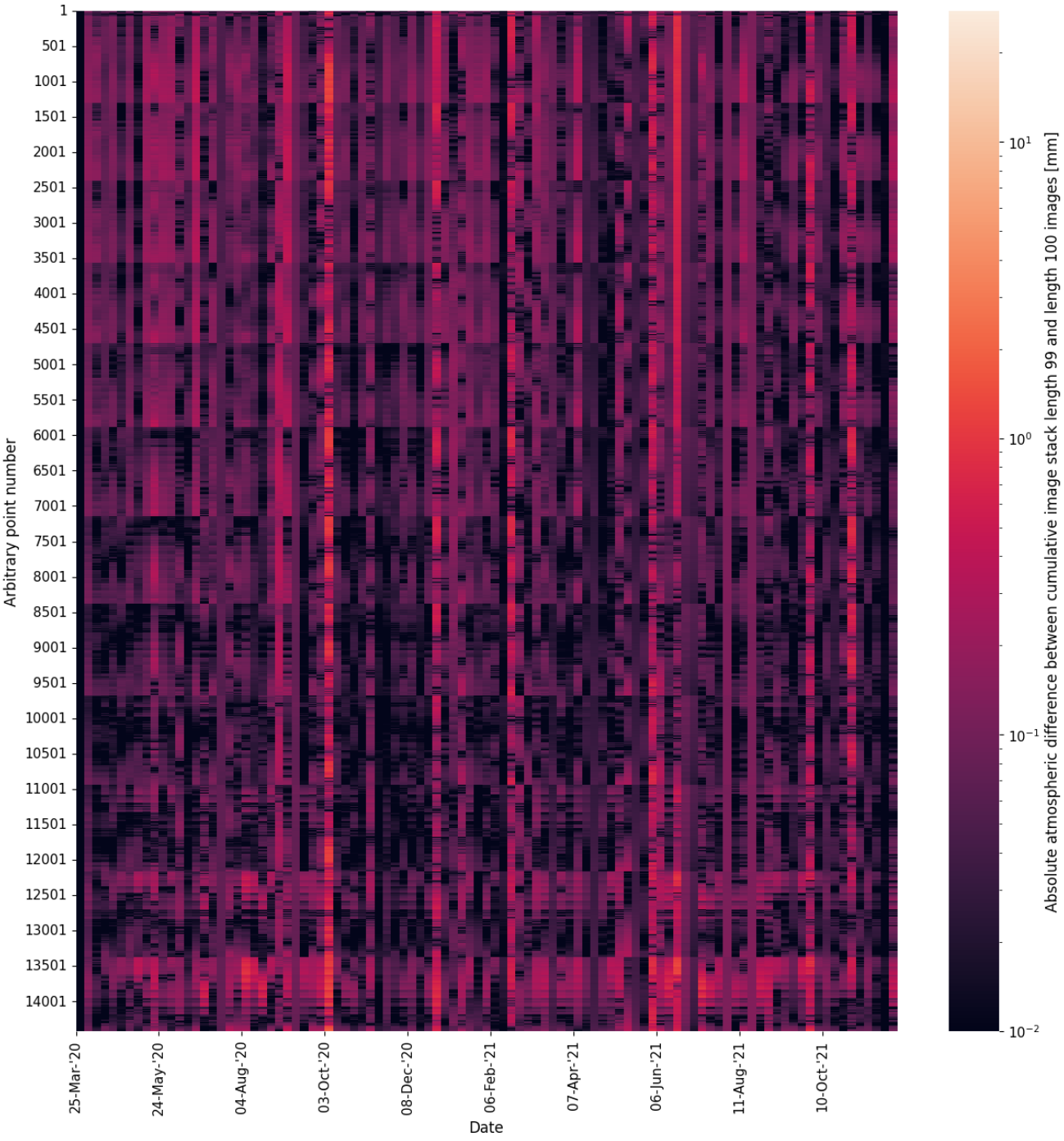

Figure A.28: Absolute Differential Atmospheric Space-Time Matrix containing atmospheric delay estimate differences of two Space-Time Matrices obtained from processing the conjunct pixels and epochs in two realizations. The horizontal axis contains the epoch number, starting from the 25th of March 2020 and the vertical axis represents an arbitrary point number (location).

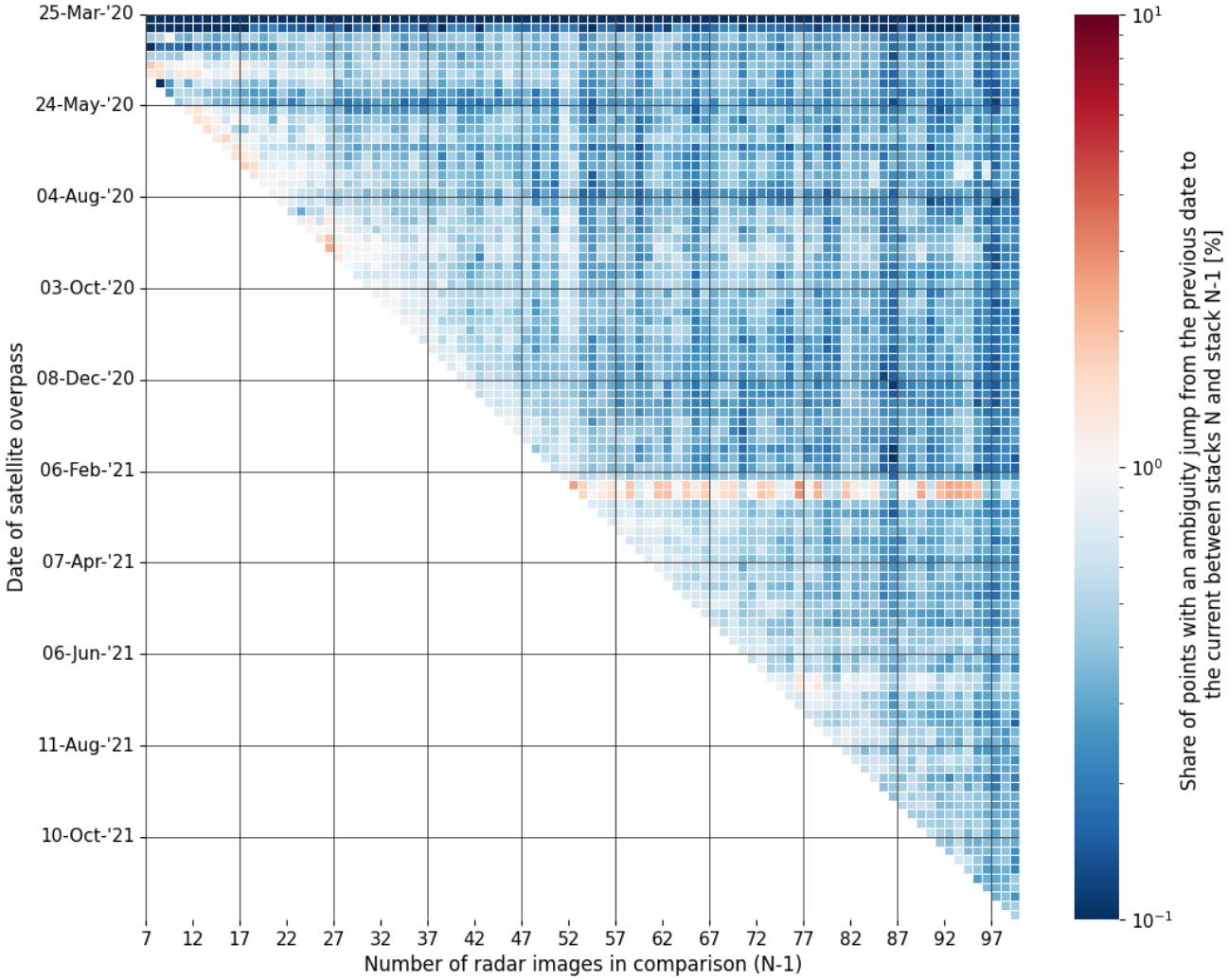

Figure A.29: Ambiguity Overview for the occurrence of cycle slips in the displacement estimates per epoch, comparing acquisition realization N with realization $N-1$. Moving horizontally, the same epoch is compared but with a different DePSI input. A vertical column contains the cycle slips of one realization comparison. Dark red indicates many cycle slips on that epoch and dark blue indicates almost no cycle slips.

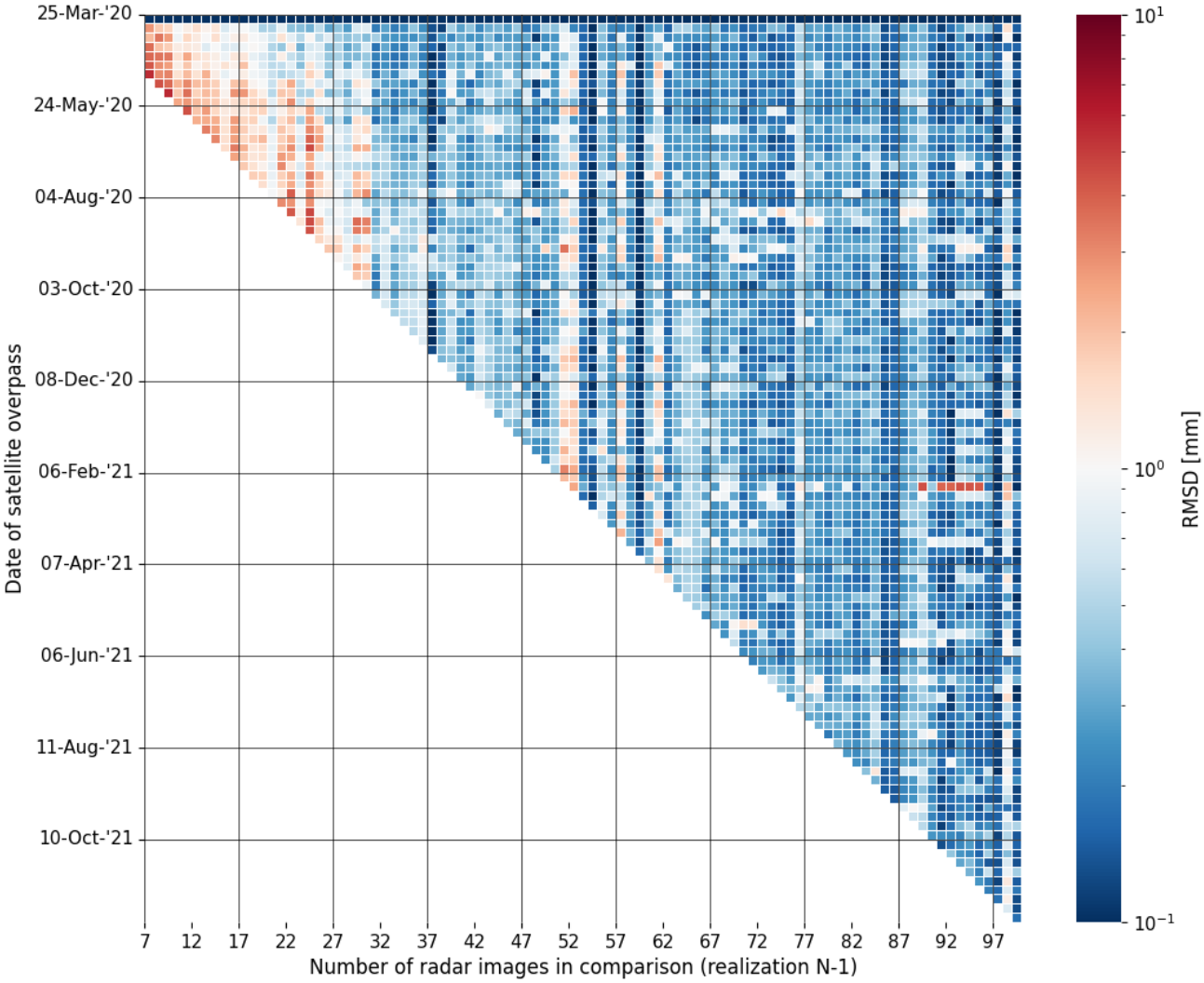

Figure A.30: RMSD Overview for the detailed version of the displacement estimates per epoch, comparing acquisition realization N with realization $N-1$. Moving horizontally, the same epoch is compared but with a different DePSI input. A vertical column contains the RMSD of one realization comparison. Dark red indicates large displacement estimate differences on that epoch and dark blue indicates almost no difference.

A.5.3. First-order network densification

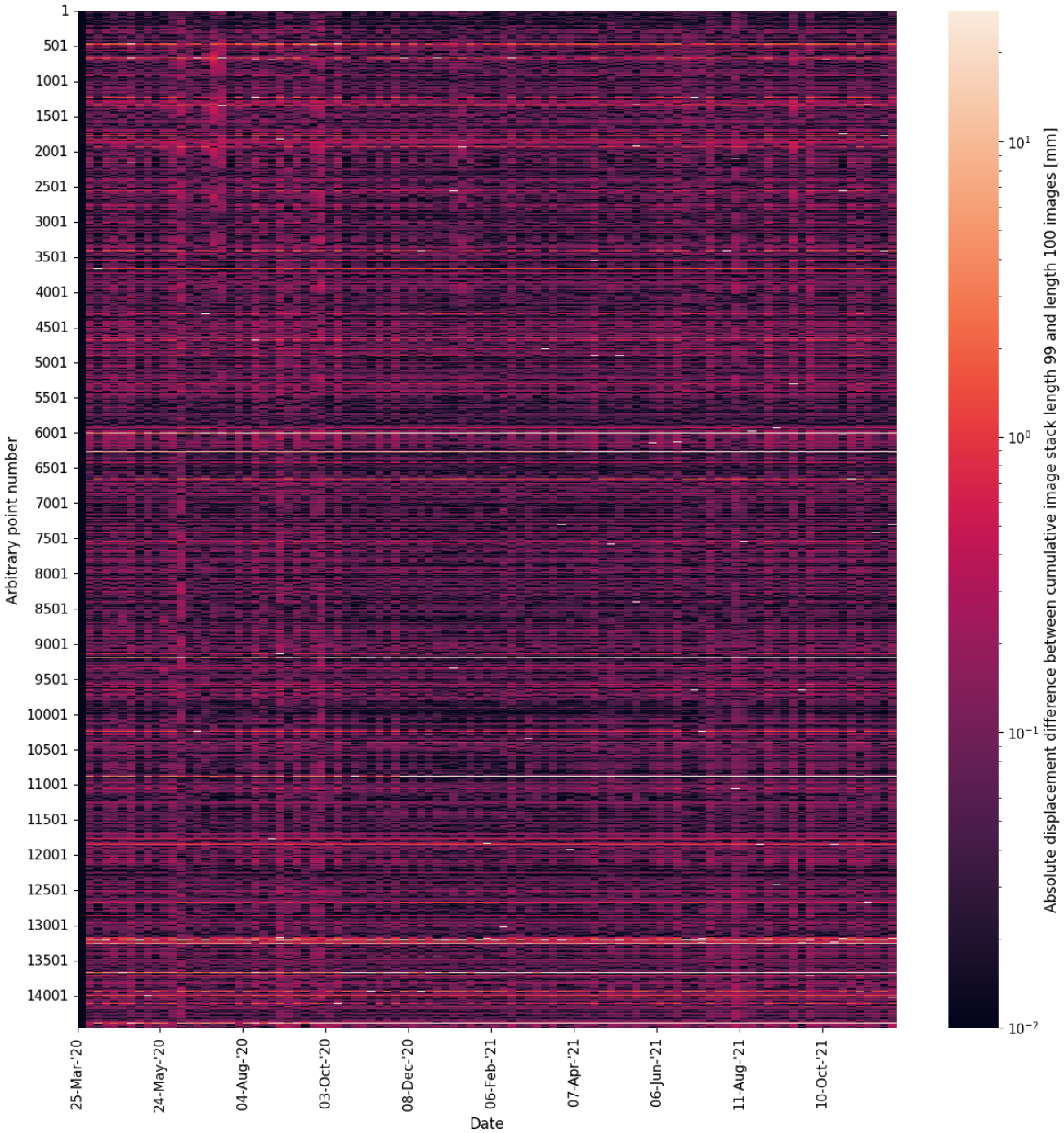

Figure A.31: Absolute Differential Space-Time Matrix containing displacement estimate differences of two Space-Time Matrices obtained from processing the conjunct pixels and epochs in two realizations. The horizontal axis contains the epoch number, starting from the 25th of March 2020 and the vertical axis represents an arbitrary point number (location).

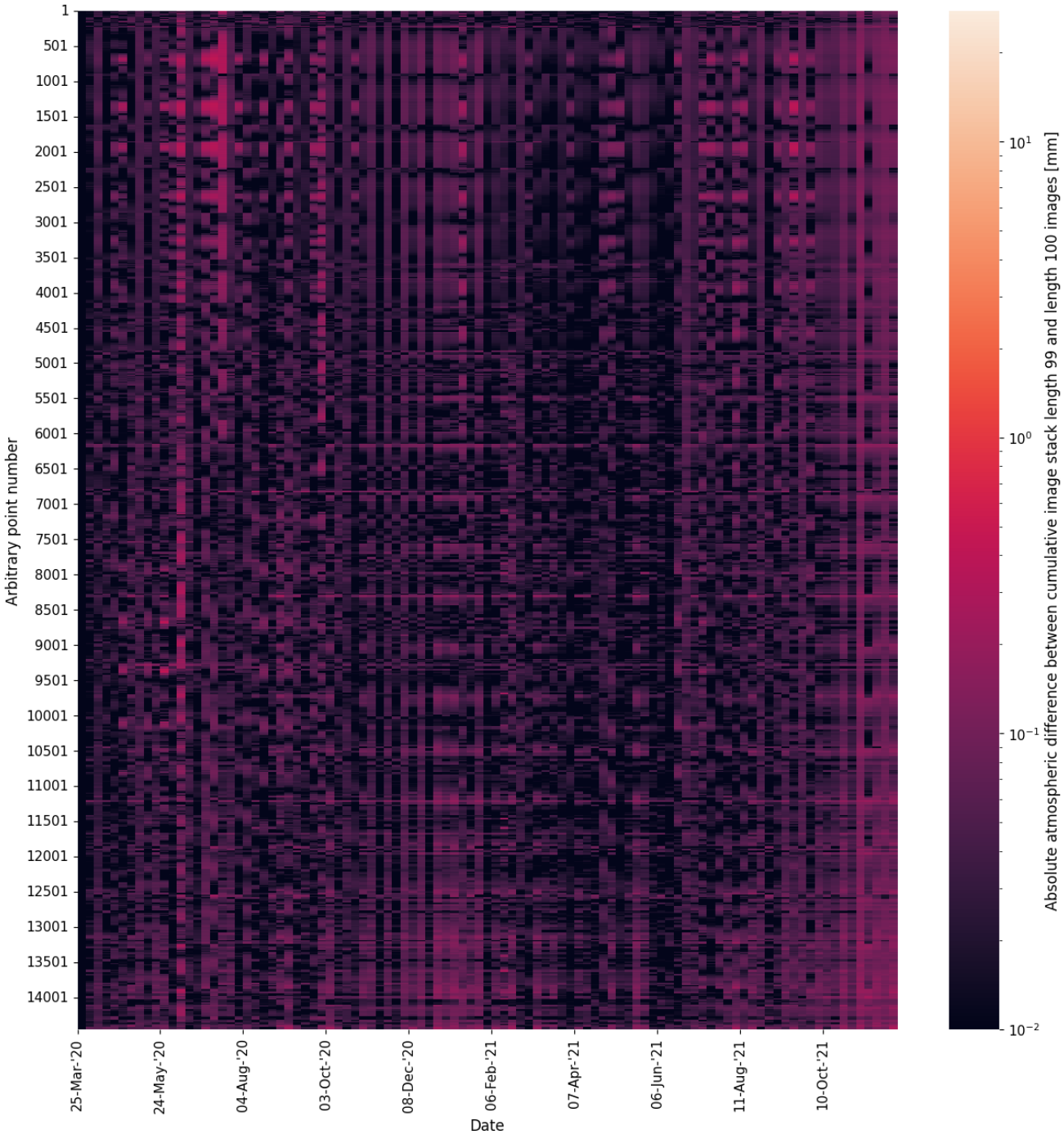

Figure A.32: Absolute Differential Atmospheric Space-Time Matrix containing atmospheric delay estimate differences of two Space-Time Matrices obtained from processing the conjunct pixels and epochs in two realizations. The horizontal axis contains the epoch number, starting from the 25th of March 2020 and the vertical axis represents an arbitrary point number (location).

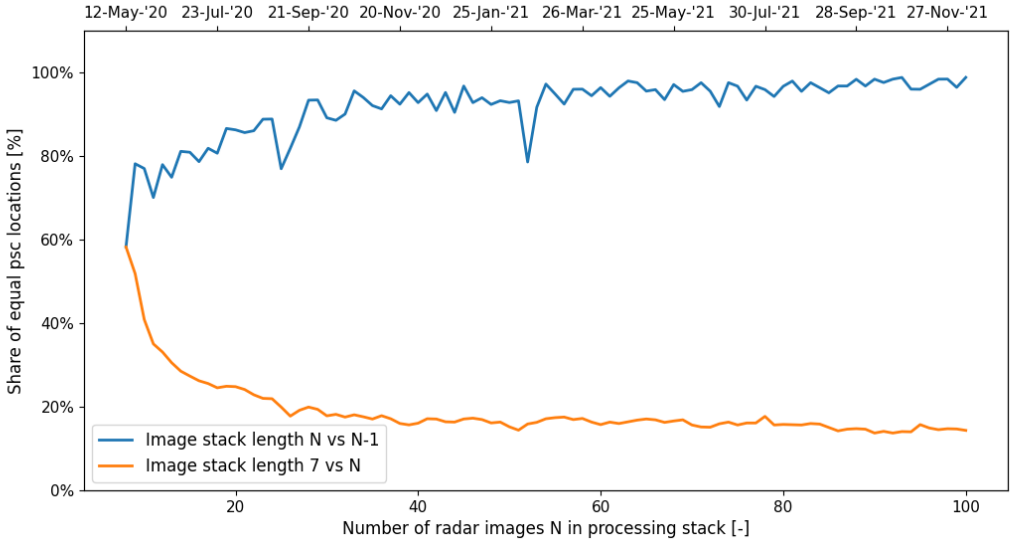

Figure A.33: Figure containing the share of identical PS1 locations over the number of realizations comparing N to $N-1$ (blue line) and N to the starting set (yellow line).

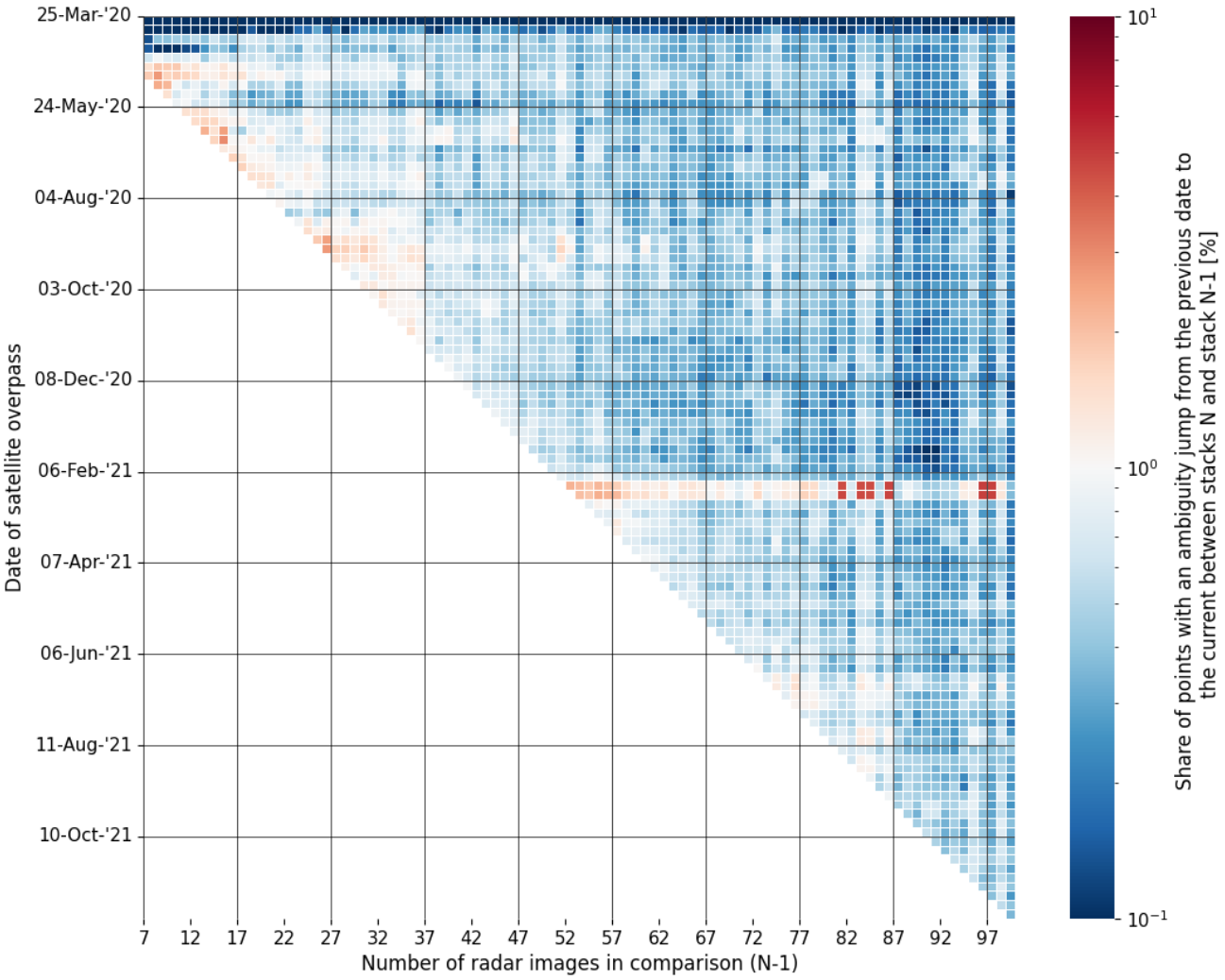

Figure A.34: Ambiguity Overview for the occurrence of cycle slips in the displacement estimates per epoch, comparing acquisition realization N with realization $N-1$. Moving horizontally, the same epoch is compared but with a different DePSI input. A vertical column contains the cycle slips of one realization comparison. Dark red indicates many cycle slips on that epoch and dark blue indicates almost no cycle slips.

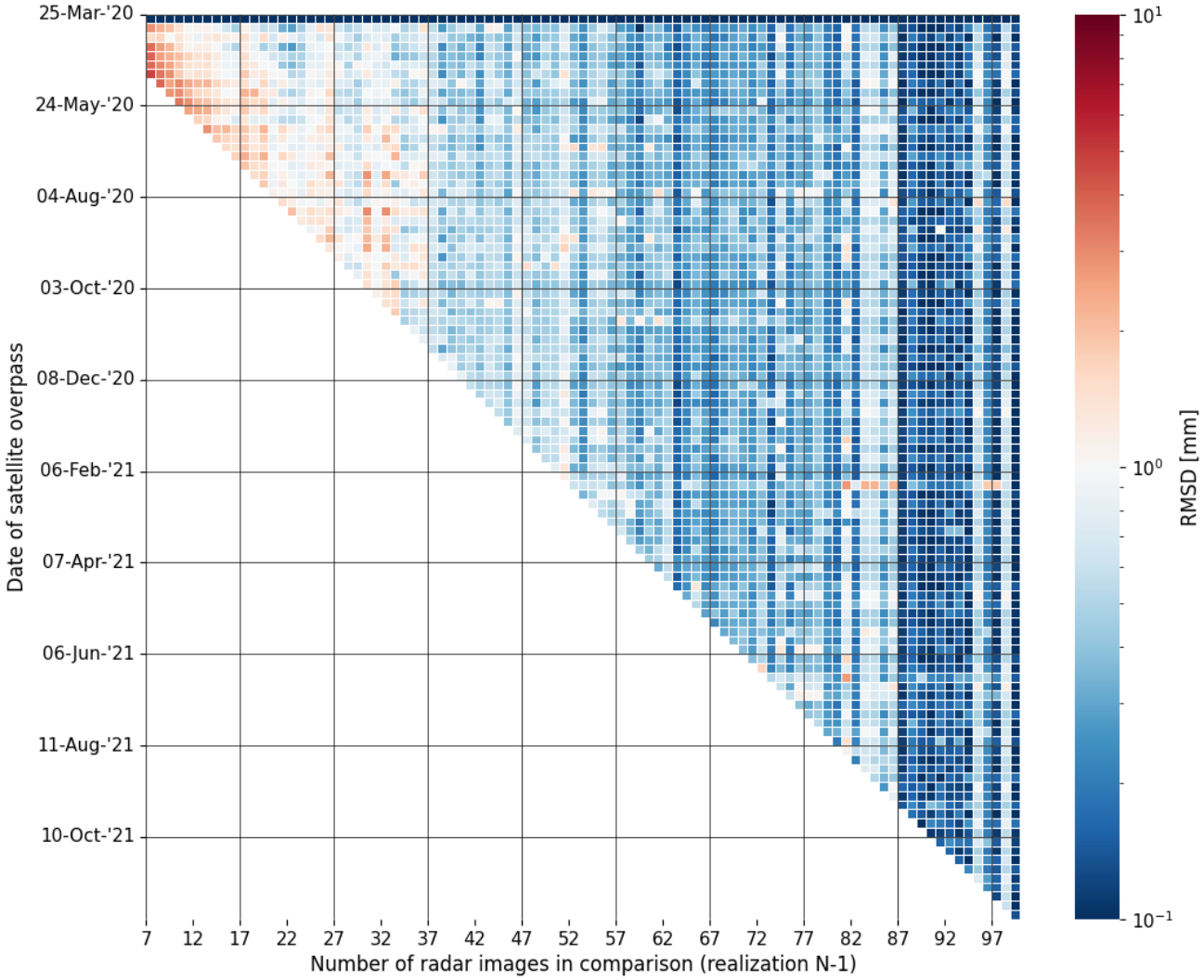

Figure A.35: RMSD Overview for the detailed version of the displacement estimates per epoch, comparing acquisition realization N with realization $N-1$. Moving horizontally, the same epoch is compared but with a different DePSI input. A vertical column contains the RMSD of one realization comparison. Dark red indicates large displacement estimate differences on that epoch and dark blue indicates almost no difference.

A.5.4. Robust Kriging

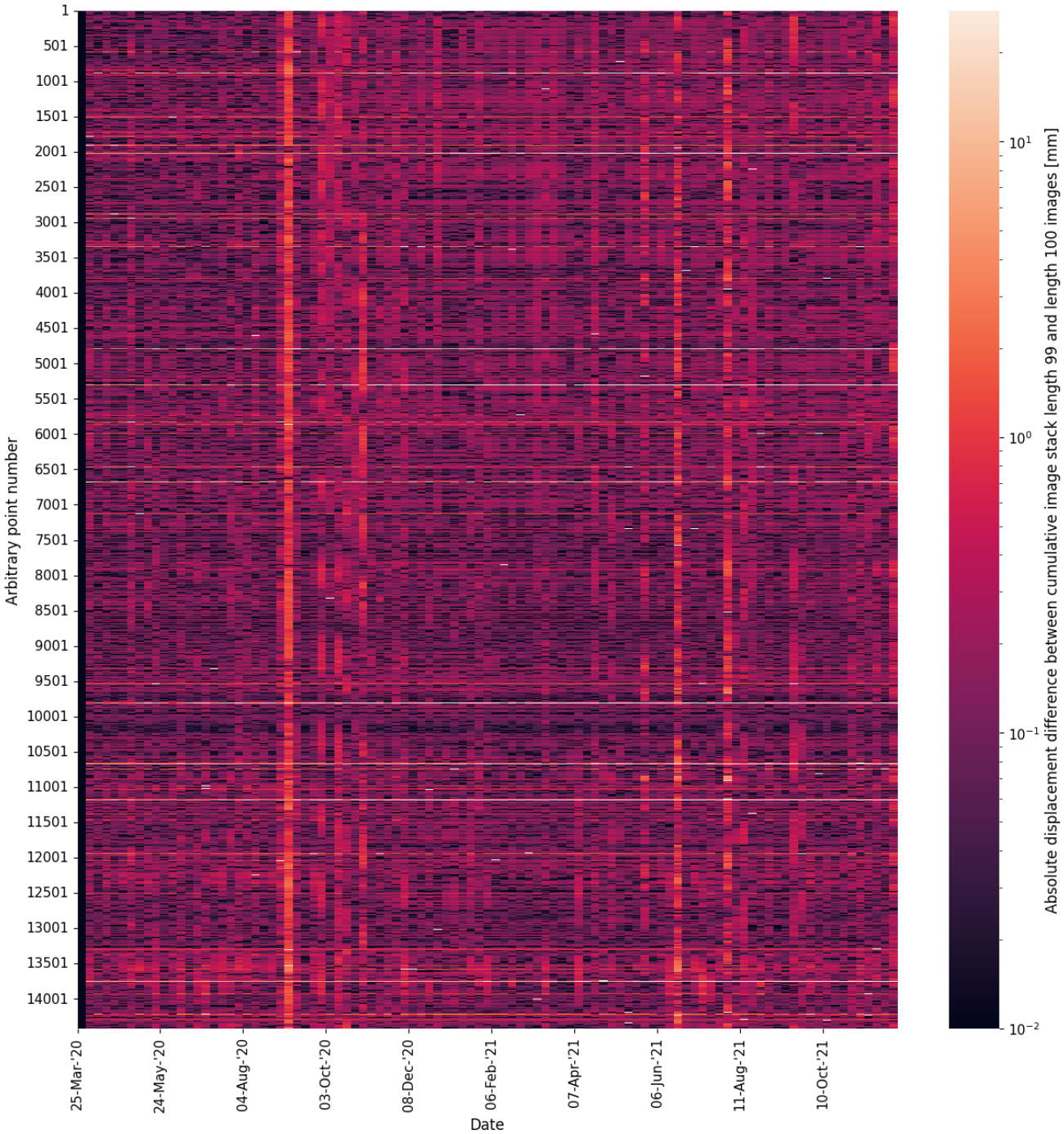

Figure A.36: Absolute Differential Space-Time Matrix containing displacement estimate differences of two Space-Time Matrices obtained from processing the conjunct pixels and epochs in two realizations. The horizontal axis contains the epoch number, starting from the 25th of March 2020 and the vertical axis represents an arbitrary point number (location).

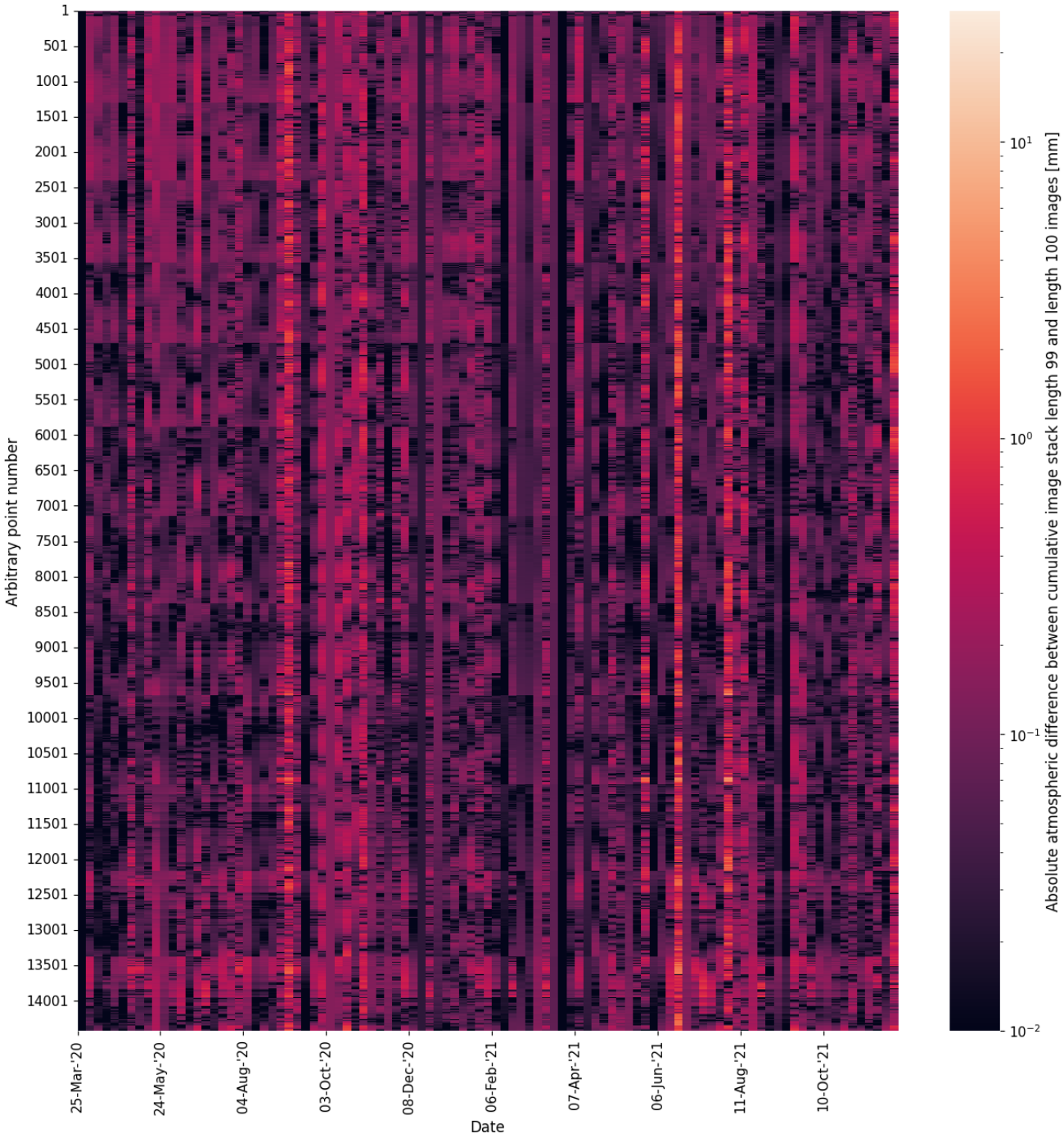

Figure A.37: Absolute Differential Atmospheric Space-Time Matrix containing atmospheric delay estimate differences of two Space-Time Matrices obtained from processing the conjunct pixels and epochs in two realizations. The horizontal axis contains the epoch number, starting from the 25th of March 2020 and the vertical axis represents an arbitrary point number (location).

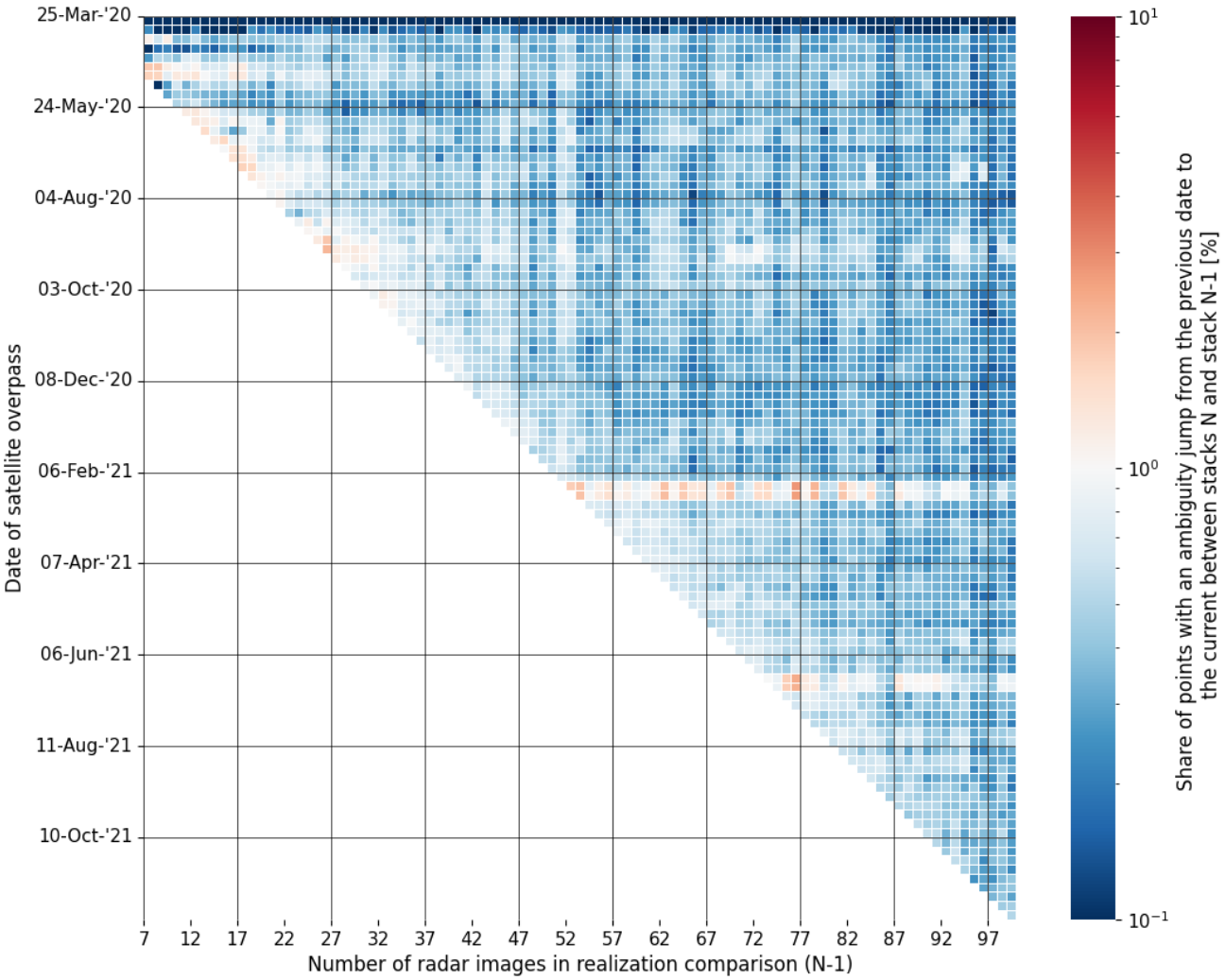

Figure A.38: Ambiguity Overview for the occurrence of cycle slips in the displacement estimates per epoch, comparing acquisition realization N with realization $N-1$. Moving horizontally, the same epoch is compared but with a different DePSI input. A vertical column contains the cycle slips of one realization comparison. Dark red indicates many cycle slips on that epoch and dark blue indicates almost no cycle slips.

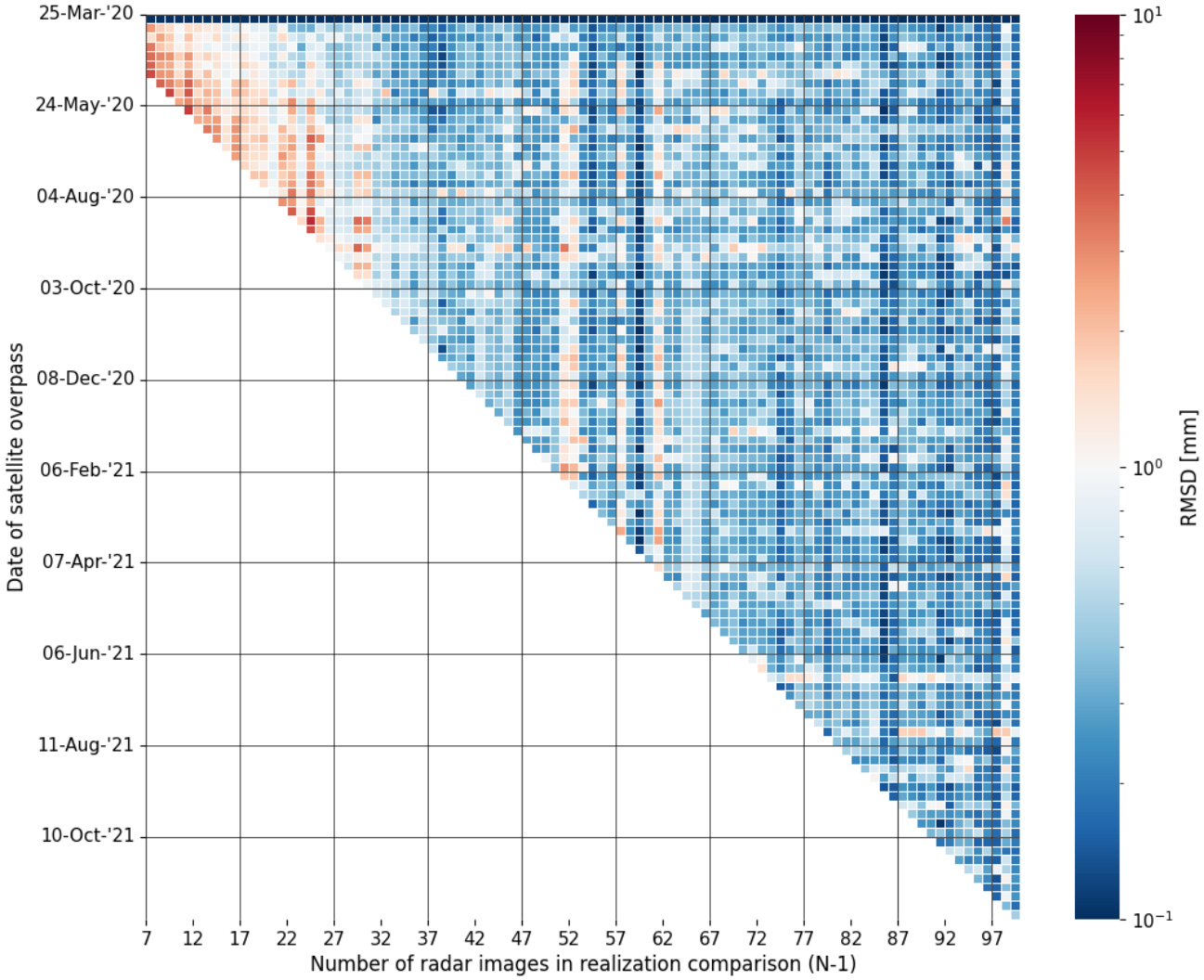

Figure A.39: RMSD Overview for the detailed version of the displacement estimates per epoch, comparing acquisition realization N with realization $N-1$. Moving horizontally, the same epoch is compared but with a different DePSI input. A vertical column contains the RMSD of one realization comparison. Dark red indicates large displacement estimate differences on that epoch and dark blue indicates almost no difference.

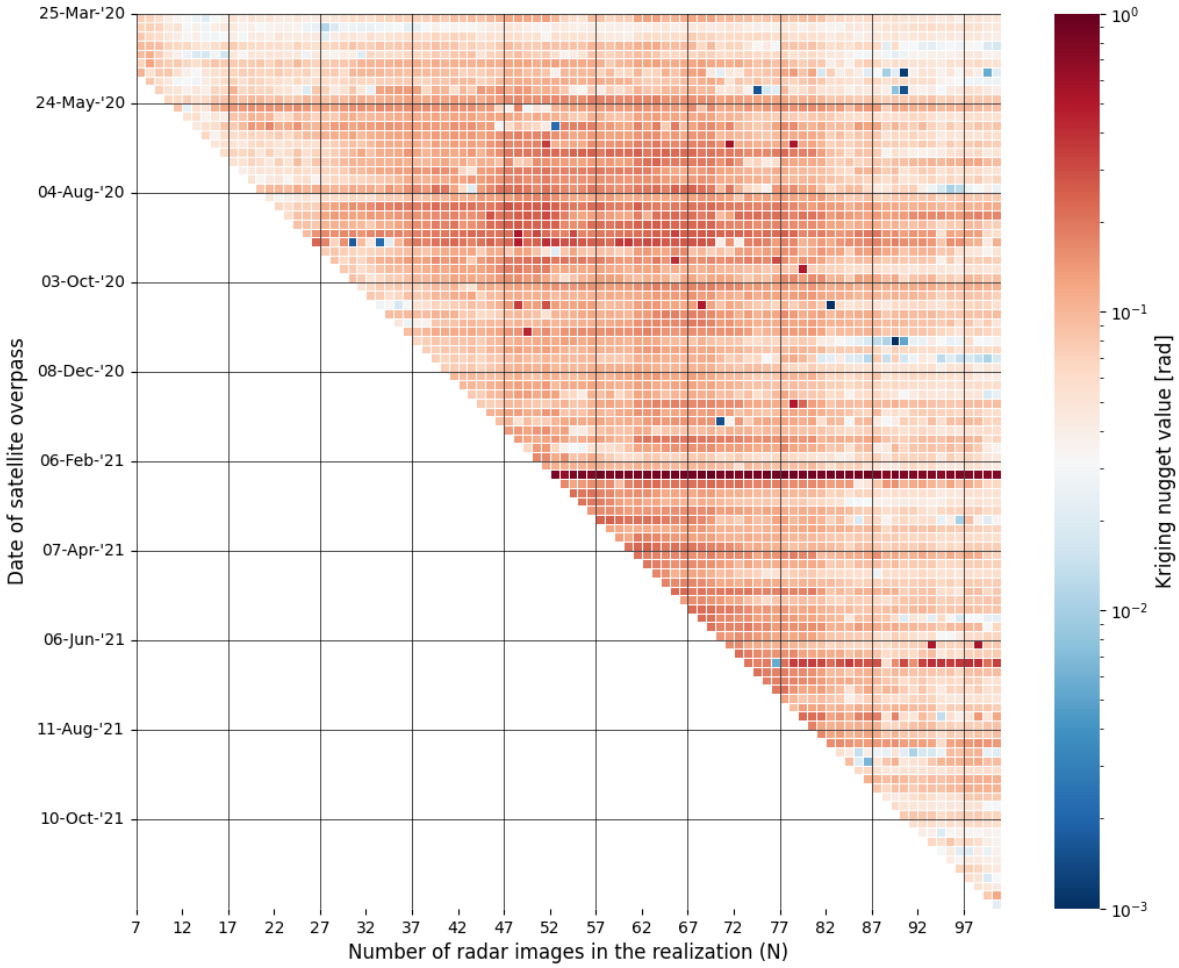

Figure A.40: Heatmap for the nugget values for each epoch over the number of images in realization N.

A.5.5. 5x5 km region

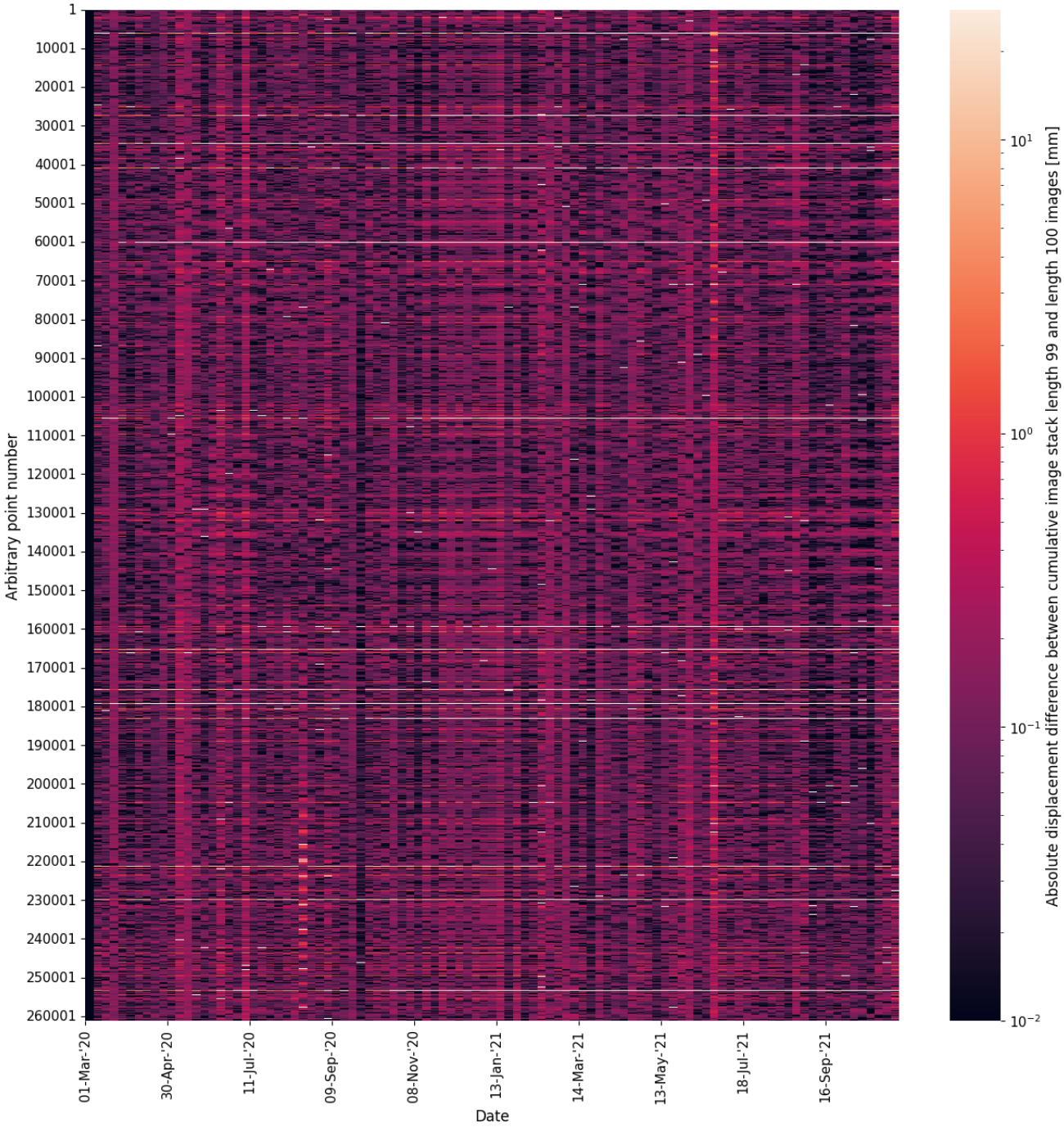

Figure A.41: Absolute Differential Space-Time Matrix containing displacement estimate differences of two Space-Time Matrices obtained from processing the conjunct pixels and epochs in two realizations. The horizontal axis contains the epoch number, starting from the 1st of March 2020 and the vertical axis represents an arbitrary point number (location).

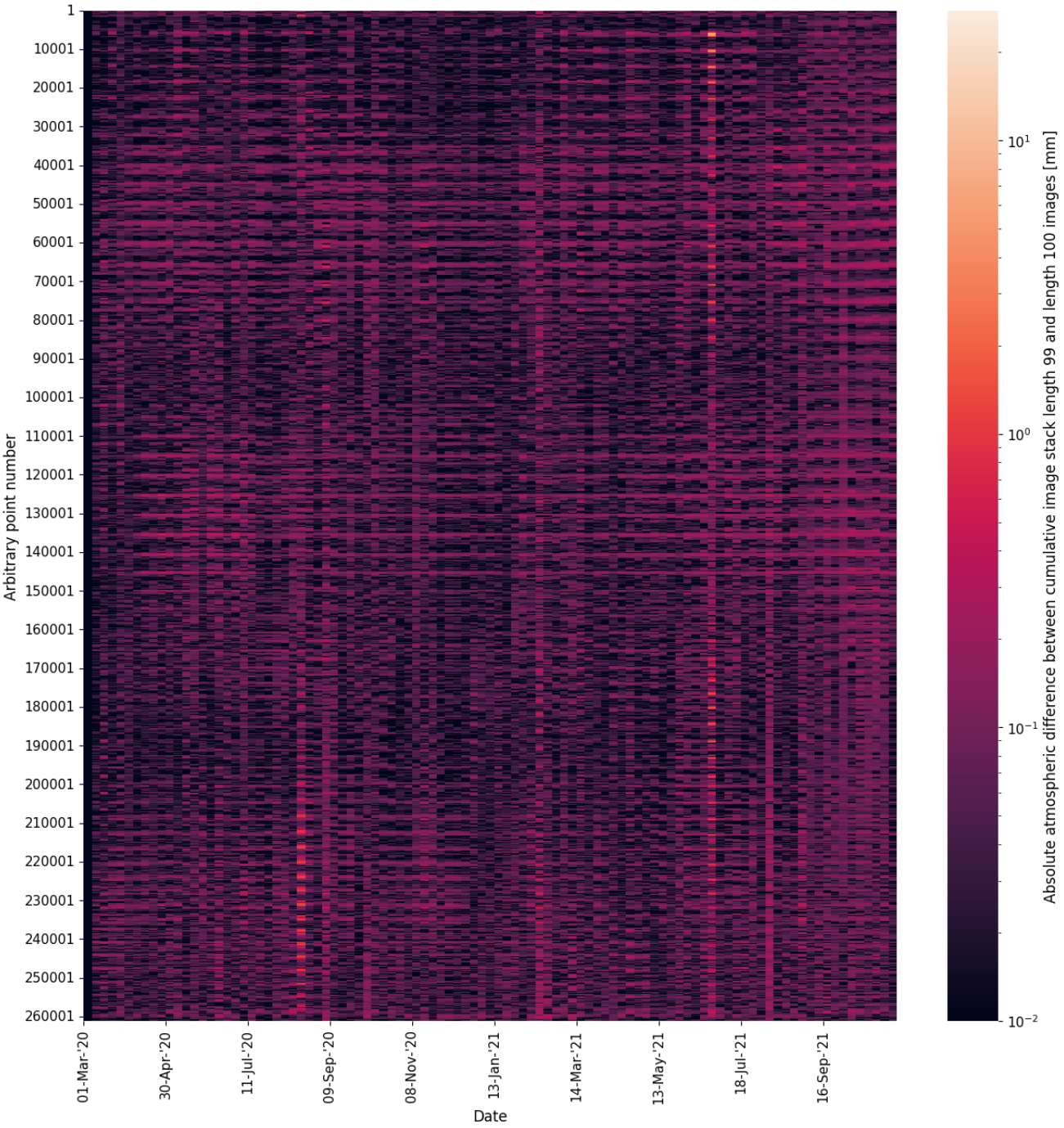

Figure A.42: Absolute Differential Atmospheric Space-Time Matrix containing atmospheric delay estimate differences of two Space-Time Matrices obtained from processing the conjunct pixels and epochs in two realizations. The horizontal axis contains the epoch number, starting from the 25th of March 2020 and the vertical axis represents an arbitrary point number (location).

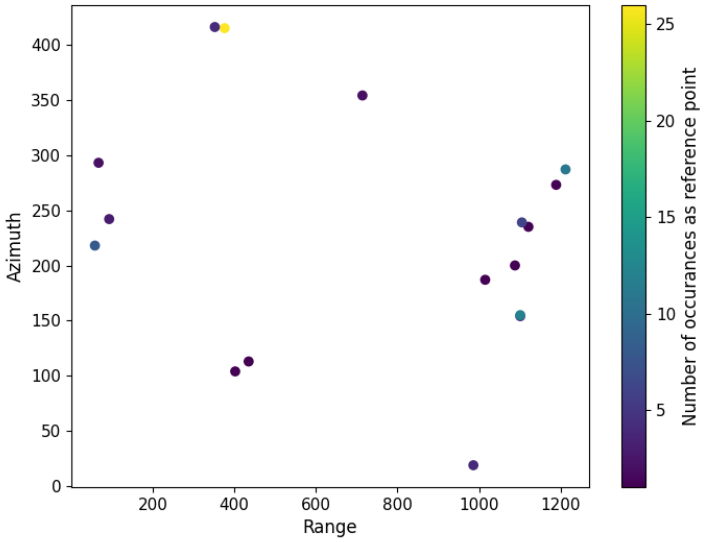

Figure A.43: Locations and number of occurrences of the reference point when the choice of reference is unrestricted.

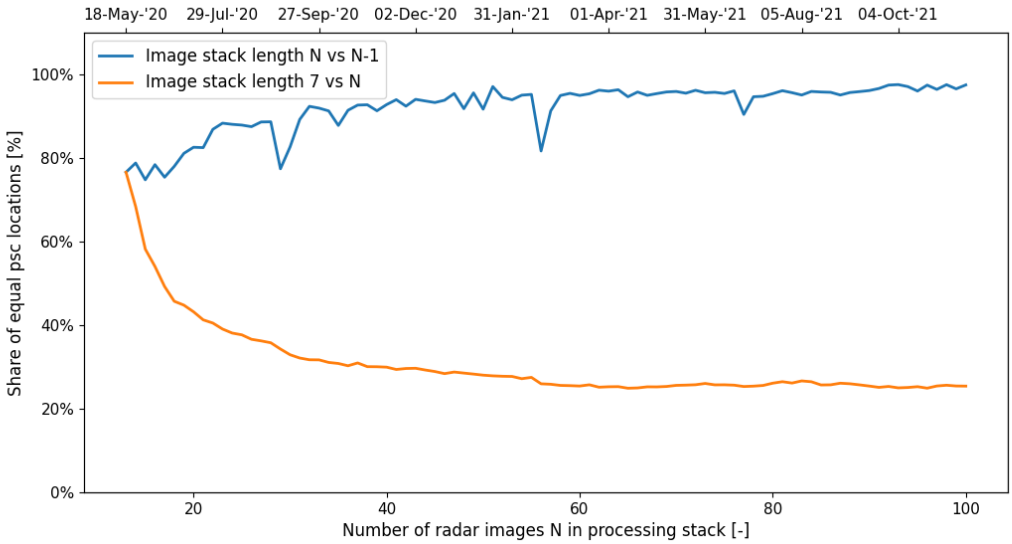

Figure A.44: Figure containing the share of identical PS1 locations over the number of realizations comparing N to $N-1$ (blue line) and N to the starting set (yellow line).

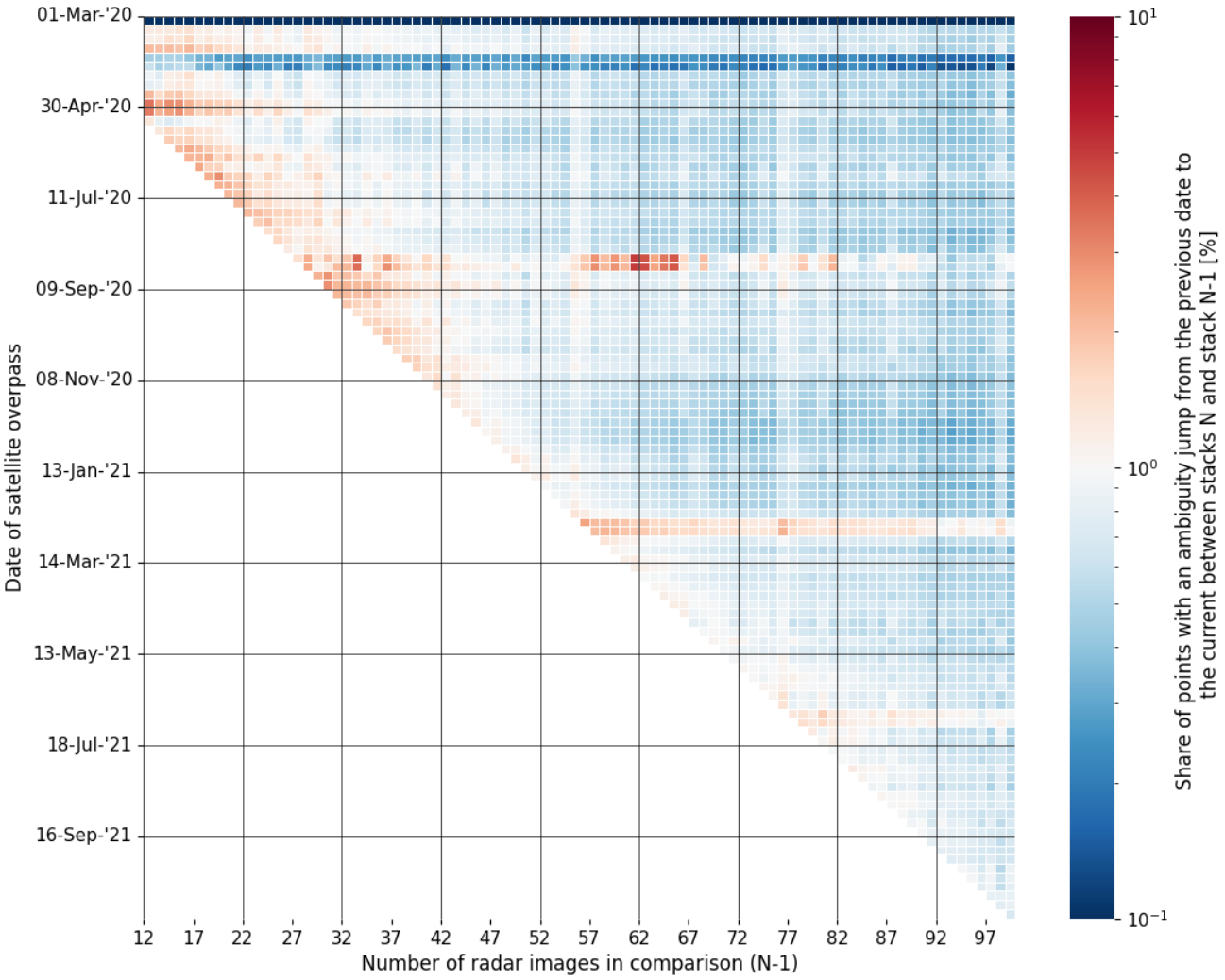

Figure A.45: Ambiguity Overview for the occurrence of cycle slips in the displacement estimates per epoch, comparing acquisition realization N with realization $N-1$. Moving horizontally, the same epoch is compared but with a different DePSI input. A vertical column contains the cycle slips of one realization comparison. Dark red indicates many cycle slips on that epoch and dark blue indicates almost no cycle slips.

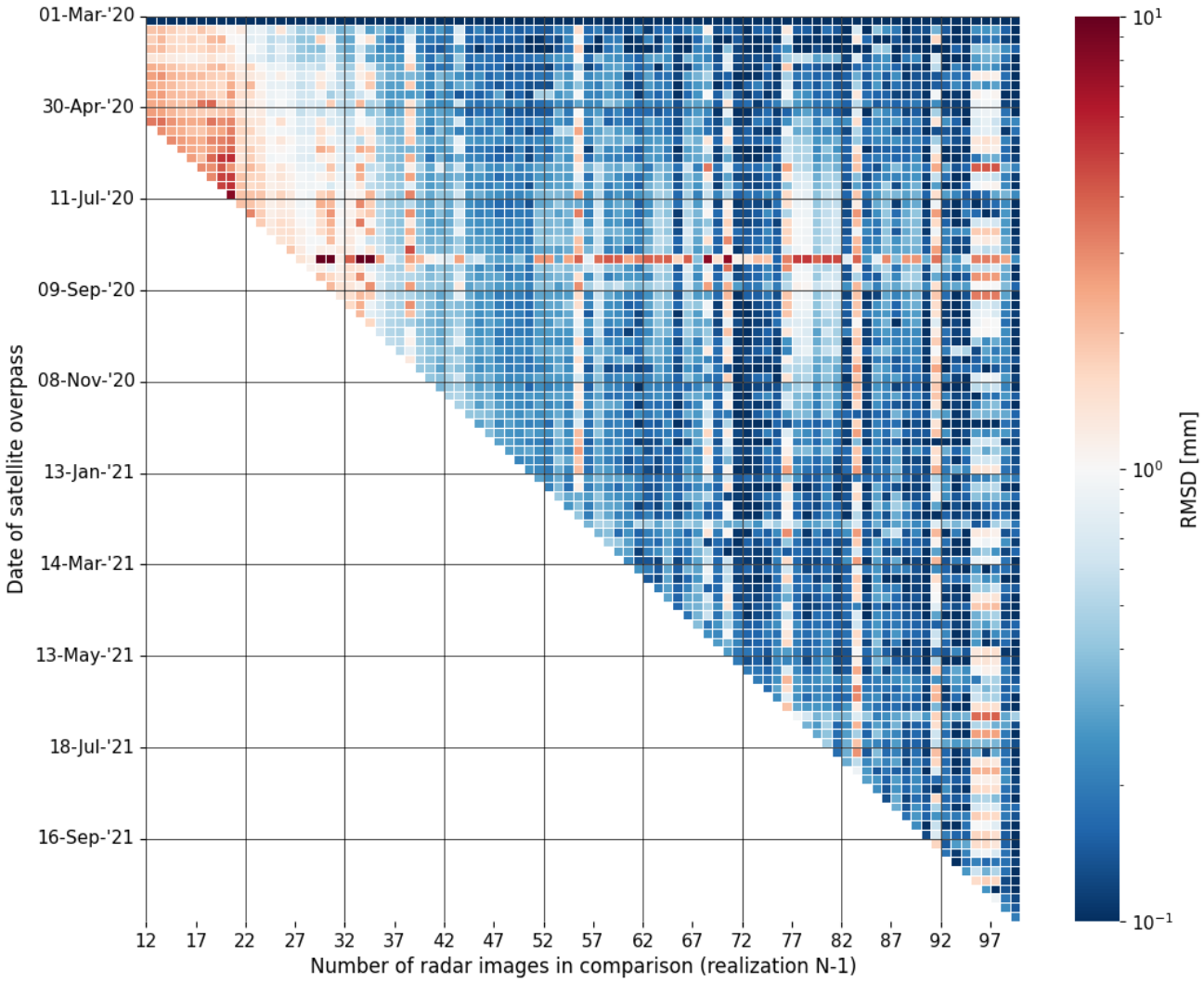

Figure A.46: RMSD Overview for the detailed version of the displacement estimates per epoch, comparing acquisition realization N with realization $N-1$. Moving horizontally, the same epoch is compared but with a different DePSI input. A vertical column contains the RMSD of one realization comparison. Dark red indicates large displacement estimate differences on that epoch and dark blue indicates almost no difference.

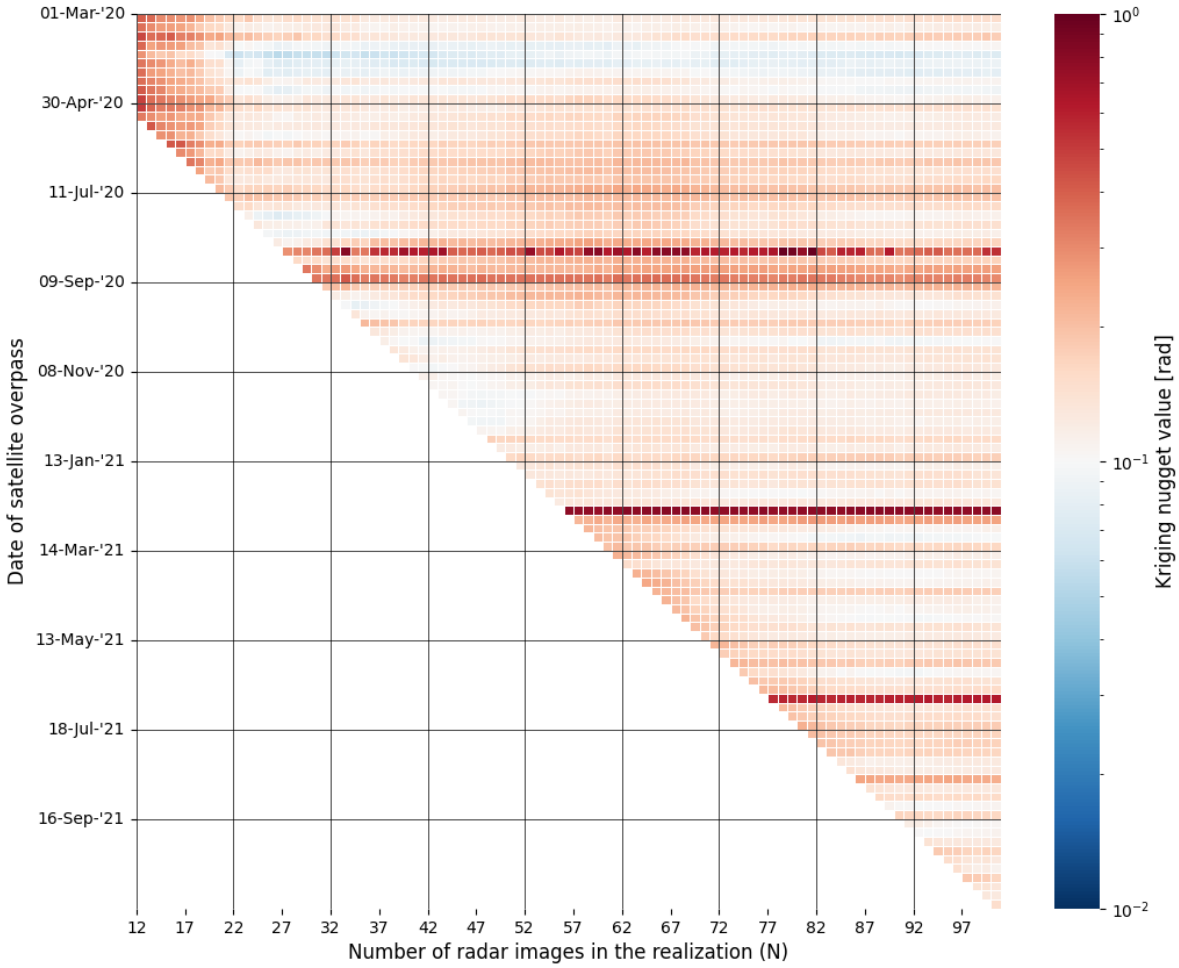

Figure A.47: Heatmap for the nugget values for each epoch over the number of images in realization N.

A.6. Expansion steady state

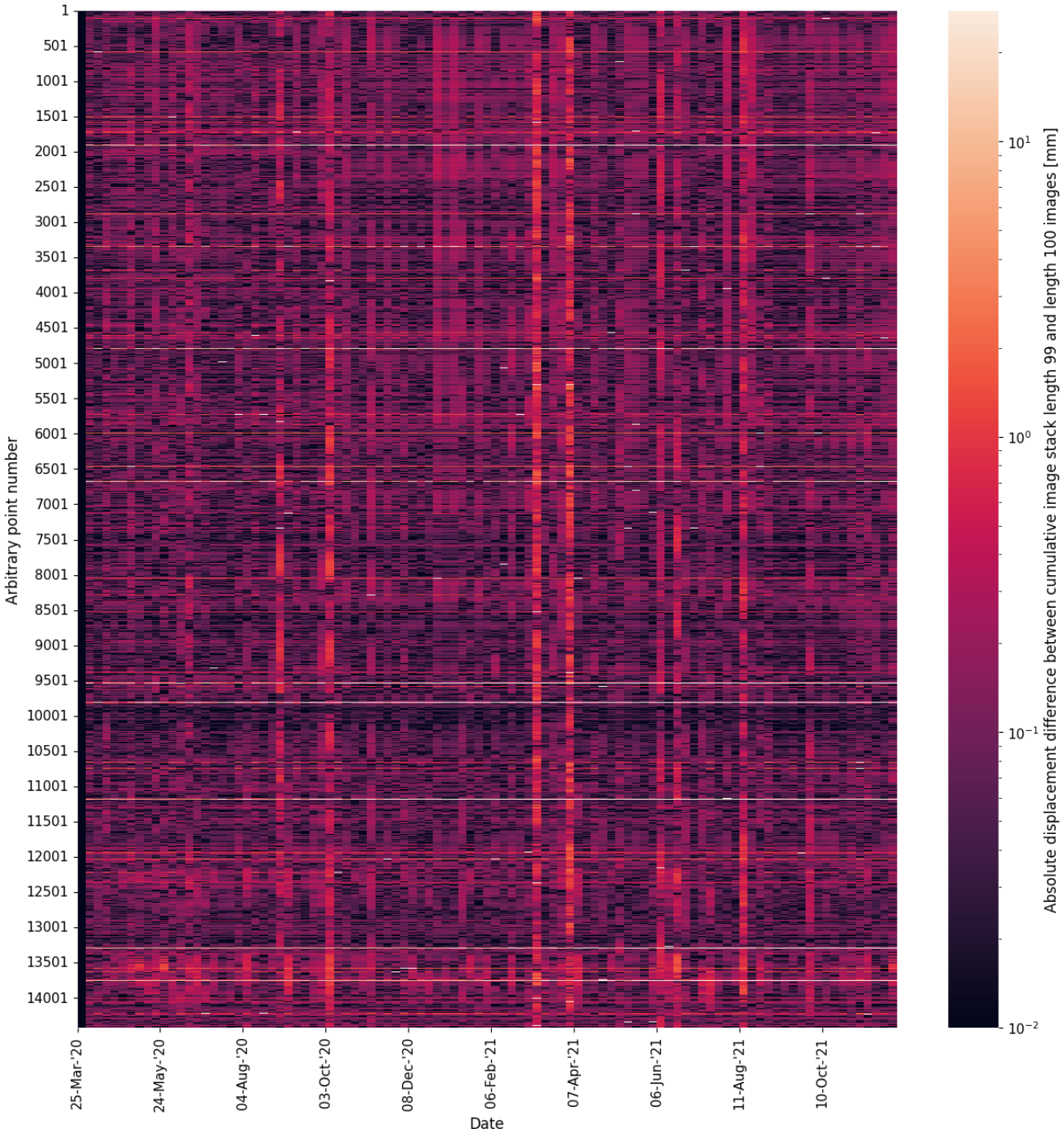

Figure A.48: Absolute Differential Space-Time Matrix containing displacement estimate differences of two Space-Time Matrices obtained from processing the conjunct pixels and epochs in two realizations. The horizontal axis contains the epoch number, starting from the 25th of March 2020 and the vertical axis represents an arbitrary point number (location).

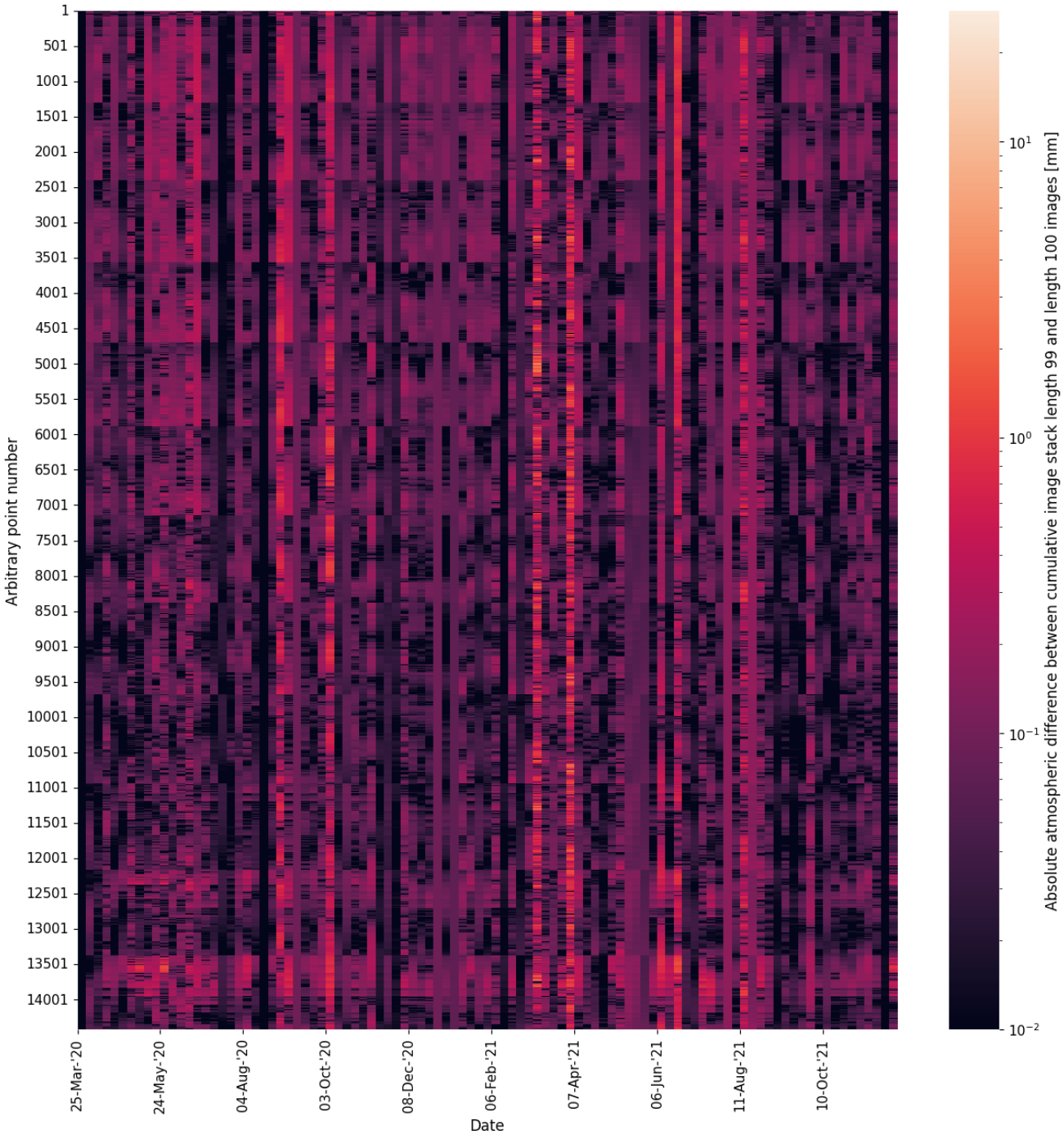

Figure A.49: Absolute Differential Atmospheric Space-Time Matrix containing atmospheric delay estimate differences of two Space-Time Matrices obtained from processing the conjunct pixels and epochs in two realizations. The horizontal axis contains the epoch number, starting from the 25th of March 2020 and the vertical axis represents an arbitrary point number (location).

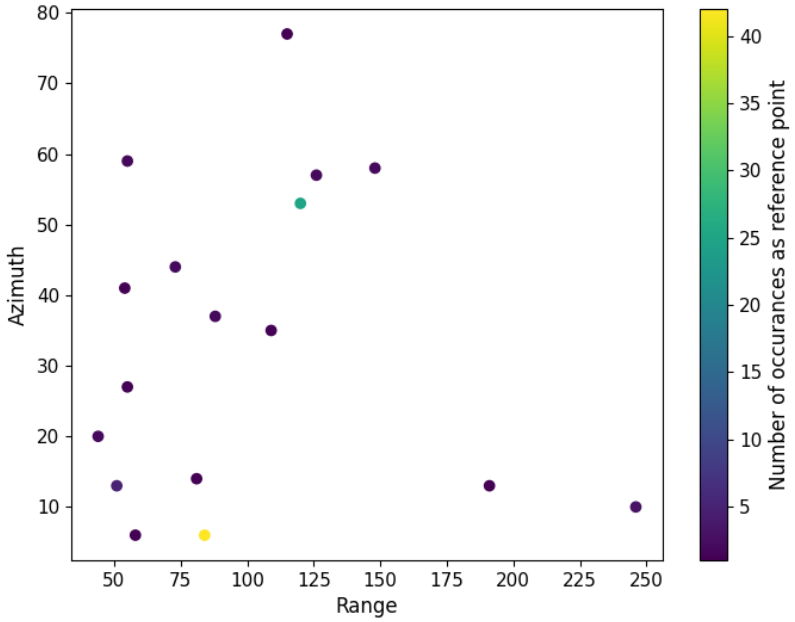

Figure A.50: Locations and number of occurrences of the reference point when the choice of reference is unrestricted.

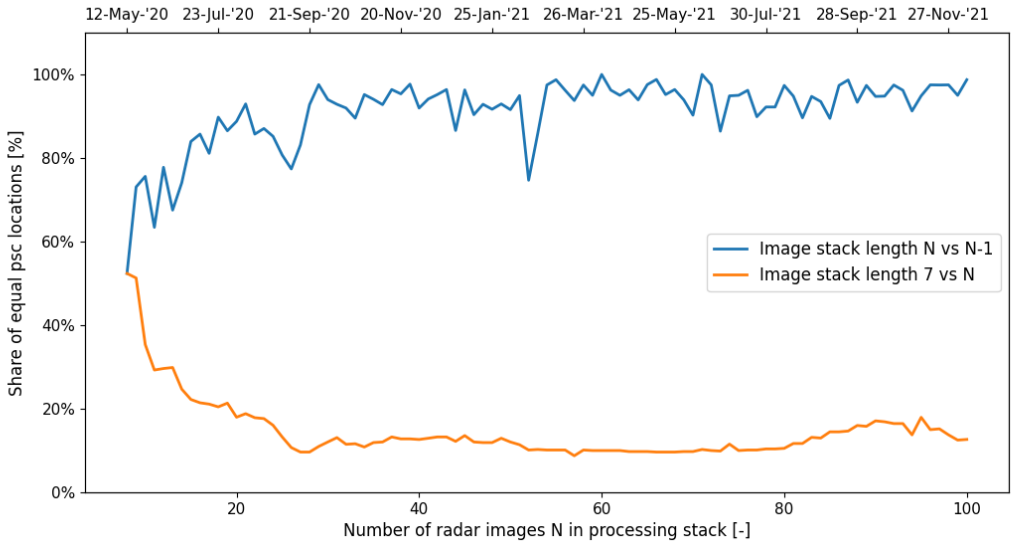

Figure A.51: Figure containing the share of identical PS1 locations over the number of realizations comparing N to $N-1$ (blue line) and N to the starting set (yellow line).

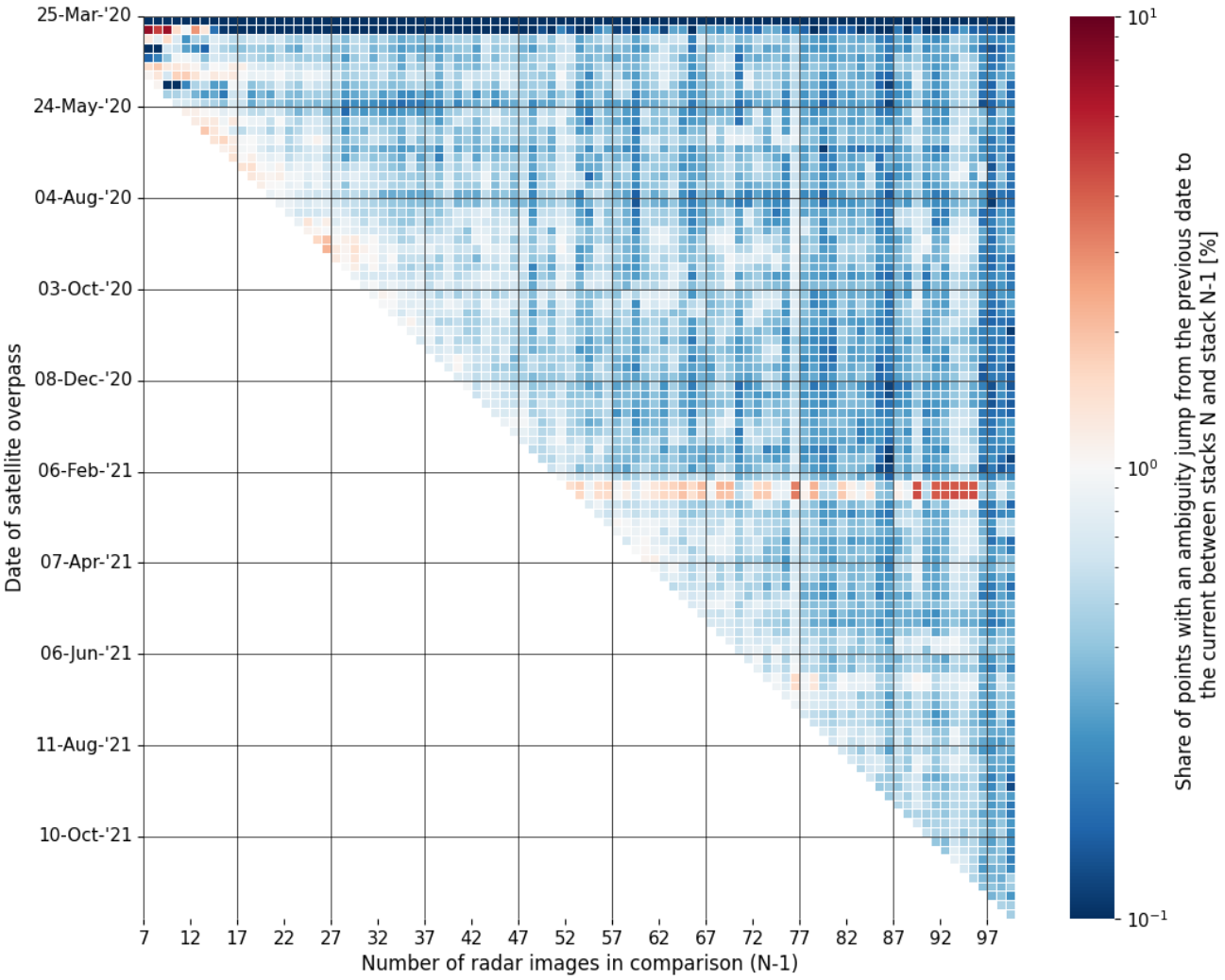

Figure A.52: Ambiguity Overview for the occurrence of cycle slips in the displacement estimates per epoch, comparing acquisition realization N with realization $N-1$. Moving horizontally, the same epoch is compared but with a different DePSI input. A vertical column contains the cycle slips of one realization comparison. Dark red indicates many cycle slips on that epoch and dark blue indicates almost no cycle slips.

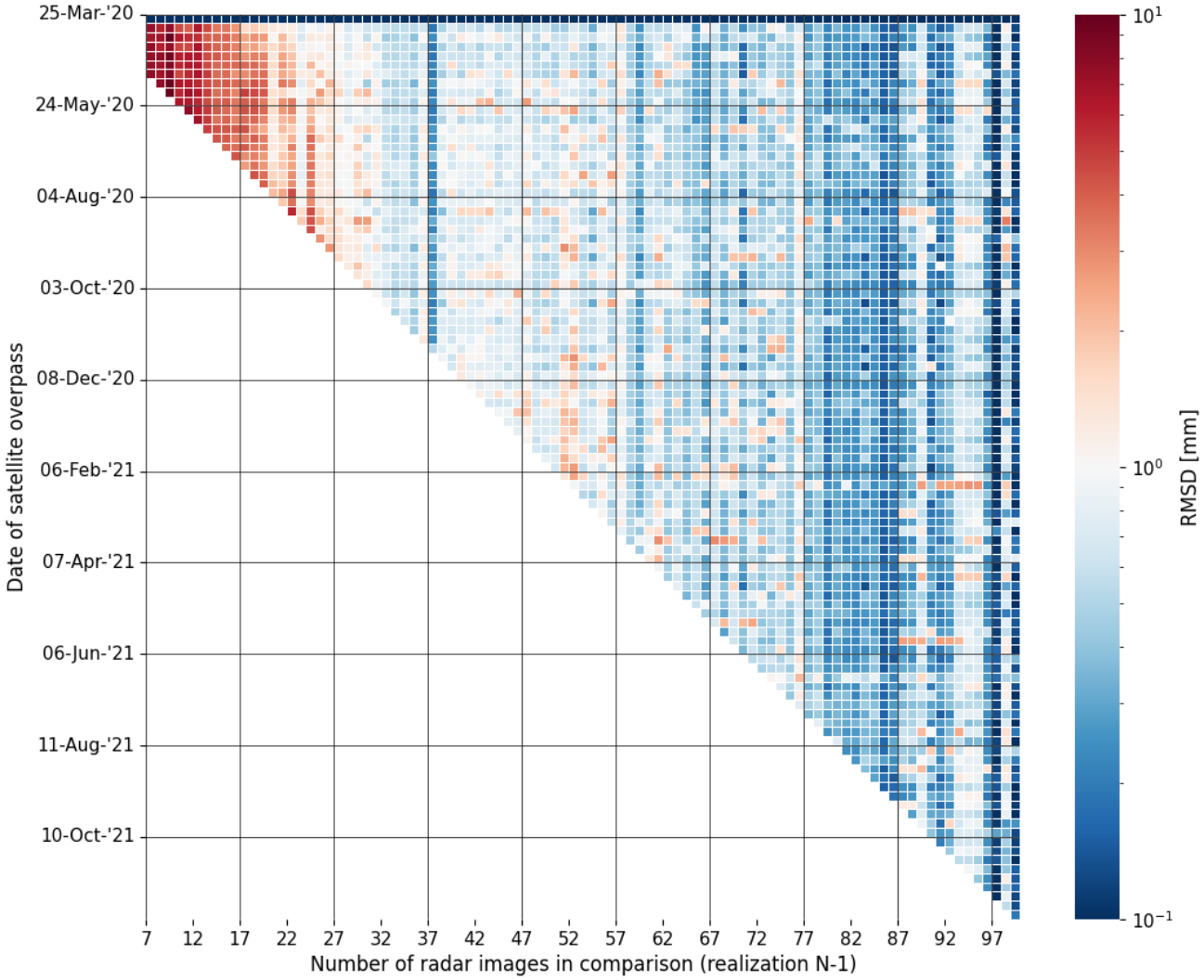

Figure A.53: RMSD Overview for the detailed version of the displacement estimates per epoch, comparing acquisition realization N with realization $N-1$. Moving horizontally, the same epoch is compared but with a different DePSI input. A vertical column contains the RMSD of one realization comparison. Dark red indicates large displacement estimate differences on that epoch and dark blue indicates almost no difference.

A.7. More strict PS2 NAD threshold

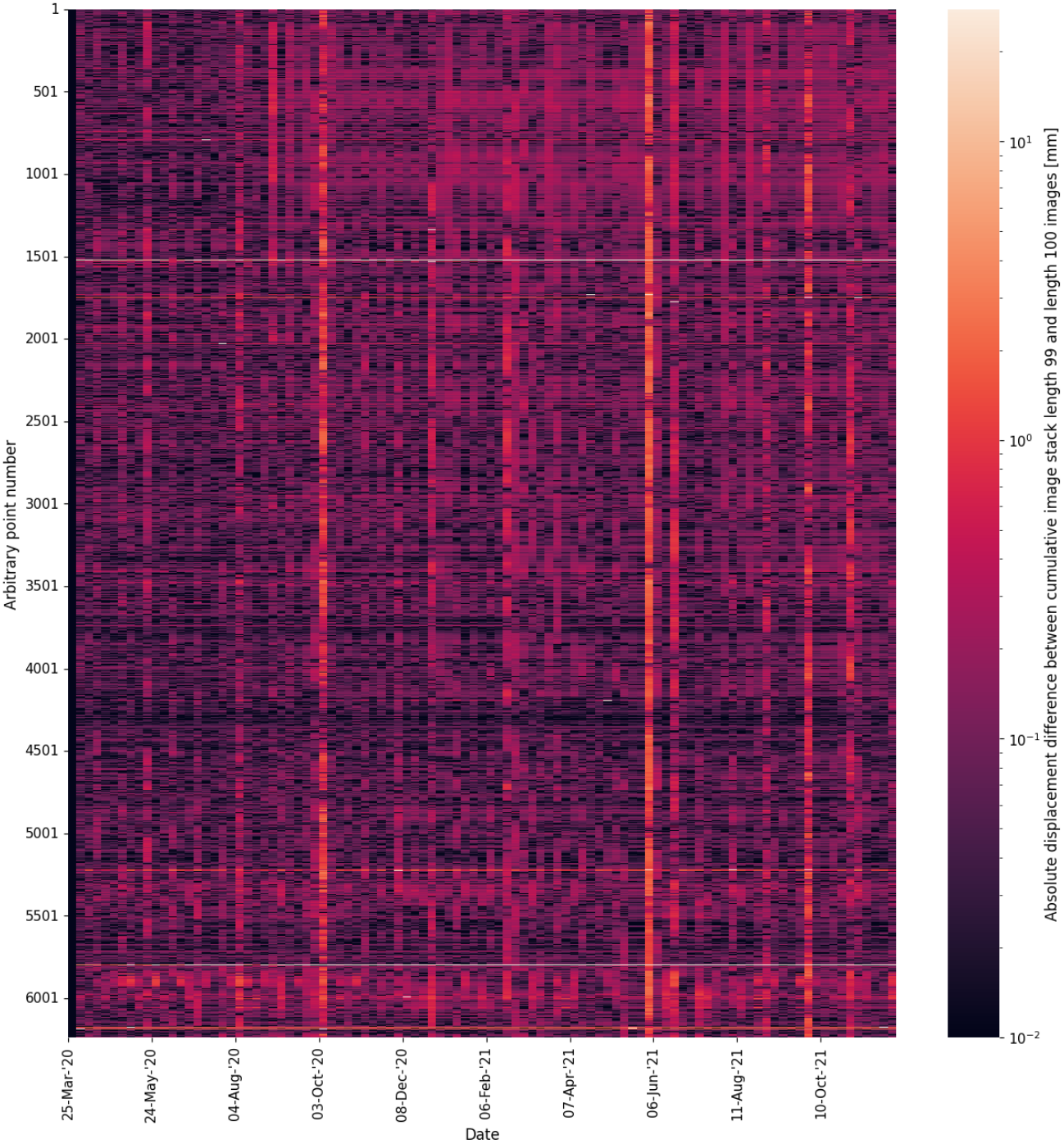

Figure A.54: Absolute Differential Space-Time Matrix containing displacement estimate differences of two Space-Time Matrices obtained from processing the conjunct pixels and epochs in two realizations. The horizontal axis contains the epoch number, starting from the 25th of March 2020 and the vertical axis represents an arbitrary point number (location).

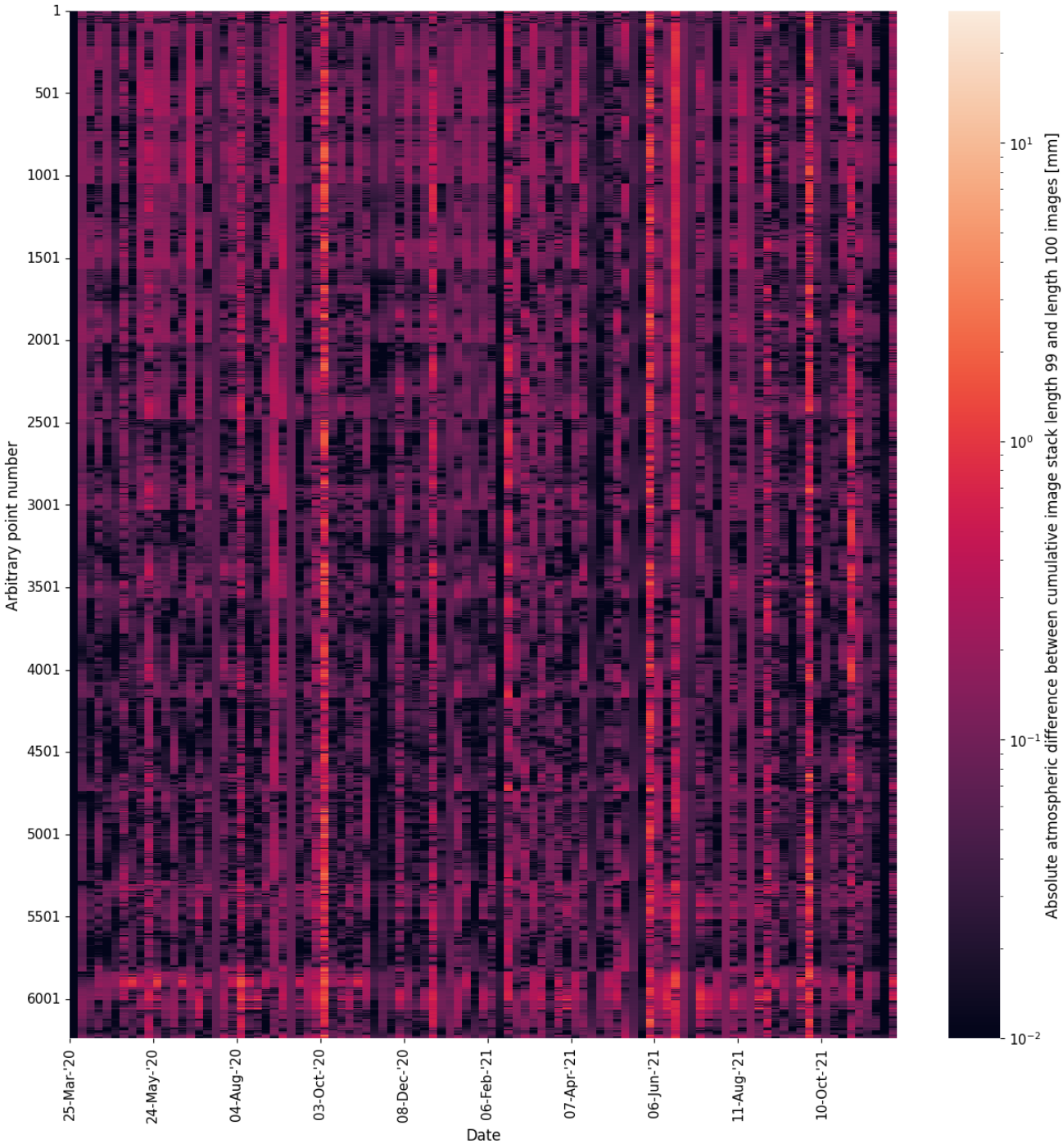

Figure A.55: Absolute Differential Atmospheric Space-Time Matrix containing atmospheric delay estimate differences of two Space-Time Matrices obtained from processing the conjunct pixels and epochs in two realizations. The horizontal axis contains the epoch number, starting from the 25th of March 2020 and the vertical axis represents an arbitrary point number (location).

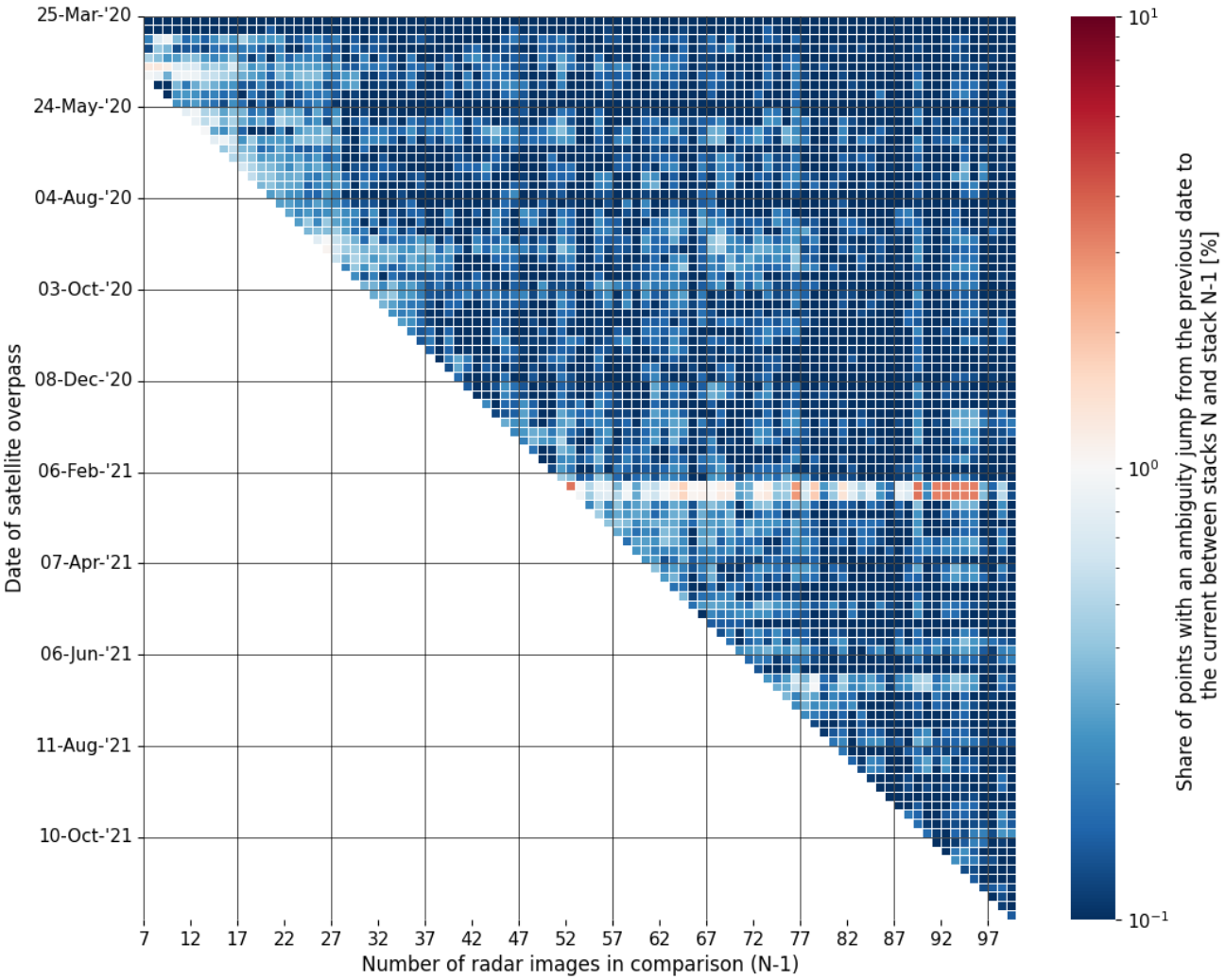

Figure A.56: Ambiguity Overview for the occurrence of cycle slips in the displacement estimates per epoch, comparing acquisition realization N with realization $N-1$. Moving horizontally, the same epoch is compared but with a different DePSI input. A vertical column contains the cycle slips of one realization comparison. Dark red indicates many cycle slips on that epoch and dark blue indicates almost no cycle slips.

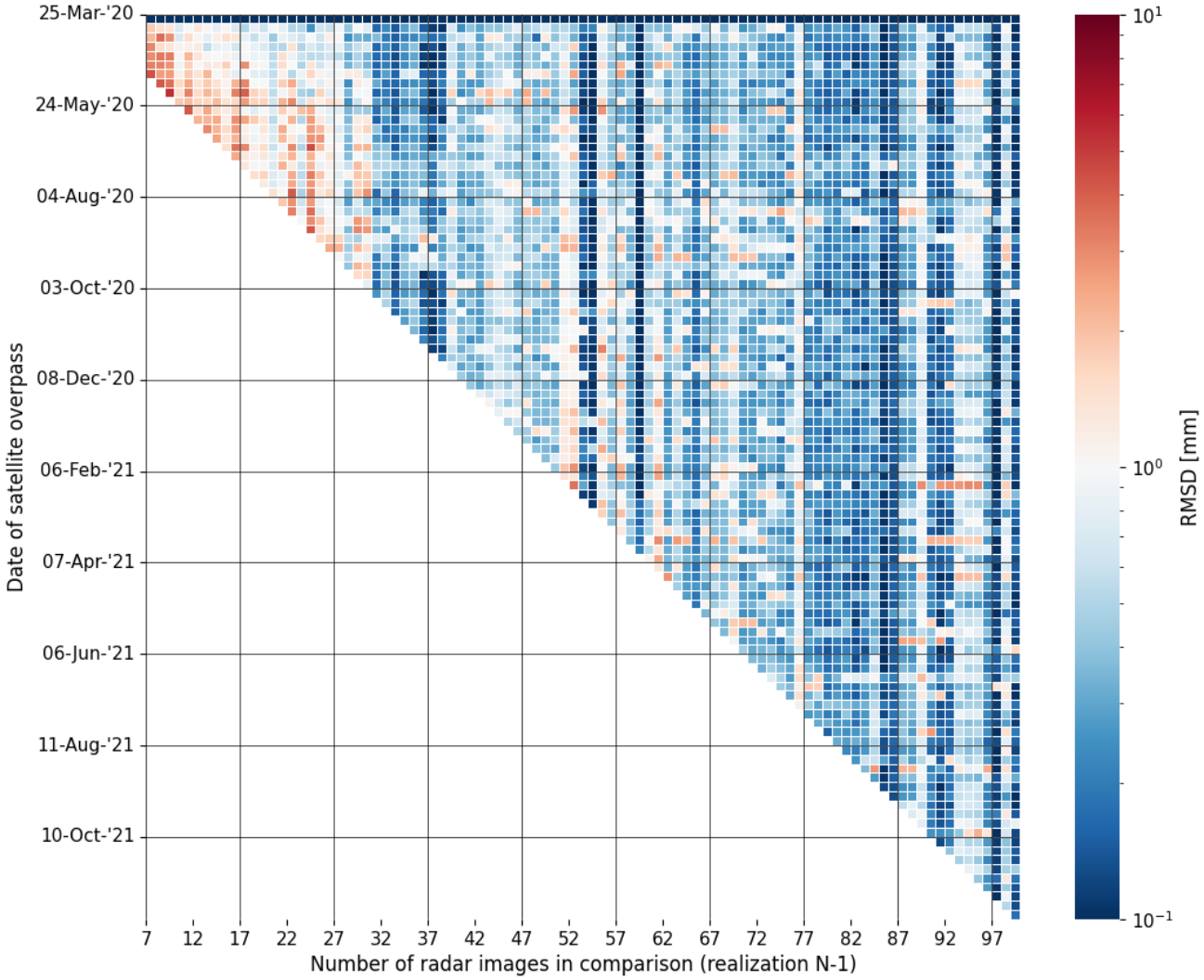

Figure A.57: RMSD Overview for the detailed version of the displacement estimates per epoch, comparing acquisition realization N with realization $N-1$. Moving horizontally, the same epoch is compared but with a different DePSI input. A vertical column contains the RMSD of one realization comparison. Dark red indicates large displacement estimate differences on that epoch and dark blue indicates almost no difference.

A.8. Combination of improvements

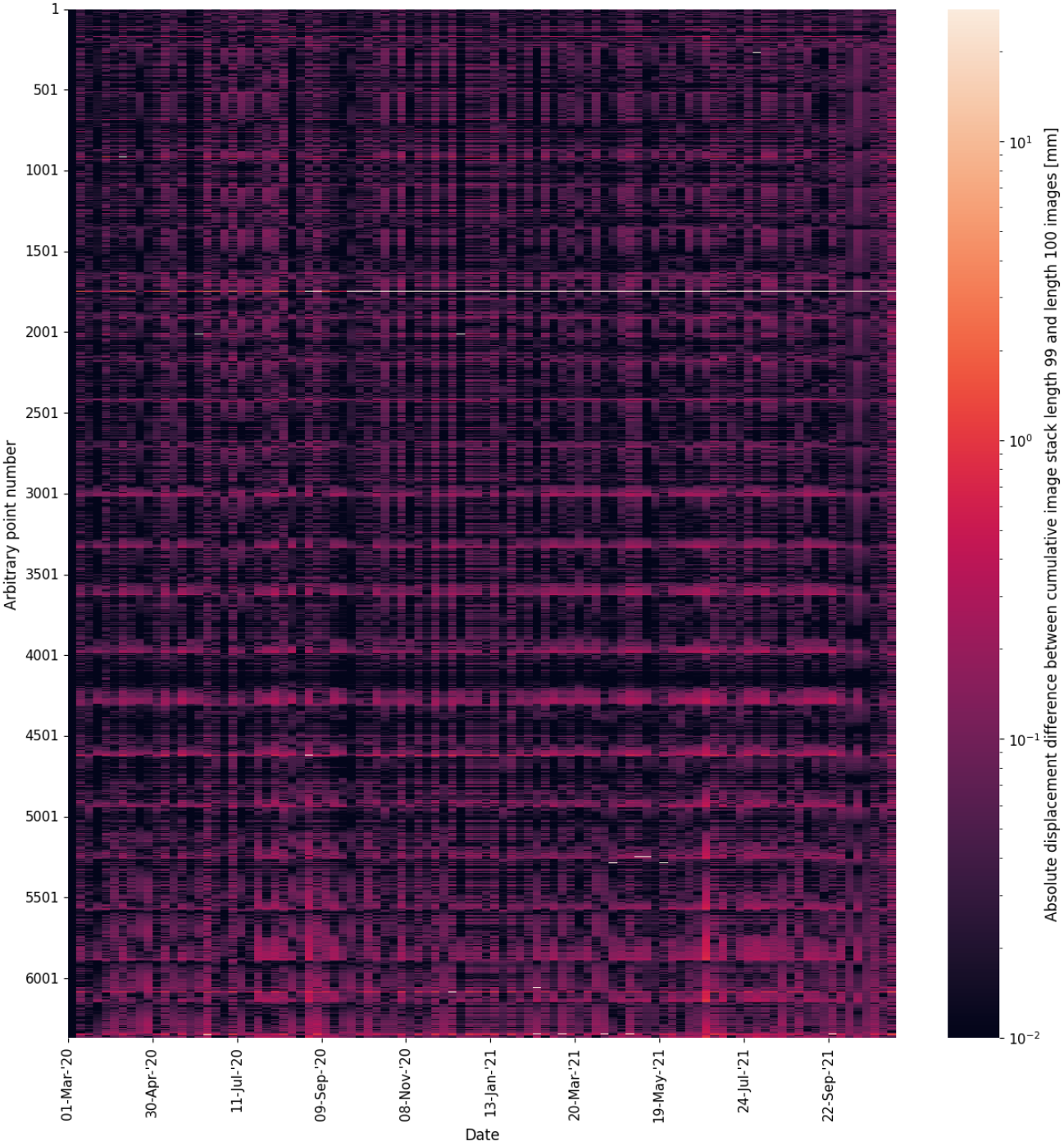

Figure A.58: Absolute Differential Space-Time Matrix containing displacement estimate differences of two Space-Time Matrices obtained from processing the conjunct pixels and epochs in two realizations. The horizontal axis contains the epoch number, starting from the 25th of March 2020 and the vertical axis represents an arbitrary point number (location).

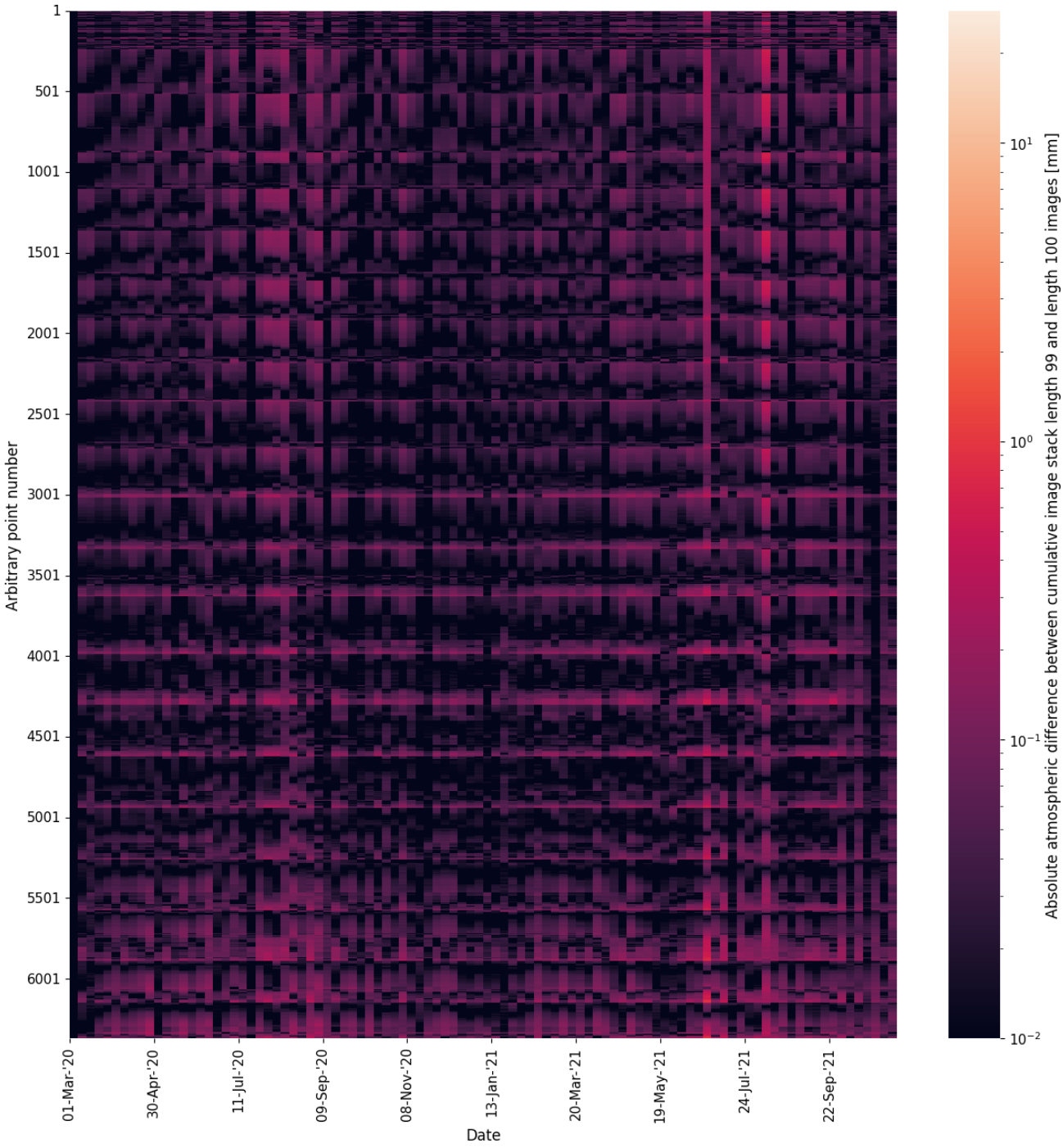

Figure A.59: Absolute Differential Atmospheric Space-Time Matrix containing atmospheric delay estimate differences of two Space-Time Matrices obtained from processing the conjunct pixels and epochs in two realizations. The horizontal axis contains the epoch number, starting from the 25th of March 2020 and the vertical axis represents an arbitrary point number (location).

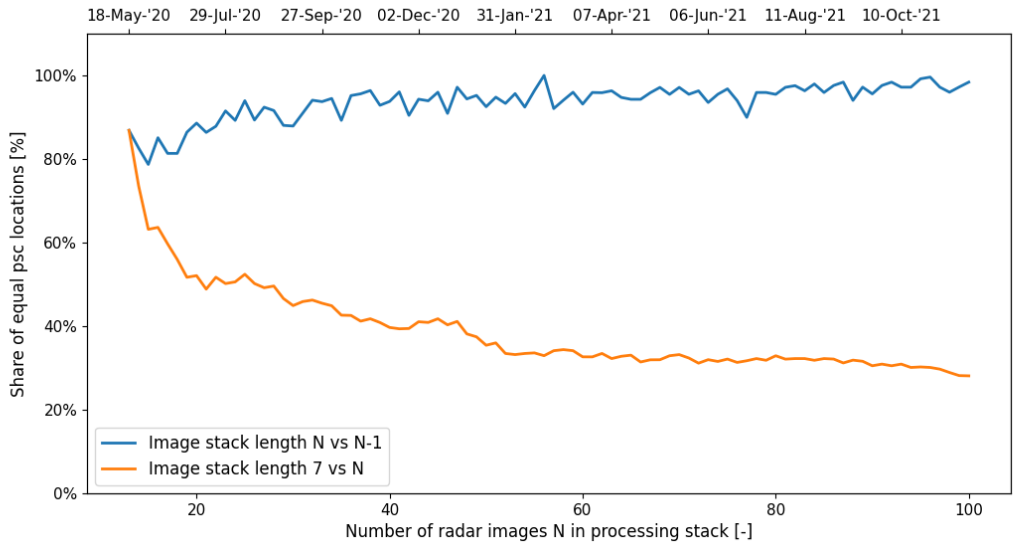

Figure A.60: Figure containing the share of identical PS1 locations over the number of realizations comparing N to $N-1$ (blue line) and N to the starting set (yellow line).

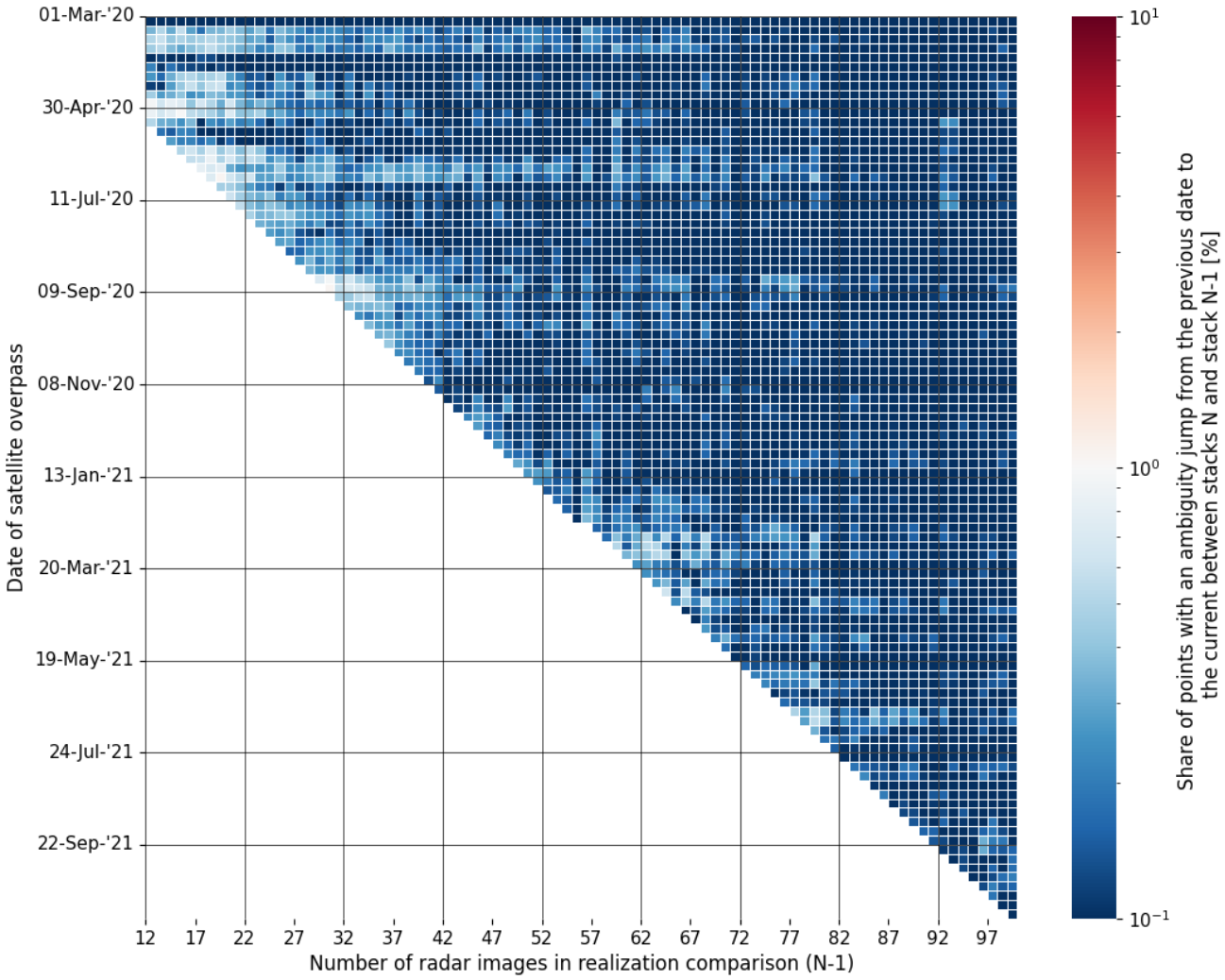

Figure A.61: Ambiguity Overview for the occurrence of cycle slips in the displacement estimates per epoch, comparing acquisition realization N with realization $N-1$. Moving horizontally, the same epoch is compared but with a different DePSI input. A vertical column contains the cycle slips of one realization comparison. Dark red indicates many cycle slips on that epoch and dark blue indicates almost no cycle slips.

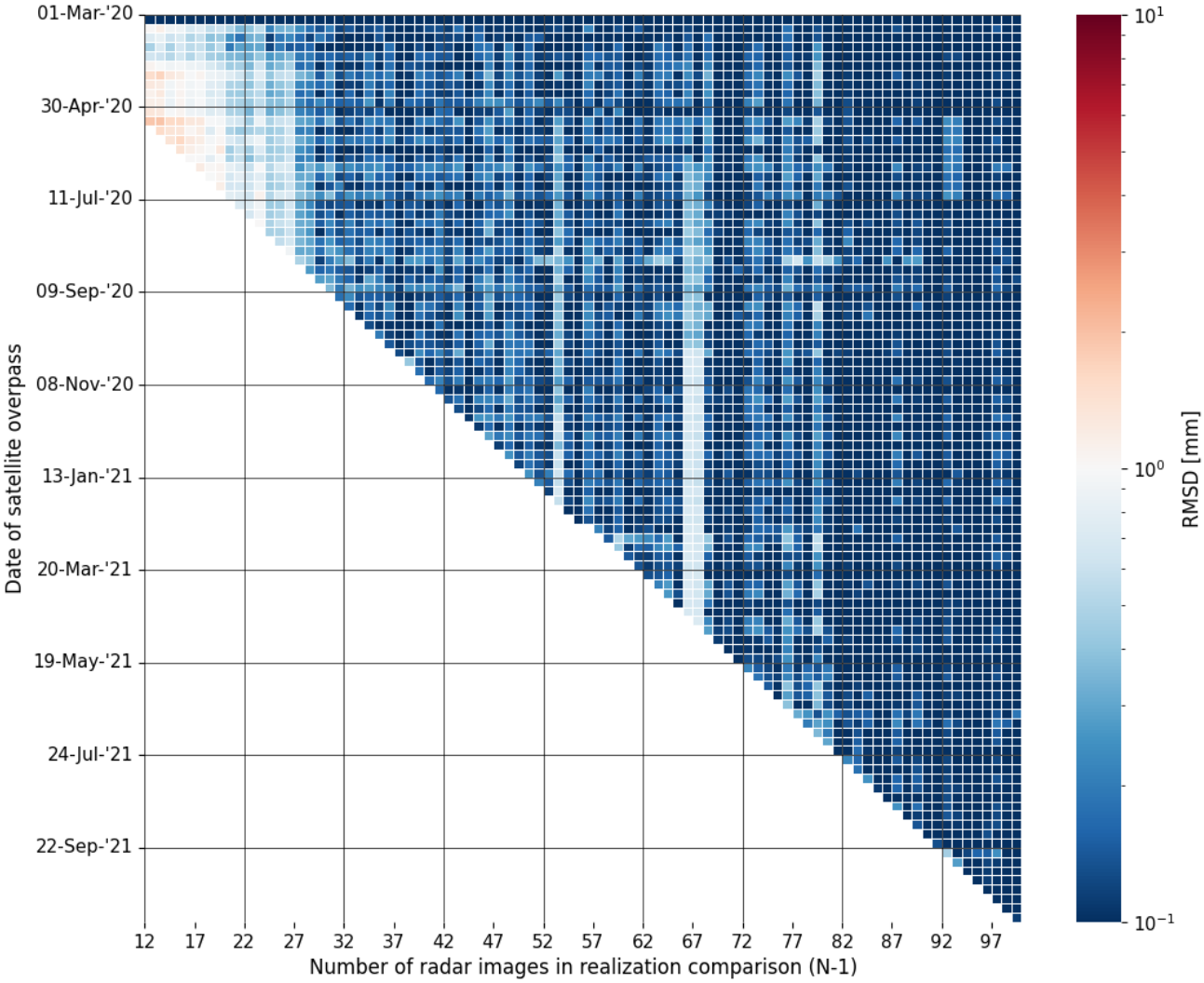

Figure A.62: RMSD Overview for the detailed version of the displacement estimates per epoch, comparing acquisition realization N with realization $N-1$. Moving horizontally, the same epoch is compared but with a different DePSI input. A vertical column contains the RMSD of one realization comparison. Dark red indicates large displacement estimate differences on that epoch and dark blue indicates almost no difference.

B

Case study figures Hondsbossche Zeewering

B.1. 5x5 km without improvements

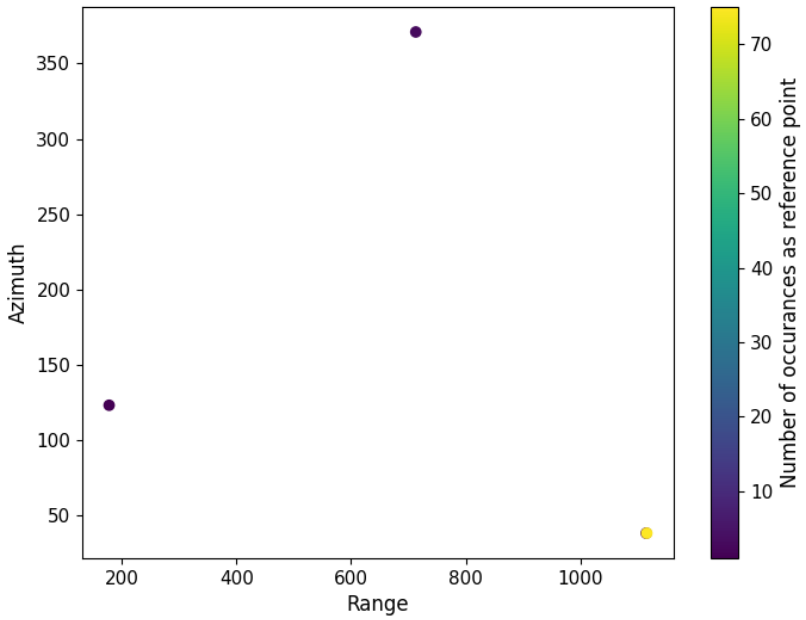

Figure B.1: Locations and number of occurrences of the reference point when the choice of reference is unrestricted.

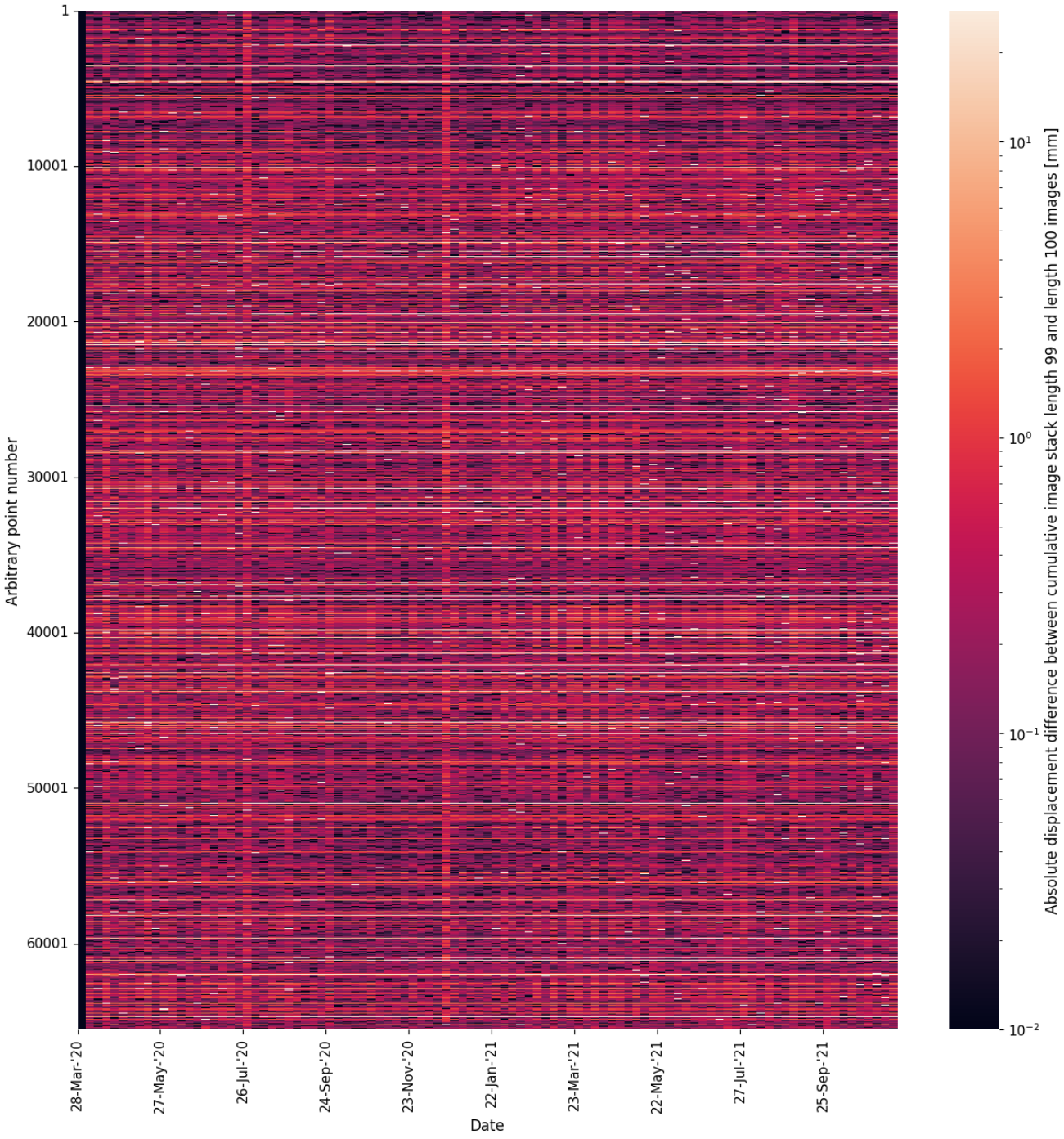

Figure B.2: Absolute Differential Space-Time Matrix containing displacement estimate differences of two Space-Time Matrices obtained from processing the conjunct pixels and epochs in two realizations. The horizontal axis contains the epoch number, starting from the 28th of March 2020 and the vertical axis represents an arbitrary point number (location).

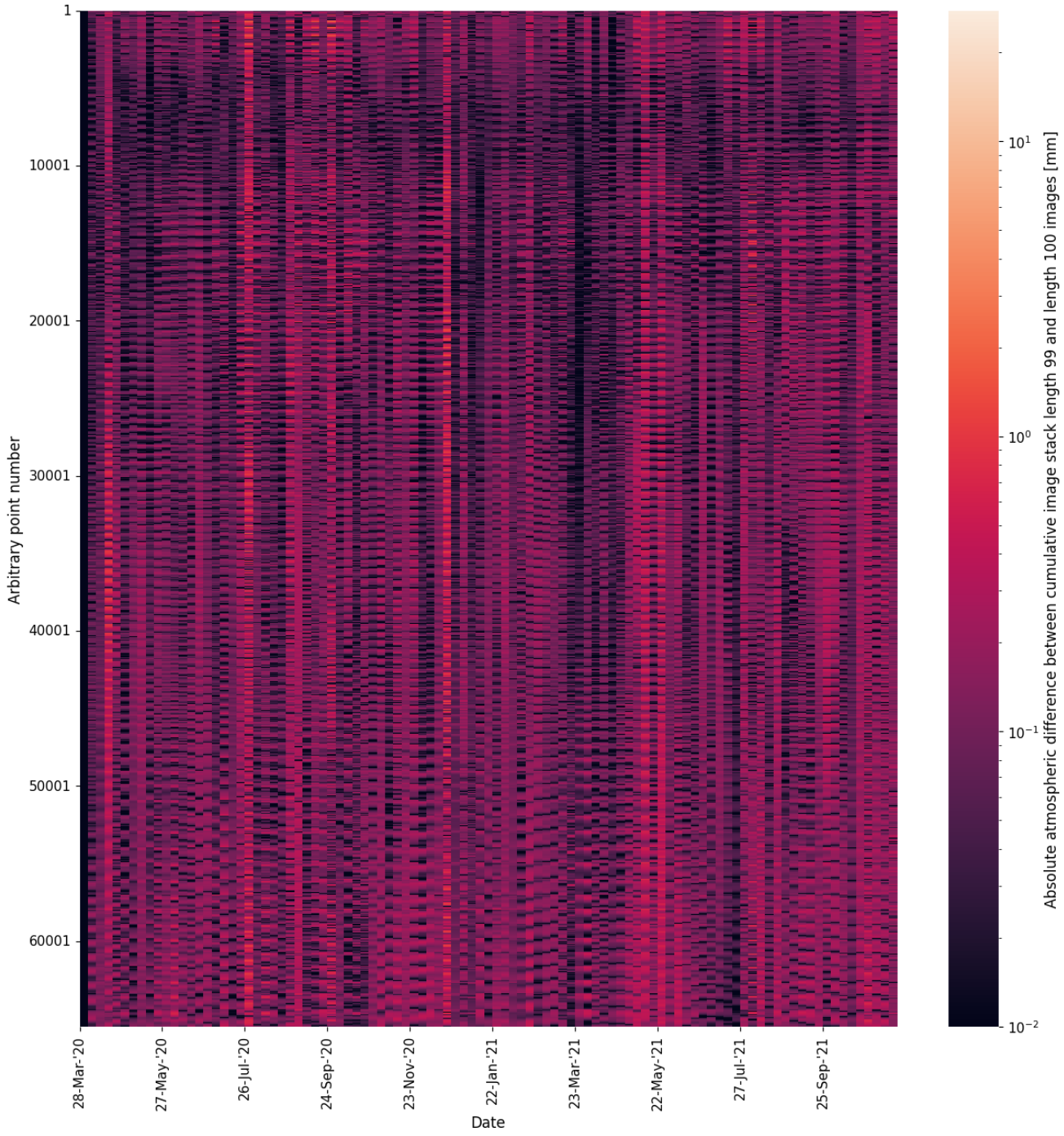

Figure B.3: Absolute Differential Atmospheric Space-Time Matrix containing atmospheric delay estimate differences of two Space-Time Matrices obtained from processing the conjunct pixels and epochs in two realizations. The horizontal axis contains the epoch number, starting from the 28th of March 2020 and the vertical axis represents an arbitrary point number (location).

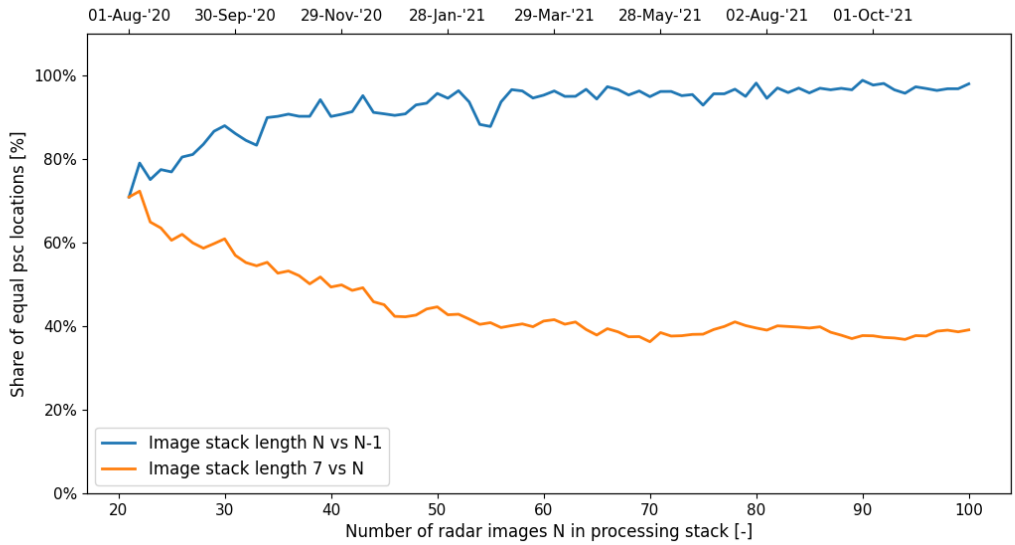

Figure B.4: Figure containing the share of identical PS1 locations over the number of realizations comparing N to $N-1$ (blue line) and N to the starting set (yellow line).

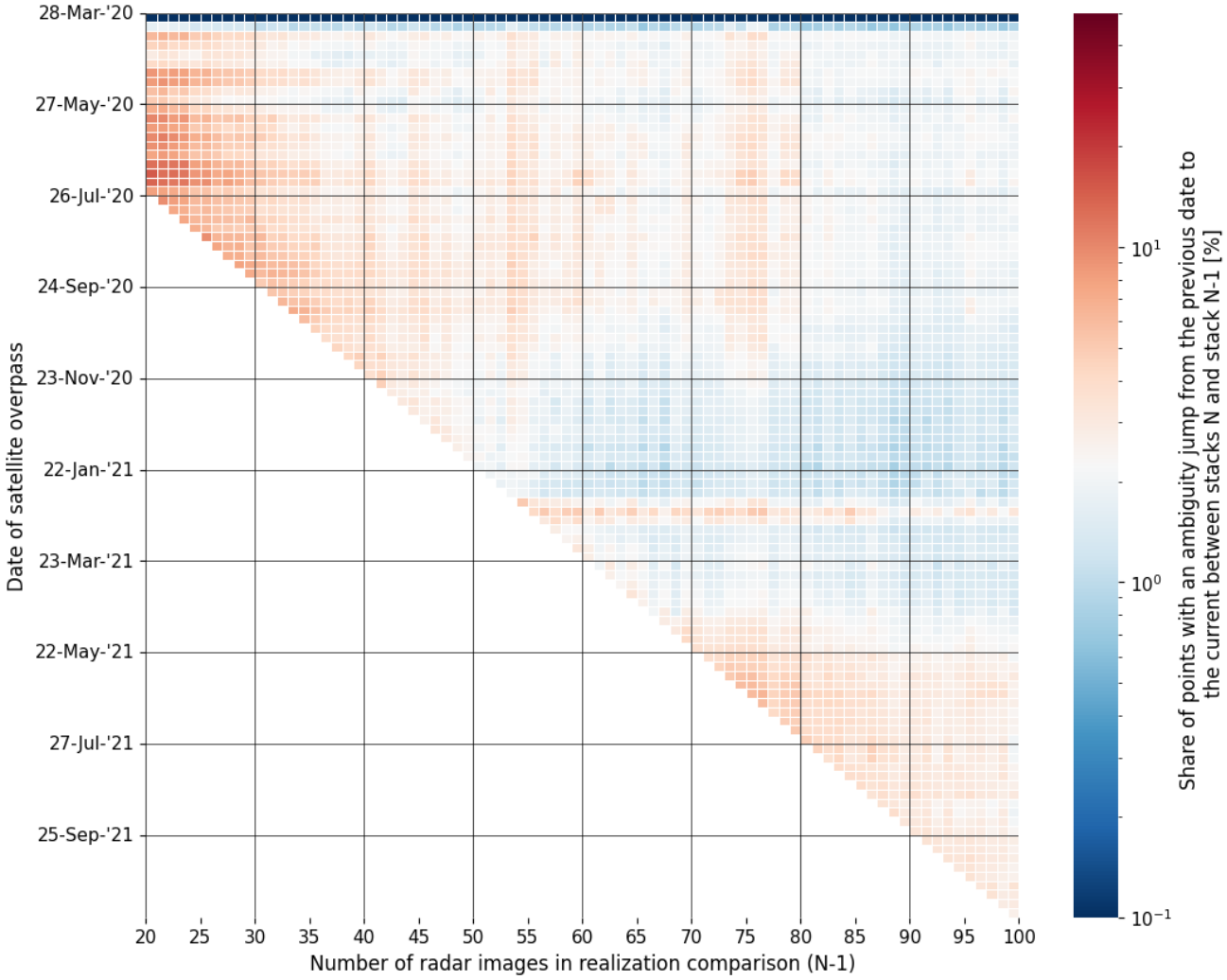

Figure B.5: Ambiguity Overview for the occurrence of cycle slips in the displacement estimates per epoch, comparing acquisition realization N with realization $N-1$. Moving horizontally, the same epoch is compared but with a different DePSI input. A vertical column contains the cycle slips of one realization comparison. Dark red indicates many cycle slips on that epoch and dark blue indicates almost no cycle slips.

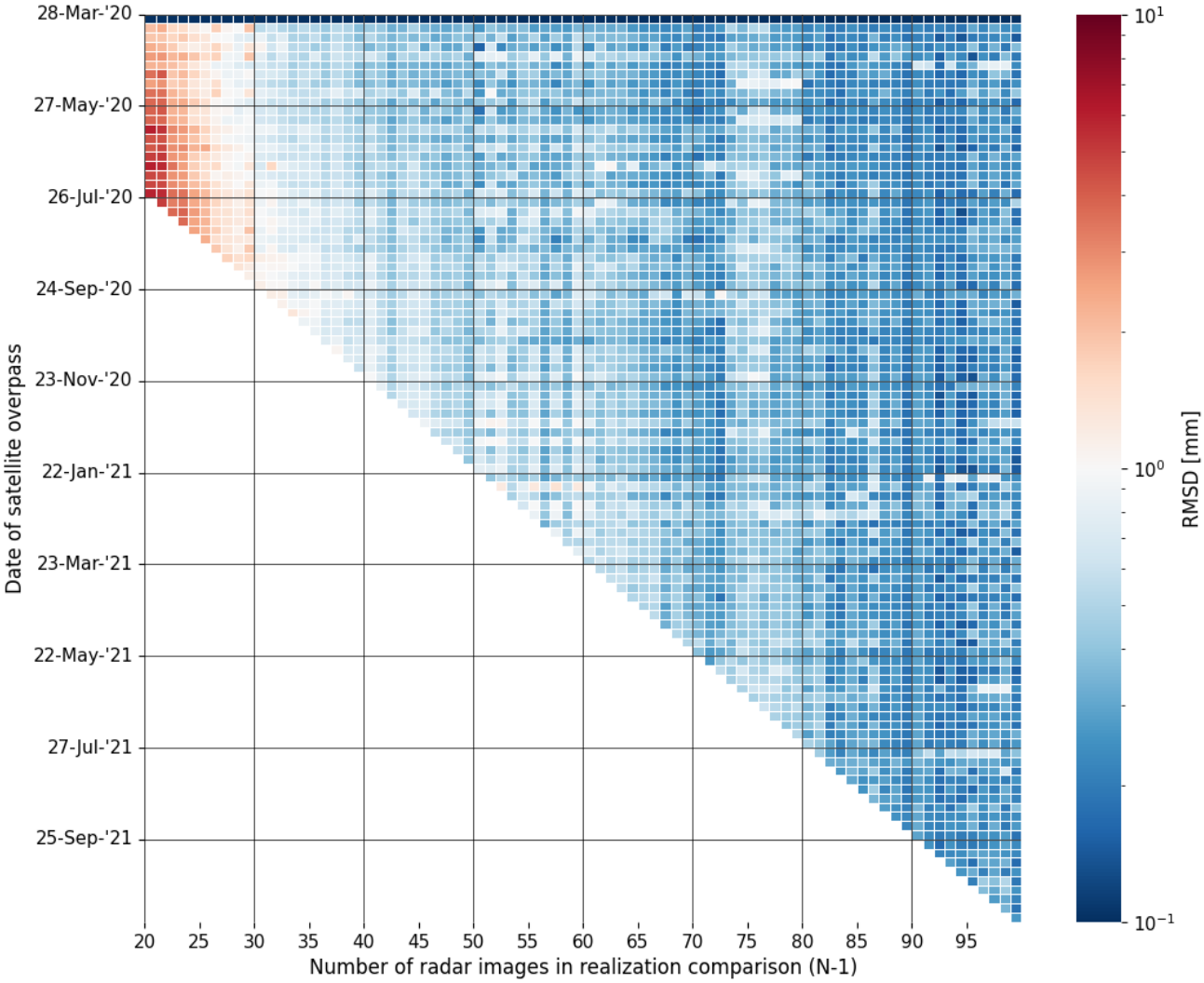

Figure B.6: RMSD Overview for the detailed version of the displacement estimates per epoch, comparing acquisition realization N with realization $N-1$. Moving horizontally, the same epoch is compared but with a different DePSI input. A vertical column contains the RMSD of one realization comparison. Dark red indicates large displacement estimate differences on that epoch and dark blue indicates almost no difference.

B.2. 5x5 km with improvements

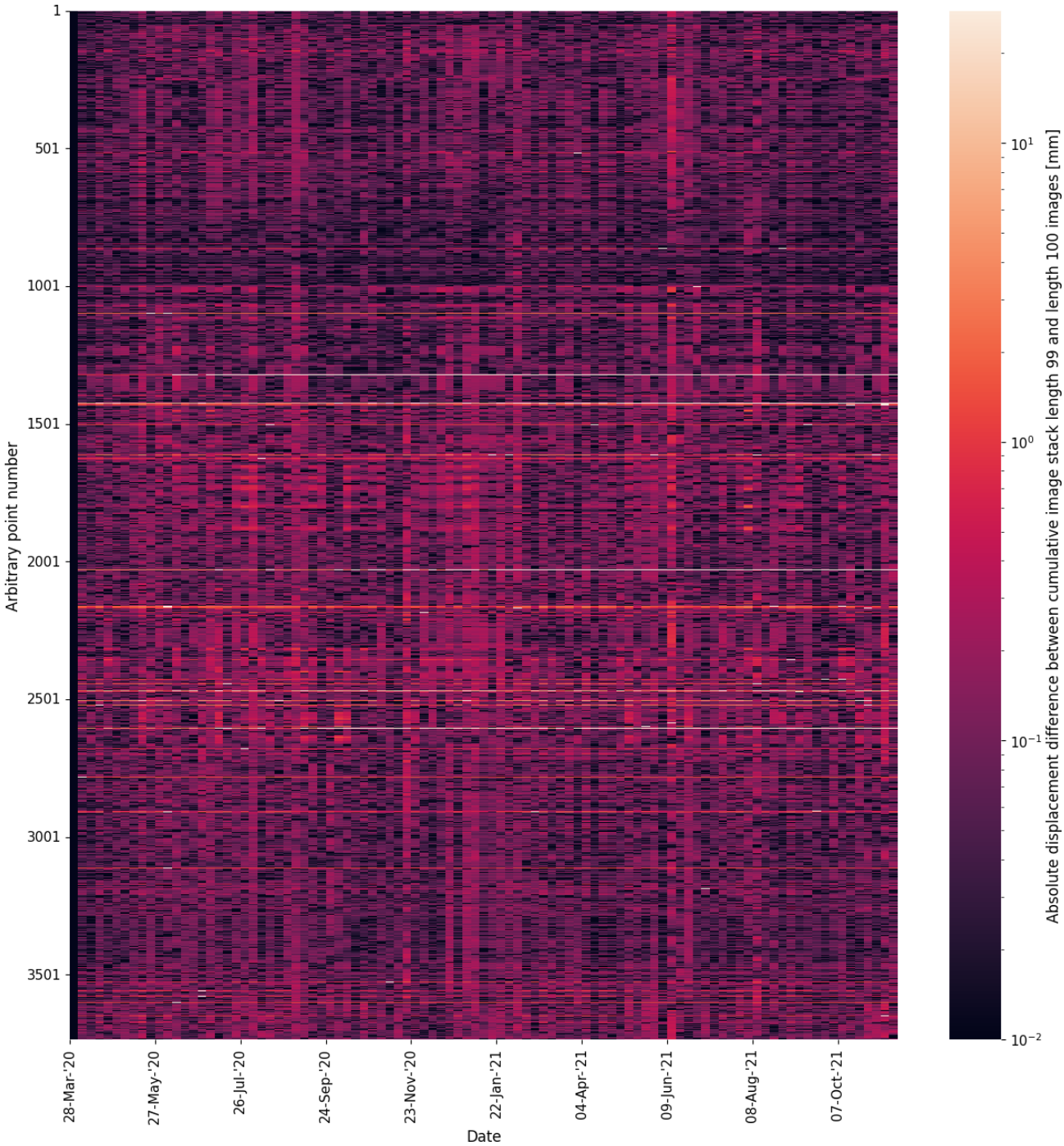

Figure B.7: Absolute Differential Space-Time Matrix containing displacement estimate differences of two Space-Time Matrices obtained from processing the conjunct pixels and epochs in two realizations. The horizontal axis contains the epoch number, starting from the 28th of March 2020 and the vertical axis represents an arbitrary point number (location).

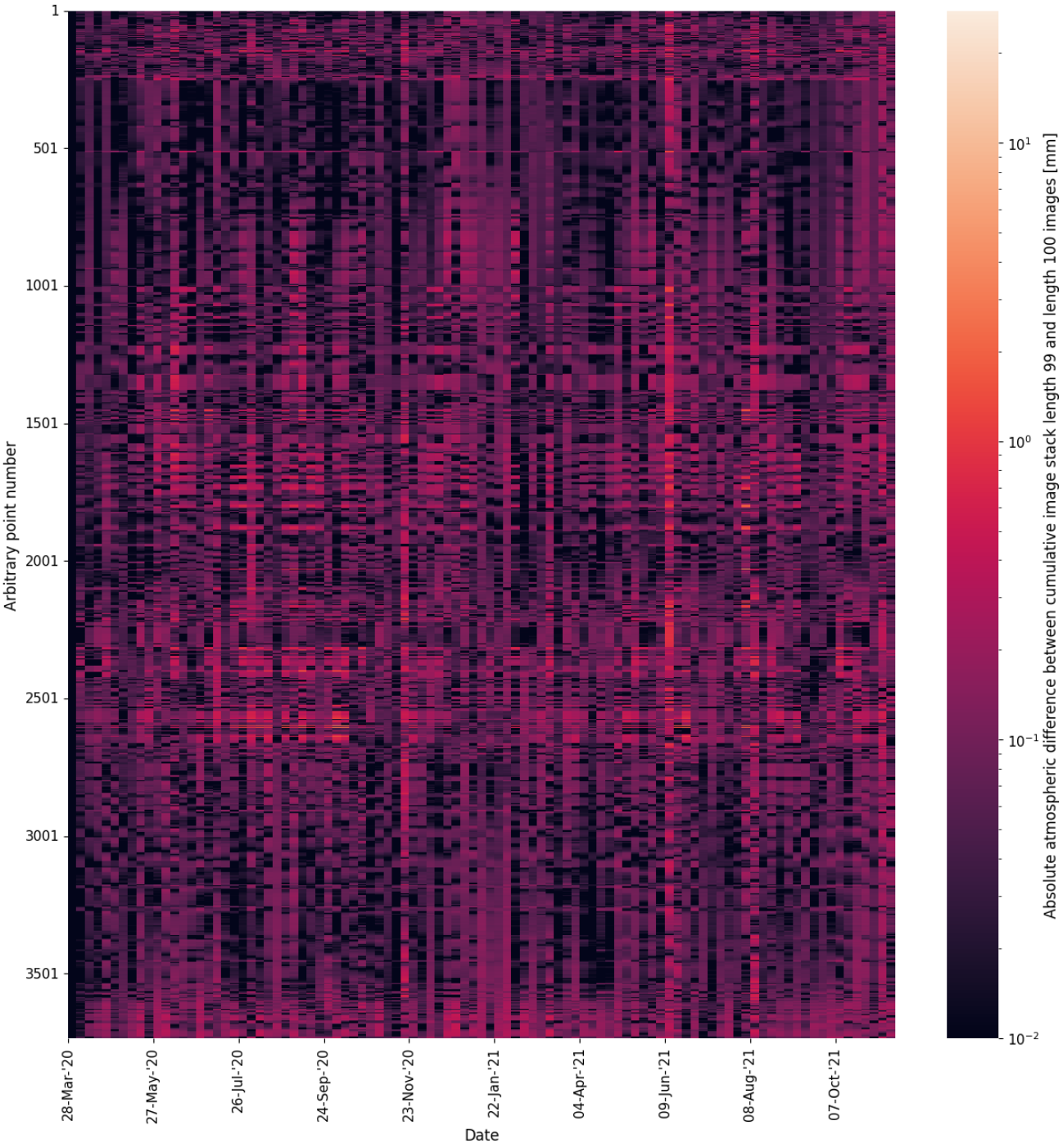

Figure B.8: Absolute Differential Atmospheric Space-Time Matrix containing atmospheric delay estimate differences of two Space-Time Matrices obtained from processing the conjunct pixels and epochs in two realizations. The horizontal axis contains the epoch number, starting from the 28th of March 2020 and the vertical axis represents an arbitrary point number (location).

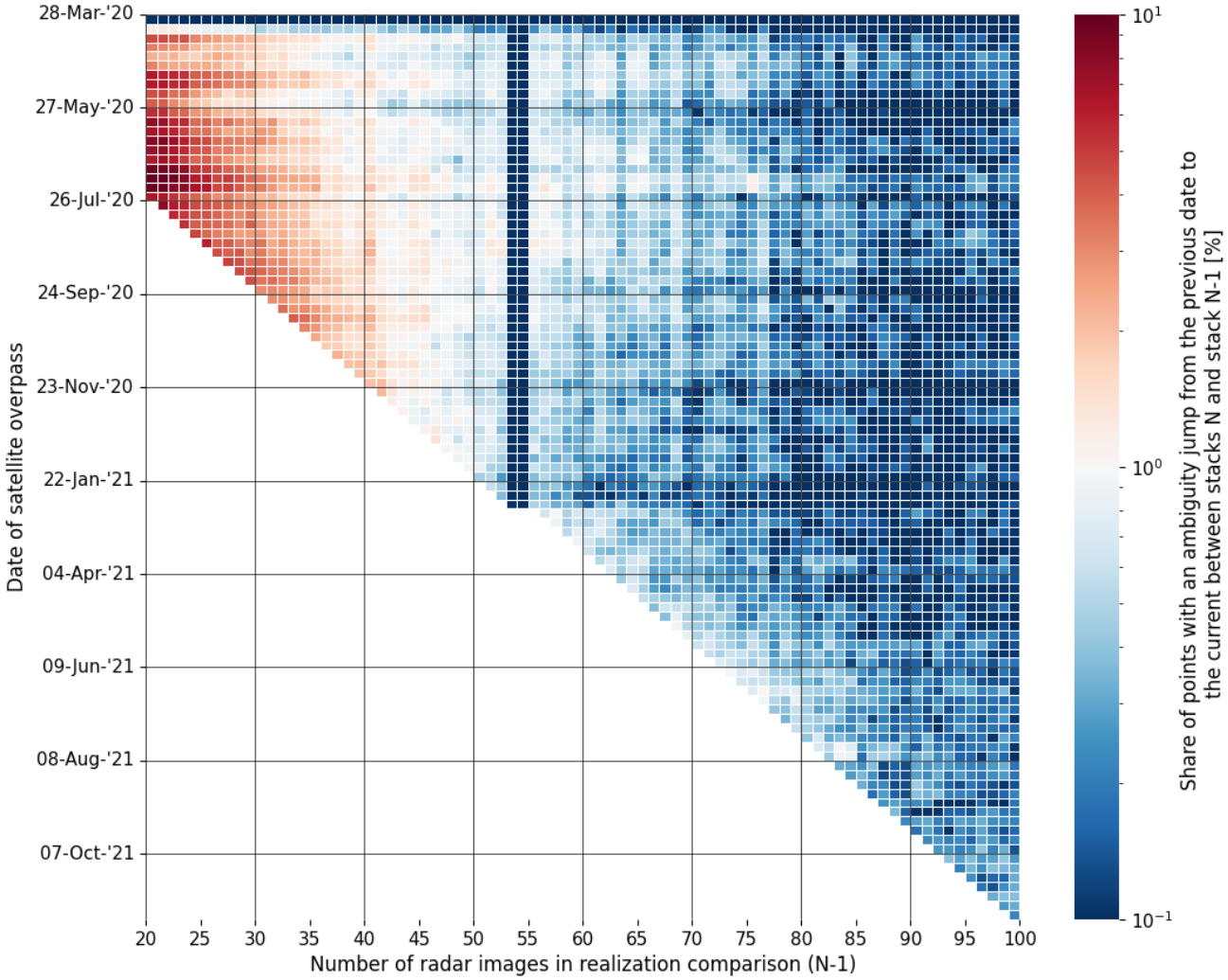

Figure B.9: Ambiguity Overview for the occurrence of cycle slips in the displacement estimates per epoch, comparing acquisition realization N with realization $N-1$. Moving horizontally, the same epoch is compared but with a different DePSI input. A vertical column contains the cycle slips of one realization comparison. Dark red indicates many cycle slips on that epoch and dark blue indicates almost no cycle slips.

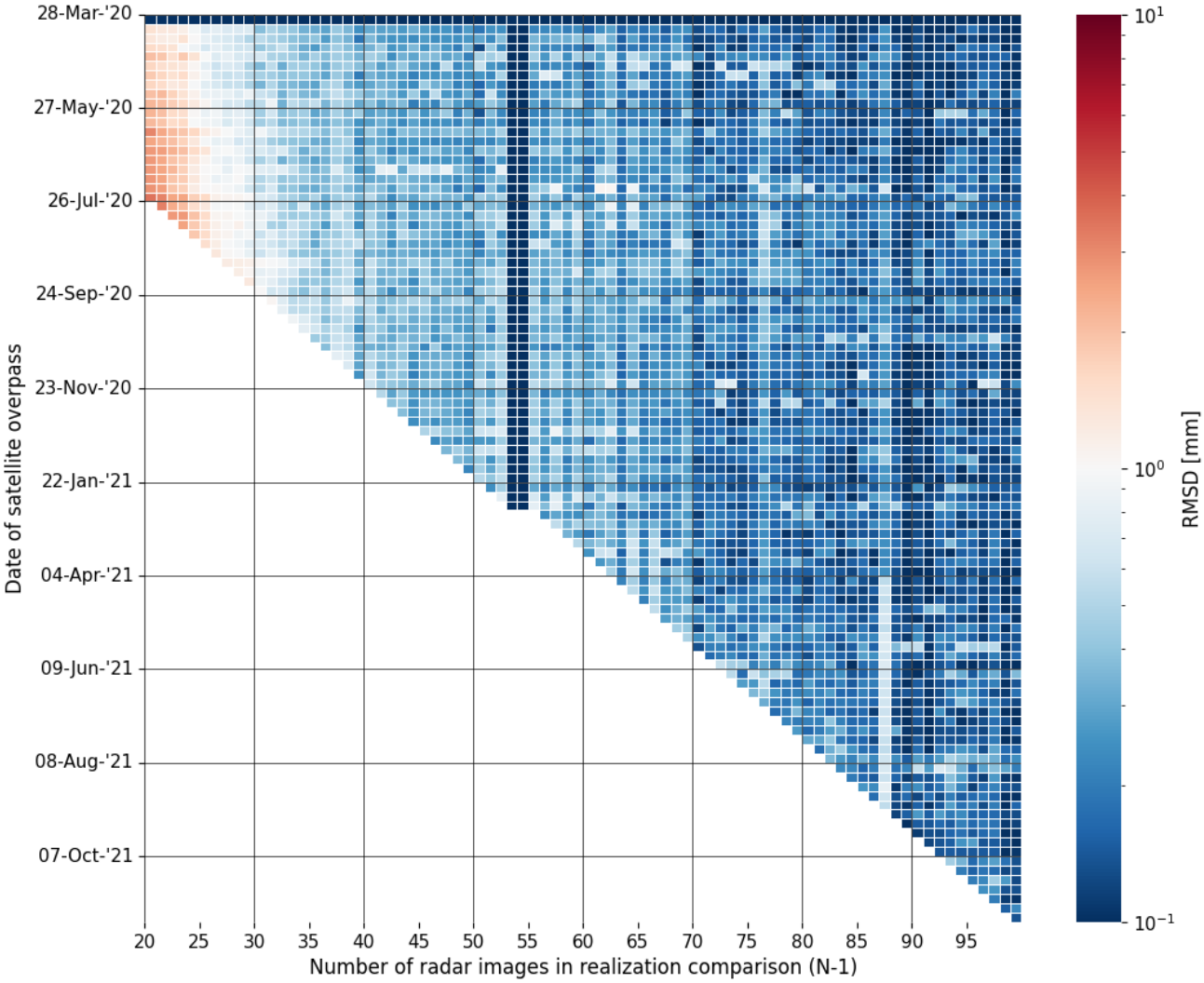

Figure B.10: RMSD Overview for the detailed version of the displacement estimates per epoch, comparing acquisition realization N with realization $N-1$. Moving horizontally, the same epoch is compared but with a different DePSI input. A vertical column contains the RMSD of one realization comparison. Dark red indicates large displacement estimate differences on that epoch and dark blue indicates almost no difference.